The Pennsylvania State University
The Graduate School
Department of Electrical Engineering

BISTATIC LIDAR MEASUREMENTS OF LOWER TROPOSPHERIC AEROSOLS

A Thesis in
Electrical Engineering

by
Timothy D. Stevens

Submitted in Partial Fulfillment
of the Requirements
for the Degree of

Doctor of Philosophy

May 1996

We approve the thesis of Tim D. Stevens.

Date of Signature

Charles R. Philbrick
Professor of Electrical Engineering
Thesis Advisor and Chair of Committee

Kultegin Aydin
Associate Professor of Electrical Engineering

Craig F. Bohren
Distinguished Professor of Meteorology

Karl S. Kunz
Professor of Electrical Engineering

Stewart K. Kurtz
Murata Professor of Materials, Research Professor of Electrical Engineering

Daniel B. Lysak, Jr.
Research Associate, Special Member

Christopher S. Ruf
Assistant Professor of Electrical Engineering

Larry C. Burton
Professor of Electrical Engineering
Head of the Department of Electrical Engineering

ABSTRACT

A study has been conducted to investigate the application of a bistatic lidar receiver to remotely determine properties of lower tropospheric aerosols, particularly the optical extinction, median radius and size distribution width. The motivation for this study is to advance our understanding of the optical scattering of aerosols with a possible long term goal of calculating extinction at many wavelengths. Single-ended remote sensing instruments, whether laser, radar, or microwave based, have difficulties determining absolute extinction along a propagation path. This is due to the large variations in the ratio of forward scatter to backward scatter for different sizes and types of particles. In fact, large variations in particle scattering as a function of angle can be used to identify particle shape, size, and width of the distribution. A bistatic linear array receiver was developed to collect information on the scattering phase function of tropospheric aerosols. Additional wavelength and angle measurements are not always useful, however, in order to estimate extinction from a single-ended instrument this additional information is necessary.

The first studies using the bistatic lidar were conducted in a marine coastal environment during the Wallops CASE I (Coastal Aerosol Scattering Experiment) program. The measurements were made under sufficiently high relative humidities that it is reasonable to use a spherical model to describe the scatterers. One of the objectives of this research effort is to determine how well a spherical scattering model (Mie theory) and a lognormal particle distribution can describe the measurements from this bistatic receiver. The results show remarkable agreement with the model on certain evenings, while at times the measurements and model show significant differences.

A trimodal lognormal distribution of aerosols was observed on September 14, 1995 to increase in size during a period of several hours when the relative humidity remained constant at 92% and the temperature decreased from 23° to 22°C. A radiation fog mode of nearly monodispersed particles grew from 6.46 μm to 8.91 μm over a period of 2.5 hours. During this same period a smaller and broader mode narrowed its distribution width as it grew from 0.166 μm to 0.237 μm. Many of the measured profiles are very sensitive to small changes in the size distribution and therefore add confidence to these extinction calculations. An error analysis determines that the mean particle radius of the radiation fog, measured from the bistatic lidar, is known to an accuracy of ±0.41 μm. Extinction coefficients calculated from the bistatic receiver data are compared with the monostatic lidar extinction determined using the Raman molecular profiles, which have been shifted to wavelengths at 607 and 530 nm. The error analysis is used to determine the dependance of extinction on each of the nine parameters. As the particle sizes grow, the bistatic lidar prediction of the extinction agrees with the extinction measured from the Raman lidar. On nights when Mie theory describes the results, an analysis is provided which examines the range of size distributions that will provide a consistent fit to the data. It has been determined that this bistatic measurement technique along with Mie theory provides a useful method to characterize aerosol scattering in a humid coastal marine environment.

TABLE OF CONTENTS

LIST OF FIGURES

LIST OF TABLES

ACKNOWLEDGMENTS

During my graduate work at Penn State I have gained much more than technical and scientific skills, I have grown and matured in ways I doubt would have been possible without the guidance and counseling of a true mentor. C. Russell Philbrick was much more than an advisor, he was a friend, role model and provider of opportunities, I will forever be indebted to him for his unselfish and caring attitude, that always wishes the best for myself and others. In a world where many believe that personal gain comes only at the expense of others, it is refreshing to have an advisor and committee that understand the importance of helping everyone to succeed, and wishing failure for no one. I have learned that my success in life will be determined more by my ability to interact with others, than by my technical or scientific knowledge.

My committee members, Christopher Ruff, Karl Kunz, Craig Bohren, Daniel Lysak, Kultegin Aydin, and Stewart Kurtz have all helped in different and unique ways, whether it was by providing technical expertise, an occasional word of encouragement, or just keeping me honest and focused. Without their continuing support and patient advise I could never have focused and completed my dissertation when I did.

Bob Smith, Franz Balsiger, Glenn Pancoast, Savy Mathur, and Mike O'Brien all deserve special thanks. Bob and Franz contributed and stimulated many ideas to this work from casual conversation, and are to be commended for their patience when offering advice. Glenn Pancoast is one of the hardest working, and resourceful people I have ever met, if it were not for his ingenuity and work ethic, neither the bistatic lidar project or the LAMP project would be the success they are today. Savy, Mike and Franz all deserve a word of thanks for their untiring assistance, and for staying up all night to help collect the data used in this thesis.

My thanks go to Preschutti & Associates for their support, and for providing me with the opportunities to experience 'real world' engineering. I am especially grateful to Joe Preschutti for his caring and understanding while I worked on my degree.

I would like to thank all those who have supported my graduate work: the Applied Research Laboratory for the Exploratory and Foundational Grant and to The DuPont company for the research fellowship and teaching fellowship. Special appreciation for the support of this dissertation goes to Dr. Juergen Richter of NCCOSC NRaD, and to Dr. Geary Schwemmer of NASA GSFC.

The development of the LAMP instrument was supported by the National Science Foundation, the U.S. Navy's SPAWAR PMW-175 Environmental Systems Program Office, the Penn State Applied Research Laboratory, the College of Engineering, and the Department of Electrical Engineering.

To my family; Mom, Dad, Laurie, and Grandparents, I would never have made it this far if it would not have been for the values instilled in me when I was young, for this I will be eternally grateful.

And finally, to my fiancee Sharon Shaw, you have given my life meaning and without your support and encouragement this thesis would never have been written. I am looking forward to the many joyful years we will spend together.

STATEMENT OF PROBLEM

This thesis describes the design, development, modeling, and experimental tests of a unique bistatic lidar measurement technique. The motivation for developing a new lidar technique was to be able to remotely determine extinction along a vertical or horizontal path, using a single-ended instrument operating at only one wavelength. The problem of determining atmospheric extinction will not be fully solved with just one investigation, but this thesis advances our understanding and solves major parts of the problem. The incentive to measure atmospheric aerosol extinction is due to its impact on commercial air traffic, electro-optical communication systems, and many military systems. The development of more accurate measurements of low altitude aerosol content for global models is also a motivation. Today there is not an acceptable method to accomplish the above goals; however, the research presented in this thesis should help us move one step closer to these goals.

The first step in solving the problem of determining atmospheric extinction was to investigate what information was available, but not being used. The information contained in the angular scattering function of the particle (or scattering phase function) has not been fully used in describing the particle properties. Nephelometers use this information in a controlled environment to collect in-situ data, but active remote sensing experiments usually observe no more than several angles at a time. In order to take full advantage of the particle information contained in the scattering phase function, a large continuous range of scattering angles would need to be measured simultaneously. A photodiode or CCD array located away from the source where it could image the entire laser beam was the answer. If the horizontal path is uniform, the receiving array could collect data from many angles at the same time.

The instrument technique, which has been developed, uses a linear diode array to image a horizontally propagating laser beam through a homogenous atmospheric path. The receiver collects radiation scattered at angles from 155° to 180°, representing a portion of the scattering phase function. However, the absolute value of the intensity as a function of angle is inaccurate due to many variables across the field of view of the receiver. An alternative is to collect two measurements, one with the laser beam linearly polarized parallel to the scattering plane, and one perpendicular to the scattering plane, then make use of the ratio of the two measurements. This ratio cancels most of the errors, pixel by pixel across the image plane, which have been introduced by the receiver and geometry of the experiment. Each single measurement is equivalent to many independent measurements due to the wide range of angles collected. Of course, this assumes that the particle distribution is uniform along the path.

The second part of the investigation was to determine how to interpret the data collected by the linear array receiver. Mie theory completely describes the scattering for a sphere with a known index of refraction. However, the question of how well tropospheric aerosols in a coastal environment could be described with a spherical model was still left to be answered. A model was developed to predict what would be measured in an atmosphere consisting of trimodal lognormal distributions of spheres, with the understanding that particles are not necessarily spherical in shape. Calculations were made using this model to determine what useful and significant structure was present when typical size distributions of particles were studied.

It was decided to test the instrument and technique in a humid coastal marine environment where modeling of the aerosols would be possible. Because the measurements are made in a marine environment some of the nuclei will consist of NaCl, and under high relative humidities they will deliquesce forming spherical solution droplets. This means that most of the time a spherical model would be a reasonable representation of the scatterers. Part of this research is focused toward determining how well a spherical model with a trimodal lognormal particle distribution will describe the data. The results from the experiments show remarkable agreement between the model and the data, and a detailed error analysis adds confidence to the measured extinction coefficients.

Chapter 1

INTRODUCTION

Scattering of visible, ultraviolet and infrared radiation by atmospheric particles has a major impact on commercial air traffic and on many military systems. It has become critically important, with many modern systems, that the electro-optical environment be properly characterized. The fact that lidar techniques are capable of describing the electro-optical scattering in a coastal marine environment, will be shown in this thesis. Most of the past applications of lidar to describe the electro-optical environment have failed to provide satisfactory results because the techniques have generally focused on measurements of the backscattered radiation at the transmitted laser wavelength. We have shown that molecular scattering from rotational and vibrational Raman backscatter can be used to directly determine the extinction profile through optical scattering regions containing aerosols and cloud layers (Philbrick et al., 1993, 1994).

A bistatic remote receiver has been designed to collect scattering angle and polarization information from a pulsed or continuous laser source. This instrument collects an image of the radiation scattered from the first few kilometers of the atmospheric path, with the idea of using the information contained in the polarization components of the scattering phase function to determine atmospheric particle mean radius and size distribution. By collecting data at a continuous range of angles relative to the laser transmitter, the additional information contained in the scattering phase function is obtained. This is analogous to an in-situ particle measurement system, such as a nephelometer, with a real-world atmospheric path. The Raman lidar extinction together with the backscatter phase function and polarization provide information about the particle size distribution that can be used to extend the extinction and transmission calculations to a wide range of wavelengths.

We desire to remotely infer accurate vertical atmospheric extinction and transmission profiles, at multiple wavelengths, through aerosol layers within the first kilometer of the atmosphere, without assuming any relationship between backscatter and extinction. This is indeed a high expectation, but we will show that the information contained in the phase function makes it reasonable to pursue this goal for lidar under certain atmospheric conditions. Current lidar techniques cannot provide a solution to this problem.

The results of Chapter 5 show that accurate visibility measurements could be made from aircraft and ships at sea without instruments located at both ends of the path. Real-time decisions could also be made to determine optimum selection or combination of sensors for any given atmospheric condition. Aerosol models are not reliable for extinction calculations over land because of the high variability of aerosol sources. But over the ocean, the aerosol composition remains relatively constant and the particle size can be related to relative humidity and wind speed, which are easily measured quantities. Problems still exist when extinction is extrapolated to wavelengths in the infrared and ultra-violet. It is our hypothesis that important information needed to describe the scatterers is contained in the phase function and polarization of the scattered lidar signal. The following sections explain the importance of tropospheric aerosols and past remote sensing techniques used to examine their characteristics.

1.1 Importance of Understanding Tropospheric Aerosols

Studies of tropospheric aerosols have generally been focused on two categories, their effects on climate, and their effects on electro-optic systems. Together with molecular scattering and absorption by gases, aerosols and clouds determine what fraction of the solar radiation incident at the top of the atmosphere reaches the Earth's surface. Not only do aerosols scatter and absorb radiation they also act as nucleation sites for cloud droplets. Consequently, aerosols and clouds play an important role in determining the Earth's climate. In this thesis, the focus is upon the local distribution of aerosols, such as would be of particular concern for electro-optical system performance.

The atmosphere optical depth has three components, one due to molecular scattering, one due to particle scattering, and a third due to absorption by gases (e.g. ozone). The aerosol scattering contribution is described by a quantity called the atmospheric turbidity. One definition of turbidity is the Linke index, which represents the number of molecular atmospheres that must be stacked one on top of the other to produce the measured attenuation of sunlight (Stephens, 1994). Turbidity is usually measured as an average quantity through the entire depth of the atmosphere, which is a good definition for radiative transfer models, but does little to predict the local attenuation of radiation due to particle scattering. Aerosols are much more difficult to model than gases because they are not evenly distributed throughout the Earth's atmosphere. The U.S. military uses several electro-optic systems that are all dependent on the transmissivity between the target and the sensor. Transmission is a parameter required as an input to computer algorithms that determine the maximum range for EO sensors under different atmospheric conditions. These models are used to evaluate the effectiveness of a particular system and to develop better and more effective EO systems. However, the ideal situation would be for the system to measure and calculate its own range in real time from measured and modeled atmospheric properties. This presents quiet a challenge because such a system would have to be single-ended and be able to fit on one platform, (e.g. ship, aircraft, land vehicle). The focus of this research is not to improve existing Navy aerosol models, NAM, NOVAM (Gathman, 1983), but to develop a better method to measure the local aerosol properties such as extinction, remotely.

1.2 Tropospheric Aerosol Definition

An aerosol is a suspension of a solid or liquid particle in a gaseous medium with a slow settling time. This definition covers just about anything that resides in the atmosphere for any length of time, but for the purposes of this thesis insects are excluded and cloud particles will be referred to separately as cloud particles. Aerosols vary greatly in concentration and in the case of haze and dust particles, also in chemical composition, making them even more difficult to model. The real and imaginary parts of the refractive index can change markedly from one type to another, and aerosols are in general not spherical, thus the theoretical properties to be described are meant only to roughly represent real aerosols.

1.2.1 Types of Aerosols

Aerosol types are classified three different ways: by size, geographical region of formation, and by production mechanism. Junge (1955) classified aerosols into three different groups based upon their geographical source region: maritime, continental, and background. He also classified them by size according to their radius as shown in Table 1.1. Whitby (1973) categorized aerosols into groups according to their production mechanism, also shown in Table 1.1. Therefore, aerosols over the ocean with a radius of 0.133 μm would be classified as maritime type II aerosols. These aerosol types will be referred to later when particle size distributions are used to test the bistatic lidar model, and invert the data collected at Wallops Island.

Table 1.1. Particle types classified according radius and production mechanism.

type I	Aitken	nucleation mode	gas-to-particle conversion	0.001-0.1 μm
type II	large	accumulation mode	coagulation/heterogenous	0.1 - 1.0 μm
type III	giant	coarse particle mode	mechanical process	> 1.0 μm

1.2.2 Aerosol Sources

There are two major sources of atmospheric aerosols: surface sources and spatial sources. Surface sources are sources located at the base of the atmosphere (e.g. oceans, deserts, people, volcanoes), and spatial sources refer to sources distributed within the atmospheric volume (e.g. clouds, gas-to-particle conversions). Extraterrestrial sources, such as dust from meteorites are negligible for the focus of this paper. A list of the major surface sources and a brief description follows. All estimates of particle mass per year are from (Hobbs, 1993).

Marine: Because the oceans cover about 70% of the Earth's surface, they are considered one of the largest single sources of atmospheric aerosols, up to 1,000 Tg/yr. The particles produced are mainly sea-salt and dimethylsulfide (CH_3SCH_3) or DMS. Navy models use wind speed to determine number densities and size of these aerosols at sea. These aerosols are also fairly constant and can be modeled much easier than aerosols over land. This type of particle is of particular concern for this study because the measurements were conducted in a coastal marine environment.

Crustal: Deserts cover about one-third of the land surface, making them the largest source of particles from the Earth's crust. These aerosols result mainly from weathering and wind-blown sand abrasion of bedrock. Crustal sources place more than 2,000 Tg/yr of aerosols into the global atmosphere.

Biomass Burning: Soot particles (mostly carbon) and fly ash are directly injected into the atmosphere during burning. This includes natural and anthropogenic influences from wildfires, vegetation burning, and agricultural waste burning. It has been estimated that biomass burning injects about 450 Tg/yr of global atmospheric aerosols.

Volcanoes: Volcanoes are not as important as the other sources for this investigation because their long term effects are in the stratosphere and while the tropospheric effects can be significant, they are localized. Most of the volcanic dust particles injected into the troposphere are too large for long distant transport and settle out quickly.

Anthropogenic: These aerosols are derived from power plants, industry, and traffic. They include nitrate, soot, fly ash, and road dust particles.

The second source of aerosols is from growth within the atmosphere, primarily clouds and gas-to-particle conversions. These particles will be significant at any location.

Clouds: Clouds are a source as well as a sink for atmospheric aerosols. When clouds evaporate without precipitating, they leave behind their chemical mass in the form of aerosol. It is estimated that clouds produce about 3000 Tg/yr of atmospheric aerosols. This source has been suggested to explain the uniform background of aerosols in the troposphere (Hobbs, 1993).

GPC: Gas-to-particle conversion occurs by either heterogeneous or homogeneous nucleation. Heterogeneous nucleation refers to the growth of existing particles by the condensation of atmospheric gas, namely water vapor. This process occurs on particles with a radius range between 0.1 - 1.0 μm. Only minor supersaturation is needed. Homogeneous nucleation also could form new particles from the size range smaller than 0.1 μm, but this process requires unlikely supersaturations in excess of 300% (Hobbs, 1993).

1.2.3 Aerosol Size Distributions

The size spectrum of aerosols is, in general, continuous and may cover over four orders of magnitude in radii, namely 0.001 μm to 100 μm. Atmospheric particles can range in excess of 1 cm for hailstones and snow. Figure 1.1 shows the range of aerosol sizes commonly observed in the atmosphere (Measures, 1984). Aerosols don't exist in the atmosphere at a single particle size, they are distributed throughout a range of sizes. For the purpose of modeling and for inverting data collected by remote sensing, a size distribution must be assumed. Many different size distributions have been used, Junge's power law, modified gamma distribution, and normal distribution just to name a few. The most successful model for continental and maritime aerosols has been the sum of three

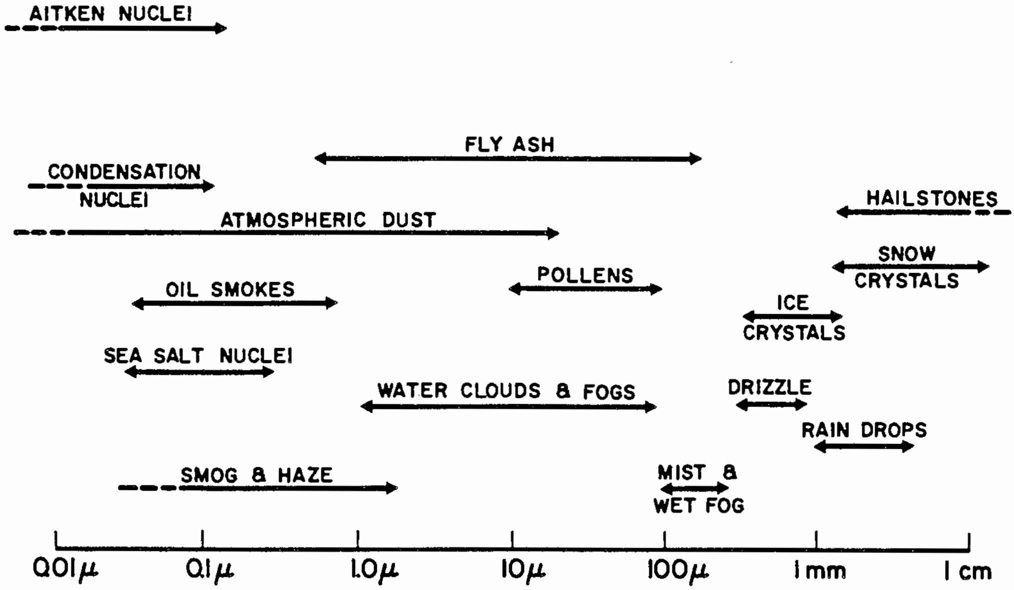

Figure 1.1. Representative diameters of some common atmospheric particles (Measures, 1984).

lognormal distributions, often referred to as the trimodal structure of aerosol size distributions. For maritime aerosols the smallest distribution is due to background aerosols, the intermediate size is dependent on the average wind speed, and the largest distribution is governed by the instantaneous wind speed (Richter and Hughes, 1991). The trimodal distribution is defined as follows,

$$n(r) = \sum_{i=1}^{3} \frac{n_i}{\sqrt{2\pi}\,\sigma_{lni}} \exp\left[-\frac{\left(\ln \frac{r}{R_i}\right)^2}{2(\sigma_{lni})^2} \right] \frac{dr}{r}, \tag{1.1}$$

where r is the particle radius in μm, n(r) is the number of particles in the size range r to r+dr per cm^3, R_i is the median particle radius in μm, n_i is the weighting for the *i*th lognormal function, and σ_{lni} is a measure of the particle polydispersity (or the width of the distribution). The geometric standard deviation σ_g is defined as $\sigma_g = \exp(\sigma_{lni})$, and

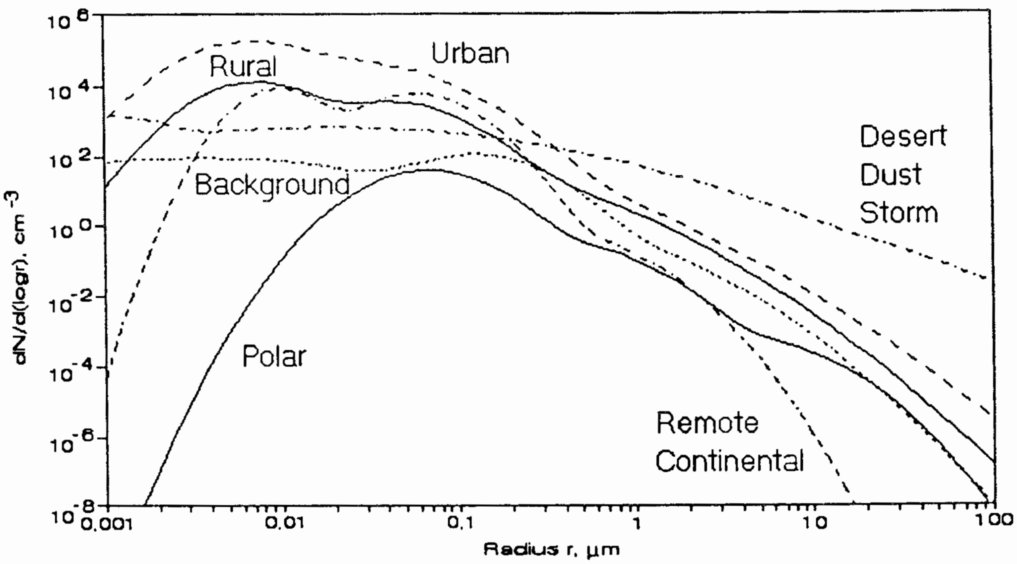

Figure 1.2. Trimodal lognormal size distributions for selected atmospheric aerosols (Hobbs, 1993).

will be used to describe the distribution width. Figure 1.2 shows an assortment of trimodal size distributions of selected atmospheric aerosols (Hobbs, 1993). The trimodal lognormal size distribution will be used along with Mie theory to model and predict the scattering phase function for a humid coastal marine aerosol. However, atmospheric aerosols are not always spherical and caution must be used when interpreting the results of the Mie calculations when compared to the data. One of the primary goals of this thesis is to determine how well Mie theory describes the data under the conditions described in Chapter 3 during the Wallops CASE I program.

1.2.4 Aerosol Refractive Index

The refractive index is a crucial variable in any inversion algorithm that attempts to infer one of the nine parameters from the above trimodal distribution model. The refractive index of many atmospheric aerosols has been measured and tabulated by (Shettle and Fenn, 1979). Examples are shown in Figures 1.3 and 1.4. The refractive index is composed of two parts; the real part and the imaginary part commonly known as the absorption index. Both must be correctly specified in order to model the results of an experiment. The absorption coefficient α, is related to the absorption index k, by,

$$\alpha = \frac{4\pi k}{\lambda} . \tag{1.2}$$

The inverse of α has the dimensions of length and can be called an e-folding distance, the distance over which a beam is attenuated by a factor of 1/e. Equation 1.2 can be used to determine whether or not a particular absorption index is reasonable. Figures 1.3 and 1.4 show plots of the real and imaginary components of the refractive index for continental and maritime aerosols (Air Force Geophysics Laboratory, 1985). At a wavelength of 0.532 μm the real part of the refractive index is about 1.5 for dust or water solubles and the imaginary part is about 0.001. This corresponds to an absorption coefficient of 23×10^3, or an e-folding distance of 40 μm. If 0.001 is a correct absorption index for dust, a beam transmitted in this medium would be reduced to 37% of its initial intensity over a distance of 40 μm. This is a rather large amount of absorption, and would definitely need to be included if one were to model this type of aerosol. Because the experiments for this thesis were conducted in a humid marine environment the values for oceanic aerosols from Figure 4 of $n = 1.38$ and $k \sim 0$ at 0.532 μm were selected for use. One other values will be used to demonstrate the effects of choosing a different refractive index. The absorption of rural and urban aerosols can be seen to be significant for the optical wavelengths in Figure 1.3, but the absorption for oceanic aerosols is negligible (see Figure 1.4).

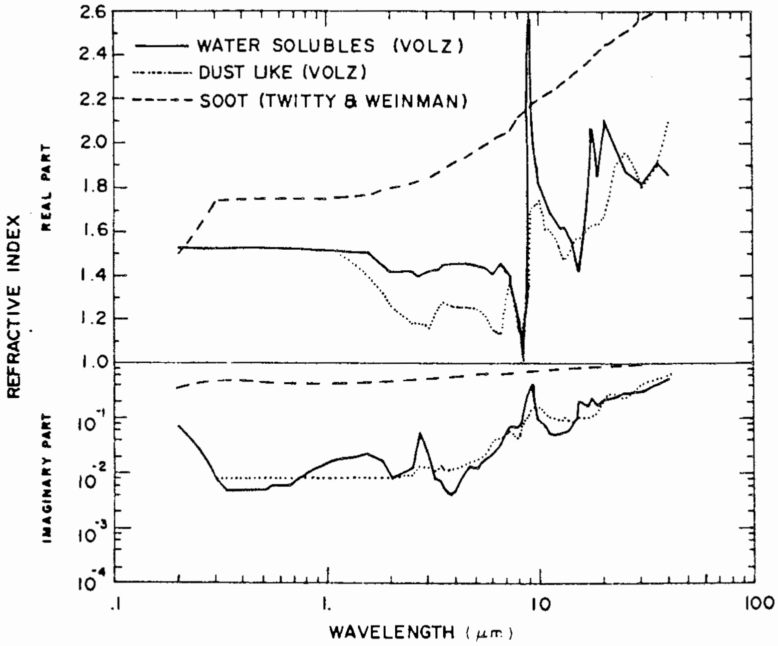

Figure 1.3. Refractive index for the dry rural and urban aerosol components (Air Force Geophysics Laboratory, 1985).

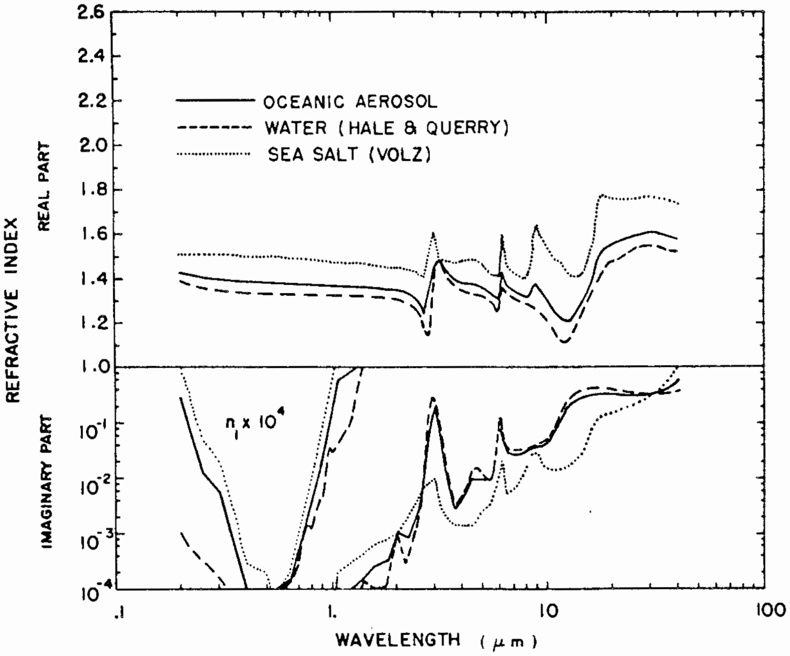

Figure 1.4. Refractive index of oceanic aerosol, water and sea salt (Air Force Geophysics Laboratory, 1985).

1.3 Remote Measurement Techniques of Aerosol Extinction

A major challenge of remote sensing has been the measurement of extinction and transmission through a cloudless region of the atmosphere. Lidar techniques provide one of the few methods capable of describing the electro-optical environment. The laser remote sensing techniques are most applicable because atmospheric particles are small compared to the larger radar and microwave wavelengths, hence scattering of such radiation does not yield any information about the particle size distribution. However, most of the past applications of lidar to describe the electro-optical environment have failed to provide satisfactory results because the techniques used have generally focused on measurements of the backscattered radiation at the laser fundamental wavelength. The following four sections will describe four lidar techniques that have been demonstrated to be effective in obtaining atmospheric extinction along the path of the laser beam. The advantages and problems with each technique will be pointed out for each method.

1.3.1 Raman Technique

We have been able to demonstrate that the Raman molecular profile can be used to determine the extinction profile through optical scattering regions such as clouds (Stevens and Philbrick, 1995). Figure 1.5 shows a cartoon of a return from a Raman-shifted signal through a cloud. The backscattered signal from the molecular profile of the Raman shifted return contains only extinction information. As long as the amount of extinction is significant, like that through a cloud, an extinction coefficient can be calculated by using the change in signal strength through the cloud in the Raman channel with the Beer-Lambert law. The signals from either the N_2 channel shifted from 532 nm to 607 nm or shifted from 355 nm to 387 nm can be used for this calculation. Our strongest signals come from the rotational Raman channels of 528 and 530 nm, both shifted from 532 nm to obtain temperature. These two channels are added together to reduce the temperature dependence before calculating an extinction coefficient. The Beer-

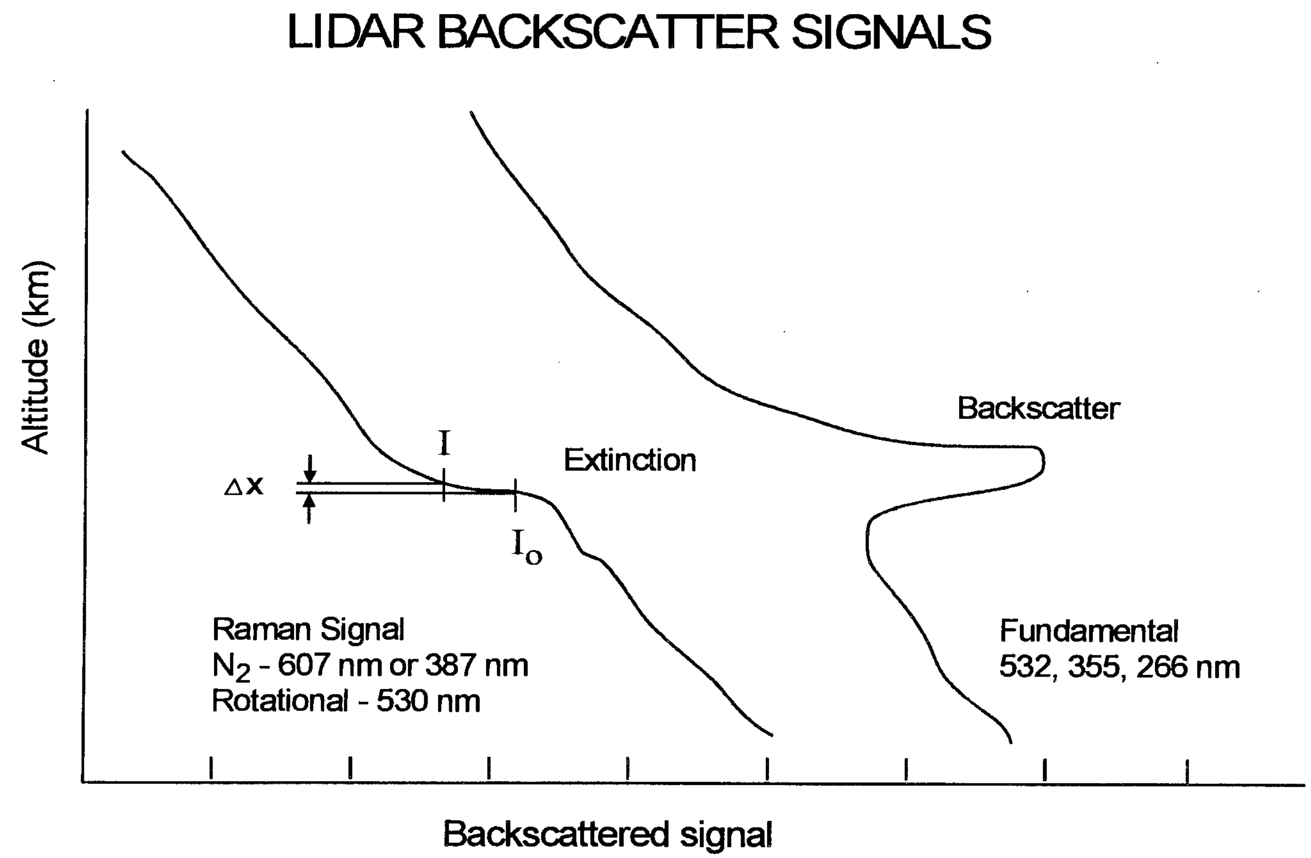

Figure 1.5. An example of how extinction can be calculated through clouds using the Raman-shifted return (Stevens et al., 1995).

Lambert law is used in the following form,

$$\alpha = -\frac{\ln\frac{I}{I_o}}{2x} = \textit{Extinction coefficient} \qquad (1.3)$$

Where x equals the range bin size in meters and α is the extinction coefficient. Because the Raman lidar return is compared to the expected return from the U.S. Standard Atmosphere, only large amounts of extinction can be calculated. We first tie the lidar signal to the US Standard Atmosphere above 10 km, where we can expect molecules to be the dominant scatterers. The Raman lidar signal is then normalized by dividing it by the U.S. Standard Atmosphere. This resultant signal is then used in the Beer-Lambert equation (1.3) to calculate the extinction coefficient point by point.

Figure 1.6 shows data obtained with the Penn State LAMP (Lidar Atmospheric Measurement Program) lidar at State College, Pa. on September 13, 1994 (Philbrick et al., 1994). Because an exponential attenuation of the transmitted signal is assumed, multiple scattering must be negligible and the cloud must be optically thin. A large cloud with its base just before 8 km can be seen in the backscattered signal from the molecular/aerosol 532 nm channel. At the same altitude the rotational Raman channel's signal decreases by about an order of magnitude. This amount of extinction is clearly large enough that any variation due to the use of the model molecular atmosphere will have little effect on the total calculated extinction. Figure 1.7 shows a plot of the extinction coefficient versus altitude calculated from the Raman profile in Figure 1.6. This type of range resolved profile can be most valuable in describing cloud layers and their effect on the propagation of electro-magnetic fields at visible wavelengths. However, if we are to determine the optical properties over a wide range of wavelengths, and through a clear atmosphere a different method must be used.

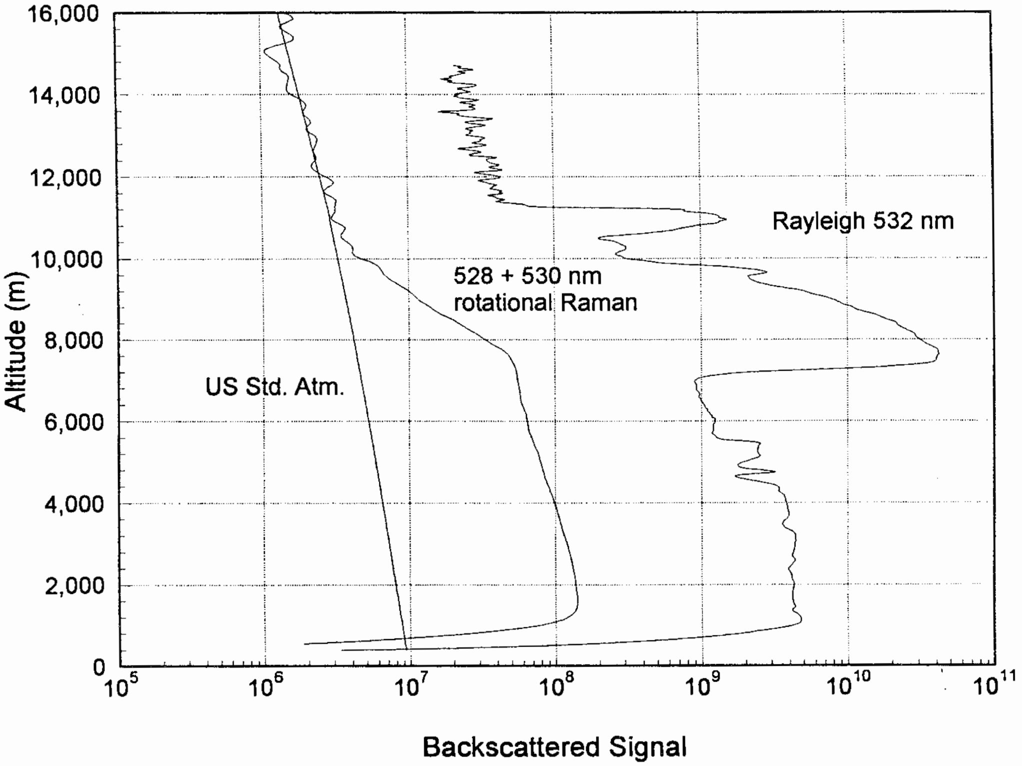

Figure 1.6. Data collected with the Penn State LAMP lidar on September 9, 1994 at State College, PA. The cloud at 8 km is seen as a strong peak in the 532 nm signal, and as a strong extinction in the rotational Raman channel (Stevens, et al., 1995).

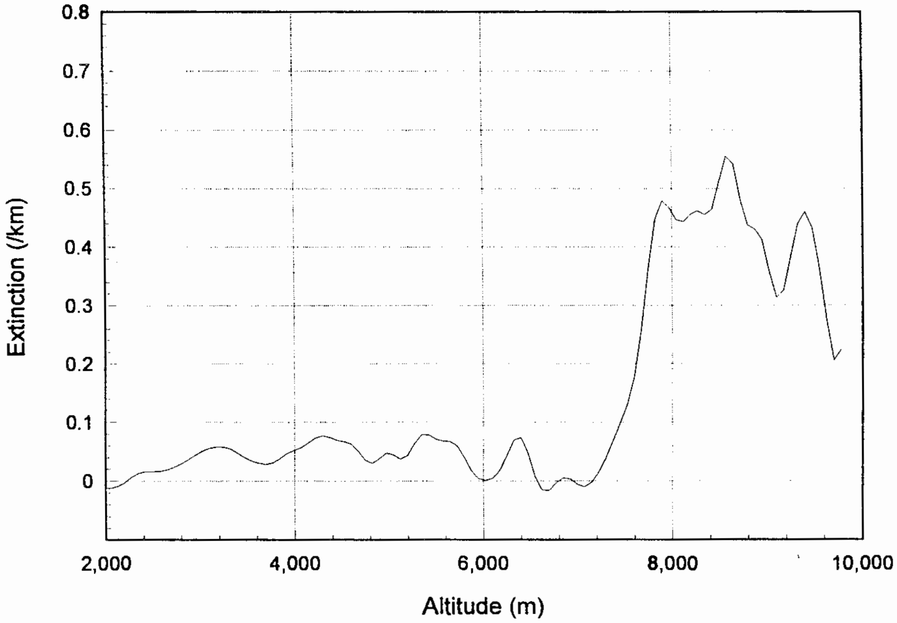

Figure 1.7. Extinction coefficient calculated directly from the rotational Raman data in Figure 1.6. A simple point-to-point calculation using the Beer-Lambert law will give reasonably accurate results for large values of extinction, like those in clouds (Stevens, et al., 1995).

1.3.2 Klett Inversion

A second method to determine extinction was developed by Klett (1981). The Klett inversion avoids the instabilities commonly associated with the inversion of the lidar equation by starting the inversion not at the near point but at the far end of the range interval. This method requires knowledge or at least a good estimate of the extinction coefficient at the far end starting point of the inversion. Klett developed this backward inversion method using the analytical solution of the single scattering lidar equation,

$$P(r) = A \cdot Q \cdot \beta(r) \cdot \frac{1}{r^2} \cdot \exp\left[-2 \int_0^r \alpha(x)\, dx \right], \tag{1.4}$$

where P(r) is the received power from range r, Q is the transmitted energy, β(r) is the backscatter coefficient, and α(r) is the extinction coefficient. The 'A' constant includes all system parameters, and efficiencies. Extinction is commonly related to the backscattered energy by the equation,

$$\beta(r) = C(r) \cdot \alpha(r)^k , \tag{1.5}$$

where C(r) and k are frequently and incorrectly assumed constant. But in order to obtain a solution to Eq. 1.4, Eq. 1.5 must be assumed correct unless other information is known about the scatterers. The solution of Equation 1.4 is then,

$$\alpha(r) = \frac{\left[P(r) \cdot r^2\right]^{1/k}}{\dfrac{\left[P(r_m) \cdot r_m^2\right]^{1/k}}{\alpha_m} - \dfrac{2}{k} \displaystyle\int_r^{r_m} [P(x) \cdot x^2\,]^{1/k}\, dx} , \tag{1.6}$$

here r_m is the range boundary where the extinction α_m, must be known or estimated. However, Klett was able to show that the influence of α_m on the resulting α(r) profile decreases strongly with the optical depth between r and r_m. This inversion method is thus especially suitable for the evaluation of lidar returns from cloudy and foggy atmospheres.

This is only true if the relationship between backscatter and extinction is known and remains constant, and multiple scattering can be neglected. For example, Eq. 1.5 is certainly not valid in cases where different types of scatterers are present either simultaneously or spatially separated. Situations, where particulate and molecular scattering are comparable in magnitude, or, where dry aerosols exist underneath clouds, are common occurrences which would not yield a correct solution to the Klett inversion. Perhaps the backscatter to extinction ratio can be obtained by another measurement technique and used in the Klett inversion. This approach will be explored in Section 1.3.3.

The Klett inversion does work rather well in the stratosphere through the H_2SO_4 aerosol particles from the Pinatubo volcano (Stevens, et al., 1993). The aerosols are uniformly distributed as shown by the particle backscatter ratio in Figure 1.8 (Stevens, et al., 1994). This ratio of the backscattered laser radiation at two different wavelengths (0.532 and 0.355 μm) remains constant through the stratospheric layer indicating that the relationship between backscatter and extinction, (i.e., the particle size distribution), also remains constant. This takes care of the one problem with the Klett inversion. The other two problems are the far end starting extinction and the value of k (the relationship between backscatter and extinction). We start the integration just above the aerosol layer where we can assume that the atmosphere consists only of molecular scatterers. The starting extinction is just that of molecular scattering (number density is taken from the U.S. Standard Atmosphere). We then make an iterative guess at a value of k and proceed to integrate the equation downward. The atmosphere is usually purely molecular just below the stratospheric aerosols at about 15 km. We used an iterative procedure to choose k such that when integrating downward, the value of the extinction would equal that of the molecular atmosphere just below the aerosol layer (usually 15 km). A plot of the extinction calculated this way for both the 0.355 and 0.532 μm wavelengths is shown in Figure 1.9. These extinction coefficients are then used to correct the lidar profiles and are shown in Figure 1.10. The data for Figures 1.8, 1.9, and 1.10 were collected during the LADIMAS campaign aboard the RV Polarstern on November 22, 1991 (Stevens, et al., 1994).

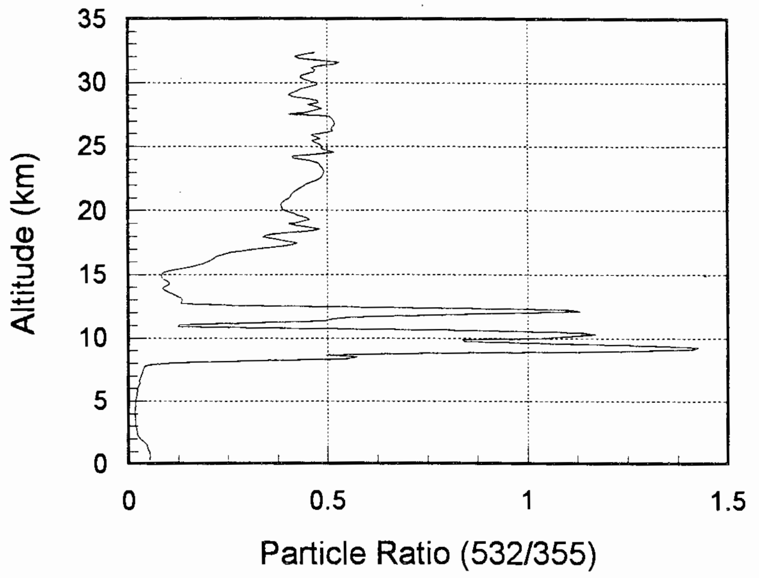

Figure 1.8. Particle backscattering ratio showing the constant value of 0.5 through the Pinatubo aerosols in the stratosphere (Stevens, et al., 1994).

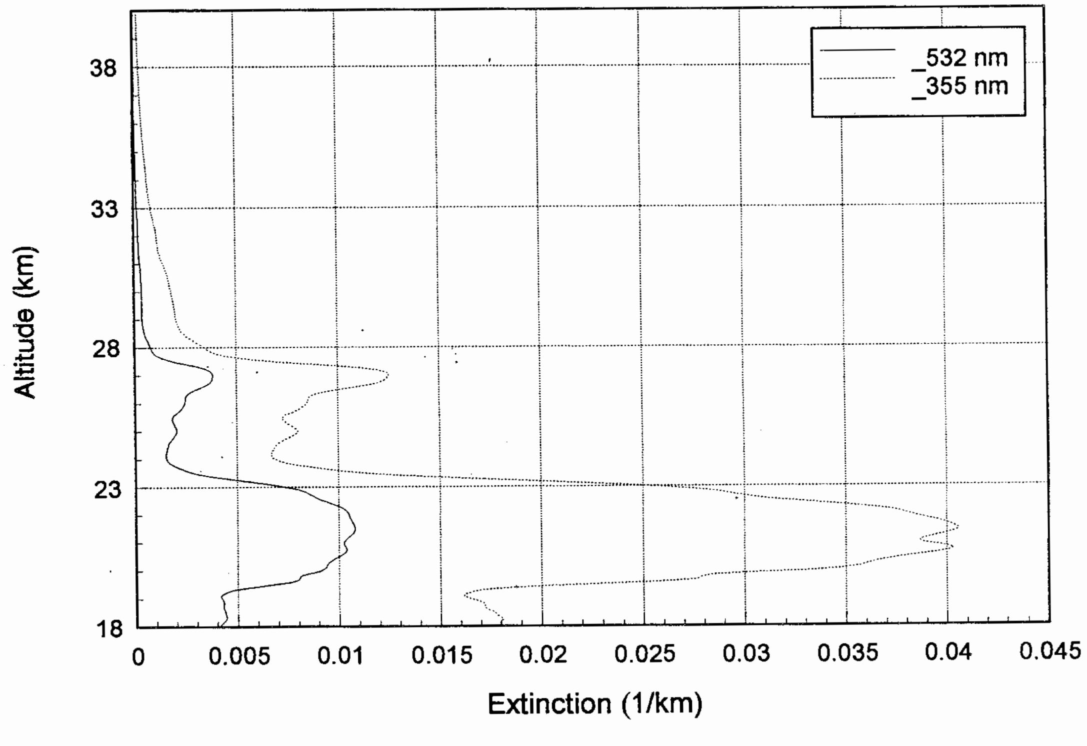

Figure 1.9. Extinction profiles calculated with the Klett inversion through the Pinatubo aerosol layer in the stratosphere. The data was collected on November 22, 1991 during the LADIMAS campaign.

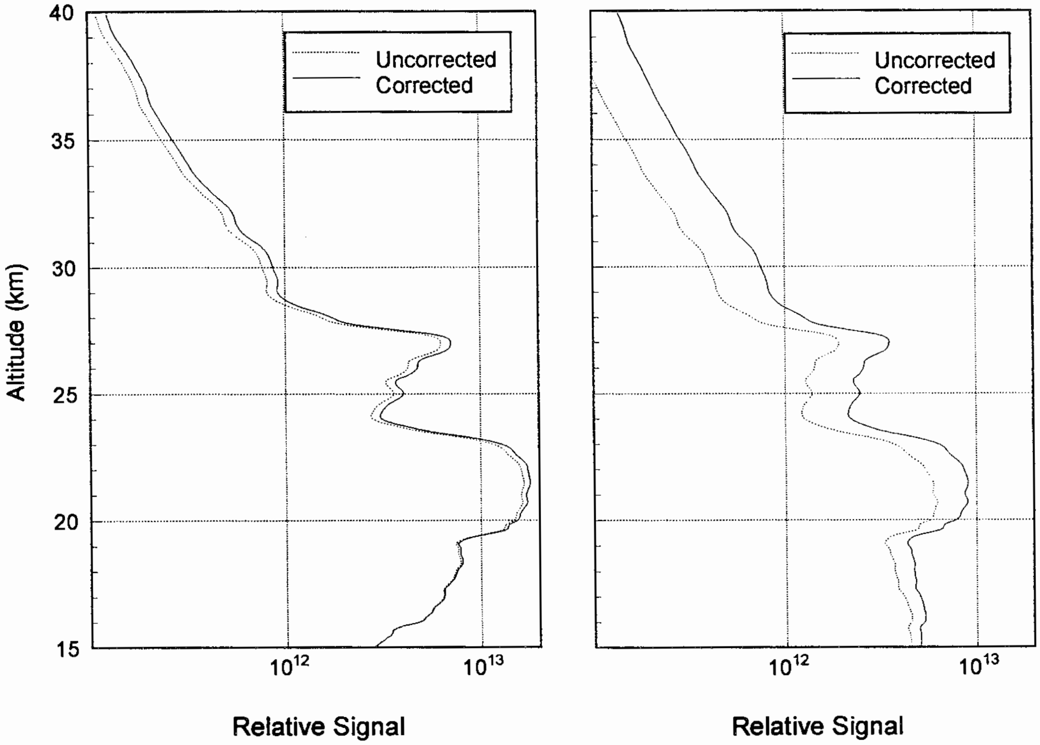

Figure 1.10. Corrected Pinatubo aerosol profiles using the extinction calculated in Figure 1.9. The 532 nm profile is on the left and the 355 nm profile is on the right.

The Klett inversion can be shown to provide accurate extinctions under very limited circumstances where the assumptions discussed in this section can be justified, but in the first kilometer of the atmosphere these assumptions are seldom valid as will be shown in the next section.

1.3.3 Double Ended Lidar Technique

A more reliable method using lidar to measure atmospheric extinction has been developed independently by (Paulson, 1987) and (Kunz, 1987). An inversion algorithm was developed using a double-ended lidar technique where the relationship between the backscatter and extinction coefficients is obtained by comparing the backscatter signal returned from a volume common to each lidar located at opposite ends of the propagation path. The mathematical formulation of this technique will not be discussed here because it is not used as part of this research. The double ended lidar technique is presented to show that the β/α ratio in general is not constant with range and that the technique of inverting a single-ended lidar return (Klett inversion) will generally produce inaccurate extinctions. Figure 1.11 shows plots of extinction calculated from both single-ended (C(r) assumed constant) and double-ended lidar backscattered returns (Richter and Hughes, 1991). These data sets show very clearly how unreliable standard inversion techniques are at obtaining extinction from a single backscattered lidar return. However, if the values of C(r) are known as a function of range and allowed to vary, standard single-ended lidar returns could be inverted to reliably obtain extinction coefficients. More information is needed about the scatterers so that C(r) can be calculated for each range bin. The ratio of the 532 nm to the 355 nm backscattered lidar return is theoretically proportional to C(r). But this has yet to be used in an inversion algorithm to accurately and uniquely calculate extinction (Rau, 1994). The double-ended lidar technique is a proven method for measuring the extinction along a path, but it is not a practical solution for instantaneous measurements above altitudes of a few meters and for locations where instruments can not be located at each of the end points. The scattering properties of atmospheric aerosols are too complicated for the simplistic single-ended backscattered inversion approach and more information is needed to characterize the processes.

1.3.4 Scanning Bistatic Lidar

The first lidars operated in a bistatic configuration using searchlights (Elterman, 1951), but quickly moved to a monostatic configuration with the invention of the laser. The scanning bistatic lidar method was originally used to obtain the physical characteristics of aerosols by (Reagan, et al., 1970), and has most recently been used by K. Parameswaran, at the Vikram Sarabhai Space Center in India (Parameswaran, et al, 1984 and 1993), and by P. Devara at the Indian Institute of Tropical Meteorology (Devara, et al., 1987 and 1991). Recently these two groups in India have been operating scanning bistatic lidar as shown in Figure 1.12. Both the transmitted laser beam and the telescope's field-of-view are steered to collect a range of angles from a given altitude. The geometry

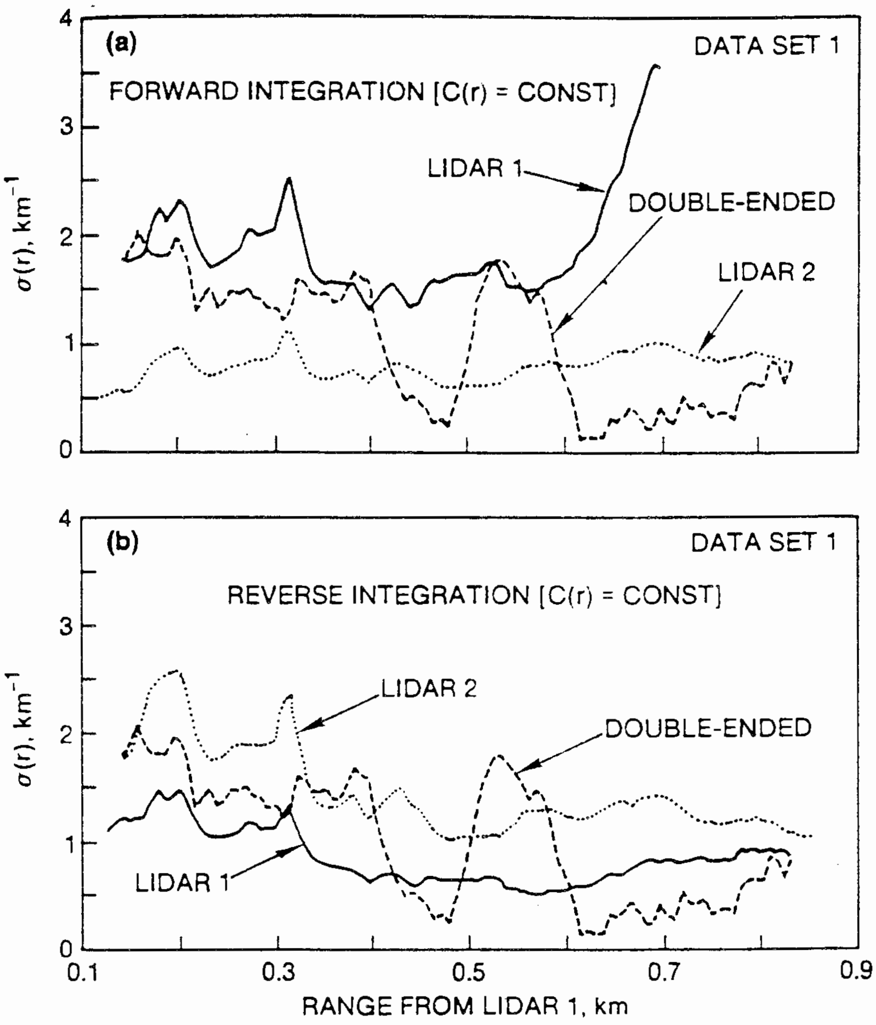

Figure 1.11. Comparison of extinction coefficients versus range calculated using forward and reverse integration on a single-ended lidar return and using the double-ended lidar technique (Richter and Hughes, 1991).

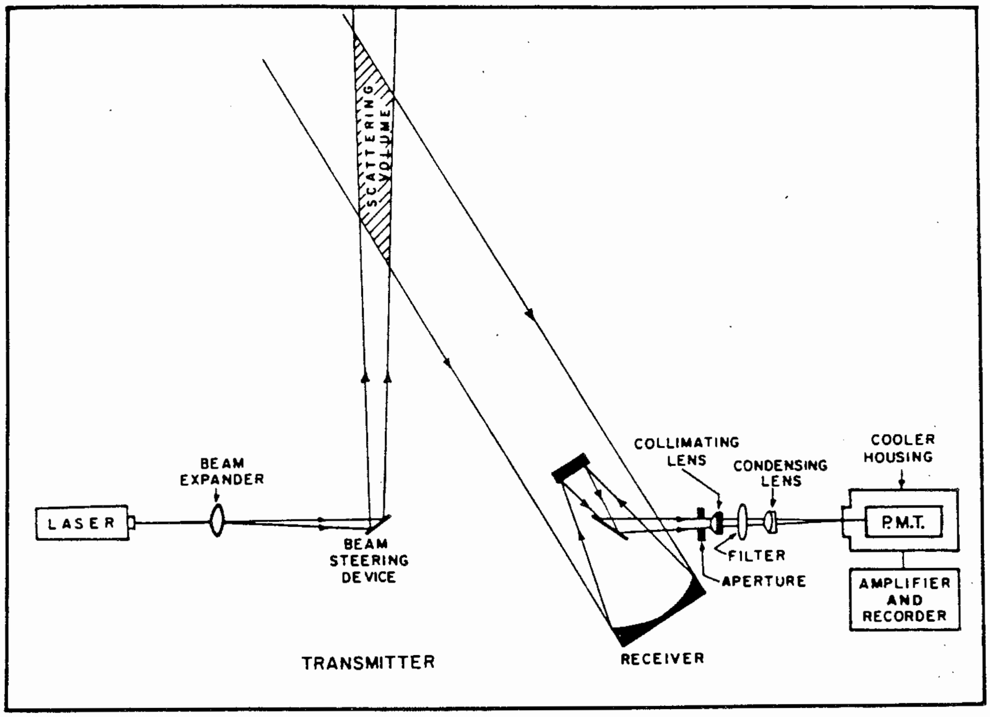

Figure 1.12. The optical layout of the experimental setup for a bistatic lidar used by P. Ernest Raj and P. C. S. Devara (Ernest et al., 1989).

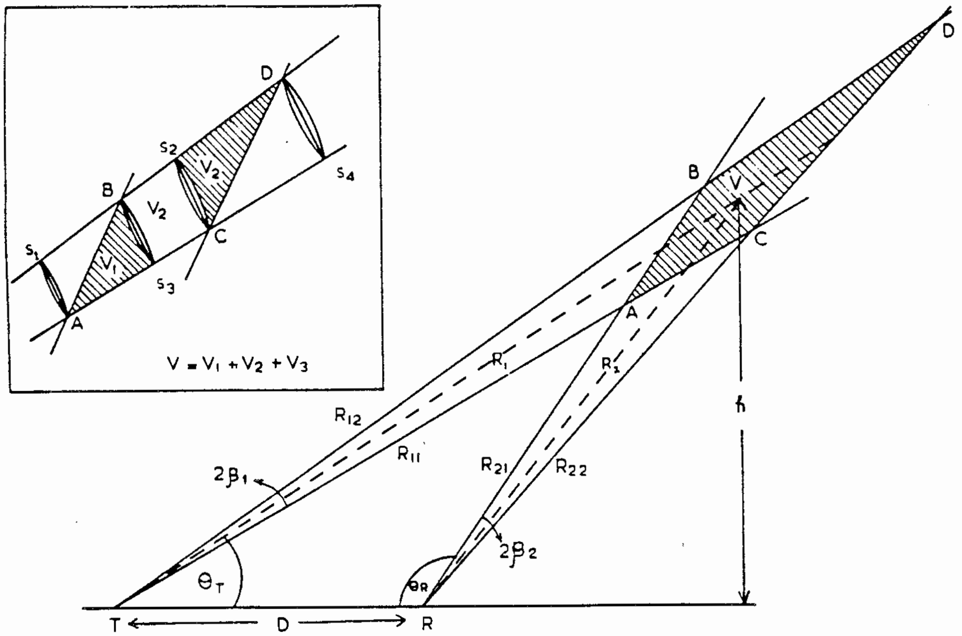

Figure 1.13. The geometry of a bistatic lidar setup used to determine the observed scattering volume (Parameswaran et al., 1993).

of this type of lidar experiment is shown in Figure 1.13.

The transmitter and receiver scan in such a way that they overlap in the same vertical plane for all elevation angles, thus ensuring a fixed scattering plane. P. Devara uses a linear polarized laser with the direction of the electric field of the incident wave parallel to the scattering plane. Each experiment collects lidar data at scattering angles ranging from 90 to 165 degrees. This data is then used to directly plot an aerosol scattering phase function between the measured angles. A spherical scattering model is then used with the Junge power law distribution to invert the data to an aerosol size distribution. The authors give an error in the determination of the size distribution of ±40%. This is probably due to the very coarse angular resolution that allows many different size distributions to describe their measurements. There are several problems with this technique for determining aerosol size distributions. First, the angle measurements on average, have about a 9 degree resolution. Chapter 4 will show that the scattering phase function can have very sharp features, on the order of degrees, especially in the larger sizes (1 - 10 μm). Second, the measurements are not taken at the same time. Time variations on the order of minutes, discussed in Chapter 5, will show how much the phase function can change in just one minute due to a small breeze and a change in number density. Third, this technique is based on relative radiance measurements between different angles, where any change would distort the reconstructed phase function. And fourth, there is too much room for error when normalizing each independent angle measurement. Chapter 2 will explain the difficulties in determining the relative radiance from one measurement to the next due to the changes in scattering volume size and changing lidar equation parameters. A better method for determining aerosol size distribution will be explained in Chapter 4.

1.4 Thesis Organization

The first chapter introduced tropospheric aerosols and past measurement techniques. Information such as aerosol types, index of refraction (both real and imaginary parts), sources, and size distributions are all explained and defined. This was so the reader would understand why certain variables were chosen for the model in Chapter 4. The last part of Chapter 1 described the pros and cons of four other methods for remotely measuring aerosol extinction coefficients.

Chapter 2 defines the difference between bistatic and monostatic lidar, and briefly describes the LAMP lidar. The design of the bistatic lidar is covered in detail along with its initial operation. This chapter also explains the disadvantages of using the data from the bistatic receiver directly, and the advantages of using a polarization ratio between two bistatic measurements. Initial results of the receiver operating in the vertical mode are presented to prove acceptable performance of the instrument.

Chapter 3 describes the measurement program at Wallops Island that was set up to test the possibilities of inferring particle size distributions from the bistatic lidar. The focus and test plan of the entire program is explained along with a description of the supporting instruments. Atmospheric conditions are also described so that some insight can be gained on what to expect from the inversion of the bistatic lidar data.

Before any inversion of the data can be accomplished, a model must first be developed. Chapter 4 describes each step involved in the making of a model for the bistatic lidar and measurement technique. Topics including Mie theory, Stokes parameters, molecular scattering and multiple scattering are described, and the assumptions and conditions related to the model are explained. The chapter ends with an example of the calculations from the model that are used to describe trimodal lognormal distributions of spherical dielectric scatterers.

Chapter 5 presents the data and modeling results for the Wallops CASE I measurement program. Both monostatic and bistatic lidar data are shown for a wide range of conditions from dry and clear to humid and misty. The bistatic lidar measurements easily differentiate clear nights from hazy nights using the inverted size distributions. Extinction, transmission, and visual range are all calculated using both the Raman lidar technique and the inversion of particle size distributions from the bistatic lidar.

Chapter 6 provides a detailed error analysis and defines three separate groups of errors that can degrade the data: modeling errors, measurement errors, and instrument errors. The effect of each error on the data is discussed, and a graphical derivation is presented to show how instrument error can propagate to the retrieval of each lognormal parameter, and into the calculation of extinction. A set of plots show how small errors in the data can lead to large errors in the retrieval of a parameter, and in turn sometimes have only small effects on the extinction. Percent errors are then given for retrieval accuracy of each mode, and the dependance of the extinction on each parameter is quantified. The end of the chapter deals briefly with the inversion algorithm used to determine the parameters of the aerosols, and on how to improve the inversion for future measurements.

Finally, Chapter 7 draws some conclusions and predicts the direction of future work. The Appendices list all the computer code, both Fortran and Matlab subroutines used to process and model the data. The last appendix lists 34 samples from each night of the processed bistatic lidar data.

Chapter 2

BISTATIC LIDAR RECEIVER AND MONOSTATIC LIDAR INSTRUMENTATION

Two instruments, a bistatic lidar receiver and a monostatic lidar, were used to collect the data used in this thesis. The LAMP (Laser Atmospheric Measurement Program) lidar, a conventional monostatic lidar, was operated in a horizontal path to collect data from the 532 nm molecular/aerosol channel, and from the Raman-shifted returns of the 660, 607, 528, and 530 nm channels. The LAMP laser beam was also used as the source for an independent bistatic receiver. This bistatic receiver collects scattered laser light from the doubled Nd:YAG at a wavelength of 532 nm.

The first lidars were bistatic configurations, but nanosecond lasers and high speed electronics made possible spatial resolution of a few feet, so in most instances a monostatic configuration is used. The bistatic arrangement involves a considerable separation between the transmitter and receiver to obtain spatial resolution, as with the linear diode arrangement used for this research. In a monostatic system the transmitter and receiver are at the same location, making a single-ended instrument. The monostatic lidar is further divided into either a coaxial or biaxial configuration. In a coaxial system the axis of the laser beam is coincident with the axis of the receiver, while in the biaxial arrangement the laser beam enters the field of view of the receiver at some predetermined range.

2.1 LAMP Laser Atmospheric Measurement Program

The LAMP instrument was designed to operate as both a middle atmosphere sensor and a lower atmosphere meteorological sensor. To accomplish this task, the profiles of many atmospheric properties including nitrogen concentration, water vapor concentration, aerosols, density, and temperature can be measured over a large altitude range simultaneously (Stevens, 1992). The LAMP lidar is a rugged self-contained transportable instrument capable of operating in almost any environment, as was demonstrated by its operation aboard the German ice breaker RV Polarstern in Antarctica during December 1991 (Philbrick et al., 1994). Figure 2.1 shows a typical block diagram for a multi-channel lidar system. For a complete description of the LAMP lidar see (Stevens, 1992).

Table 2.1 provides a summary of the LAMP lidar. The instrument uses a pulsed Nd:YAG laser transmitting near-infrared radiation of 1064 nm at a pulse repetition frequency of 20 Hz. Nonlinear optical crystals are used to obtain output at the doubled and tripled, or quadrupled wavelengths. Thus, the lidar can be operated using either the 532 and 355 nm wavelengths or the 532 and 266 nm wavelengths, simultaneously. The

Table 2.1. Current Penn State lidar parameters.

PENN STATE LAMP LIDAR PARAMETERS				
Power aperture product = 1.55				
TRANSMITTER				
Type: Continuum NY-82, Seeded Nd:YAG				
	Fundamental	Doubled	Tripled/mixed	Quadrupled
Wavelength	1064 nm	532 nm	355 nm	266 nm
Pulse energy	1.5 J	500 mJ	250 mJ	80 mJ
Bandwidth		80 MHz		
Pulse length		7 ns		
Pulse rate		20 Hz		
RECEIVER				
Type: f/15, Cassegrain telescope				
Focal length	609 cm			
Primary diameter	40.6 cm			
Secondary diameter	10.2 cm			

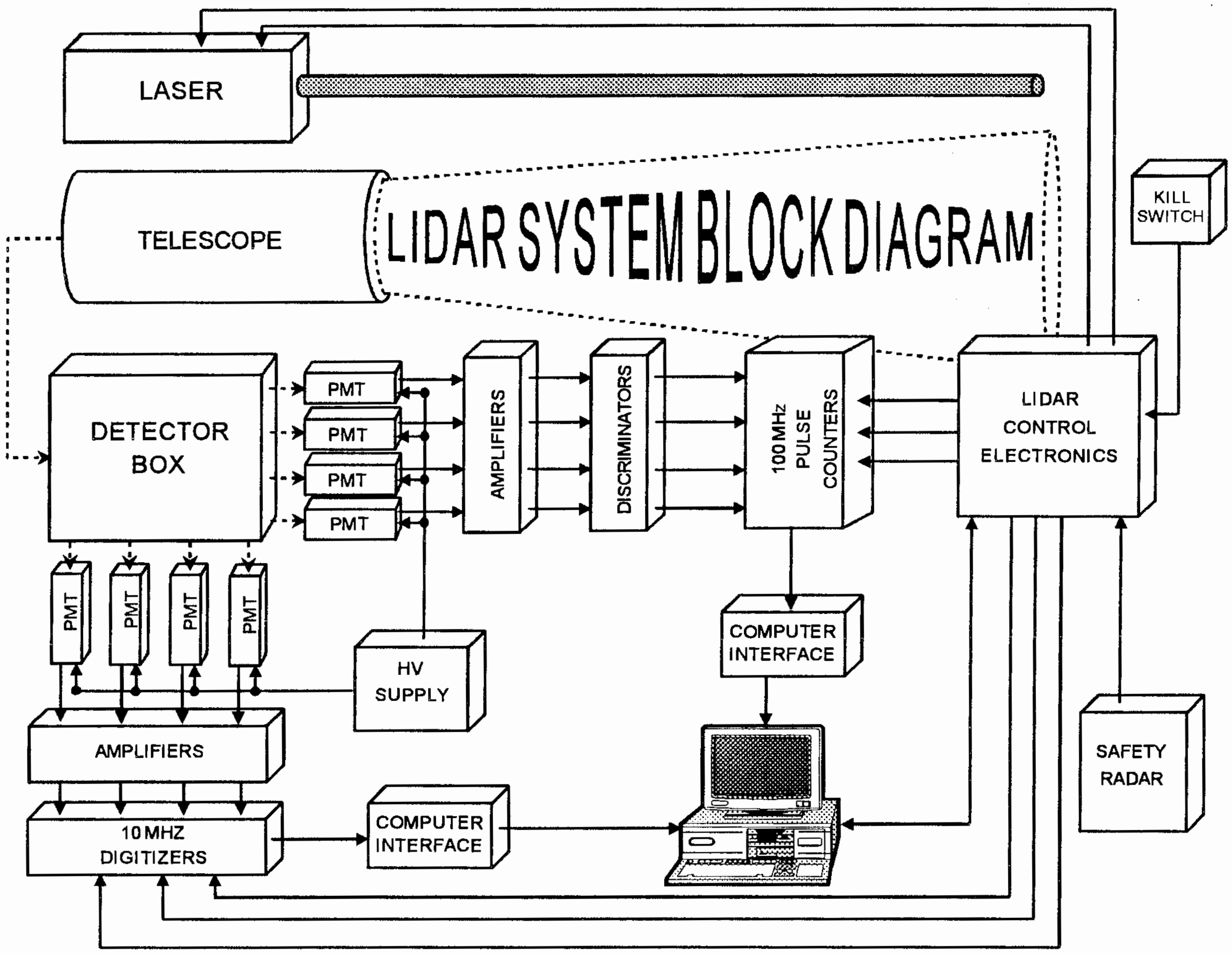

Figure 2.1. Typical lidar block diagram showing eight detector channels, four digitizing, and four photon counting. System could be either monostatic or bistatic.

LAMP lidar has been equipped with a new beam-steering platform for the primary optical flat, which enables the laser and the field-of-view of the telescope to be precisely positioned to a particular point in space. This allowed us to operate the lidar horizontally with the laser beam stopped by a target board 3 km away during the Wallops CASE I program. During most of the operating period on a horizontal path, the laser was set up to transmit one wavelength, 532 nm. When the lidar was operated on the vertical path, it was set up to transmit two wavelengths, 532 nm, and 266 nm.

The output signal from the telescope is directed by a 1.0 mm optical fiber into one of two detector boxes. The detector boxes separate the backscattered lidar return into the different wavelength components and direct the signal onto the surface of one of several photomultiplier tubes. Detector box #1 was designed with a high-speed optical shutter to collect data from the ground to 80 km. Because the atmospheric density decreases by about eight orders of magnitude from the surface to 80 km, an optical shutter was needed to split the return signal into two channels to cover the large dynamic range. Table 2.2 summarizes the data collecting-capabilities of this detector box. This detector box was used during the LADIMAS campaign on the RV Polarstern but not during the Wallops CASE I program.

Table 2.2. LAMP lidar high and low altitude detection system.

Detector Box #1			
Type: High and low altitude, high speed shuttering system			
Channel	wavelength	Electrical signal	Altitude range
Molecular/Aerosol	532 nm	digitized - 10 MHZ	0 - 15 km
Molecular/Aerosol	355 nm	digitized - 10 MHZ	0 - 15 km
Molecular	532 nm	photon count - 100 MHZ	15 - 80 km
Molecular	355 nm	photon count - 100 MHZ	15 - 80 km
Raman H_2O (532)	660 nm	photon count - 100 MHZ	0 - 7 km
Raman N_2 (532)	607 nm	photon count - 100 MHZ	0 - 10 km

The second detector box was designed as a low-altitude meteorological detection system. Table 2.3 lists all the capabilities of this detector box. This system processes the backscattered laser signals derived from the 532 nm wavelength and either the 355 nm or the 266 nm wavelengths. Lower atmospheric temperatures are obtained from the rotational Raman shifted returns from 532 nm to 528 and 530 nm. The water vapor mixing ratio can also be calculated from the vibrational Raman return scattered from both the 532 and 355 nm or from the 532 and 266 nm transmitted laser pulses. More complete information is available on this detector system from (Haris, 1995). For the purposes of this thesis, the rotational Raman temperature channels are used to calculate extinction at 528 and 530 nm as explained in Chapter 1. The vibrational Raman nitrogen channel is also used to calculate extinction at 607 nm. These Raman channels along with the direct backscatter of the 532 nm aerosol/molecular channel are used to determine the uniformity of the scatterers along the 3 km horizontal path at Wallops Island, as described in Chapter 3.

From the standpoint of the bistatic measurements, the main role of the LAMP lidar was to supply a 532 nm laser source for the bistatic receiver. Linear polarizations, both parallel and perpendicular to the scattering plane, were required from the 532 nm

Table 2.3. LAMP lidar low altitude water vapor and temperature detector system.

Detector Box #2			
Type: Low altitude multi-wavelength temperature and water vapor detector			
Channel	wavelength	Electrical signal	Altitude range
Molecular/Aerosol	532 nm	digitized - 10 MHz	0 - 15 km
Raman H_2O (355/266)	407/294 nm	photon count - 100 MHZ	0 - 7/3 km
Raman N_2 (355/266)	387/283 nm	photon count - 100 MHZ	0 - 10/5 km
Raman O_2 (266)	277 nm	photon count - 100 MHZ	0 - 5 km
Raman temp #1 (532)	528 nm	photon count - 100 MHZ	0 - 10 km
Raman temp #2 (532)	530 nm	photon count - 100 MHZ	0 - 10 km
Raman H_2O (532)	660 nm	photon count - 100 MHZ	0 - 7 km
Raman N_2 (532)	607 nm	photon count - 100 MHZ	0 - 10 km

transmitted laser beam during the Wallops CASE I experiment. The LAMP lidar was fitted with a quartz 90° polarization rotator mounted in a specially designed remote controlled translation stage. This added the capability of remotely rotating the laser's polarization a full 90° in just 5 seconds. It is important that only one linear polarization component be transmitted at a time, so measurements were made to see how pure each polarization component was. Without the rotator inserted the laser transmits 100% vertically polarized light. With the rotator inserted the transmitted laser light is 98% horizontally polarized and 2% vertically polarized. This will contribute a negligible amount of cross polarized signal to the receiver. There is also a 3% loss through the rotator, So we expect a 3% stronger signal with the rotator removed. The data does show an offset in the ratio of the two polarization components which agrees with this expectation.

Although the LAMP lidar was used with the bistatic receiver, any lidar with a sufficiently high output power operating in the visible could also be used. Initial tests of the bistatic receiver were conducted with the Penn State LAPS (Laser Atmosphere Profile System) lidar because of its even greater output power, which made initial tests and alignments easier. The following section describes the bistatic receiver along with some initial results and data processing techniques.

2.2 Linear Diode Array Bistatic Lidar Receiver

The original motivation for the design of the bistatic lidar was to be able to gather information about the particle scattering phase function. Monostatic lidars can only measure particle scattering at 180°. The only way to collect scattered radiation at angles other than 180° with a lidar system is to set up a bistatic receiver located some distance from the laser. As was discussed in Chapter 1 bistatic lidar is not new. However, this linear diode array bistatic lidar and measurement technique are unique variations on the standard scanning bistatic lidar. The bistatic receiver and measurement technique make possible a more precise method to determine aerosol size distribution and even absolute number density under certain circumstances. Before measurements can be discussed, the instrument and its capabilities will be presented.

This bistatic receiver does not scan, but remains fixed with respect to the laser. The scattering volume's distance from the receiver is derived from the location of the laser's image on a photodiode array. This type of receiver is small, about twice the size of a regular SLR camera, making it ideal as a permanent fixture at several locations. The receiver is also independent of the laser/lidar system and requires no electrical connection to the laser source. Either a pulsed or continuous laser can be used as a source for this receiver. Multiple receivers could be set up on ships or at airports for the application of the technique to continually monitor atmospheric aerosol variability and optical transmission.

2.2.1 Instrument Design Considerations

The bistatic receiver collects an image of the radiation scattered from the first few kilometers of the atmospheric path to help determine atmospheric particle size distribution parameters. The instrument is a straightforward use of a linear photodiode array detector in the image plane of a standard 35 mm SLR camera. The actual receiver construction in this case is a hand held unit composed of three parts: a Ricoh XR-10m SLR camera, a digital control and data storage box, and a power source (either a 6 v battery, or an extension cord). Figure 2.2 shows the configuration of the system mounted on a tripod.

This receiver is essentially a very sensitive, high resolution digital camera. The camera images the laser light onto an EG&G monolithic linear photodiode array. The array has 1024 photodiode elements with a 25 μm center-to-center spacing. Each element has a 100:1 aspect ratio of 25 μm x 2.5 mm making it easy to align the laser beam onto the array. The device consists of a row of silicon photodiodes, each with an associated junction capacitance on which to integrate photo-current. The sensitivity of the array is 2.9 x 10^{-4} C/J/cm^2 at 750 nm, and its peak quantum efficiency is about 80% at 650 nm.

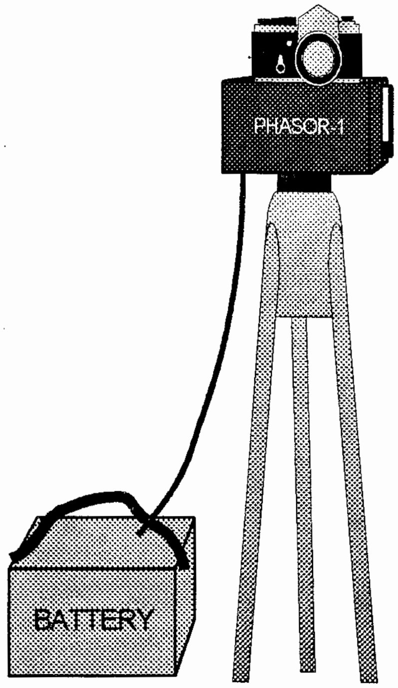

Figure 2.2. Bistatic remote receiver designed to collect angle and polarization dependant scattering from a lidar/laser system.

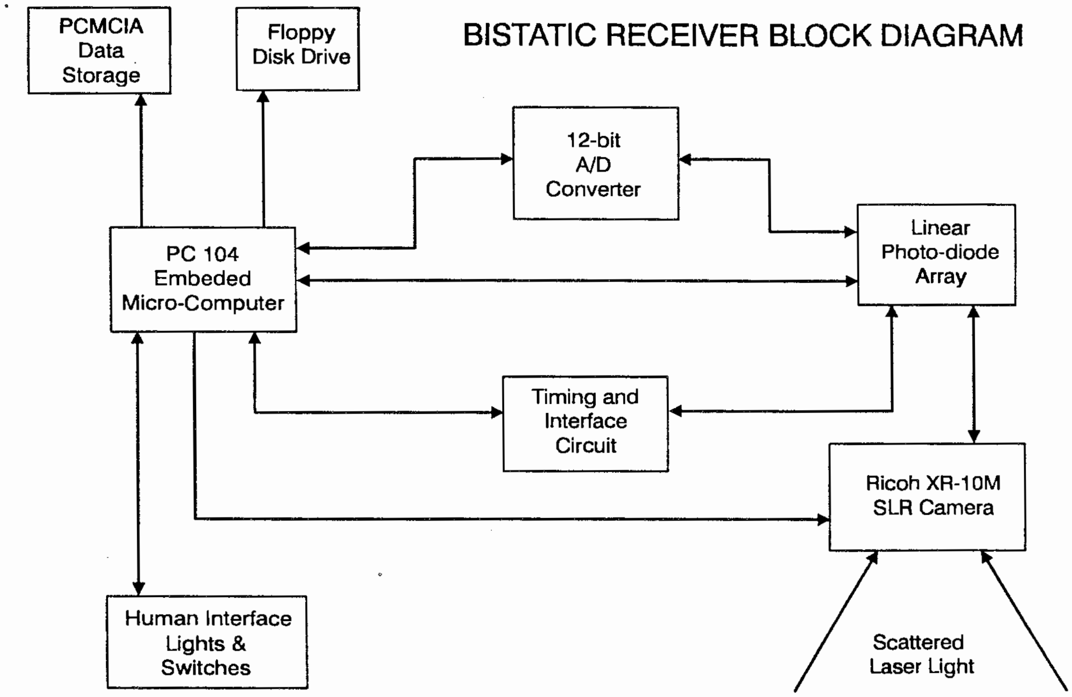

Figure 2.3. Bistatic receiver block diagram.

Figure 2.3 shows a block diagram of the bistatic receiver. The data collection process starts from the human interface block with a remote start switch. The embedded microcomputer reads the input and starts a series of events defined by the data acquisition and control program (see Appendix A). The scattered laser light is filtered by a 10 nm bandwidth 532 nm filter and focused onto the photodiode array by a 50 mm focal length lens. First, the array is cleared and then the shutter is opened for about fifteen seconds (300 laser shots). The data is digitized with a 12 bit, 100 kHz digitizer and transferred directly to RAM. A background sample is then digitized with the shutter closed and also stored directly to RAM. The background is subtracted from the signal and saved to a PCMCIA solid state memory card. One data cycle requires about 50 seconds, and 100 samples can be saved to one PCMCIA card. A data set is composed of an image with the laser plane of polarization parallel and perpendicular to the plane containing the beam and the local vertical. At the end of each 30-minute data set, the data is then saved to a standard 3.5" floppy disk. The subtraction of a background noise sample with the shutter closed is important because of the accumulation of dark counts during the sampling period. This is because the first pixel sampled has less dark count than the last pixel sampled, due to the finite time to read out each of the 1024 pixels, and due to the fact that the background accumulation rate is temperature sensitive.

After the construction of the receiver was completed, it was tested to determine how well it performed as a linear detector. Figure 2.4 shows a test pattern used to test the linearity and dynamic range of the receiver. Figure 2.5 shows an example image of the test pattern and an image of a white sheet of paper at a 1/60 second shutter speed. The image of the white sheet of paper outlines the test pattern as would be expected. Multiple images were photographed at a range of shutter speeds, starting at ½ second and going to 1/1000 second. This test covered a signal range from strong saturation of the array to a small signal to noise ratio at 1/1000 second shutter speed. Examination of Figure 2.5 shows several features of the instrument, which lead to the conclusion that the instrument performed as expected. The results in Figure 2.5 also show the nonlinearity of the instrument across the field-of-view of the camera, a problem with which every good

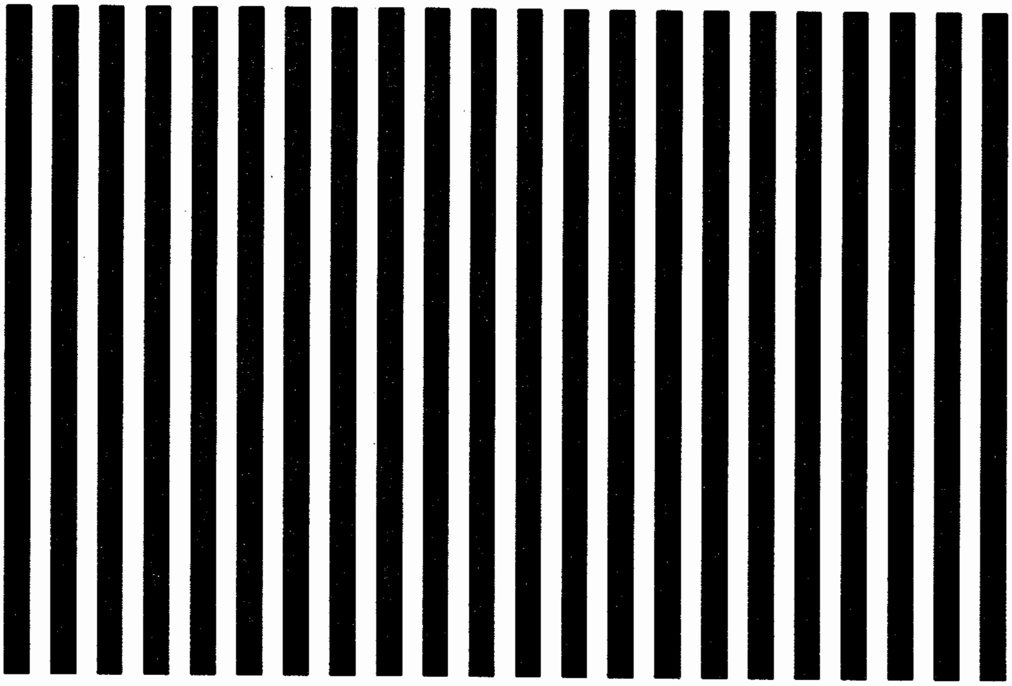

Figure 2.4. Test pattern used to conduct initial tests of the bistatic linear diode array receiver.

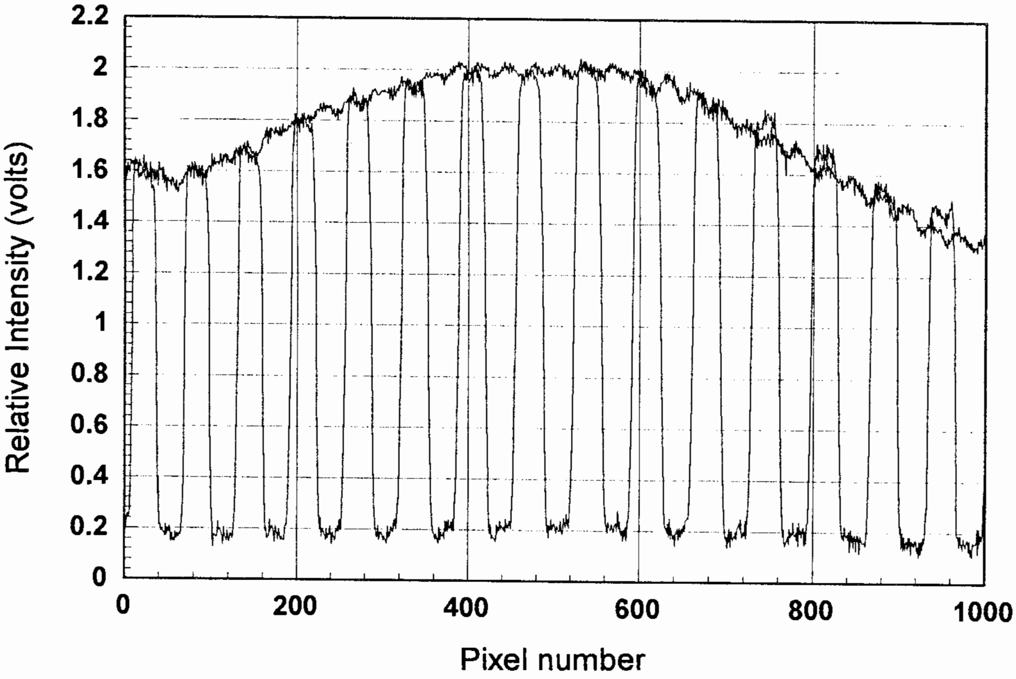

Figure 2.5. An Image of the test pattern in Figure 2.4 with a 1/60 second shutter speed and an image of a blank white sheet of paper are shown to verify the operation of the bistatic receiver.

photographer must deal. The camera's lens system simply collects less light off axis by a factor of $\cos^4(\theta)$ than it does on axis. These images were collected with a 24 mm focal length wide-angle lens so the effects are even greater than with the standard 50 mm focal length lens. The diode array is 25.6 mm long, which corresponds to a full angle field-of-view for the array of 50°. Multiplying the maximum signal at the center of the array by $\cos^4(\theta)$ yields: $2 * \cos^4(25) = 1.35$. This is what is observed at the 1000th pixel, but not at the 1st pixel as would be expected, which is probably due to non-uniform lighting in the test area. The non-linear response across the field-of-view could probably be corrected analytically but would only add uncertainty and error to the final reconstruction of the scattering phase function. This factor is one of the many reasons that a ratio of two measurements is used to provide a more robust measurement. Finally, Figure 2.5 also demonstrates the dynamic range of the instrument, although it will be shown later that this type of measurement needs very little dynamic range. Figure 2.6 shows the same test pattern imaged with a shutter speed of 1/500 second. Here we can see useable signal levels down to less than 0.05 volts. The array saturates at about 5.0 volts, therefore the dynamic range of the instrument is greater than two orders of magnitude. For typical lidar measurements of the atmosphere this dynamic range would be inadequate, but due to a changing effective sampling volume from the geometrical arrangement, this is sufficient for these measurements (see section 2.3). Figures 2.5 and 2.6 provide no information about the sensitivity of the instrument; imaging the laser beam in the atmosphere was the true test of the instrument's sensitivity.

Another problem with imaging a large field-of-view onto a linear array is the angular response of the narrow-band filter. Figure 2.7 is a plot of the spectral response of the transmission for the 532 nm band-pass filter at normal incidence and at 15° off-normal incidence. The vertical black line at 532 nm indicates the wavelength of the laser line. The filter was purposely chosen with a wide band-pass of 10 nm, so that off-normal incident light would still pass through the filter. It can be seen from Figure 2.7 that an angle greater than 15° would shift the filter's pass band away from the laser line. Therefore, the full angle for the field-of-view for the array could be no larger than 30°.

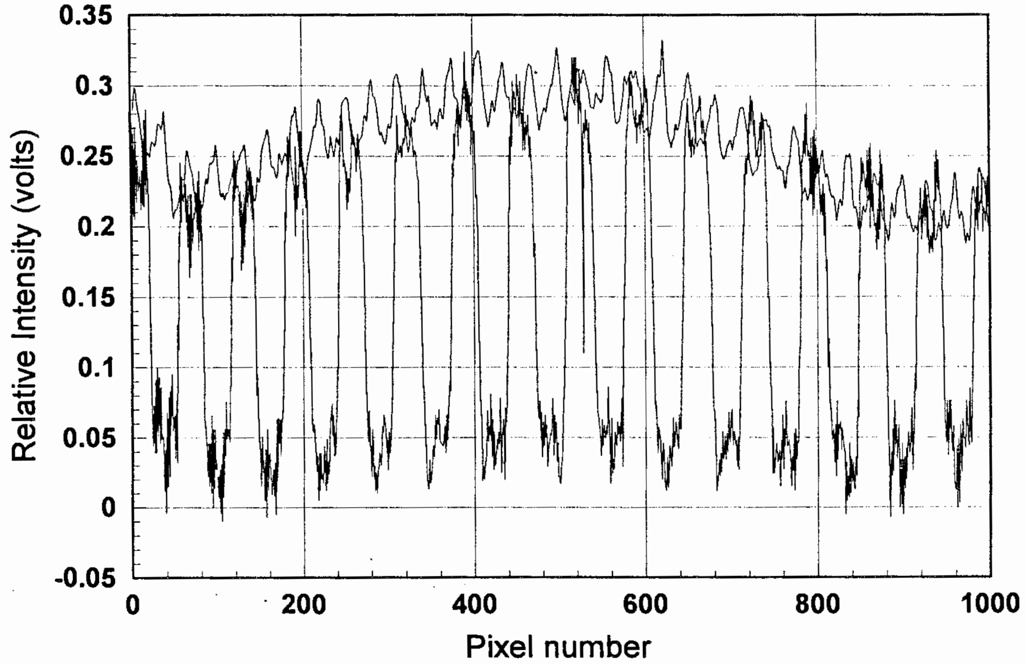

Figure 2.6. Image of the test pattern in Figure 2.4 with a shutter speed of 1/500 seconds. This image helps to determine the dynamic range of the diode array.

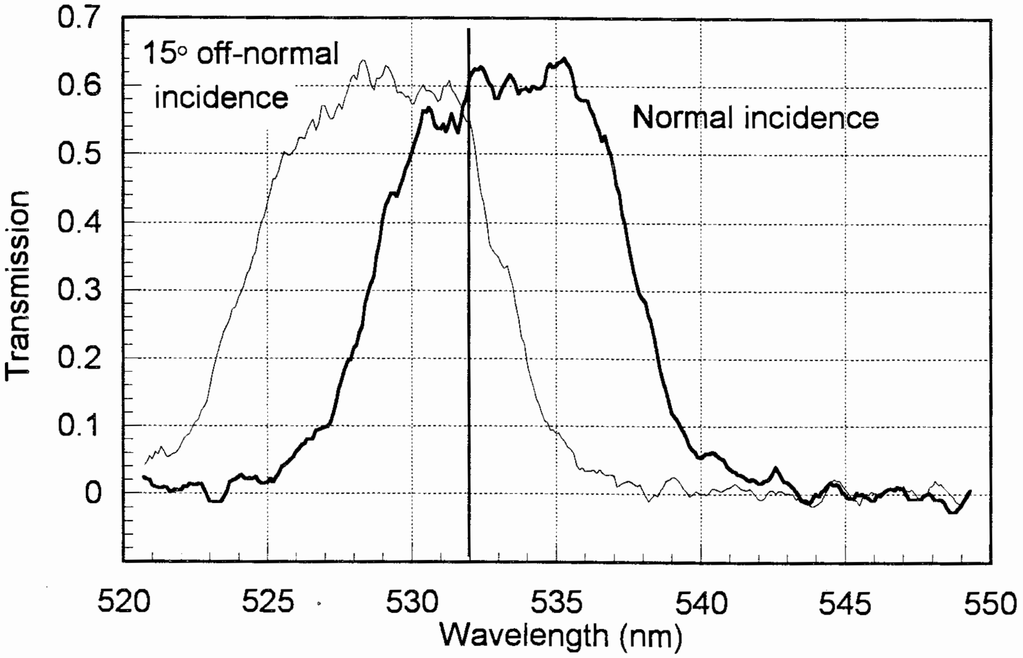

Figure 2.7. Filter spectral response of the transmission measured on a spectrophotometer. This shows the dependance of the filter band-pass on the angle of incidence.

This was the deciding factor in using a standard 50 mm focal length lens instead of a wide-angle lens to image the laser beam. The 25.6 mm array in the backplane of the camera along with the 50 mm focal length lens define a full angle field-of-view of 26°, however this does not solve the problem. From Figure 2.7 it can be seen that transmission is not a constant with changing angle over the 26° range of incidence. This would be another correction to apply to the angular data in order to reconstruct an accurate scattering phase function. The measurement technique used in this thesis cancels these effects because it relies upon the ratio of two measurements at different polarizations.

2.2.2 Modes Of Operation

Figure 2.8 shows two modes of operation for the lidar and bistatic receiver, vertical and horizontal. Each mode of operation has its advantages and distinct measurement capabilities. The initial tests of the bistatic receiver were conducted with the laser pointed vertically. The data inversion process is more difficult for the vertical mode of operation than for the horizontal mode because the end point of the laser beam is not as well defined and because the atmosphere is not vertically uniform. More than one receiver would be needed for optimal vertical profile measurements. However, the vertical case will be presented first because it was used to initially test the receiver. When operating in the vertical mode the camera is positioned so that the infinity point of the laser is imaged onto the last pixel of the array. The last pixel with a signal is assigned a value of infinity for its altitude, and the inversion is processed downward. Because of the geometry, the last pixel has a range of about 8 km to infinity, and the first pixel has a range size of about 1 cm. This means that an error in assignment of the end point could cause large errors at high altitudes, but relatively small errors within the first kilometer. Figure 2.9 shows a plot of altitude versus angle for the vertical mode and with the receiver positioned 18 m from the laser. This plot shows the range of scattering angles that would be observed from a 60 m thick layer between 40 and 100 m. The bistatic receiver will be able to observe scattered radiation at angles between 155 and 170 degrees with this geometry. It will be

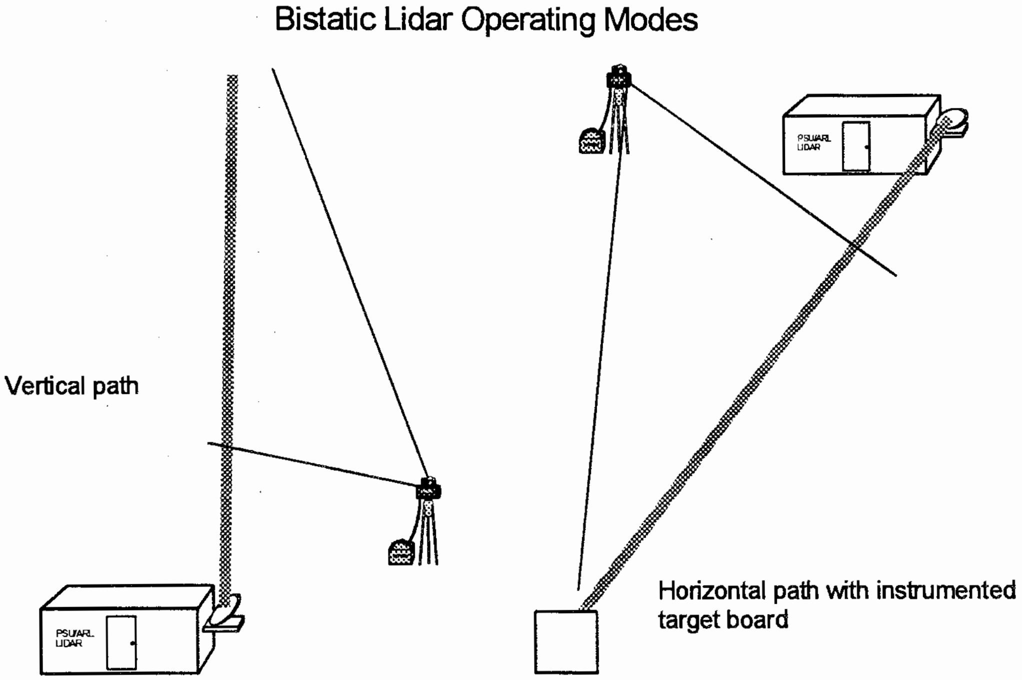

Figure 2.8. The lidar and bistatic receiver can be operated both vertically and horizontally. By operating a receiver with a linear array off-axis from the laser beam, angular scattering information can be collected about the aerosols.

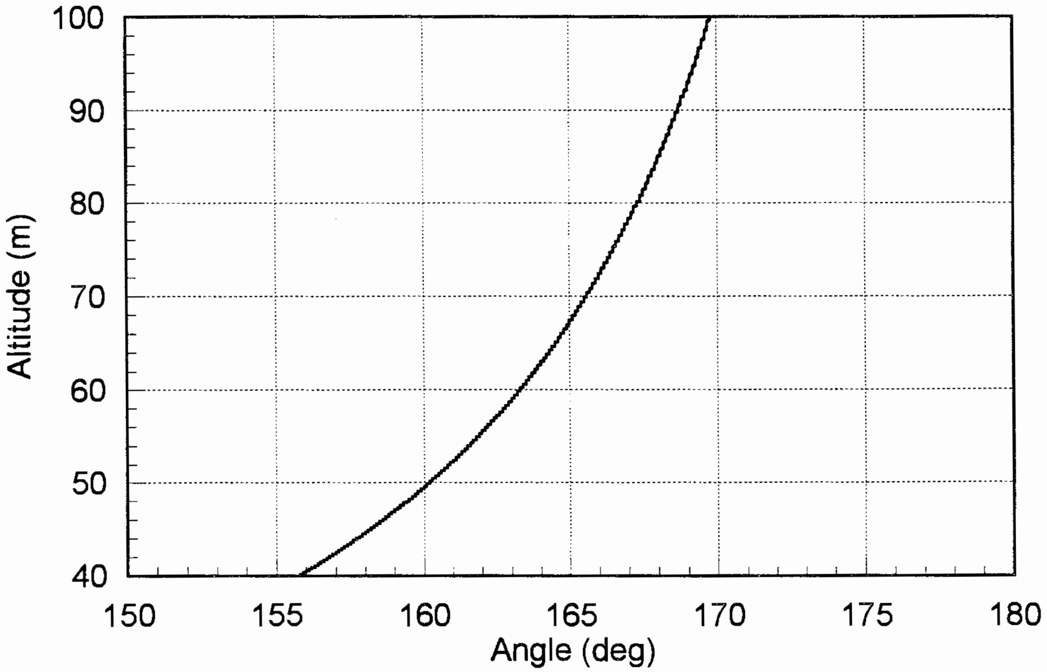

Figure 2.9. Plot of altitude versus angle for a receiver located 18 m from the laser transmitter. The plot shows the maximum range of angles that can be observed with the laser pointed vertically.

shown later that this angle range is where the most valuable backscattering information is contained. The optimal position of the receiver would be slightly different depending on the height of the aerosol layer. But the maximum range of observed angles will always be 15 degrees for small layers when operating in the vertical mode. The vertical mode of measurement is more useful for obtaining aerosol profiles close to the ground than for determining aerosol size distributions. Monostatic lidars are not able to measure accurate aerosol profiles below about 1 km, due to the fact that the receiving telescope is generally a far-field instrument. When the aerosol layer is at least 60 m thick, a large enough range of angles could be obtained in a single measurement to calculate a size distribution. In most cases several bistatic receivers would have to be located at different distances from the laser source. This would allow several different angle measurements at the same point in space for the required range of angular scattering measurements between 155° and 175°.

When operating in the horizontal mode the experiment is similar to a large scale nephelometer instrument. Figure 2.10 shows how the bistatic receiver collects the scattered radiation from many angles at one position. The assumption is made that the scatterers are uniform through the region being measured, which becomes a more exact representation as the horizontal measurement distance becomes smaller. It will be shown in Chapter 3 that the scattering angles of 155 to 175 degrees are covered within only 140 m for the CASE I experiment. If we can treat the 140 m long scattering volume as consisting of a homogenous aerosol distribution, then the bistatic receiver can observe the scattering phase function between 155 and 175 degrees. The scattering phase function is not directly fitted to a model due to the uncertainties in the relative intensity from one scattering element/angle to the next. Instead, the scattering phase function from parallel transmitted polarization is compared with the scattering phase function from perpendicular transmitted polarization. This ratio eliminates almost all of the instrument error and problems associated with the changing scattering volume size. A model of this ratio is then used to invert the data to a size distribution, as will be shown in Chapter 5. It will be shown that this method using the ratio of these two scattering components is much more

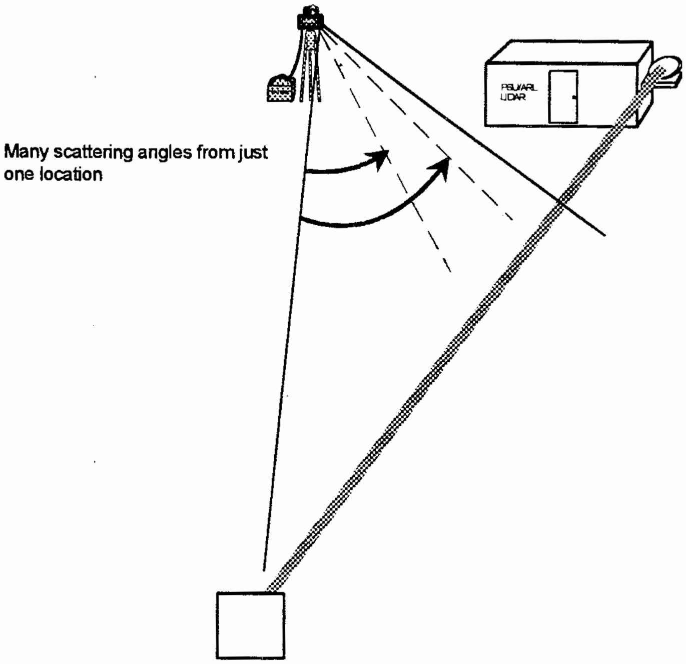

Figure 2.10. Horizontal mode of operation demonstrating the ability of the receiver to collect many scattering angles from just one location. The lidar N_2 return is used to check the uniformity of the aerosols along the path.

stable, well behaved and sensitive to the actual aerosol size distribution than a reconstruction of the scattering phase function from independent angle measurements. If the aerosol distribution is uniform over the full path length to the target board, then scattering angles can be observed from 155 up to nearly 180 degrees. The N_2 Raman channel from the LAMP lidar provides a check on the homogeneity of the scatters along the path. The slope of the nitrogen profile is a measure of the extinction along the path, as was discussed in Chapter 1. Therefore, if the extinction is constant along the path, then the aerosol distribution is also constant along the path. Figure 2.11 shows the relationship between scattering angle and distance from the laser source. This curve was calculated for a separation of 15.24 m (50 ft.) between the laser source and the bistatic receiver. Here we can see that the angles from 155 to 175 degrees correspond to a distance of 35 to 175 m in front of the laser source. Chapter 3 will describe the horizontal geometry of the experiment for the Wallops CASE I program more completely.

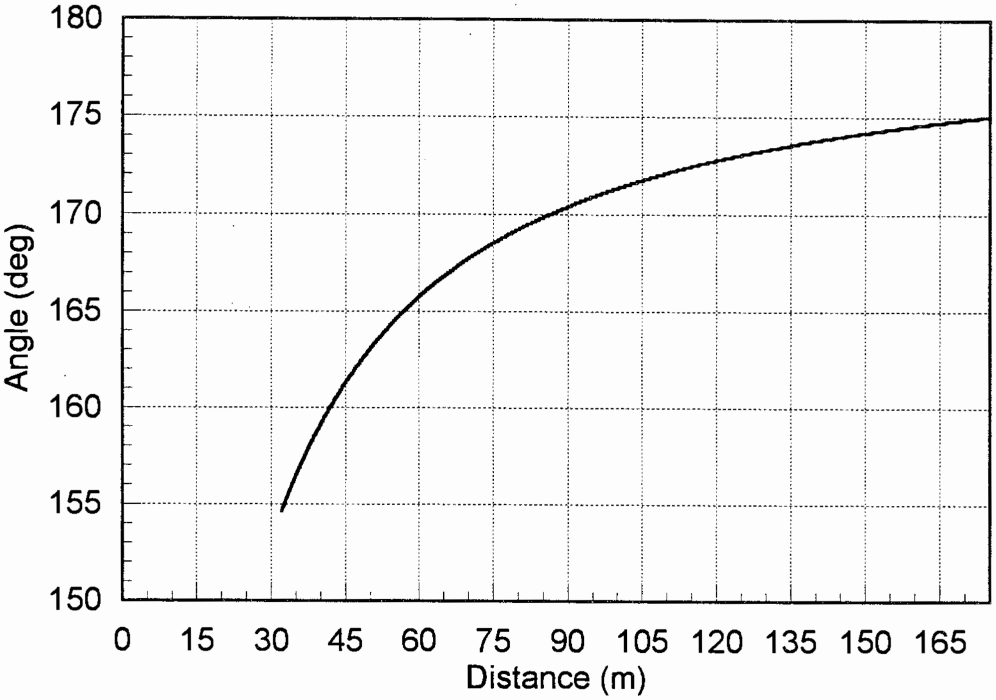

Figure 2.11. A plot of the relationship between scattering angle and distance from the source, calculated for a distance of 15.24 m between the source and receiver.

2.2.3 Initial Results

The first atmospheric tests of the bistatic instrument were conducted at The Pennsylvania State University using the LAPS lidar operating in the vertical mode. The LAPS lidar was used because it transmits the highest output power compared to our other lasers, which made the first tests and alignments of the instrument easier.

Figure 2.12 is a plot of unprocessed data from the photodiode array. The ordinate is digitized voltage minus background and the abscissa is the pixel number out of 1024. This data was collected using the LAPS (Lidar Atmospheric Profile Sensor) laser on March 14, 1995 in State College, PA. The data was averaged for 10 seconds (300 laser pulses), and the receiver was located 7.62 m from the laser. There were no clouds that night so the last pixel with signal was assigned an altitude of infinity for data processing. The data was processed to provide a profile of relative signal versus altitude. Figure 2.13 shows a schematic diagram of the geometry involved in processing the raw data in Figure

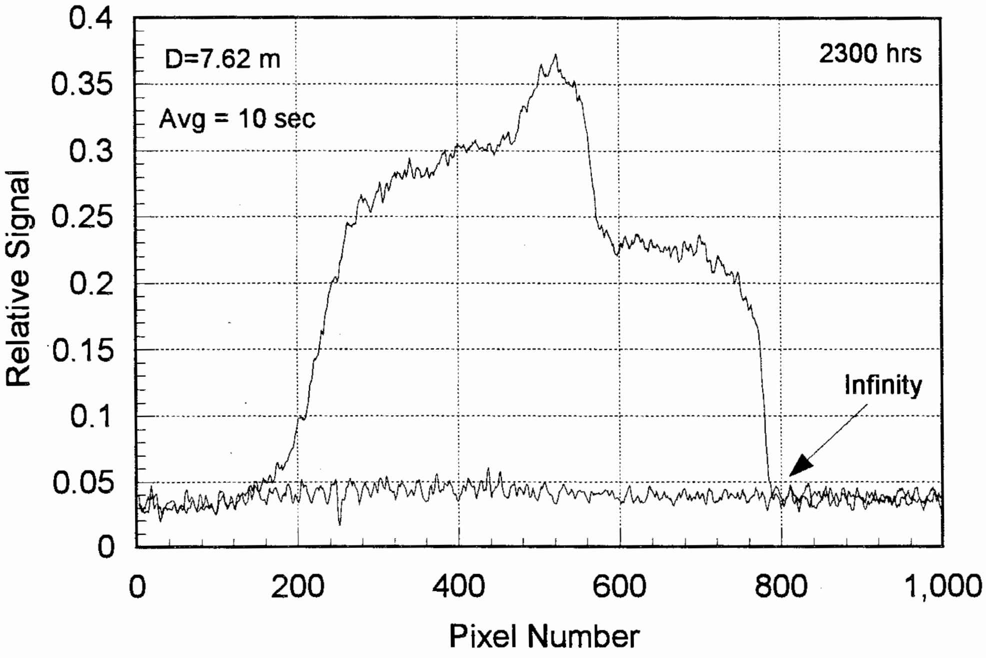

Figure 2.12. Raw data collected at Penn State with a bistatic receiver using a linear photodiode array on March 14, 1995.

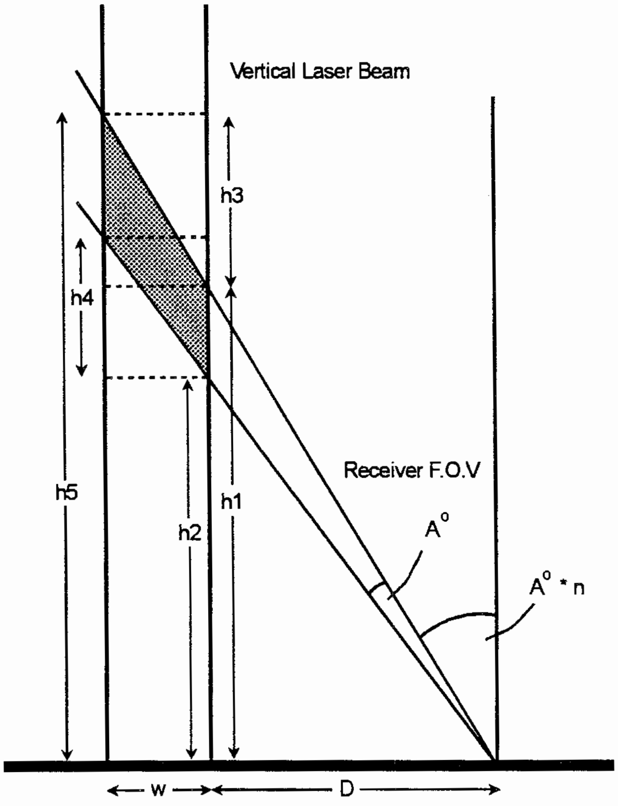

Figure 2.13. A schematic diagram showing the geometry for a bistatic linear photodiode array lidar receiver. The shaded area represents the scattering volume.

2.12. One edge of the field-of-view (f.o.v.) points vertically and the other edge intersects the laser beam 26 degrees down from vertical. So the minimum observable height will be twice the separation of the laser and receiver, i.e., tan(90-26). The pixel resolution is 0.0254 degrees, for the 50 mm focal length lens, and is denoted by A° in Figure 2.13. The scattering volume is shown as the shaded region and its size is defined as h_5-h_2. The height of each scattering volume is defined as $h_2+.5(h_5-h_2)$ and is used to determine the height associated with each pixel. As the altitude increases the scattering volume also increases, as can be seen from the geometry in Figure 2.13. Therefore, the relative signal must be corrected for the size of the volume being measured. A correction for $1/R^2$ must also be applied due to the increasing distance between the scatterers and the receiver. The $1/R^2$ correction and the increasing scattering volume nearly balance, which causes the raw data profile on a clear night to be almost a straight line. Therefore, the instrument requires relatively little dynamic range. Figure 2.14 shows a plot of the data from Figure 2.12 with these corrections applied. It can now be seen that an aerosol layer exists between about 60 and 80 m. To obtain the maximum angle range for a layer at this height, the receiver should have been placed 18 m not 7 m from the laser. The height resolution in the layer is between 0.2 and 0.4 m. Aerosol profiles of this resolution, and this close to the ground, are very difficult to obtain with other instruments. Monostatic lidars are not able to reliably measure aerosol scattering closer than about 1000 m from the surface because their telescopes are generally far-field instruments. Figure 2.15 is one more example of an aerosol profile that shows the capabilities of this bistatic receiver. These profiles were collected the same night and were separated by two minutes. The variability of aerosols near the Earth's surface is shown here by the sizable decrease of the signal in only two minutes.

All other data have been collected in the horizontal mode because more information can be obtained on the angular scattering of the aerosols. The following chapter will describe the Wallops CASE I experiment and the atmospheric conditions.

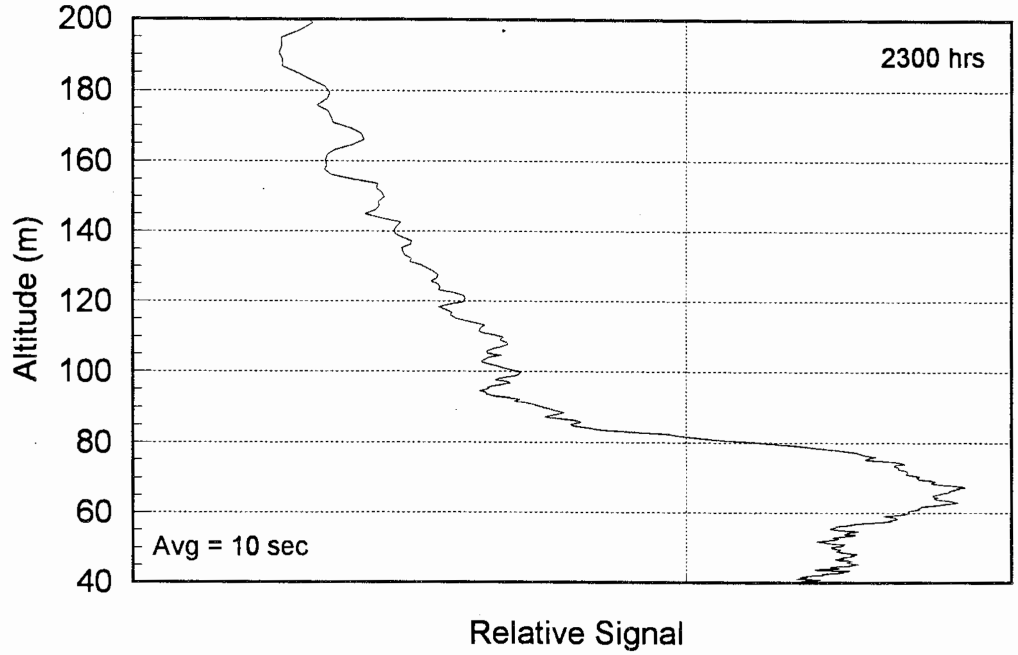

Figure 2.14. A profile of the first measurements from a bistatic receiver collected on March 14, 1995 with an integration time was 10 seconds, and spatial resolution through the aerosol layer of less than 0.4 m.

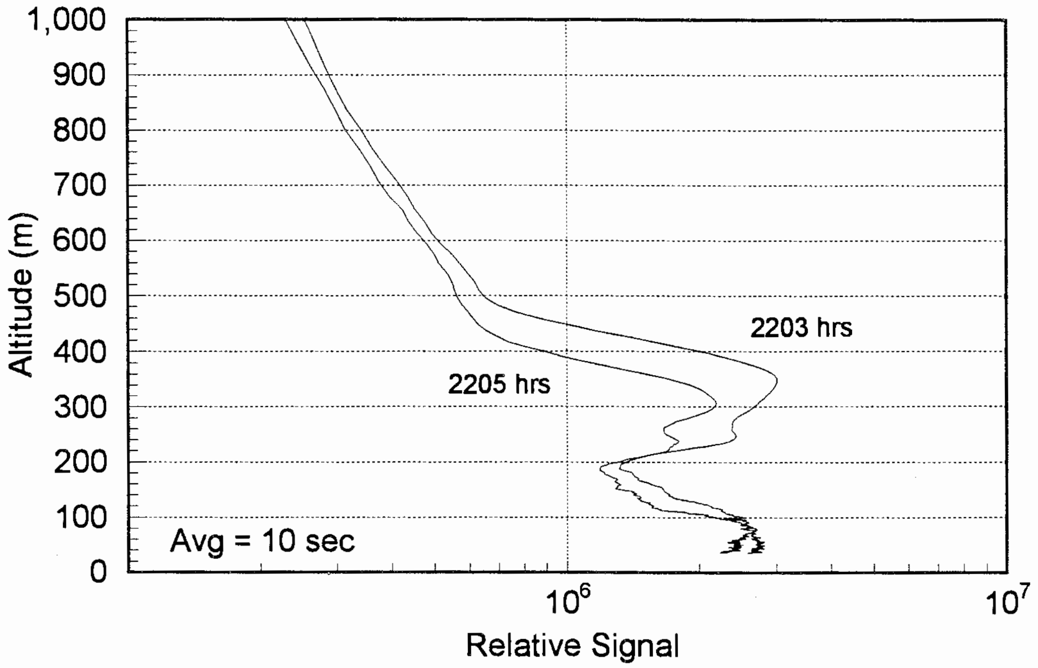

Figure 2.15. The profiles from two processed data sets from the same night as those in Figure 2.14. These profiles were collected about one hour earlier than the profiles in Figure 2.14 when an aerosol layer was observed at 300 m.

Chapter 3

WALLOPS CASE I 1995 MEASUREMENT PROGRAM (COASTAL AEROSOL SCATTERING EXPERIMENT)

Although the bistatic receiver described in Chapter 2 can be operated in either the vertical or horizontal mode, accurate size distributions are much easier to obtain when operating horizontally. This is because the receiver collects backscattered radiation from many angles at only one location, as was shown in Figure 2.10. There are few locations where a high power pulsed laser could be operated along a 3 km horizontal path near a coastal environment with controlled air space. One such location is Wallops Island Virginia, a NASA rocket-launching site. This location was chosen for its humid, misty, coastal marine environment and for an unobstructed 3 km path over a salt marsh. The measurement program, coastal aerosol scattering experiment (CASE), was conducted for three weeks during September, 1995. This experiment was a precursor to a larger Navy-sponsored campaign called EOPACE (Electro-Optical Propagation Assessment in the Coastal Environment) to study surf-generated coastal aerosols and background continental aerosols. EOPACE was conducted in January 1996 and included measurements from in-situ particle sizing instruments to help verify the calculations from the bistatic receiver data.

3.1 Measurement Focus and Test Plan

The CASE experiment addressed several topics including daytime and nighttime water vapor mixing ratio, daytime and nighttime ozone profiles, and data comparison with several NASA aircraft overflights. The vertical lidar profiles are also being compared to in-situ measurements from ozonesondes and rawinsonde balloons. A second lidar from NASA GSFC also measured vertical and horizontal water vapor mixing ratios. However, the focus of this thesis is on the horizontal lidar measurements. The goal of the horizontal measurements during the Wallops CASE I program was to collect data with the bistatic receiver for a range of particle size distributions, and to answer the following questions:

- How sensitive is the scattering between the angles of 155° and 175° to changes in particle size distributions?
- How well does Mie theory describe the observed data?
- What range of particle sizes can be measured using a 532 nm laser?
- Would the extinction calculated from the Raman N_2 (607 nm) lidar channel agree with the extinction calculated from the bistatic lidar data?
- Finally, what additional experiments and changes would have to be made to improve the measurement technique?

The data sets collected during the CASE I program answered all these questions for the humid coastal marine environment.

The LAMP lidar was transported to Wallops Island on August 29, 1995, and located beside the Q-6 radar site at U-70 on the mainland. Figure 3.1 shows the positions of the lidar on the mainland and target board on the island. The target board was mounted to a meteorological tower 18 m above the ground and 3.28 km from the lidar. The target board served several purposes. First, it provided a beam stop for the laser. Second, the signal return from the target board was a relative indication of extinction along the path. And finally, knowing the exact position of the target board made the inversion of the bistatic receiver data more accurate. Data was collected every night from September 7 to September 20. Supporting instruments included a local weather station and three remote temperature and humidity probes. The weather station was located at the laser source and measured wind velocity, temperature, relative humidity, and displayed the dew point. The three temperature and humidity probes were evenly spaced between the target board and laser and placed in protective wooden enclosures three feet from the ground. These probes are used to help analyze and verify the changing fog particle sizes calculated from the bistatic receiver data. They are also used to compare the horizontal lidar temperature and water vapor measurements with the ground measurements. Figure 3.1 shows the three

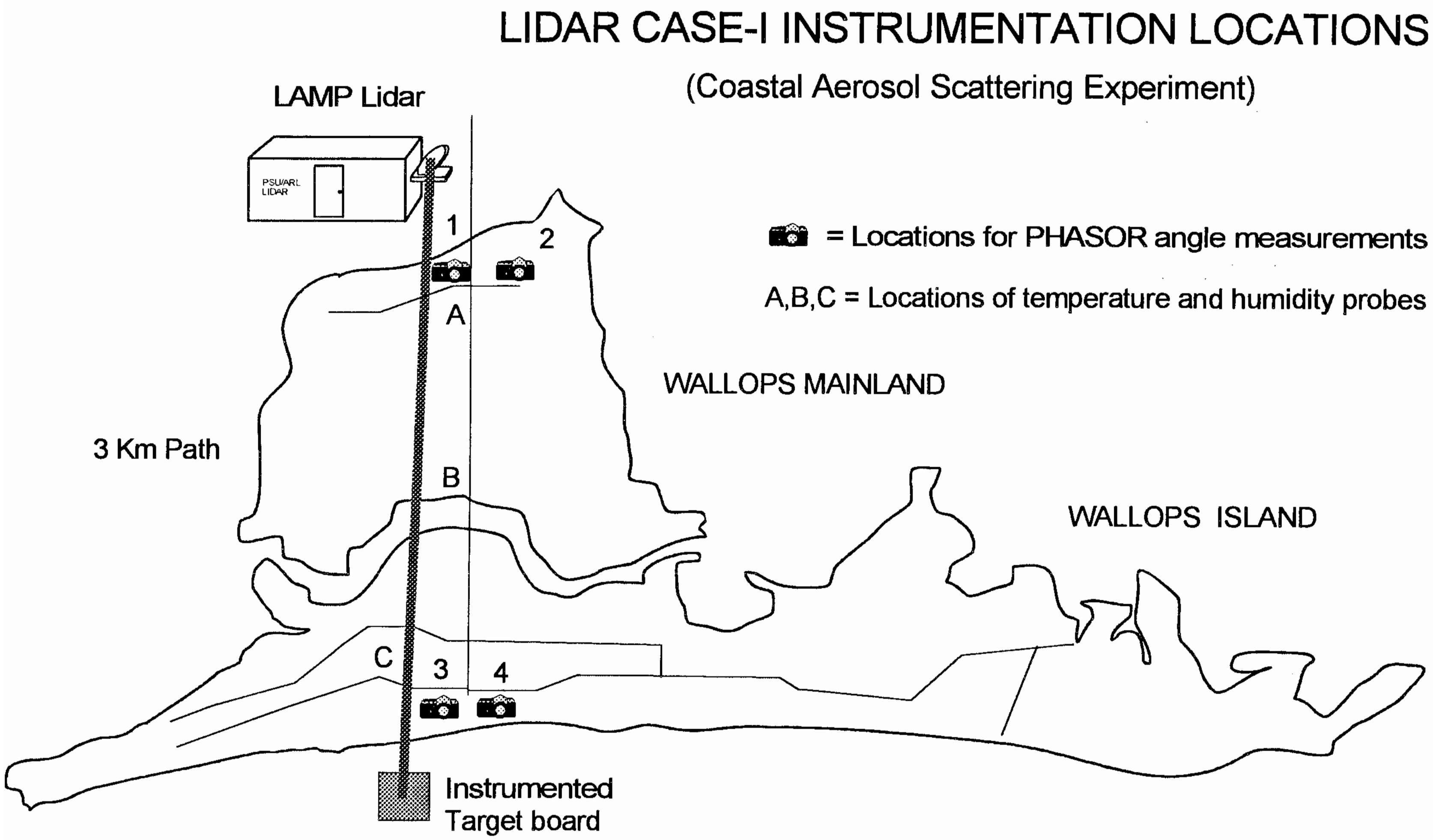

Figure 3.1. Instrumentation locations at the Wallops Mainland and Wallops Island for the CASE I measurement program.

locations of the temperature and humidity probes. The following section describes the experimental test procedures.

3.2 Experimental Setup and Operation

One bistatic receiver was used as shown in Figure 3.1 at position 1, although future experiments could benefit from multiple receivers located at positions 2, 3, and 4. Additional receivers could be used to collect forward scattering information or to collect several scattering angles from the same volume. However, It will be shown that one properly placed receiver is sufficient for horizontal measurements as long as the observed 140 meter path is uniform. Bistatic vertical measurements become more difficult because the sampled volume cannot be considered uniform. At least two receivers would be needed to determine a particle size distribution in the vertical mode. Valuable information can still be obtained from a bistatic receiver even if particle sizing is not the main goal. For example, a bistatic receiver is the only way to measure the near field properties directly in front of a lidar system.

3.2.1 Instrumentation Geometry

The LAMP lidar was positioned so that the laser beam could be easily steered from pointing vertical to horizontal to illuminate the target board 3.28 km away. It was important that the laser path was almost perfectly horizontal so that it would not be propagating through different layers of a stratified atmosphere. This helped to ensure a uniform and homogenous scattering volume along the 140 meter measurement path. The bistatic receiver's position was also important to obtain a large range of angles in a short distance. Figure 3.2 is a schematic showing the placement of the bistatic receiver with respect to the lidar. The two were separated by 15.24 m which imaged the scattering path, between 35 m and 175 m, and corresponded to scattering angles between 155° to 175°. Placing the receiver further from the laser increases the length of the scattering volume

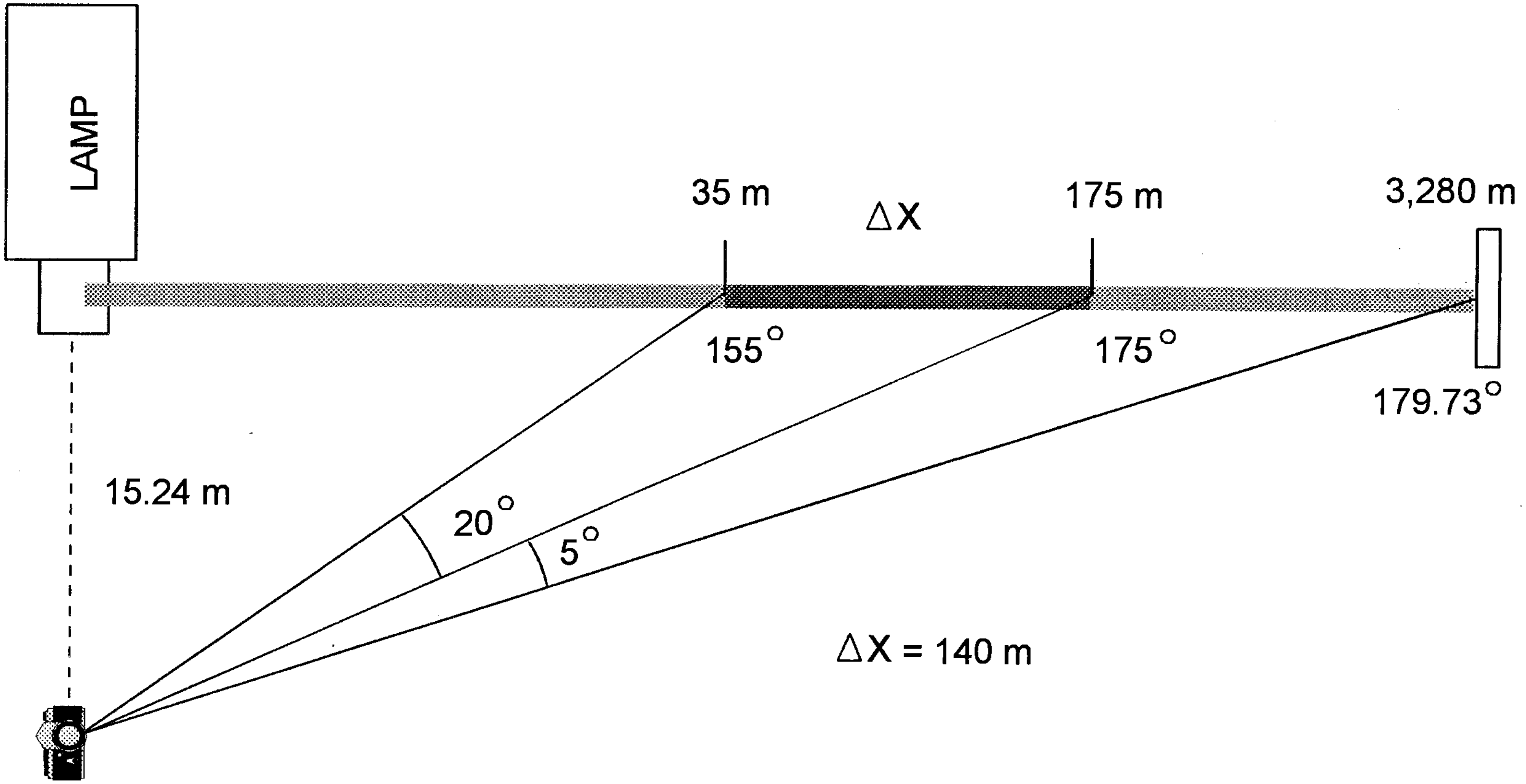

Figure 3.2. Geometry for the bistatic receiver's placement with respect to the laser. Here the 20 degree range of angles over the 140 meter path can be seen. Also the large distance of more than 3 km for only a 5 degree range of angles from 175 to 180 degree scattering.

and moves it farther from the source. Placing the receiver closer to the laser decreases the scattering volume's length but moves the scattering volume too close to the laser for accurate measurements from the lidar. The 15.24 meters between the lidar and the receiver seemed to be a good compromise between the size of the scattering volume and distance between the scattering volume and the lidar (see Figure 2.11). As can be seen from Figure 3.2 the distance between 175 m to 3280 m covers less than 5°, so one must use care when analyzing data from 175° to 180°. A 3 km path is much less likely to be uniform than a 140 m path. The return from the lidar's Raman channels represents scattering from molecules only, therefore these channels can be used to monitor changes in extinction along the horizontal path. On nights when the Raman channels show a constant extinction with distance, it can be assumed that the atmospheric path is uniform for the full 3.28 km. These data sets are used to fit models between 155° and 180°.

The LAMP lidar has been outfitted with a polarization rotator to rotate the laser's electric field between parallel and perpendicular to the scattering plane. In order to guarantee that only one linear polarization is received, the location of the receiver should be in the same plane as the scatterers. If the receiver is lower or higher than shown in Figure 3.3, the scattered radiation will not be parallel or perpendicular to the scattering plane, and the scattered light will be elliptically polarized. This would be acceptable if linear polarizers were used at the receiver (see Chapter 4). It is important that the ratio between the two polarizations be used instead of a single measurement. Direct measurements would have to account for the differences in extinction of the laser beam at each point on the scattering path. This would cause the return from larger angles to appear at artificially lower radiances compared to the return from smaller angles in close. A reconstructed phase function from this data would be distorted. Because extinction is independent of polarization if the scatterers are spherical or randomly oriented, the ratio of scattered irradiances for the two polarization states is the same at the scattering volume as at the receiver.

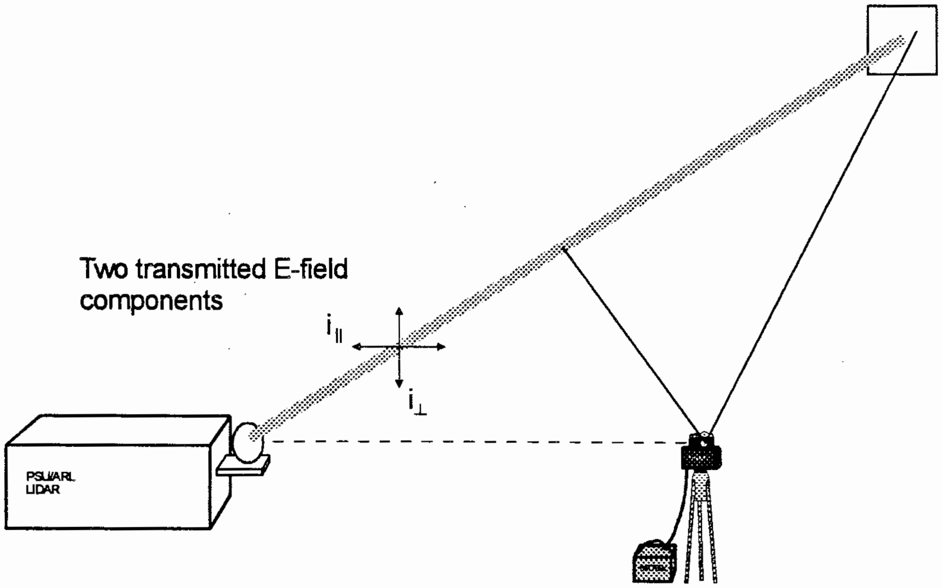

Figure 3.3. The bistatic receiver must be in the same plane as the scatterers in order for the polarizations to be pure. By working with the ratio of the two electric field components, the difference in extinction due to different path lengths is canceled.

3.2.2 Data Collection Process

Every evening started with vertical lidar measurements to correlate with other systems in the area and to gather a base data set of atmospheric conditions. Both 266 and 532 nm are transmitted when operating the lidar with the laser pointed vertically. The rotational Raman channels at 530 and 528 nm are compared to produce a temperature profile. The vibrational Raman channels at 660 (H_2O) and 607 (N_2) nm were compared to determine water vapor mixing ratios at night; the channels at 294 (H_2O) and 285 (N_2) nm are compared to determine water vapor mixing ratios during the day. Ozone profiles were determined in the lower troposphere from the ratio of 276 (O_2) to 285 (N_2) nm. And a 532 nm channel observed particle and molecular backscattering. Around 11:00 pm the lidar would be shut down and the laser positioned horizontally onto the target board 3.28

km away, using a low power configuration for the laser. After the laser was locked on target, 30 one-minute data sets would be automatically collected. When operating in the horizontal mode only the 532 nm wavelength would be transmitted, which was done to obtain the maximum laser power in the visible to improve the signal strength for the bistatic receiver. The 528 and 530 nm rotational temperature channels were also used to determine the temperature and extinction along the path. Horizontal water vapor mixing ratios also were calculated from the 660 and 607 nm channels. The 607 nm vibrational Raman return from nitrogen was used to calculate absolute extinction along the horizontal path. The combination of the molecular and particle scattering signal at 180° was measured using the 532 nm channel.

Because this type of bistatic setup is new, the experiment was not automated, and each 15 second data set was manually started. One measurement with the bistatic receiver takes about 50 seconds. This includes 15 seconds for the integration of the signal, 15 seconds for a dark count background integration, and 20 seconds to download the data to memory. The laser was turned off for 5 seconds after each one minute run making it easy to coordinate the lidar measurements with the bistatic receivers measurements. All measurements were collected at one minute intervals. When the laser turned off and then back on, the bistatic receiver was triggered for a 15 second measurement. At the end of the integration of the laser data set, the polarization rotator was inserted into the path of the laser beam by radio remote control. This process would be repeated 30 times for a 30 minute data set. At the end of 30 minutes, the collected data included 15 samples each with the electric field parallel and perpendicular to the scattering plane. This would yield 15 ratios of the two polarization components. Table 3.1 summarizes the dates and times when bistatic lidar data was collected. Brief descriptions of the atmospheric conditions and number of profiles are also listed. A total of 680 individual data sets were collected during all kinds of conditions from dry, to misty and foggy, to damp and rainy. Appendix E contains samples of the bistatic lidar data for each night of measurements along with the atmospheric conditions.

Remote temperature and humidity loggers were placed at points A, B, and C in Figure 3.1 at 2:00 pm each afternoon. The loggers would collect data every minute for 24 hours and then the data were downloaded at 1:00 pm each afternoon prior to redeploying the loggers. These data sets were used to observe the dew point as the temperature dropped each evening. As the temperature dropped on humid evenings we observed larger particle sizes in the data, indicating the formation of radiation fog. The combination of lidar data, bistatic receiver data, and point temperature and humidity data have been used to determine and verify calculated particle size distribution parameters.

Table 3.1. Summary of the bistatic lidar data collected during the CASE I program.

BISTATIC LIDAR DATA SUMMARY FOR THE WALLOPS CASE I PROGRAM

680 Data sets, 11 hrs. and 20 min., Collected from 9-7-95 to 9-20-95

Date	# of profiles	Start time	End time	Target bin	Conditions
9-7-95	50	12:55 am	2:12 am	50	Clear path with low clouds, RH=90%
9-8-95	30	11:57 pm	12:44 am	75	Windy, RH=80%, rain at 12:50 am
9-9-95	30	3:40 am	4:18 am	61	Visibly misty, RH=96%, clouds
9-10-95	30	12:10 am	12:50 am	23	Clearest night, no clouds, RH=53%
9-13-95	50	12:00 am	2:44 am	58	Visibly misty, RH=82%,266&532 nm
9-14-95	90	10:51 pm	3:00 am	76 & 40	Very hazy, RH=93%,ends RH=68%
9-15-95	20	11:30 pm	12:00 am	46	Windy and fairly clear, RH=71%
9-17-95	240	10:00 pm	6:30 am	33	Ran till morning, misty, RH=90%
9-18-95	50	12:20 am	1:44 am	61	Slightly hazy, breezy, RH=92%
9-19-95	50	12:00 am	1:20 am	39	Very clear, windy, RH=78%
9-20-95	40	11:50 pm	2:22 am	50	Fairly clear, calm, RH=88%

3.3 Atmospheric Conditions and Expected Results

In order for Mie theory to accurately describe the aerosols, they must be spherical and of known composition. If the scatterers are small compared to the wavelength with small absorption indices they can be described with Rayleigh theory regardless of their shape. For a wavelength of 532 nm the molecular scattering limit occurs at about a 30 nm particle radius, although there is a continuous crossover between Rayleigh and Mie theory (see Chapter 4). Both the small background aerosols and the larger aerosols in a humid environment can be modeled using Mie theory. The coastal marine environment was chosen as the first test for this bistatic measurement technique. The marine aerosol is most often modeled with a trimodal lognormal distribution, with the smallest mode centered around 4 nm, which would fall in the small particle or molecular scattering region. Large modes are also modeled with Mie theory as the humidity increases.

One of the first goals was to be able to tell the difference between a misty night and a clear night just from inverting the bistatic receiver data. To do this we needed to collect data on clear and dry nights when possibly only one small background aerosol mode would exist. We also needed to collect data on humid and hazy or foggy nights when possibly three aerosol modes would exist. And finally we needed to collect data on calm nights when the temperature slowly dropped and the aerosols would grow in size throughout the evening due to the condensing of water vapor onto the particles. Data was collected during all of these atmospheric conditions, and photographs were taken to document the laser beam propagating through the aerosols.

Figure 3.4 is a photograph showing the laser propagating horizontally to the target board. The second white container was used as office space. At the left of the photograph is the bistatic receiver located perpendicular to, and 15.24 m from the laser beam. This photograph was taken by C. R. Philbrick with a 10 second exposure to image the laser beam, and a flash was used to illuminate the receiver setup. The photograph in Figure 3.4 was taken during a clear night as can be seen by the minimal scattering from the laser beam and from the distant lights. Figure 3.5 is another photograph of the laser beam

Figure 3.4. A photograph of the laser propagating toward the target board. The bistatic receiver can be seen located next to the white office container.

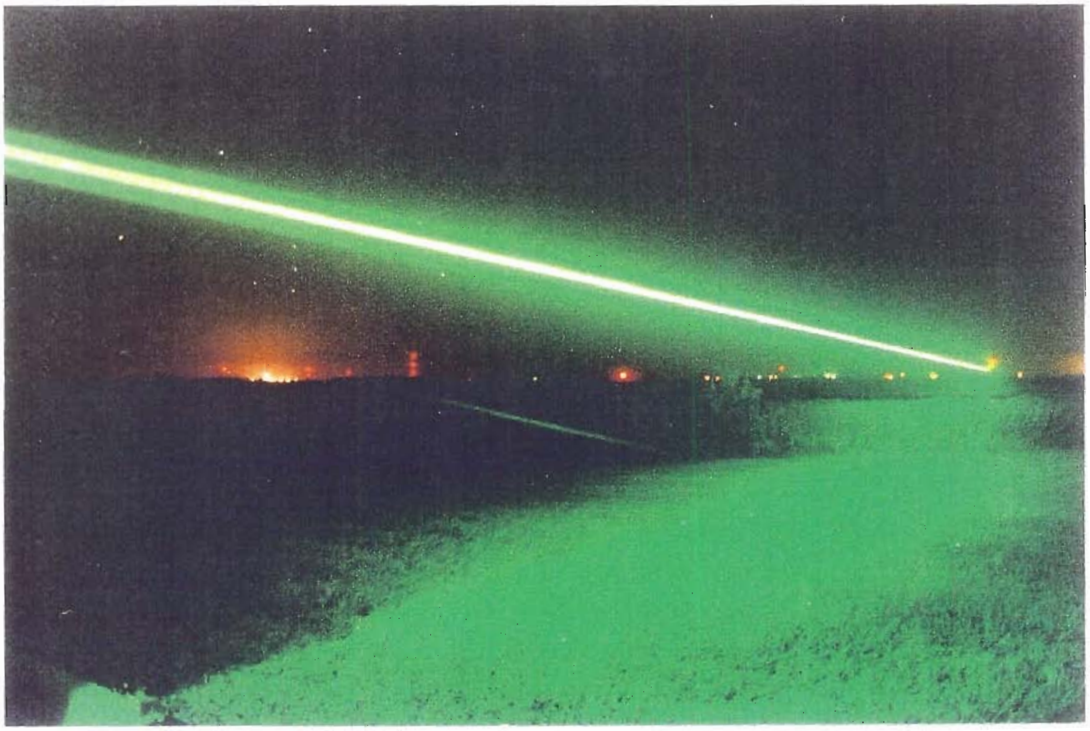

Figure 3.5. This photograph shows what the bistatic receiver sees on a clear night. The bright spot at the end of the laser beam is the target board.

propagating to the target board on a clear night. Here the target board can be seen as a bright spot of light at the end of the beam. This photograph is useful because this is exactly what the bistatic receiver sees when it images the laser beam. On a hazy night the target board would not be visible at the end of the beam. The beam is of relatively uniform intensity throughout the 3.28 km path also indicating that there are few if any large particles to scatter the laser radiation. Data from this night will be presented in Chapter 5 to show that the aerosol scatterers were indeed small. The relative humidity was about 53% and the inversion of the bistatic lidar data yielded a uni-modal size distribution with a median radius of 2 nm. This is consistent with the observed background aerosols in marine environments (Hobbs, 1993). Five of the nights were clear with conditions similar to the nights in Figures 3.4 and 3.5, and the bistatic data were consistent from one night to the next. The repeatability was very promising because the instrument had not been tested for particle size measurements before, and the imager had to be repositioned and realigned each evening.

Figures 3.6 and 3.7 are photographs of the laser beam with the photographer looking back toward the lidar container and the target board behind him. Both of these nights were visibly misty with an appreciable extinction along the laser beam. Figure 3.7 was taken while looking back at the laser with it continuing directly over head. Figure 3.6 was photographed just off to the side and looking back at the laser. These two perspectives clearly show three effects that should be pointed out from observations of the laser propagating through the larger aerosols on this night. First, Figure 3.6 shows a much larger glow around the laser beam than in Figure 3.4 on a clear night. Figure 3.4 shows a very uniform and tight ring of scattering around the laser beam, while figure 3.6 shows a non-uniform and much increased glow due to the scattering of the laser light by larger particles. Second, both Figures 3.6 and 3.7 show the extinction of the laser beam as it propagates toward the target board. This can be seen in the center of the beam as its brightness decreases nearer the target board due to increased extinction. The transmission to the target board was measured to be about 19% on this night, whereas, on clear nights the transmission would be about 89%. Finally, Figure 3.7 shows scattering of light out

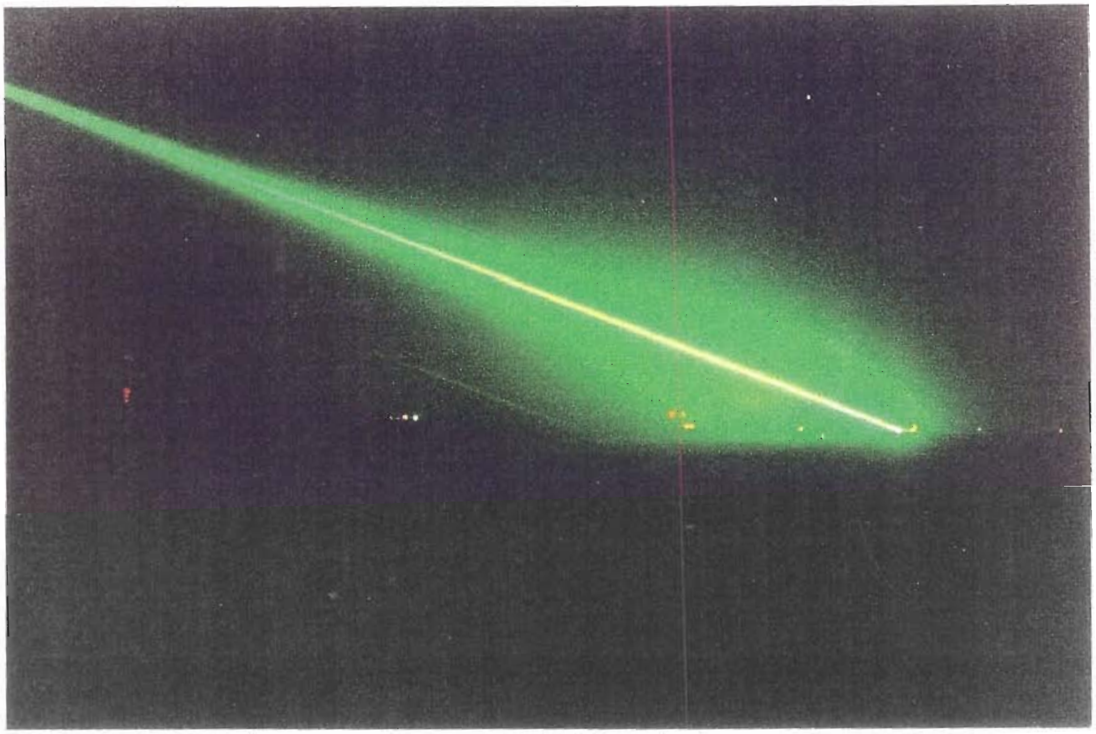

Figure 3.6. This photograph shows what the laser looks like when being attenuated by mist on a humid night.

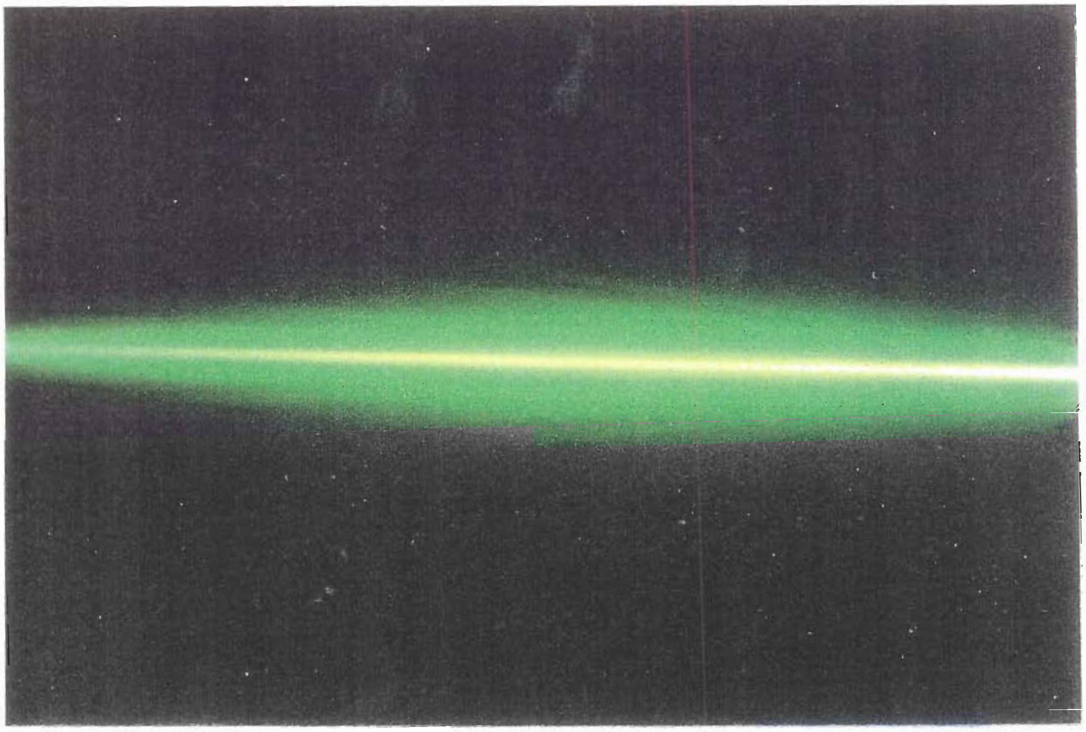

Figure 3.7. A photograph looking back at the laser with the target board directly behing the photographer. The extinction can be seen as rays of light are scattered out of the collimated laser beam.

of the laser beam. The scattering can be seen as streaks or rays of light leaving the collimated beam at small angles, which could not be seen on clear evenings like those in Figure 3.4. On the evenings like the case shown in Figure 3.7, a fine mist was visible and the relative humidity was over 90%.

The bistatic lidar receiver showed distinct differences for the varying atmospheric conditions that will be discussed in Chapter 5. Extinction coefficients will be calculated using the Raman channels from the lidar and then compared to extinction coefficients calculated from the aerosol size distribution determined from the bistatic receiver.

Chapter 4

BISTATIC LIDAR MODEL AND THEORY

Although the bistatic receiver can be operated in either the vertical or horizontal mode, accurate size distributions are much easier to obtain from the uniform size distributions observed when operating horizontally, therefore all modeling will be done for the horizontal mode. There are two general classes of problems involving the theory of the interaction of electromagnetic waves and small particles. The first being the direct problem and the second the inverse problem. The direct problem is solved with a model using known parameters and theories to determine the specific outcome, in our case the scattered radiation field. The inverse problem is solved with an appropriate inversion technique using theories and a measured scattered radiation field to determine the characteristics of the scatterers. The direct problem is like determining what kind of tracks a particular dragon would leave, and the inverse problem is like determining what kind of dragon left these particular tracks as described by (Bohren and Huffman, 1983).

Before any inverse problem can be attempted, the direct problem must first be solved. This means that the situation must be accurately modeled before the results of the experiment can be inverted to the desired parameters. The problem of accurately determining the collection of particles responsible for scattering a collimated laser beam is a difficult one, and usually declared impossible in an uncontrollable medium like the atmosphere. There is good reason for skepticism because many parameters must be known, and many more must be measured. But this is not necessarily a cause for despair, because often supplementary information about the particles can be obtained from reasonable assumptions about the atmospheric conditions. This is akin to narrowing your search to only hoofed animals when you observe hoof prints, instead of modeling and searching through all known animals to find the desired track makers. This same logic is applied to narrow the parameters that must be inverted to determine the distribution of particles that scattered the observed radiation field. If measurements are made in a humid environment it would be reasonable to assume spherical scatterers. But in a desert environment the shape of the aerosols would most definitely not be spheres. In problems as complicated as particle sizing in a free atmosphere, intelligent assumptions must be made and careful observations recorded about the environmental conditions at the time of the experiment. Even then, the calculated size distributions must be cautiously examined. This chapter focuses more on modeling calculations of the direct problem than on inversion, because without a reasonable model an inversion would not be possible.

4.1 Conditional Constraints (Assumptions) and Parameters

It is a good practice to define the constraints that are placed on the model; these are conditions that allow the model to predict only certain aerosol distributions. This could also be viewed as assumptions about the aerosols being measured. This experiment was designed so that the constraints should be considered conditions of the particles rather than assumptions. There are two parts to the model, one part is the modeling of the scattering theory, and one part uses the size distributions and models the bistatic lidar experiment. The scattering is modeled with Mie theory using a subroutine from (Bohren and Huffman, 1983). The bistatic lidar model is written using both Fortran and Matlab subroutines. The following is a list of the parameters that are supplied to the model:

- Transmitted wavelength
- Index of Refraction (particle composition)
- Particle Size Distribution
  (8 parameters for a tri-modal log-normal distribution)
- Scattering Angle
- Polarization.

The model provides the ratio of the intensities of two orthogonal electric field components scattered at angles between 155 and 180 degrees. This model has limitations and will only work under specific conditions as are listed as follows:

- particles must be spherical,
- multiple scattering must be negligible,
- the real and imaginary part of the index of refraction must be known reasonably well,
- the particle size distribution must be lognormal with at most three modes,
- the atmosphere must be horizontally homogeneous within the 140 m long measuring volume,
- the number density of the particle group being measured must be large enough to allow at least one particle per scattering volume, and,
- the particle sizes must fall between 1 nm and 250 μm.

Some of these are limitations of the scattering theory while others are conditions dictated by the experiment. For example, to accurately model the fields scattered from a distribution of randomly shaped, and randomly oriented particles would be a major investigation in itself, if it is even possible. So, the first experiment using this bistatic technique was conducted in a humid marine environment instead of a dry desert. Spherical models are much easier to work with and allow easier testing of this measurement technique. The spherical model will be shown to predict the results of the experiment rather well under most conditions.

Ideally, N parameters could be inverted as long as there are N number of independent pieces of information, and given a perfect model. There are a total of 11 variables when trying to obtain a trimodal lognormal size distribution. Nine variables are needed to describe the three modes of the distribution, and two are needed to represent the real and imaginary part of the index of refraction. The model was designed such that the nine distribution variables can easily and quickly be altered to find the best fit to the data. But for each refractive index, calculations can take up to one hour. This is because a large matrix is calculated for each scattering component; one for the incident field parallel to the scattering plane and one for the incident field perpendicular to the scattering plane. For every change in the index of refraction two matrices are calculated like that shown in Table 4.1 consisting of 175 columns by 500 rows or 87,500 elements. Each matrix is a large table of scattered intensities for a given particle radius and scattering angle. The radius range is from 1 nm to 250 μm evenly divided by 500 in logarithmic steps. The angle range is from 155° to 180° and evenly divided by 175 steps. Once each matrix is calculated, a Matlab routine reads them both into memory. These two matrices are the data that the Matlab program uses to model the final profile observed by the bistatic lidar. The inversion routine could vary the refractive index along with the nine distribution parameters when looking for the best fit of the model to the data, but this would take several hours just to run through one iteration. This wasn't necessary because the index of refraction can be estimated fairly accurately for the conditions during the Wallops experiment.

Table 4.1. Scattering matrix calculated using Mie theory.

	Angle: 155 to 180° , linear steps of 1/7°, 175 columns.					
Particle radius: 1 nm - 250μm log steps of 0.01. 500 rows.		155°				180°
	1 nm					
		Scattered intensities for single radius' with a fixed index of refraction.				
	250μm					

4.2 Mie Scattering Theory

This section is not intended to give a full mathematical description of Mie theory, but to outline some of the results of the theory and how they are useful. Complete derivations of Mie theory can be found in van de Hulst (1957) or in Bohren and Huffman (1983), as well as many other texts. Mie scattering theory is simply a rigorous solution of Maxwell's equations for the interaction of an electromagnetic plane wave with a sphere. The sphere has a radius r, and an index of refraction m, which is complex, with the imaginary part being related to the absorption coefficient. A perfectly conducting sphere is the easy case to solve because all electric fields must go to zero at the surface of the sphere, and no fields can exist inside the sphere. For a dielectric sphere the solution becomes more complicated because fields now exist inside the sphere. So, the full solution includes both scattered fields outside the sphere and standing waves inside the sphere. Of course the fields outside the particle are the only fields we have access to in a remote sensing experiment.

Section 4.2.1 will define what is meant by the scattering plane, and will explain what amplitude scattering matrix elements must be computed to describe the bistatic experiment.

4.2.1 Calculation of the Scattering Parameters

Figure 4.1 shows a laser propagating in the +z direction with the electric field oriented in the y-z plane. The scattering direction and the forward direction of the propagating laser beam define the scattering plane. From this diagram we can see that the scattered field along the dotted line defines a scattering plane perpendicular to the transmitted electric field, therefore the detected intensity is termed $I_\perp$, meaning that the radiation is polarized perpendicular to the scattering plane. By observing at 90° from the dotted line along the solid line, the received radiation is now polarized parallel to the scattering plane. This is because the scattering plane in part, is defined not by the

Scattered E-Field Components For Bi-Static Lidar

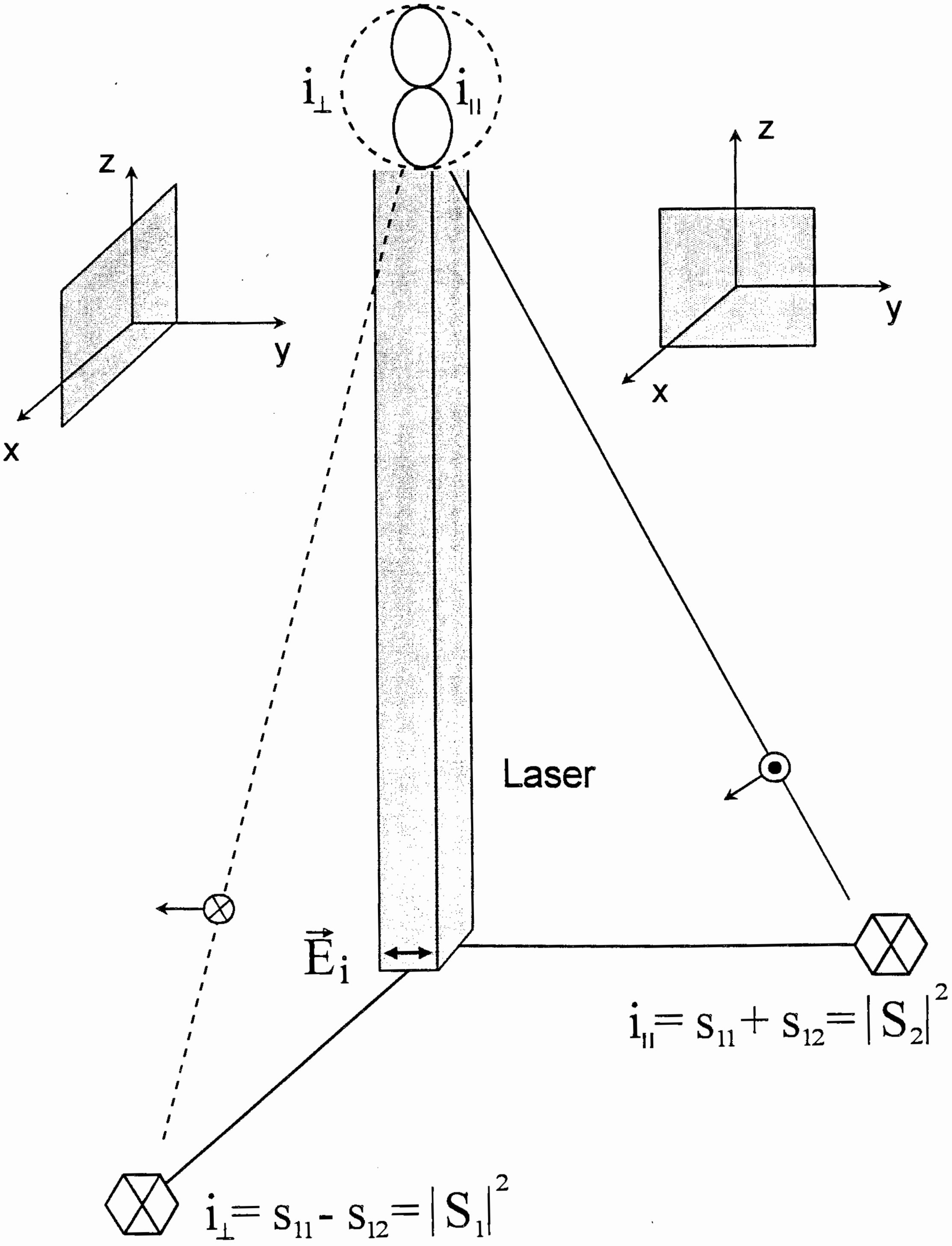

Figure 4.1. Geometry for a bistatic lidar setup, operating vertically, to show which components of the electric field will be measured at each location. The scattering plane is also defined for two different scattering locations.

polarization of the incident radiation but by the direction of propagation. This is a very important distinction because one can change one's observational view point, from parallel to the scattering plane to perpendicular to the scattering plane, simply by rotating the polarization of the source. For the bistatic lidar experiment described in Chapter 3, the laser's polarization was rotated instead of placing two receiver at 90°, as shown in Figure 4.1. Future experiments could be conducted with two instruments, as shown in Figure 4.1, so that simultaneous measurements could be made of both polarization components. The next step in determining what Mie parameters must be calculated is to define the amplitude scattering matrix, which is the relationship between the incident and scattered fields.

The relationship between incident and scattered fields can be written in matrix form as follows,

$$\begin{pmatrix} E_{\parallel s} \\ E_{\perp s} \end{pmatrix} = \frac{e^{ik(r\ z)}}{-ikr} \begin{pmatrix} S_2 & S_3 \\ S_4 & S_1 \end{pmatrix} \begin{pmatrix} E_{\parallel i} \\ E_{\perp i} \end{pmatrix}, \tag{4.1}$$

where the elements S_1, S_2, S_3, and S_4 are functions of the scattering direction and make up the amplitude scattering matrix. This amplitude scattering matrix is what is calculated in most Mie scattering subroutines including BHMIE. So it is essential that one knows what these four variables represent before modeling a particular experiment. For the simplifying case of homogeneous spherical particles and for incident linear polarizations, $S_3 = S_4 = 0$.

For the experiments in this thesis we made two measurements of the scattered light: One with the incident light polarized parallel to the scattering plane, and one with the incident light polarized perpendicular to the scattering plane. From Figure 4.1 it is shown that $|S_1|^2$ is calculated for incident light polarized perpendicular to the scattering plane, and $|S_2|^2$ is calculated for incident light polarized parallel to the scattering plane. The ratio of $|S_2|^2$ to $|S_1|^2$ is then used to model the data. If the particles are spheres, perpendicularly polarized incident light yields perpendicularly polarized scattered light, and parallel polarized incident light yields parallel polarized scattered light. If the collection of particles is not spherical and randomly oriented, the scattered radiation will be partially linearly polarized with an unpolarized component proportional to the non-sphericity of the particles. This fact can be used to determine when a large portion of the scattered radiance is due to non-spherical particles. During the CASE I program a cross polarizer was used to look for electric field components oriented 90° to the transmitted polarization. A signal detected this way could be due only to two factors, multiple scattering, or scattering from non-spherical particles. This test was conducted several times each evening during the measurement program at Wallops Island to look for this depolarization effect.

Many groups have made measurements of the scattered radiances at angles between 0° to 180°, but not including 0° and 180°, using polar nephelometers. B.S. Pritchard and W.G. Elliott were one of the first to obtain measurements in fog and clear air with a nephelometer, and plot two of the scattering matrix coefficients for several wavelengths (Pritchard and Elliott, 1960). Since Pritchard and Elliot, Hunt and Huffman have developed compact polar nephelometers using polarization modulators to measure all the scattering matrix coefficients from nearly 0° to 180° for a variety of particles (Hunt and Huffman, 1973, 1974). Hunt and Huffman compared their measurements of latex spheres dispersed in water. with Mie calculations using a gaussian size distribution given by the manufacturer of the spheres. They show excellent agreement between the data and the theory. Because of the geometry of the polar nephelometer, it is much easier to directly measure an accurate scattering phase function for one polarization component than for the experiment described in Chapter 3. Therefore, the ratio of two polarization components was not needed to compare the measured data with Mie theory. More recently a Japanese group used a polar nephelometer to measure the scattering components parallel and perpendicular to the scattering plane (the same components measured during CASE I) to determine the complex index of refraction of the particles (Hayasaka et al., 1992). They did this by using an iterative method to fit a spherical model to their data between 5° and 175°. All these past measurements with polar nephelometers form a basis for the bistatic lidar measurements described in this thesis.

4.2.2 Molecular Scattering

Another important factor in the bistatic lidar model is the role molecules play. When the atmosphere is fairly clear, dry, and containing few large aerosols, the scattering will be due mostly to particles and molecules in the Rayleigh scattering region. This is significant because under these conditions the nitrogen and oxygen molecules must be included in the model. In fact it will be shown latter in Chapter 5 that the addition of molecules can actually help to determine absolute number densities of the first aerosol mode.

There are a number of ways that molecular scattering could be included in a Mie scattering theory model. One way would be to calculate the Rayleigh scattering cross section for each angle of interest. The Rayleigh differential scattering cross section is given by (Measures, 1984; Zuev, 1982),

$$\frac{d\sigma_R(\theta,\varphi)}{d\Omega} = \frac{\pi^2(n^2-1)^2}{N^2\lambda^4}\left\{\cos^2\varphi\cos^2\theta + \sin^2\varphi\right\}, \tag{4.2}$$

where θ is the scattering angle, ϕ is the azimuthal or polarization angle, N is the number density of atmospheric molecules, and n is the refractive index of air. In the case of the Wallops experiment ϕ is either 0° or 90° depending on whether the incident electric field is parallel or perpendicular to the scattering plane, and the scattering angle, θ, ranges between 155° and 180°. Equation 4.2 does not include the effects of molecular anisotropy and is therefore is correct only for small spheres. The small differences between molecular scattering and scattering from a sphere small compared to the wavelength partially explain why the sky is not 100% polarized. For the purposes of this thesis the difference between the scattering phase function for a small sphere and for the assortment of molecules in the atmosphere is negligible. Another way to include molecular scattering would be to find an equivalent sphere that scatters with the same cross section as the combination of atmospheric molecules at the Earth's surface. As the particles becomes considerably smaller than the wavelength, Rayleigh scattering theory will apply. Because the field must remain uniform through the sphere, the particle can not have a significant absorption coefficient. An increase in the absorption, or refractive index, has the effect of decreasing the limit of the particle's radius for Rayleigh scattering. The rough limit where spherical scattering can be approximated with molecular or Rayleigh scattering, is (van de Hulst, 1981; Bohren and Huffman, 1983),

$$m \frac{2\pi r}{\lambda} < 0.5 \,, \tag{4.3}$$

where m=1.38 is the index of refraction for wet aerosols, and λ=532 nm is the wavelength of the laser. Aerosol scattering can be approximated with Rayleigh theory up to a radius of about 30.6 nm. In general, if the particles are much smaller than the wavelength in all dimensions, their shape can still have large effects on the scattering. But the aerosols encountered on Wallops Island had a very small absorption coefficient, therefore the shape of aerosols that are small compared to the wavelength would have little effect on the scattering. This can explain some of the success of Mie theory when applied to atmospheric aerosols that can not be modeled as spheres. In many cases the first mode of a trimodal aerosol distribution is mostly made up of particles smaller than 30 nm. In fact, some of the second mode is also made up of particles smaller than 30 nm, as will be shown in Sections 4.2 and 5.2.

Using the above information, an equivalent dielectric sphere can be found that scatters radiation with the same scattering cross section as oxygen and nitrogen molecules but with a slightly different scattering phase function due to the anisotropy of molecules. For the mixture of atmospheric gases which occur at the Earth's surface, the total Rayleigh cross section from (4.2) becomes,

$$\sigma^{R}(\lambda) = \frac{8\pi}{3}(5.45)\left[\frac{550}{\lambda(nm)}\right]^{4} \times 10^{32}\ m^{2} \,. \tag{4.4}$$

The Rayleigh scattering cross section at 532 nm is then $\sigma^{R}(532\text{nm})=5.22\times10^{-31}\ \text{m}^{2}$. The total scattering cross section for an isotropic dielectric sphere is given by (Measures, 1983),

$$\sigma(\lambda) = \frac{8\pi}{3} r^2 \left(\frac{2\pi r}{\lambda}\right)^4 \left\{\frac{n^2-1}{n^2+2}\right\}^2 , \tag{4.5}$$

where r is the particle radius, n is the particle's refractive index, and the 8π/3 results from integrating the scattering angle over 4π steradians. The equivalent dielectric sphere we are looking for has a refractive index of 1.38, the same as that of the modeled aerosols. Using $\sigma(532\text{nm})=5.22\times10^{-31}$ m^2 from above and $\lambda=532$ nm in (4.5) we find r=0.197 nm. Thus, a dielectric sphere with a refractive index of 1.38, and a radius of 0.197 nm, should scatter radiation similar to the mixture of atmospheric gases at the surface of the Earth. A check on the lower limits of the Mie subroutine, BHMIE, can now be made. The scattering cross section for the above dielectric sphere was calculated using BHMIE from 0.1 nm to 250 μm. Figure 4.2 shows this curve along with a line representing the Rayleigh scattering cross section of 5.21×10^{-31} m^2 calculated above for atmospheric gases. These two lines cross at about 0.198 nm, the same radius as calculated using (4.5). Figure 4.2 is slightly different from similar plots shown in the literature, where scattering efficiency is usually plotted, rather than scattering cross section. Scattering efficiency is a normalized cross section and is sometimes used because it is a dimensionless quantity. The scattering cross section represents the effective scattering cross sectional area of the particle. The two are related as follows,

$$Q_{sca} = \frac{\sigma(\lambda)}{\pi r^2} , \tag{4.6}$$

Q_{sca} is the scattering efficiency and r is the particle radius. The scattering efficiency converges at about two due not only to the particles ability to block radiation with its physical cross section, but also due to scattering around its edges, that is diffraction. It can be seen from Figure 4.2 that the scattering cross section ranges over 26 orders of magnitude for a particle radius range of only six orders of magnitude. Through the small particle scattering range, the scattering cross section is proportional to r^6. Now that an

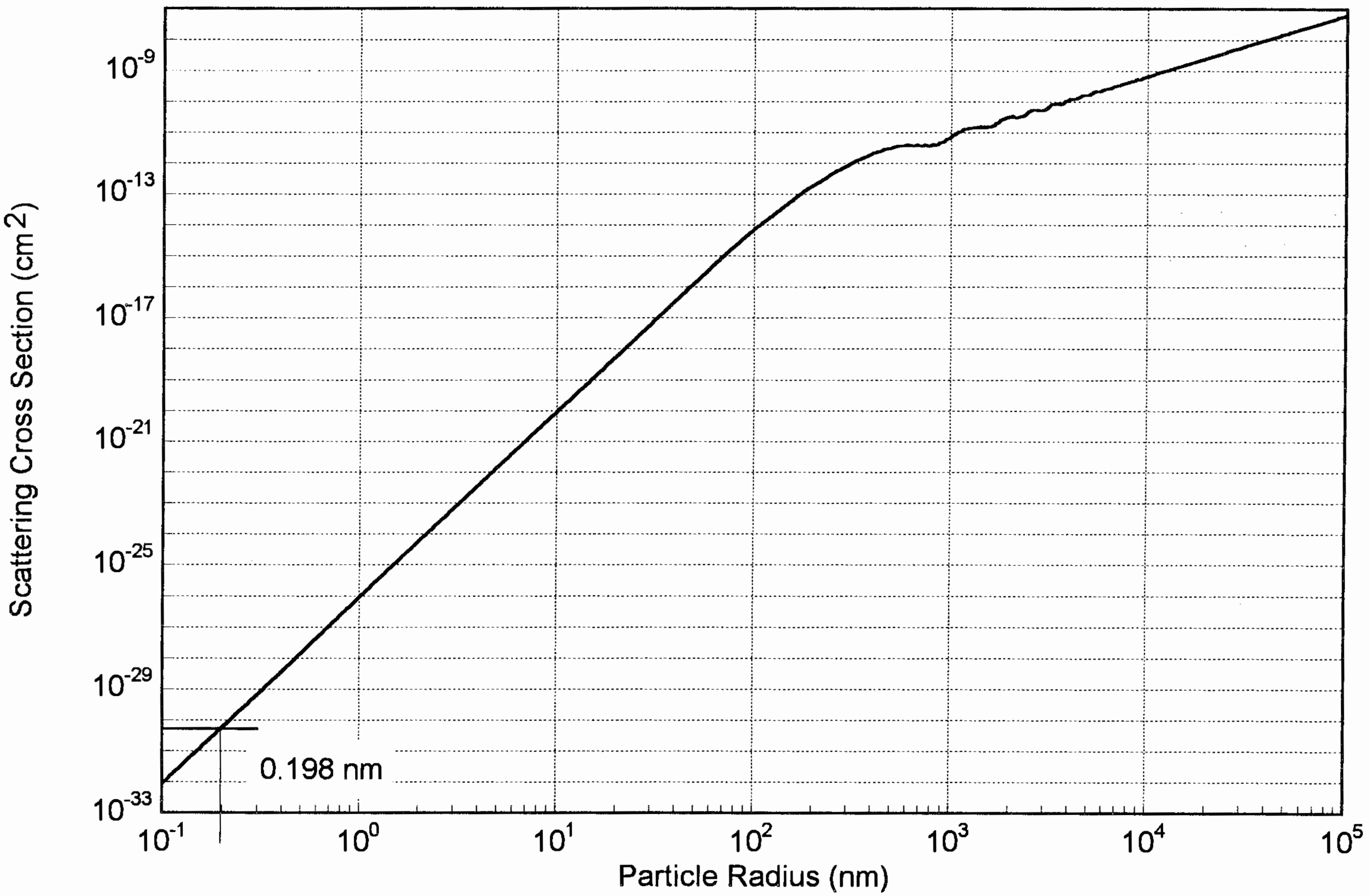

Figure 4.2. A Plot of scattering cross section versus radius for a spherical particle with refractive index of 1.38, and at a wavelength of 532 nm. This Plot was generated using the Fortran subroutine BHMIE.

equivalent radius has been found for the molecular scatterers, the model just needs to include a spike of the right number density and at the equivalent radius. This addition of the molecules to the distribution of particles will be shown in Section 4.3.

4.2.3 Extinction and Multiple Scattering

An important part of the bistatic lidar model was to be able to predict extinction at many wavelengths, based on the angular measurements at 532 nm. Once a particle size distribution has been calculated it is possible to calculate the extinction at any wavelength due to that particle distribution. However, the accuracy of the calculated extinction will depend greatly on how representative the inverted size distribution is compared to the actual particle size distribution. If the calculated size distributions are off by a small amount, it may not effect the extinction coefficients calculated at wavelengths close to the measuring wavelength. But, as the extinction is calculated at wavelengths farther away from the measuring wavelength, the errors in extinction will become very large. This is why infrared transmissometer measurements would be very helpful in determining the accuracy of the calculated size distributions. Unfortunately an IR transmissometer was not available during the Wallops measurement program. Chapter 6 will show the effects of small changes in the particle size distribution on the extinction at distant wavelengths.

If multiple scattering is negligible the intensity of a beam of light after being attenuated along a path of distance x is,

$$I = I_o \, e^{\alpha_{ext} x} , \tag{4.7}$$

and the percent transmission is just I/I_0. The extinction is due to both scattering and absorption and related to the particle number density N, as follows (Bohren and Huffman, 1983),

$$\alpha_{ext} = N \left(C_{sca} + C_{abs} \right) . \tag{4.8}$$

Extinction by coastal aerosols is due almost entirely to scattering, so the absorption cross section is assumed to be zero. The total extinction coefficient for a distribution of particles is,

$$\alpha_{ext} = \sum N_j C_{sca,j} , \tag{4.9}$$

where N_j is the number of particles of radius j, per unit volume and $C_{sca,j}$ is the corresponding scattering cross section. The model calculates the scattering cross section at wavelengths, 266, 355, 532, 607, 1064, 3500 nm, and creates a table of scattering cross section versus radius to be used in the Matlab model. Once a size distribution has been calculated, it is used to determine the number density N_j for each particle size to be added in the summation of (4.9). The absolute extinction can also be calculated from the Raman channels of the lidar as was explained in Chapter 1. This extinction from the lidar is then used to either estimate the number density for each particle size distribution, or on clear nights to verify the extinction calculated from the particle size distributions, which will be explained in Chapter 5.

Extinction measurements can be used to calculate the transmission and visual range along the 3 km measurement path to help put the calculations in perspective. The visual range is defined as,

$$Visual\ range = S = \frac{3.9}{\alpha_{ext}} , \tag{4.10}$$

where S is the path length when the minimum contrast for the eye reaches 2%. A typical visual range for a clear sky (very few aerosols) would be 49 km. This is equivalent to saying that a mountain 49 km away could just barely be distinguished from the horizon sky with the eye. The visual range for a purely molecular atmosphere (at 532 nm) is 217 km. These values will be used in Chapter 5 to put the results of the particle size distributions into perspective.

As was mentioned earlier, multiple scattering must be negligible for this bistatic model to work. If the contributions from multiple scattering are significant it becomes impossible to associate an intensity with a particular scattering angle. This is because each photon is most likely scattered more than once, therefore losing the information of the particle's phase function and polarization reference in the process. The best we can do is to recognize when multiple scattering has become significant, and not apply the bistatic lidar model or the Beer-Lambert law (4.7) in those cases. Multiple scattering can be detected in two ways. In the Wallops experiment, because the transmitted electric field was always parallel or perpendicular to the scattering plane, the scattered radiation should also be polarized parallel or perpendicular to the scattering plane. A linear polarizer can be inserted at the receiver to check for cross polarized radiation. If a significant signal is detected, then either there is a strong multiple scattering component, or the particles are far from being spherical. In either case, the bistatic lidar model and the Beer-Lambert law cannot be used. Multiple scattering occurs when the optical depth of the medium being traversed by the light becomes large. This increases the probability that the light ray will interact with more then one particle in the scattering process. The probability of multiple scattering can be increased by either adding more particles or by increasing the path length. The optical depth is defined as,

$$\tau = \alpha_{ext} \Delta x \, , \tag{4.11}$$

where Δx is the path length. According to van de Hulst (1957) multiple scattering is negligible when, $\tau < 0.1$. When the optical depth is greater than 0.3 multiple scattering becomes a significant factor. There is a grey area between 0.1 and 0.3 when a correction might need to be applied. If we use 0.3 as an upper limit, and consider that our path length is 0.35 km (about 175 m out and back) for the Wallops experiment, then extinction coefficients up to 0.857 km^{-1} are acceptable. Thus, multiple scattering should be a problem only during heavy fogs, in clouds, or for long path lengths. The largest extinction coefficient found during the Wallops program was 0.56 km^{-1} at 352 nm.

4.3 Particle Size Distributions

The next part of the bistatic lidar model is to include a suitable size distribution for the scatterers. Many analytical models have been used to represent aerosol size distributions, including the following mathematical functions:

- Power law distribution
- Modified gamma distribution
- Lognormal distribution
- Generalized distribution

Deepak and Box (1982) provide an excellent survey of these distribution functions and how they are used. Junge (1955) was among the first scientists to recognize the necessity for a logarithmic scale to represent the wide range of particle sizes and concentrations. The Junge distribution or power law distribution is widely used to model cloud particle and rain drop sizes. The lognormal size distribution was introduced by Davis (1974) as a better representation of particles originating from a single source through a single production mechanism (d'Almeida et al., 1991). The lognormal distribution emphasizes the individual components in a mixture of particles of different origins. A lognormal size distribution has also been chosen for the Navy Aerosol Model (NAM) (Richter and Hughes 1991). An advantage of the lognormal distribution is that each component has its specific median radius, standard deviation and number density. Therefore, each production mechanism can be represented with different lognormal parameters. At Wallops Island, the first aerosol mode could represent a background aerosol, the second mode could represent a type II maritime aerosol, and a third mode could exist due to the formation of a light fog or mist. These different atmospheric conditions will be shown in Chapter 5. The following is a list of additional references where the use and applicability of a lognormal distribution for representing tropospheric aerosol size distributions is described: Hobbes 1993, Amato et al. 1988, Kent et al. 1983, Hobbs and McCormick 1988.

Patterson and Gillette have chosen the lognormal distributions rather than other distributions for several reasons; "the choice is reasonable theoretically because soil-derived aerosols are produced as a result of comminution processes (e.g., sandblasting) in the soil, and such processes do result in lognormal distributions (Epstein, 1947); and finally the lognormal distribution is convenient mathematically because the parameters of the volume and surface moments of the distribution are related in a simple way to the parameters of the number distribution" (Patterson and Gillette, 1977). Fitch and Cress have also conducted in-situ measurements of tropospheric aerosols and compared their results with a bimodal lognormal distribution (Fitch and Cress, 1983). Both groups, Patterson and Gillette and Fitch and Cress, present lognormal distribution parameters that are comparable to the results shown in Chapter 5 of this thesis. Section 5.2.3 presents a short discussion comparing the results from these groups plus some others to the results in Chapter 5. Some of the many other references of groups who use a mixture of two or three lognormal distributions to model aerosol data are: Whitby, 1978, Tanka et al., 1983, Hayasaka et al., 1991, and Harrison and Pio, 1983.

We have chosen the lognormal distributions to model the aerosol size distributions during the Wallops measurement program. On clear nights only one lognormal function was needed, while on hazy or foggy nights up to three lognormal functions were needed to fit the model to the data. The model allows up to four lognormal distributions, but fitting these four distribution functions to the data becomes extremely difficult.

The form of the lognormal distribution used for this work was introduced in Chapter 1 and is repeated here,

$$n(r) = \sum_{i\,1}^{3} \frac{n_i}{\sqrt{2\pi}\,\sigma_{lni}} \exp\left[- \frac{\left(\ln \frac{r}{R_i} \right)^2}{2(\sigma_{lni})^2} \right] \frac{dr}{r}\,, \tag{4.12}$$

where r is the particle radius in μm, n(r) is the number of particles in the size range r to r+dr per cm^3, R_i is the median particle radius in μm, n_i is the weighting for the *i*th lognormal function, and $\sigma_{\text{ln}i}$ is a measure of the particle polydispersity (or the width of the distribution). This form of the lognormal function follows that of (Crow and Shimizu, 1988; Aitchison and Brown, 1957). There is much confusion with the lognormal function in the aerosol literature and one must refer directly to literature written about lognormal functions to be sure the proper terms and form of the equation is used. For example, Eq. 4.12 is often incorrectly written with base 10 logarithms instead of natural logarithms to describe atmospheric aerosol distributions. As long ago as 1936 Krumbein suggested the use of natural logarithms to make the lognormal function conform with particle size distributions measured using the standard grading of sieve-meshes (Aitchison and Brown, 1957). However, many groups continue to use the base 10 logarithm (Patterson and Gillette, 1977; Fitch and Cress, 1983; Hobbs, 1993) which causes confusion when trying to compare results from one experiment to another. The parameters of the distribution are also often misused or incorrectly reported. For example, many of the references listed previously, report a mean radius when they probably used a median radius. This is an important distinction because the mean radius is not a robust parameter and is a function of the variance of the distribution. Tanaka et al. (1983) avoid any confusion with the lognormal parameters by using the well defined terms of median radius and geometric standard deviation (see Crow and Shimizu, 1988). Buhrman and Granqvist (1975) also report the geometric standard deviation to describe the distribution width of fine Al particles for a lognormal distribution. Therefore, this thesis will present all the results in terms of the median radius and geometric standard deviation as follows. The median or geometric mean of the distribution, R_i, is directly used in Eq. 4.12 and is related to the arithmetic mean R_a, by,

$$R_a = \exp\left[\frac{1}{2}\sigma_{\ln}^2\right]R_i \,. \tag{4.13}$$

The width of the distribution will be defined as the geometric standard deviation σ_g, and is related to $\sigma_{\ln}$ in Eq. 4.12 as,

$$\sigma_g = \exp[\sigma_{\ln}] \tag{4.14}$$

The standard deviation of the distribution is β, and defined as,

$$\beta = \exp\left(0.5\,\sigma_{\ln}^{2}\right)\sqrt{\exp\left(\sigma_{\ln}^{2}-1\right)}\;R_{i}\;. \tag{4.15}$$

Finally, the coefficient of variation, η, for the lognormal distribution is defined as the ratio of the standard deviation to the arithmetic mean.

$$\eta = \sqrt{\exp\left(\sigma_{\ln}^{2}-1\right)} \tag{4.16}$$

Figure 4.3 is an example distribution showing all nine parameters needed to describe the trimodal lognormal function. These functions are usually plotted on logarithmic scales because each distribution is often separated by several orders of magnitude in number density. This distribution is used in Matlab along with the scattering matrices calculated in Fortran to model the results of the bistatic lidar. The model allows particle sizes from 1 nm to 250 μm in the distribution. Particles less than 1 nm are too close to the equivalent sphere radius for a molecule and sizes above 250 μm pose difficulties for the BHMIE subroutine. Particles above 250 μm are also outside the most probable range of aerosols encountered at Wallops Island. Only in the case of heavy fog or light drizzle would these particle sizes become important.

Figure 4.4 is an example of a particle size distribution calculated in Chapter 5. Here we can see three separate particle modes and the inclusion of molecules at the radius calculated in Section 4.2.2. This size distribution was calculated from bistatic lidar data on a visibly misty evening. It was very calm, the temperature was dropping through the night and a radiation fog was slowly forming. Although the temperature never dropped enough to form a thick fog, this case provides a classic example of why multiple modes are needed to describe the distribution of aerosols in the troposphere. The results of this evening will be discussed in more detail in Chapter 5. The lognormal parameters along with the total particle number density for each mode are listed in Table 4.2. Each mode in the distribution along with the molecular component is added to obtain a total

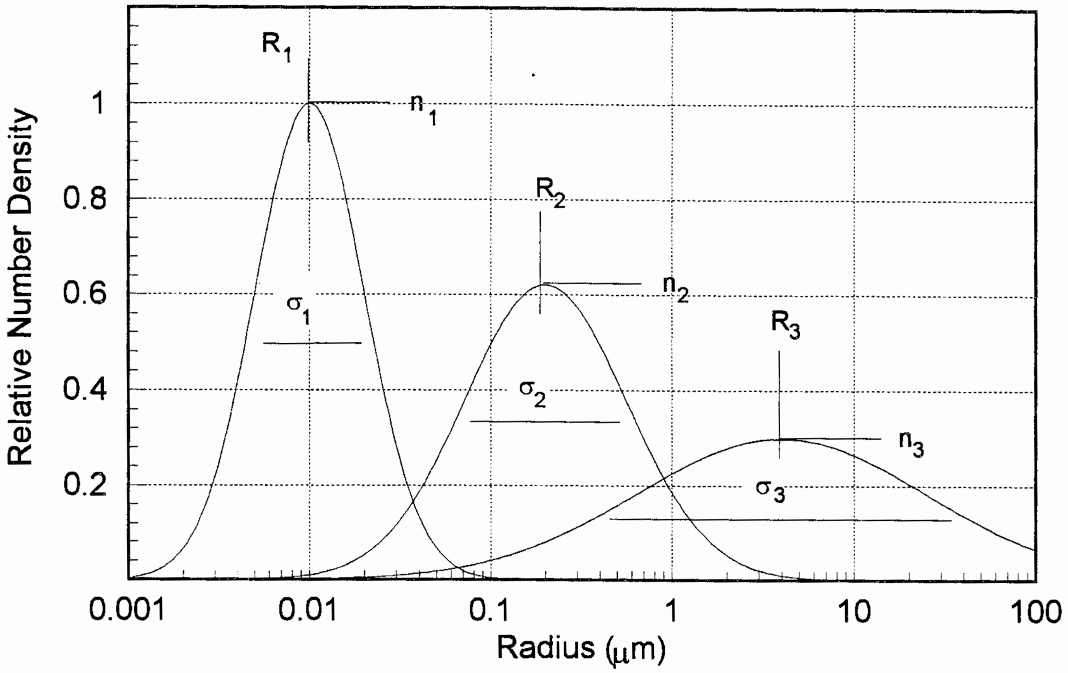

Figure 4.3. Example of a trimodal lognormal distribution showing all nine parameters and calculated using equation 4.12.

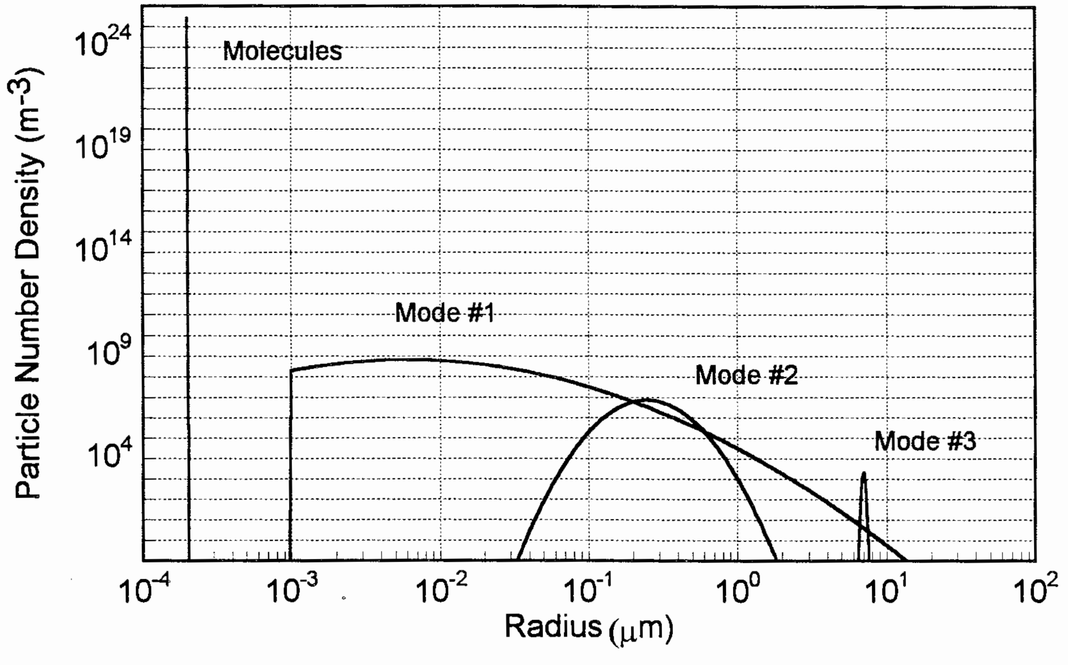

Figure 4.4. Plot of a trimodal lognormal particle size distribution using the bistatic lidar model developed under Matlab. The addition of 2.54×10^{25} molecules per m^3 is shown at the equivalent Mie radius calculated in Section 4.2.2.

Table 4.2. Parameters for the trimodal lognormal distribution in Figure 4.4.

Distribution Parameter	Mode #1	Mode #2	Mode #3
Median radius	$R_1 = 6$ nm	$R_2 = 0.25\ \mu m$	$R_3 = 8.85\ \mu m$
Geometric standard deviation	$\sigma_g = 3.16$	$\sigma_g = 1.4$	$\sigma_g = 1.02$
Number density weighting ($m^{-3)}$	$N_1 = 18 \times 10^8$	$N_2 = 6.0 \times 10^6$	$N_3 = 103$
Total number density (m^{-3})	7.53×10^{10}	2.62×10^8	4.50×10^3

distribution like that shown in Figure 4.5. The model multiplies this total distribution function by the scattering matrix of Table 4.1 for the perpendicular scattered component and then for the parallel scattered component. The results of the two multiplications are divided to obtain the ratio of the two components. This ratio versus scattering angle is the final output of the bistatic model.

When looking at the third mode of the distribution in Figure 4.4 it is important to recognize when a distribution is too small to be measured with a collimated laser beam. For example, the third mode of the distribution in Figure 4.4 has only 4,500 particles per cubic meter. To put this in perspective, we must determine the average scattering volume viewed by each pixel of the bistatic receiver. The laser beam is 5 cm in diameter, and the length along the beam viewed on average by one pixel is about 30 cm. Keep in mind, this calculation is only for the particle scattering region 175 m away from the receiver. This corresponds to a scattering volume of about 600 cm^3. A reasonable particle number density would be one that would provide at least one particle per scattering volume. One particle per 600 cm^3 is equivalent to a particle number density of 1,670 m^{-3} . So, the particle number density of the third mode in Figure 4.4 is almost equivalent to three particles per scattering volume.

Table 4.3 is a summary of parameters for models of aerosol size distributions described by the sum of three lognormal functions. These parameters were adapted from Hobbs (1993) to give a sample of what should be expected when particle size distributions are calculated from the bistatic lidar data in Chapter 5.

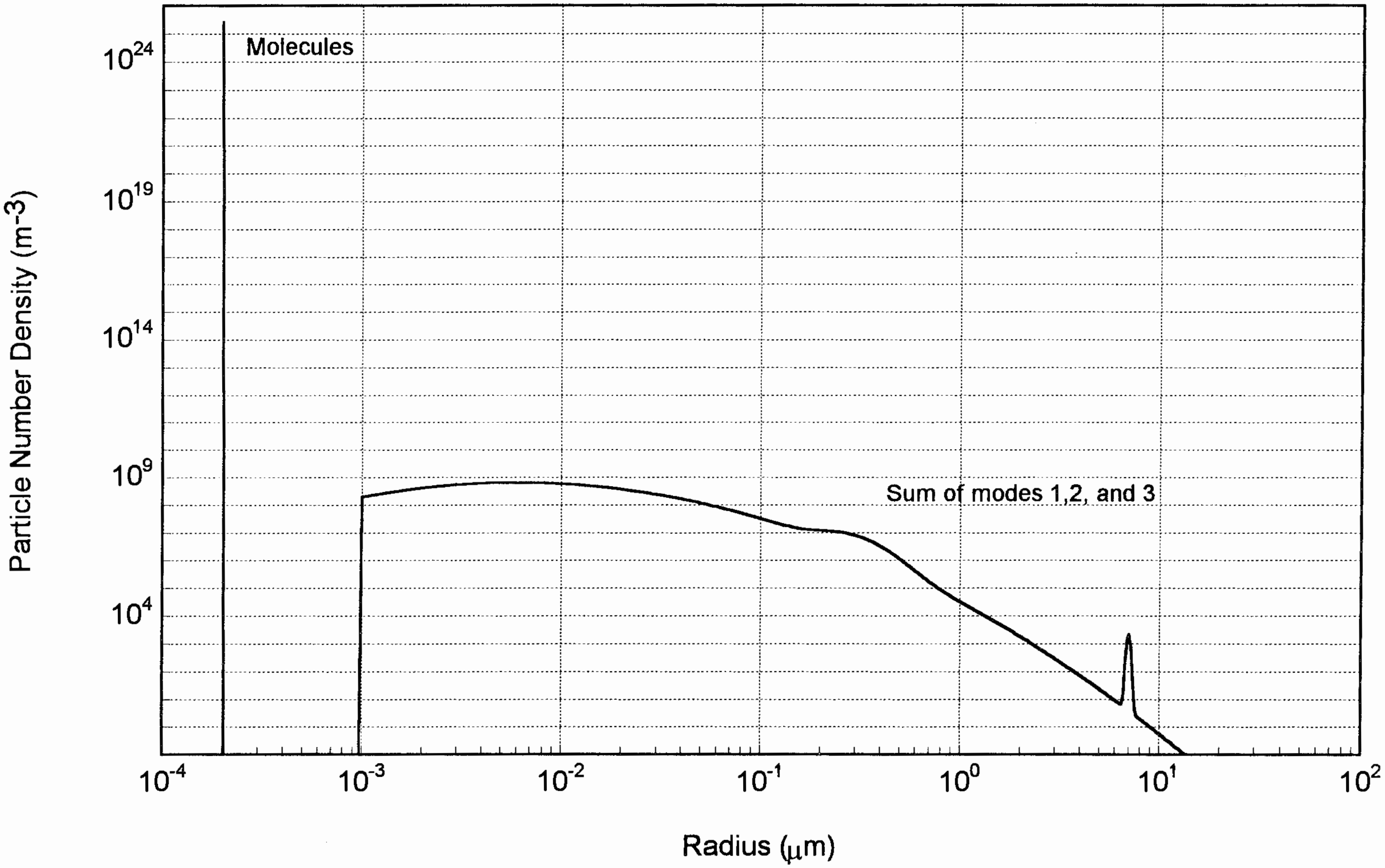

Figure 4.5. Summation of the three modes from the trimodal lognormal size distribution of Figure 4.4. This function is used as a weighting for the scattering matrix in Section 4.1 to obtain the modeled intensity received by a bistatic lidar.

Table 4.3. Parameters of lognormal functions describing aerosol size distributions.

Aerosol	*i*	N_i (cm^{-3})	R_i (μm)	σ_g
Background	1	2.97×10^2	0.0036	4.41
	2	13.75×10^1	0.127	1.79
	3	14.62×10^1	0.259	2.66
Maritime	1	3.06×10^2	0.0039	4.54
	2	15.34×10^1	0.133	1.62
	3	7.05×10^0	0.29	2.49
Rural	1	15.31×10^3	0.0074	1.68
	2	3.39×10^2	0.0269	3.60
	3	4.58×10^3	0.0419	1.85

4.4 Model Output

Several important elements required for the development of a bistatic lidar model were discussed in Sections 4.1 to 4.3. First, the assumptions about the model and the atmospheric conditions the model was intended to describe were reviewed. The variables, both known and unknown, were discussed. Next, in Section 4.2.1 mathematical detail on how to calculate the observed intensity was discussed, based upon a combination of the two amplitude scattering matrix elements, S_1 and S_2. This led to an explanation of the experimental setup and the intensities which would be measured. The next section, 4.3, explained when and how molecular scattering and spherical dielectric scattering are related. This is important because atmospheric molecules must be included in the model and also because the scattering from a large portion of the aerosol population can be approximated with Rayleigh theory. Extinction calculations were described to explain how the bistatic lidar model can calculate an extinction for any wavelength given a particle size distribution. Finally, the model to describe the particle size distribution was discussed. The reason for using a lognormal distribution was explained, and examples of common and possible trimodal distribution were plotted in Figures 4.4 and 4.5. All of these elements will be put together in this section by plotting full model outputs for simple and complex cases. The simple cases will be used to verify that there are no bugs in the model. Many examples will be presented to establish an understanding of the ratio of $I_{\parallel}/I_{\perp}$ for several particle sizes and distribution widths.

The first step in the model is to determine the appropriate index of refraction. Next, the Fortran programs calculate a scattering matrix covering particle sizes from 1 nm to 250 μm, and angles from 155 to 180°. This matrix is indicated in Table 4.1. Two of these scattering matrices are computed, one for the parallel component and one for the perpendicular component. Because these two matrices take about one hour to calculate, on a 100 MHZ 486 PC, it is difficult and time consuming to run the model at any desired index of refraction. The index of refraction could be another continuous variable if the Fortran and Matlab models were both run on a super computer. The next step is to read both matrices into Matlab as variables. Matlab then takes the nine distribution parameters as inputs, and models the distribution function and molecular number density. This distribution function is applied to each scattering matrix separately before dividing to obtain the ratio $I_{\parallel}/I_{\perp}$. This is an important point because the distribution of the ratio is not the same as the ratio of the two distributions, neither mathematically or physically. This point can be seen just by figuring what was actually measured. For the experiment at Wallops Island one polarization was measured and then the polarization rotated 90° to the first, was measured. Each measurement independently had a distribution of particles applied to it, therefore the same must be done when modeling the experiment. This is unfortunate because twice as much memory and time is required to handle the two individual matrices instead of just one of the ratios. Once each matrix has had a distribution applied to it, Matlab returns a vector of intensity versus angle. This vector represents one measurement with the bistatic lidar over an angle range of 155° to 180° and with a distribution of spherical scatterers. These two vectors are divided element by element to determine the final output of $I_{\parallel}/I_{\perp}$ versus angle. Refer back to Figure 4.1 to recall what the ratio $I_{\parallel}/I_{\perp}$ physically represents.

First a few simple examples of the model using only one mode will be shown to verify the output with common sense. All the plots in this chapter will use 1.38 for the index of refraction, and the imaginary part will be set to zero under the assumption of no absorption. Figure 4.6a-c shows three plots of the two electric field components, parallel and perpendicular to the scattering plane. The first plot was calculated for a particle radius of 10 nm and with no distribution, although a small distribution will not change the plot. This is what would be expected for Rayleigh scatterers, the forward scattering is equal to the backscatter, and the parallel component goes to zero at 90°. Figure 4.6b is the same plot as 4.6a except the particle radius in now 30 nm, the size mentioned in Section 4.2.2 as the point where the scattering is no longer considered molecular. Here we can see that the forward scattering is slightly stronger than the backscattering. Around this particle size the shape of the particle now becomes a factor in the scattering intensity and phase function. The observed scattering intensity has also increased significantly, about one order of magnitude from that in Figure 4.6a to Figure 4.6b. The model does not normalize the scattering intensity for each individual radius, so the scattering intensities are related from one radius and distribution to another. This is necessary because of adding so many different intensities to obtain a total distribution function. The dependence of the scattering cross section on the sixth power of the radius can also be seen in Figures 4.6a and b. Because the forward scattering is being favored more in Figure 4.6b, it is difficult to relate these scattering intensities at each angle to a total scattering cross section. Figure 4.6c shows the effect of the particle size above the Rayleigh range. Here the forward scattering is 100,000 times greater than the forward scattering in the preceding graph, and four times stronger than its own backscattering. The parallel component of the electric field does not go to zero at 90°, it now approaches zero at about 94°. Figure 4.6d shows the ratio of the two components $I_{\parallel}/I_{\perp}$ for the case of Rayleigh scattering from Figure 4.6a. This ratio is called the Rayleigh ratio and has a $\cos^2$ dependance with scattering angle. This is what the bistatic lidar would measure if there were no aerosols in the atmosphere. On very clear nights at the Wallops Island, CASE I program, the

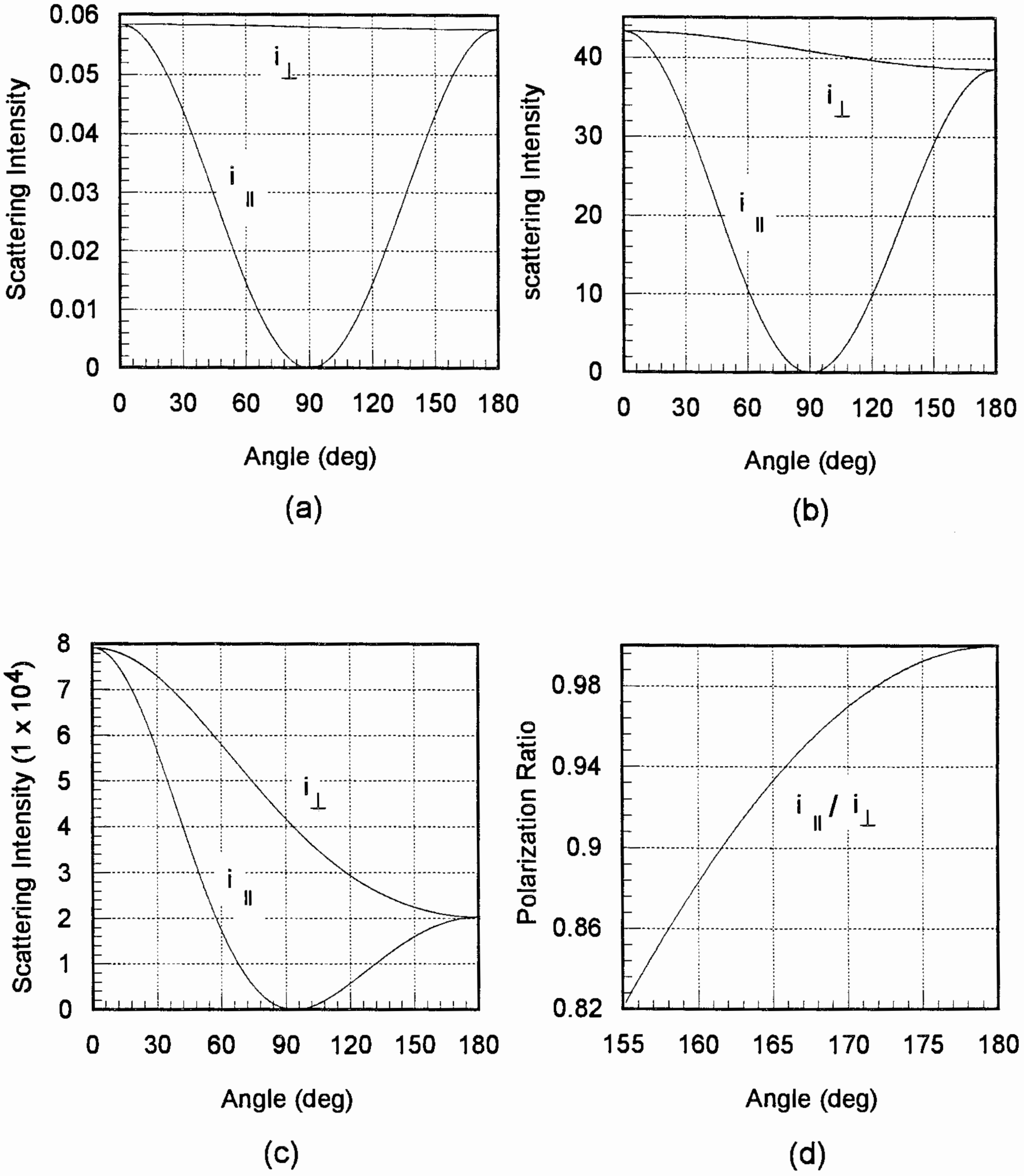

Figure 4.6. Plots of both the parallel and perpendicular components with no particle distribution for (a) 10 nm, (b) 30 nm, and 100 nm particle radii. The transition out of the molecular/Rayleigh scattering region can be seen. The ratio of the components in (a) is plotted in (d) to show what the bistatic lidar would see in an atmosphere without aerosols.

observed profile looked similar to Figure 4.6d.

The next step in testing the model is to evaluate the calculation of a single-mode distribution. Figure 4.7a shows a couple of examples of single distributions, like those of modes 1 and 2 in Figure 4.4. The first plot shows both the parallel and perpendicular components for a particle radius of 6 nm and a geometric standard deviation of σ_g=3.16. A distribution width of σ_g=3.16 is a wide distribution, but common for the small aerosols background present in most areas (see Table 4.3). This distribution of sizes smooths all the fine structure out of the curves. However, a sizable difference in the scattering intensity still remains between 90° and 180°. Figure 4.7b shows the ratio of the parallel to the perpendicular component of scattered radiation between the angles of 155° and 180°. Different distribution widths were plotted to estimate how much variation would result in the measured ratio. The ratio appears to be very sensitive to the changes in the distribution width. However, as the width decreases, the ratio will approach that of molecules and then the differences are much smaller, because the distribution will contain fewer large particles. Figure 4.8a shows a second case of the two electric field components from larger type II aerosols. This aerosol size of 0.25μm, with a geometric standard deviation of σ_g=1.4, is typical of the second mode in most trimodal distributions. The ratio of the parallel polarization component to the perpendicular component is plotted in Figure 4.8b. Three different distribution widths are displayed to show the large differences in the ratios for small changes in σ_g. This distribution is the second mode from the trimodal distribution in Figure 4.4. Significant differences can be seen in both ratios with changing distribution widths and with changing median radii. This appears to make the measurement technique very sensitive to the particle size distribution as will be shown in Chapter 5.

It is difficult to get a feeling for how the ratios change with particle radius and distribution width just by looking at a few examples. From the previous figures it would appear that a 6 nm particle could be distinguished from a 0.25 μm particle. But how much does the ratio of the two electric field components vary with radius? This question is

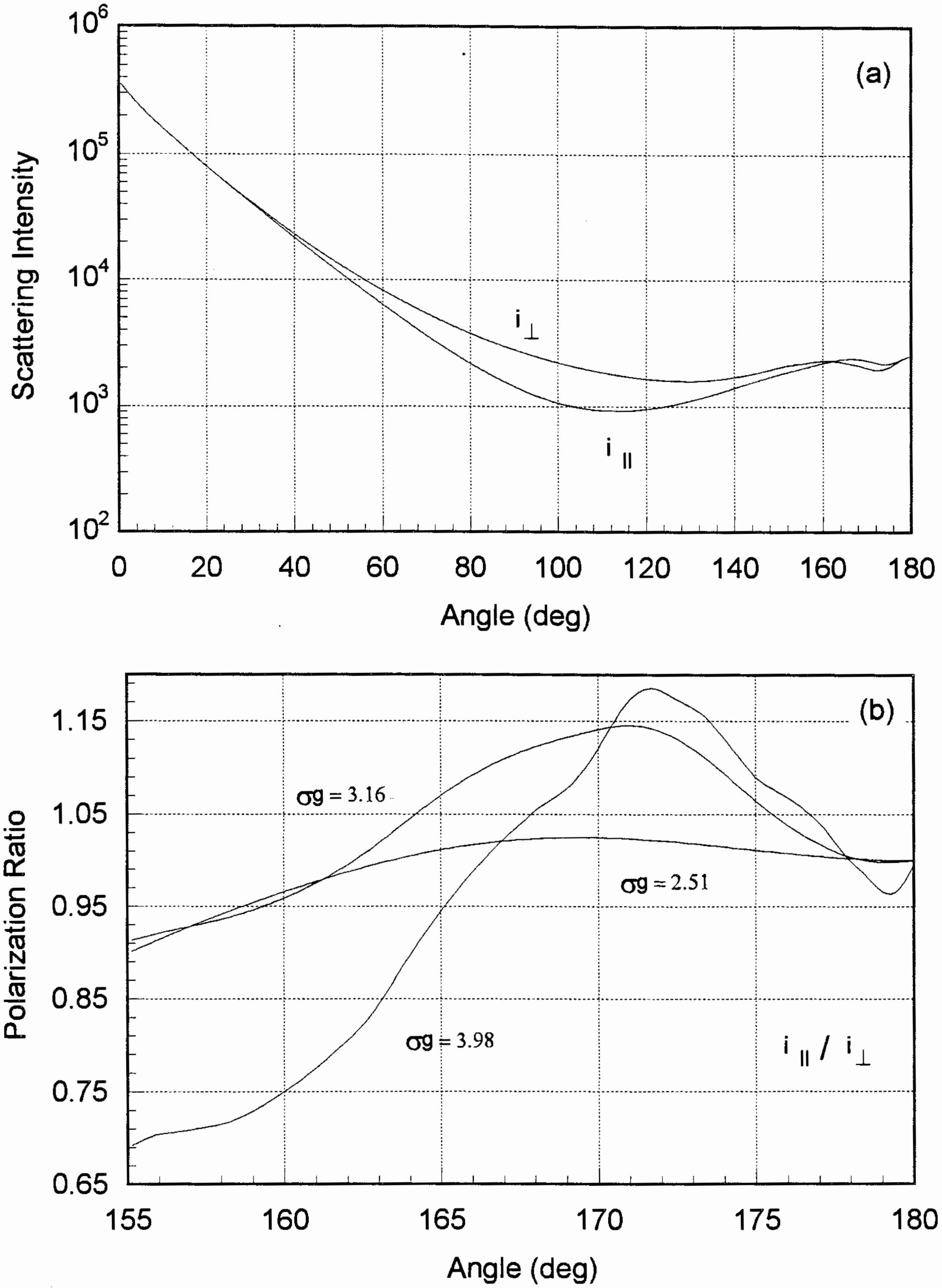

Figure 4.7. (a) The two components of scattered radiation according to Mie theory calculated using a single lognormal particle distribution with a radius of 6 nm and geometric standard deviation of σ_g=3.16. (b) The Ratio of the two components plotted in (a). Three different size distribution widths were chosen to see how much the ratio would vary.

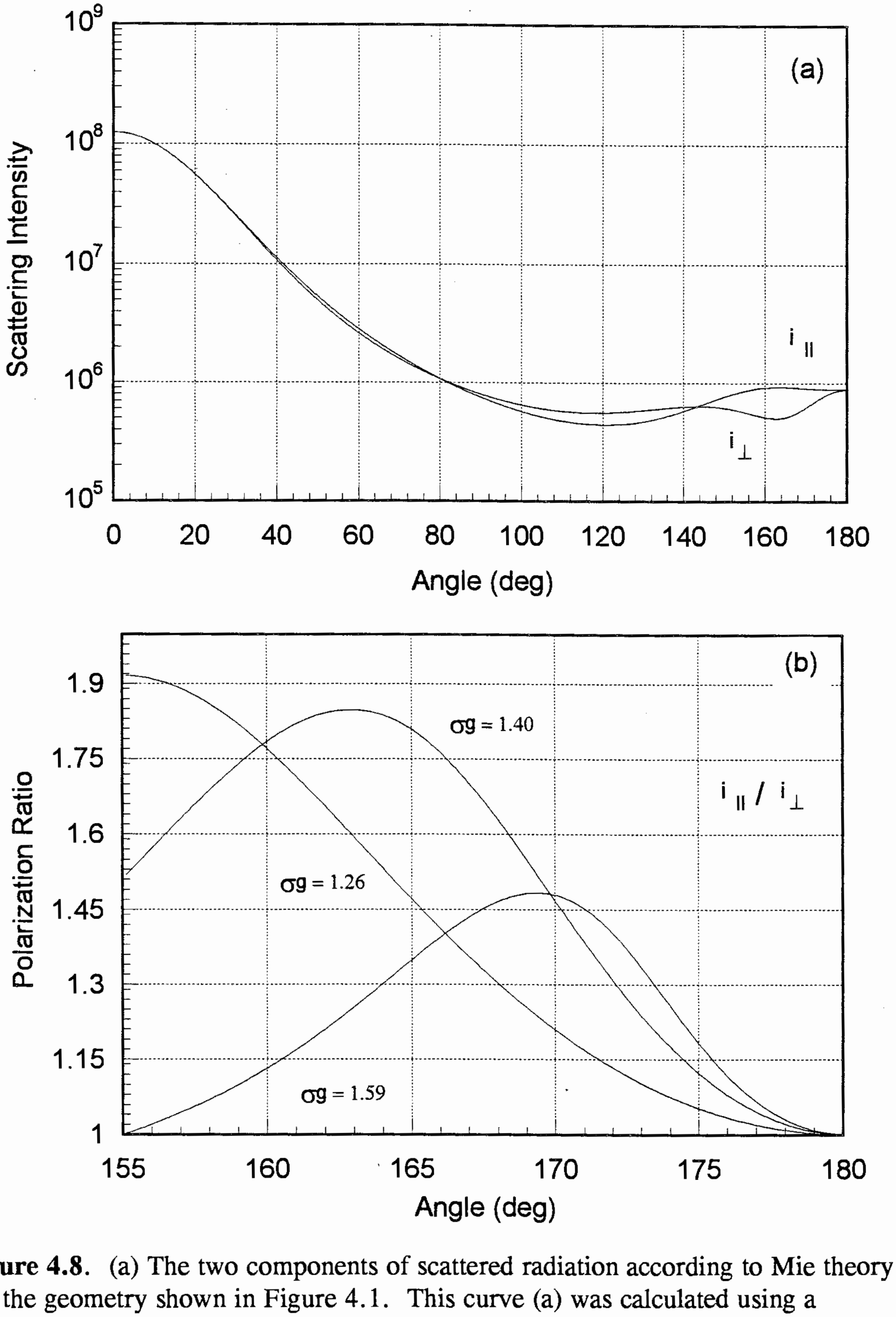

Figure 4.8. (a) The two components of scattered radiation according to Mie theory for the geometry shown in Figure 4.1. This curve (a) was calculated using a lognormal distribution with median radius of 0.25 μm and a geometric standard deviation of $\sigma_g = 1.4$. (b) Ratio of the two components plotted in (a). The ratio shows significant differences with changing distribution widths.

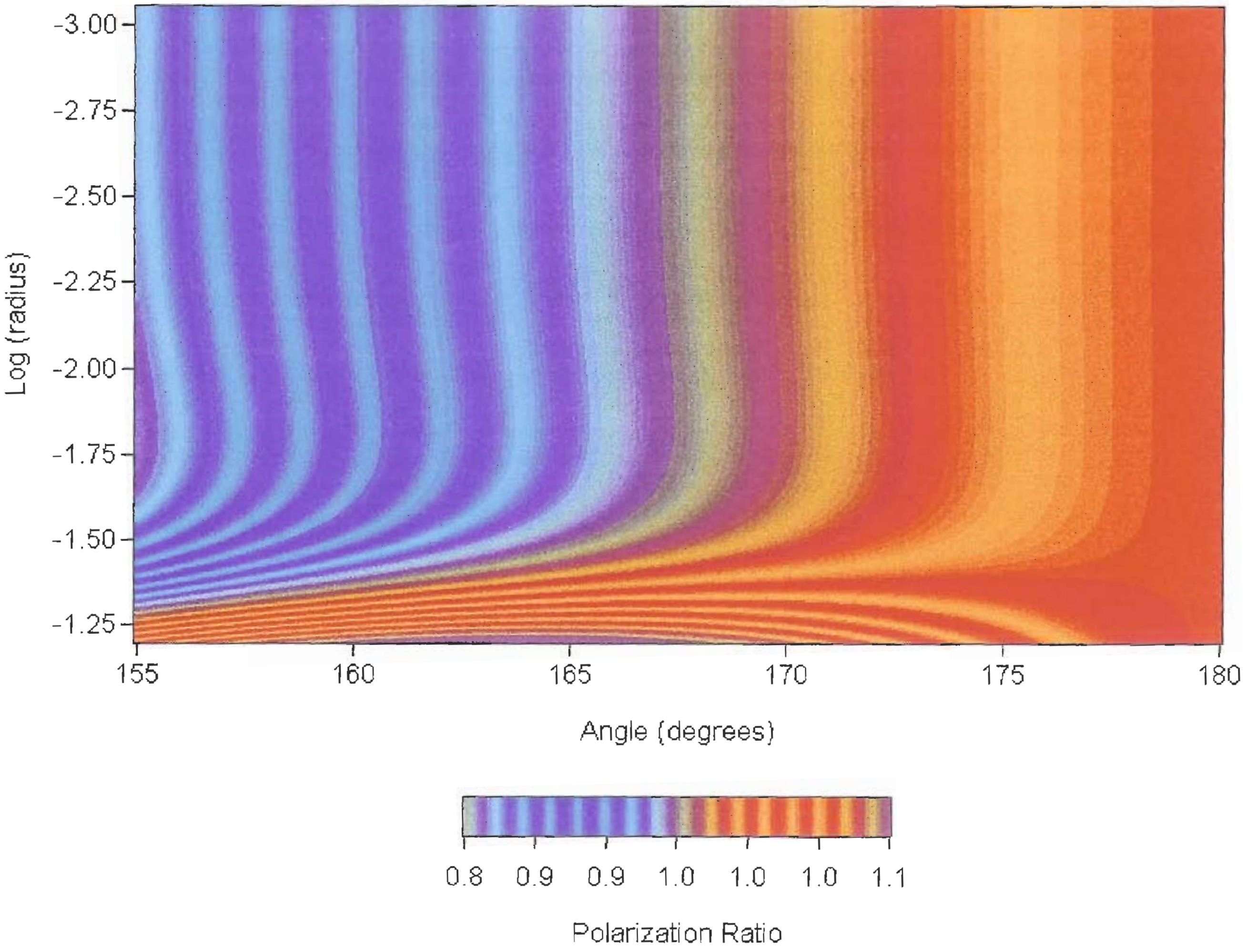

Figure 4.9. A Color plot showing the ratio of the scattering components for a range of particles sizes from 1 nm to 50 nm. It can be seen that as the median radius of the particle distribution changes, the color (which represents the ratio of I-parallel divided by I-perpendicular) does not change. These particles are in the molecular scattering region.

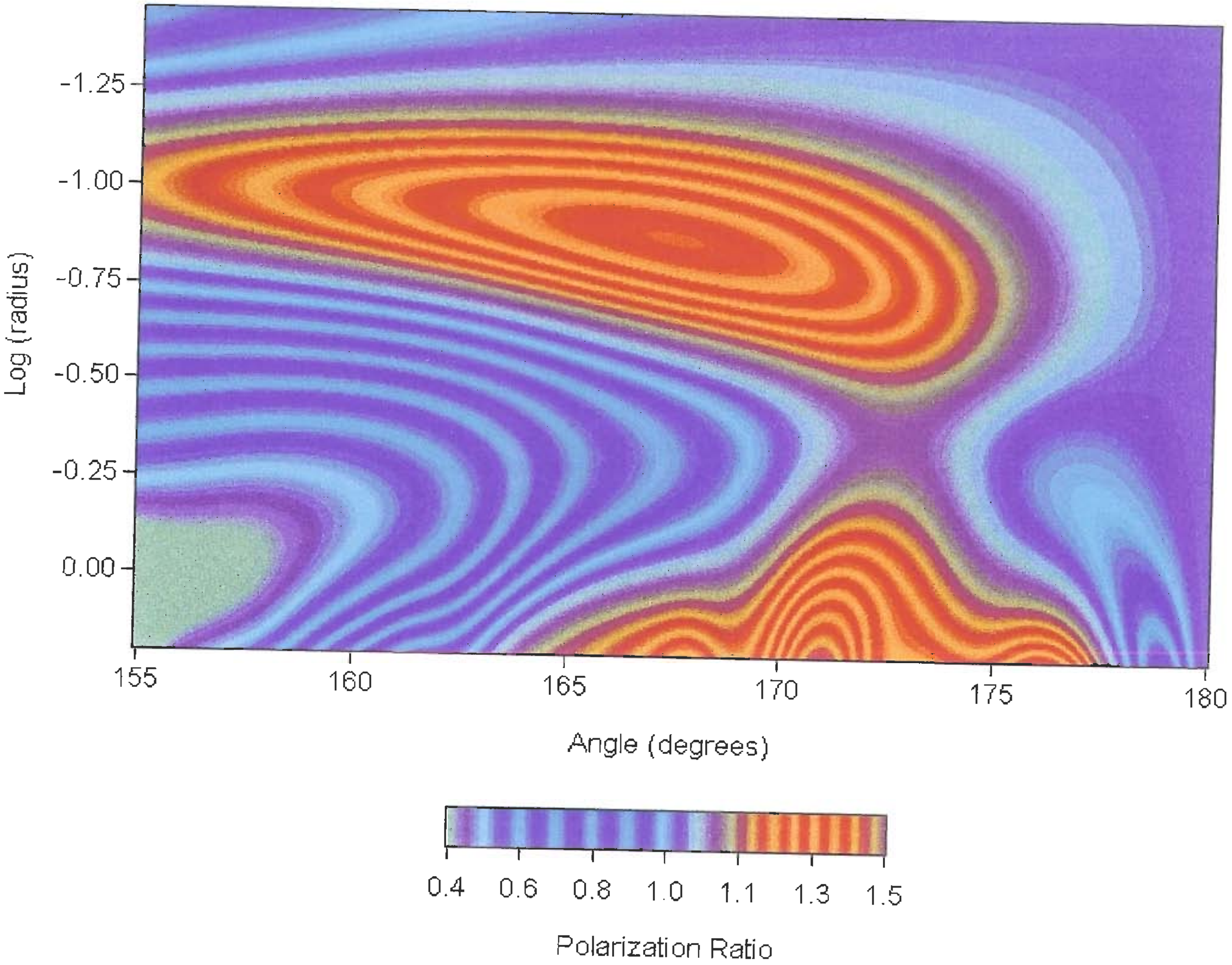

Figure 4.10. This plot is the same as the plot in Figure 4.9 except the particle sizes are plotted between 30 nm and 1.8 μm. Here we can see contours are being crossed as the particle radius changes. this indicates that these particle sizes could be distinguished from one another using the bistatic lidar.

partially answered with the following three color plots. Using a single mode lognormal distribution, with a geometric standard deviation of $\sigma_g = 1.8$, the ratio of the parallel to the perpendicular electric field components was calculated for 600 different radii between 1 nm and 1000 μm. Figure 4.9 is a plot of the radii from 1 nm to 56 nm. Log of the radius is plotted on the ordinate and the angle of the scattering is plotted on the abscissa. The angle range of 155° to 180° are the angles that were used in the measurements during the Wallops Island CASE I program. The changing color represents the value of the ratio. It can be seen that the color does not change with radius until about -1.50, or 30 nm. This is the point where the scattering cannot be approximated with Rayleigh scattering theory anymore. It should also be noted that the ratio changes very little with angle, also indicative of Rayleigh scattering. Figure 4.10 is the same type of plot as Figure 4.9 except this plot covers particle sizes from 30 nm to 1.77 μm. As the particle radius changes, the ratio of the two components changes fairly rapidly, which can be seen from the number of contours being crossed. From Figures 4.9 and 4.10 it can definitely be seen that there is information about the scatterers contained in this ratio. Figure 4.11 is the final color plot showing the upper range of the model from particle sizes of 1 μm to 1000 μm. Around 10 μm the ratio oscillates with angle. This would be the upper radius limit where 532 nm could be effectively used for particle sizing. These three color plots help to visualize the variations in the ratio of the parallel component to the perpendicular component with changing particle median radius. Unfortunately, it would be impossible to see how the ratio changes with a continuous range of distribution widths in the same type of graph. It should be noted that the last three plots used only one distribution and that distribution remained constant in width ($\sigma_g = 1.8$) for all median radii. This can be misleading because in the real world particles of different sizes do not distribute themselves alike, this is why a trimodal lognormal distribution is of value.

Figure 4.12 summarizes by putting all the pieces together in one example, Mie theory, trimodal lognormal distribution, atmospheric molecules, and the ratio of the two electric field components. Figure 4.12a shows the three mode of a lognormal distribution

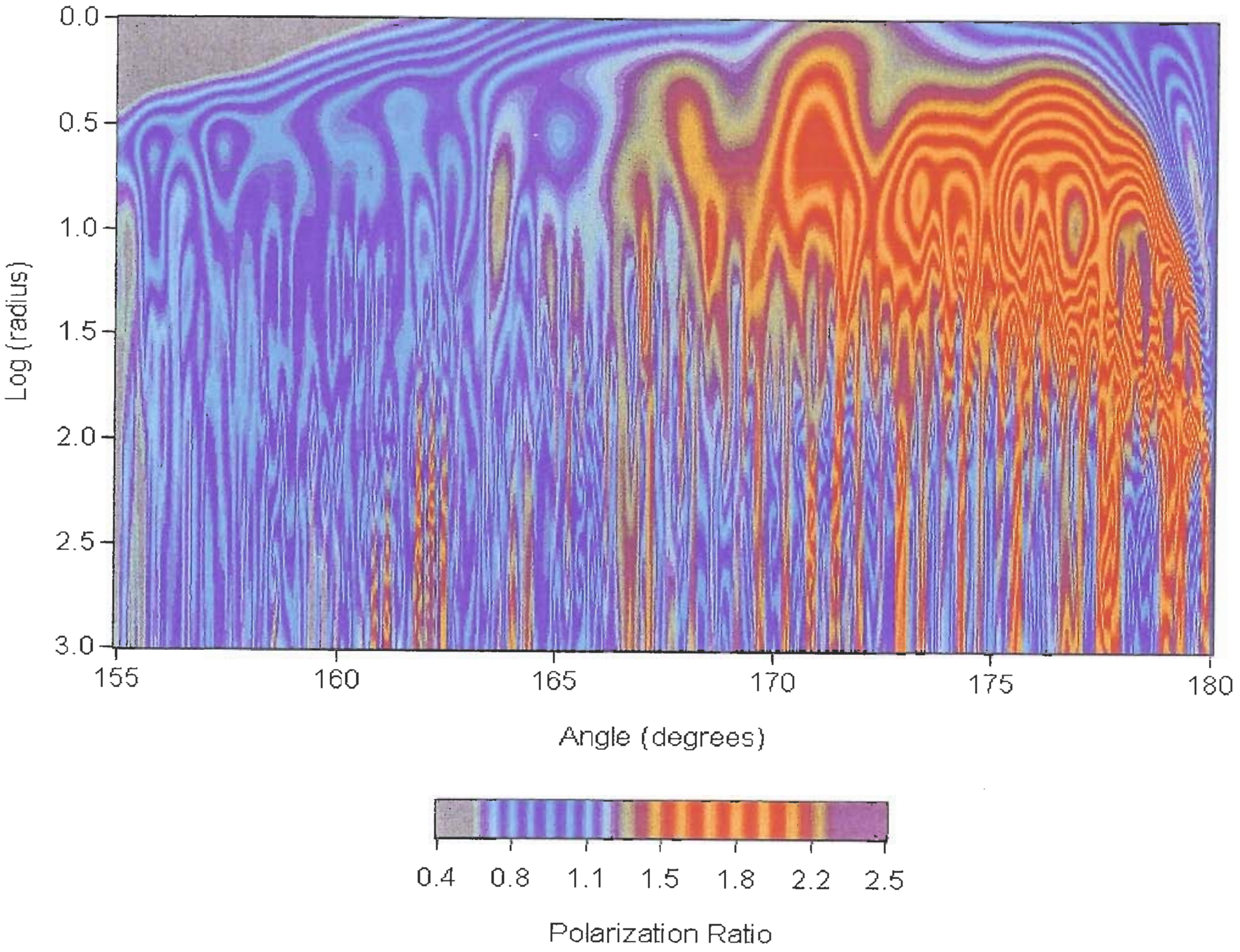

Figure 4.11. This color plot shows the last group of particle sizes modeled with the bistatic lidar model. The range of particle sizes is from 1 μm to 1000 μm with a geometric standard deviation of $\sigma_g = 1.8$. The ratio of the two intensities for particle sizes larger than about 10 μm starts to oscillate.

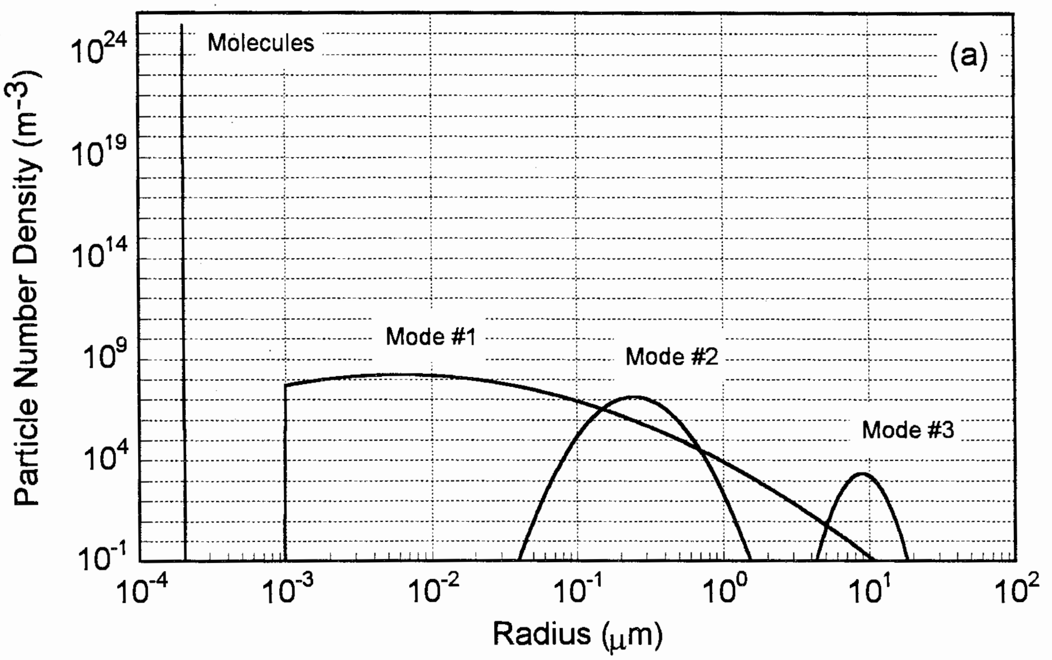

Mode #1	Mode #2	Mode #3
R = 6 nm	R = 0.247 μm	R = 8.91 μm
σg = 3.16	σg = 1.35	σg = 1.18
N = 483 /cm ^{3}	N = 10.3 /cm ^{3}	N = 0.0009 /cm ^{3}

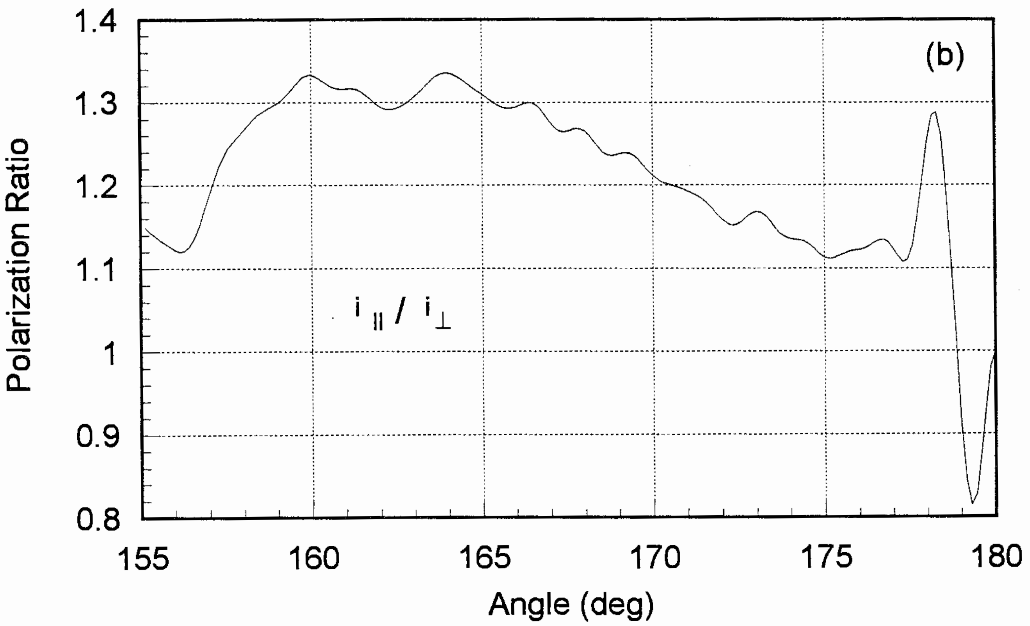

Figure 4.12. (a) A Trimodal lognormal distribution with the addition of molecules at the equivalent Mie radius. This distribution was used in the bistatic lidar model to compute the ratio of the parallel electric field component to the perpendicular component in (b). This is an example of the complete model from input (a) to output (b).

along with the addition of the molecular background of 2.54×10^{19} molecules per cm^3. This distribution is then applied to each of the two scattering matrices calculated with the Fortran program. The output is the ratio of the distribution of the parallel component to the distribution of the perpendicular component, and is shown in Figure 4.12b. If the bistatic lidar operated on an evening when the atmosphere contained spherical aerosols distributed like those in Figure 4.12a, the output from the ratio of the two electric field components would look like Figure 4.12b.

This chapter described a bistatic lidar model, the Stokes parameters, the amplitude scattering matrix and the distribution of aerosols in the atmosphere. Assumptions were made and limitations placed on the model and theory. It was made clear that the model applies only to spherical scatterers or particles small compared to the wavelength. However, the Mie theory is only one part of the model, a different theory could be used for different conditions when the assumption of spherical scatterers is not valid. For example, a scattering model describing desert aerosols could replace Mie theory, to model the results of a bistatic lidar in the desert environment.

The next chapter will use this model with an inversion technique (described in Chapter 6) and a lot of trial and error to determine the best match for several data sets collected during the Wallops Island CASE I program.

Chapter 5

DATA ANALYSIS AND RESULTS

In Chapter 4 the bistatic lidar model was explained, and example outputs were generated to demonstrate what might be expected from real data. This chapter will focus on the data from both the monostatic and bistatic lidars. Data are shown from several nights to provide examples of both clear and hazy conditions. The temperature, relative humidity, and wind speed will be shown with each plot to help verify the data collected from both the bistatic receiver and the Raman lidar return. Because the Raman lidar has been previously evaluated (Philbrick, 1994), it will be used to verify and sometimes tie off extinction values for calculation of the particle size distributions from the bistatic lidar data. This will be accomplished by comparing the extinction calculated from the Raman lidar (Chapter 1) with the extinction calculated by the model from the best fit to the bistatic lidar data.

Due to the complexity of inverting a linear data array of 1024 data points to obtain a nine-parameter distribution, most of the data inversion was done by trial and error beginning with standard distributions such as those shown in Figure 4.4. However, a Newton-Rapson inversion routine was used to determine the best fit to the data on clear nights when only one mode (three parameters) existed. This inversion sub-routine was also used with three modes to minimize the error between the model and data once a reasonably good fit to the data was already accomplished manually. The last section of this chapter will show some of the cross polarization results and explain what conclusions can be made about them.

This chapter will not spend much time on the error of the data or how well the model fits to the data. Error analysis and the goodness of the fit for each parameter will be quantified in Chapter 6. The error is relatively constant over time, therefore, error bars will only be plotted on two of the bistatic lidar data in Chapter 6.

5.1 Horizontal Monostatic Lidar Data Analysis

The first step in analyzing the data is to define the conditions during the night of the measurements. The temperature, relative humidity and wind speed were all recorded each minute of the day. On September 14, 1995 the conditions were hazy and humid, a perfect night to observe large particles. Photographs of the laser propagating through the aerosols on this night were shown in Figures 3.6 and 3.7. Unfortunately, the bistatic lidar measurements were not started until 11:00 pm, after the haze had already formed. Figure 5.1b shows a plot from 11:00 pm to 3:00 am of the temperature and relative humidity. The wind speed is indicated in miles per hour next to each data point. Here we can see that the relative humidity remains constant at about 90% until about 1:30 am, while the temperature slowly dropped from 23°C to 22°C. After 1:30 am the wind speed increased to 5 mph and brought with it a warmer and drier air mass. The temperature decrease of 1°C does not seem like a large change, but from Figure 5.1a, it is apparently large enough to cause significant changes in the average extinction coefficient calculated from the Raman 607 and 530 nm lidar channels. Each time the temperature dropped, the extinction along the horizontal path would increase, until the new air mass was blown in and the extinction went down to that of a clear night. The zero wind speed, falling temperature, and increasing extinction would suggest that the existing particles are increasing in size due to condensation of water vapor onto their surfaces. Section 5.2.2 will display some results of the bistatic lidar data inversion that would seem to support this point. But first an example will be presented to show how the total path extinction is calculated from a Raman lidar return.

Figure 5.2 shows plots of the Raman 607 and 530 nm return signals after being filtered and range corrected by multiplying the signal by the square of the distance. These data were collected between 11:00 and 11:30 pm on the night of September 14, and correspond to the first data point in Figure 5.1a. The data is averaged over 30 minutes and filtered with a three-point Hanning filter to provide a more uniform signal, thus making it easier to draw a straight line to approximate the average extinction over a region

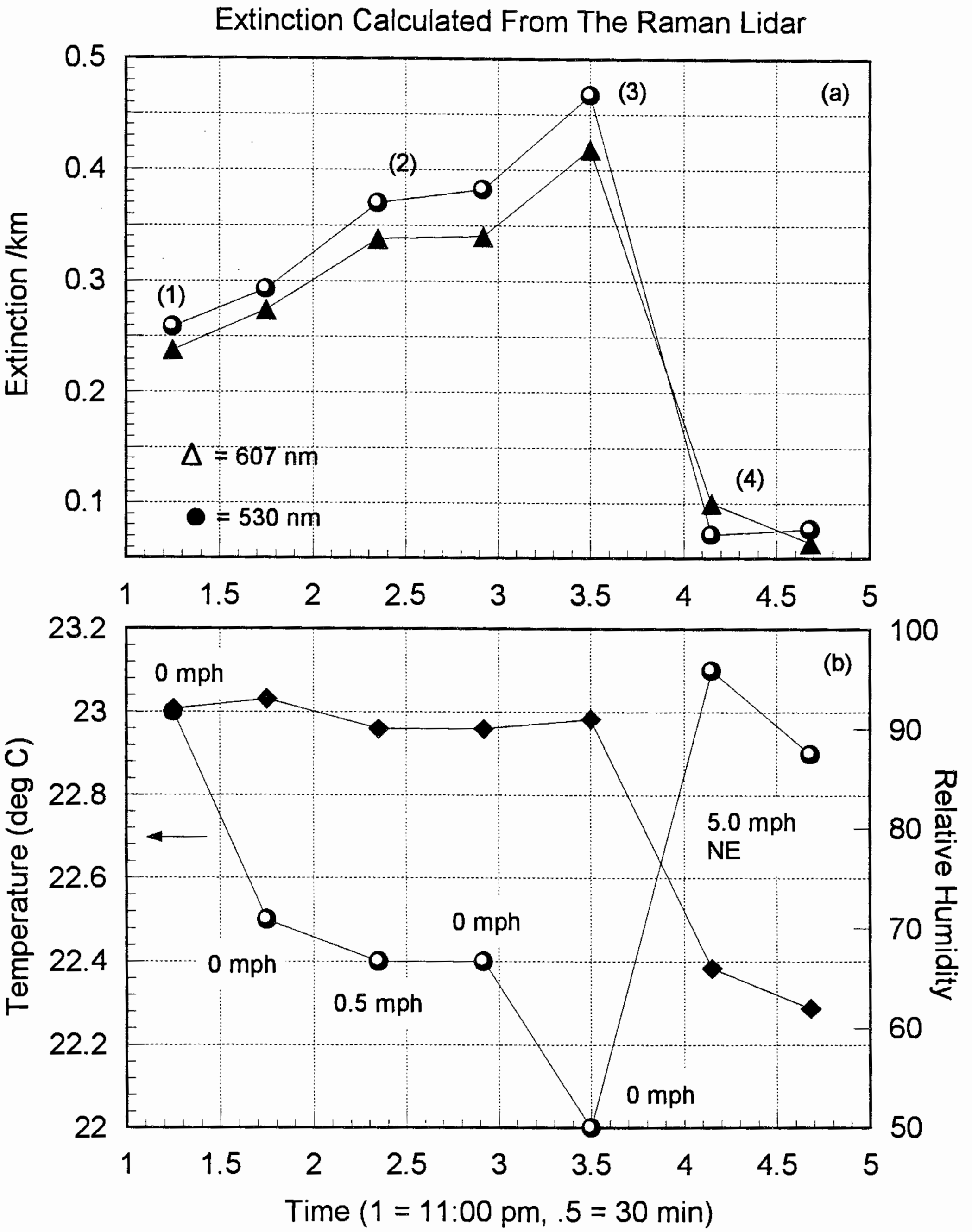

Figure 5.1. (b) A Plot of the temperature and relative humidity versus time from the lidar weather station on the night of September 14, 1995. (a) Corresponding plots of extinction coefficients from the Raman lidar at 607 and 530 nm, at the same times as the above temperature and relative humidity plots. The increases in extinction can be seen to follow the decreases in temperature.

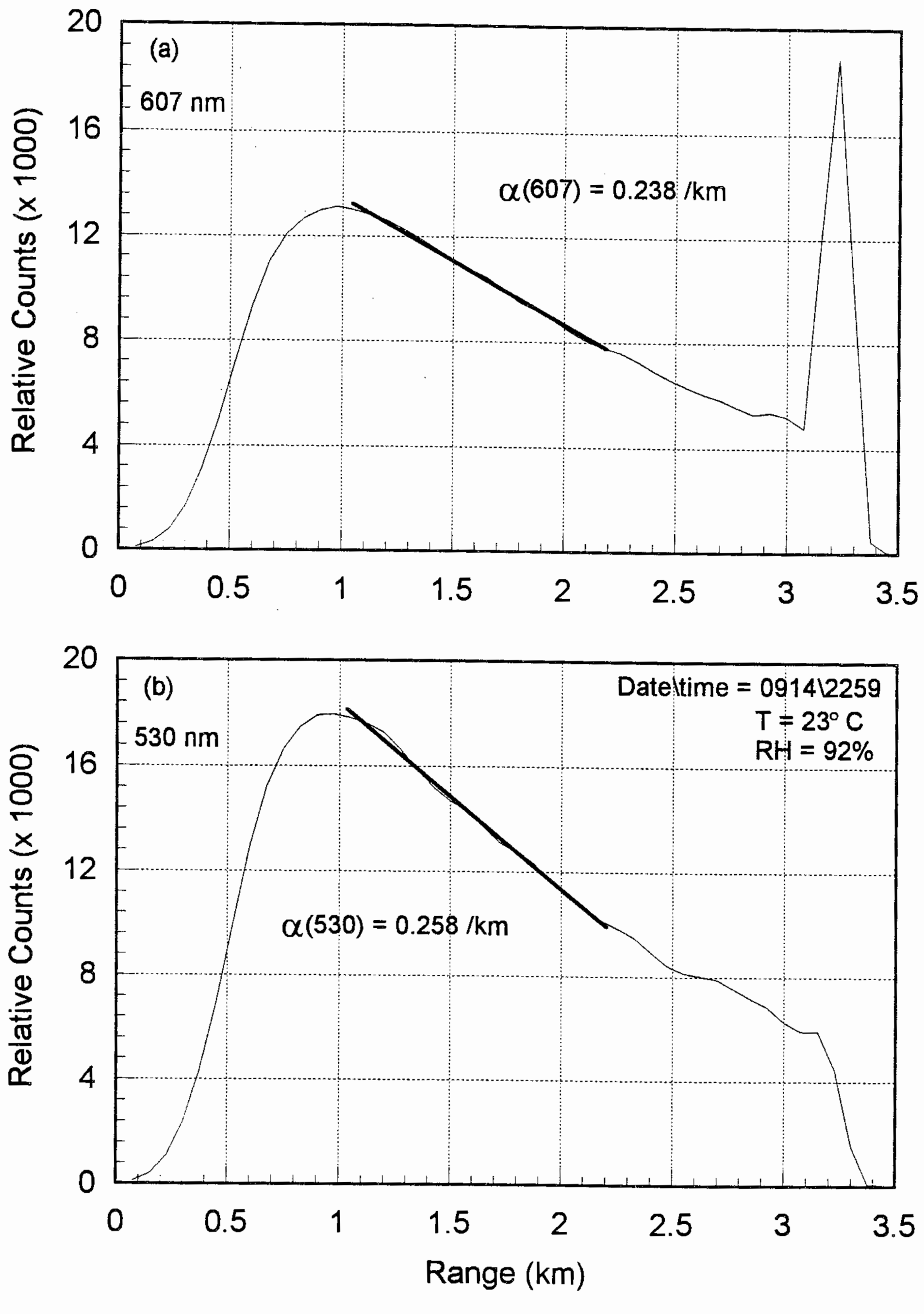

Figure 5.2. Raman lidar 607 nm (a) and 530 nm (b) returns on September 14, 1995, a hazy night with a trimodal particle distribution. The thick solid line represents the average slope of the curve and is proportional to the average extinction coefficient. The extinction coefficients from these plots corresponds with the first points in Figure 5.1.

of the lidar return (shown as a thick solid line in both figures). After the signal has been range corrected, the only reason for the signal to decrease in amplitude with range would be due to extinction. Therefore, the slope of the curve is directly proportional to extinction described by the Beer-Lambert law, Equations 1.3 and 4.7. The target board, at 3.28 km, is visible only because of bleed through of 532 nm radiation passing the blocking filter at 607 nm. The target board is not visible in the signal of Figure 5.2b because the 530 nm filter has a much higher blocking capacity at 532 nm. Between about 1 km and 2.25 km the slopes of both curves in Figure 5.2 remain constant indicating extinction coefficients of $\alpha_{607}=0.238$ km^{-1} and $\alpha_{530}=0.258$ km^{-1}. But, between 2.25 km and the target board, the slope of the curves decreases indicating less extinction at the longer ranges near the ocean. This difference in extinction is typical of most evenings, probably because the last kilometer is near the ocean and could contain a slightly different group of scatterers. But the last kilometer only contributes to the scattering between 179° and 180°, which may explain why the model does not fit well near the target board on hazy nights. However, it will be pointed out in Chapter 6 that the largest differences in scattering between spherical and non-spherical particles also occur near 180°.

The relative error in the Raman profile is typically a little more than the inverse of the square root of the number of counts. For Figure 5.2a this corresponds to a maximum error of about 0.014 counts per 500 ns, due to the large number of counts after averaging for one half hour. Errors this small cannot be seen on the plot scaled from 0 to 14,000. Most of the error in calculating the extinction this way is due to the uncertainty in the determination of the average slope of the curve. This is why many samples were averaged. After trying multiple fits to the curve to obtain the average slope, the error in the estimation of the average path extinction coefficient is about ±5%. This error is due to the fact that the extinction is not perfectly constant along the horizontal path, but varies slightly with time and space. This should be remembered when near instantaneous extinctions are inverted from the 15 second bistatic lidar data. The comparison of the two extinction calculations is used primarily to show trends or overall conditions such as a clear or hazy atmospheric path.

The next examples will be from a typical clear night. Four of the evenings had similar conditions, with temperatures between 19°C and 21°C, and relative humidities between 70% and 80%. It will be shown that only one aerosol mode existed on these evenings. Figure 5.3 shows plots of the 607 nm (a) and the 530 nm (b) Raman channels from the night of September 19, 1995. Again, thick solid line represents the average slope used to calculate the extinction coefficient at that wavelength. The average extinction coefficients calculated from these data are $\alpha_{607}=0.058\ \mathrm{km}^{-1}$ and $\alpha_{530}=0.069\ \mathrm{km}^{-1}$. The extinction is calculated at both wavelengths to check the model at a frequency other than the one used for the inversion. However, 607 nm is not sufficiently far from 532 nm to allow a determination of how accurately the particle size distribution has been modeled. In this set of plots the slope of the curve appears to increase, indicating less extinction, after 2.25 km. The extinction on this night was relatively small, only about five times that from molecules only. The extinction coefficient of a pure molecular atmosphere at sea level (standard pressure) is $\alpha_{532}=0.013\ \mathrm{km}^{-1}$. This can be calculated from the total Rayleigh scattering cross section (4.28) and the extinction coefficient (4.32) with the total number of molecules at the surface ($2.54\times10^{25}\ \mathrm{m}^{-3}$) all given in Chapter 4. Figure 5.4 shows one more example of a typical clear night. These data were collected on September 15, 1995 and show similar extinction coefficients as in Figure 5.3, $\alpha_{607}=0.049\ \mathrm{km}^{-1}$ and $\alpha_{530}=0.055\ \mathrm{km}^{-1}$. Even though Figures 5.3 and 5.4 look alike, they are both shown to demonstrate that when the atmospheric conditions (temperature, humidity, wind speed) are similar, the lidar data, both Raman and bistatic, will consistently measure the same results. These figures will be referenced later to verify inversion results from the bistatic lidar.

A final example will show data collected on an extremely clear night. Figure 5.5 shows the Raman 607 nm return from the evening of September 10, 1995. The temperature was 17.6°C, the relative humidity was 54%, and the wind speed was 5 mph. There was a problem with the lidar on this evening. The laser pulses were not always transmitting at the same time with respect to the data collection timing. This caused the

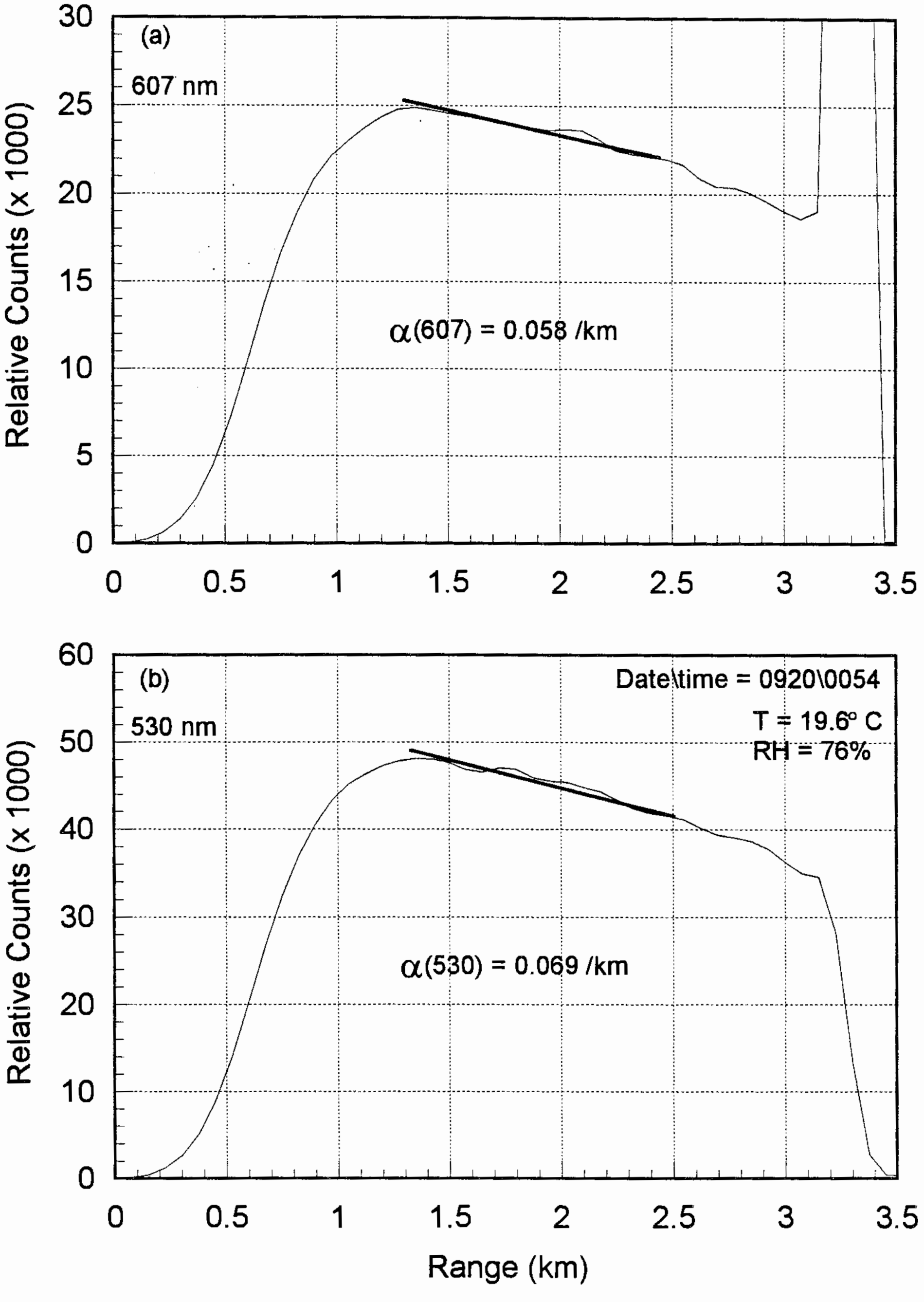

Figure 5.3. Raman lidar returns at (a) 607 nm and (b) 530 nm from September 19, 1995, one of four clear nights. The extinction during this night was only about 5 times greater than that from a pure molecular atmosphere.

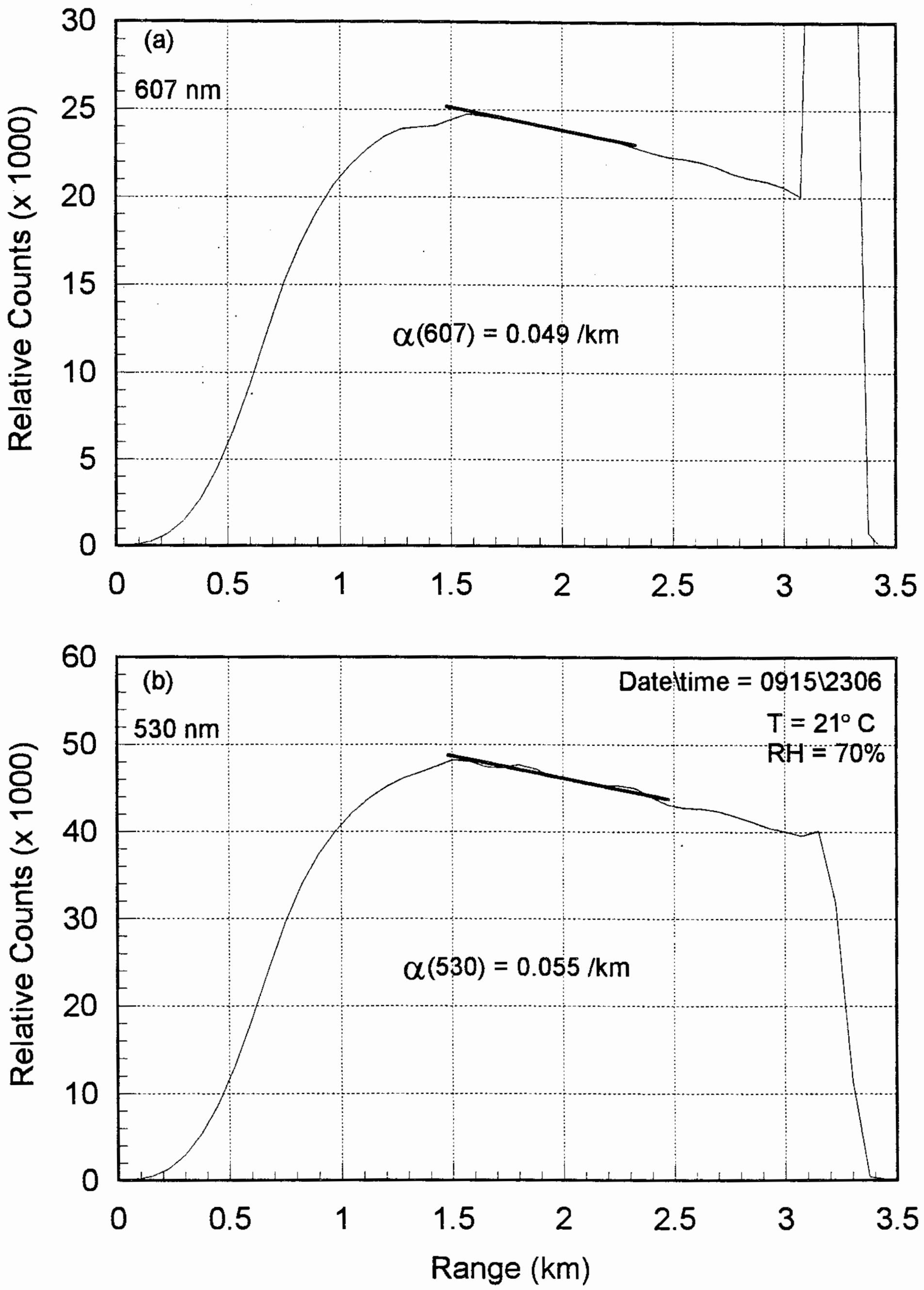

Figure 5.4. One more example of a typical clear night like that in Figure 5.3, collected on September 15, 1995. The Raman lidar returns were used calculate extinction at 607 nm (a) and 530 nm (b). Two evenings of the same conditions are shown to provide confidence that the bistatic lidar data measures the same particle distributions under similar conditions.

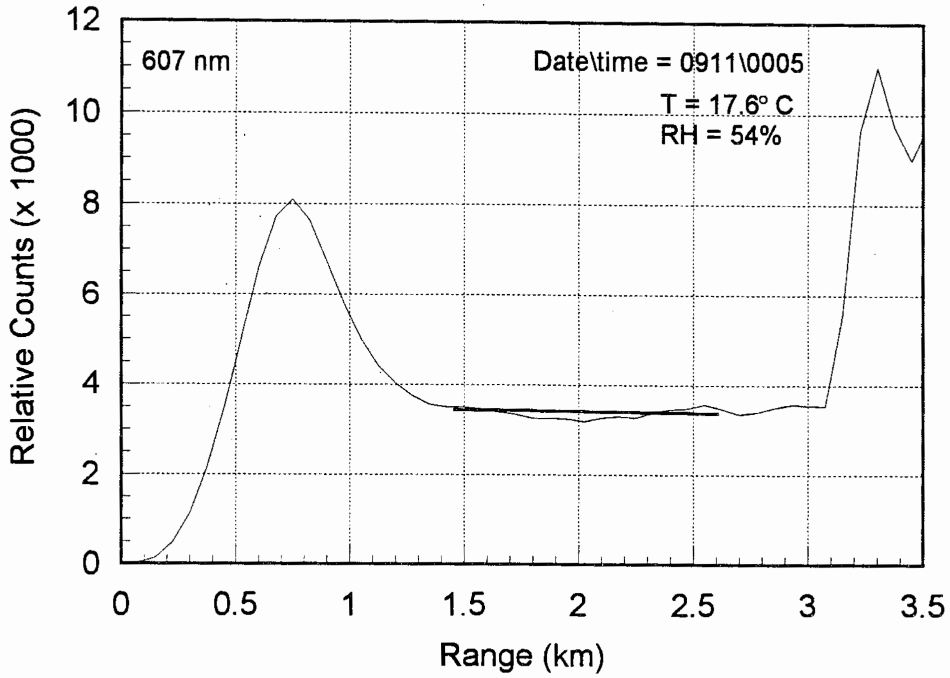

Figure 5.5. An Example of the conditions on an extremely clear evening of September 10, 1995. The extinction is small enough that it cannot be accurately determined from this data. This data is partially corrupted due to a timing problem with the laser. The evidence of this can be seen in the extra wide target board and from the hump in the data between 0.5 and 1.0 km.

hump between 0.5 and 1.0 km, and the slight increase in signal at 2.5 km. Unfortunately, this was the only night that exhibited these very clear conditions. From Figure 5.5 in the region of the thick solid line it can be seen that the slope of the curve is indeterminate due to a very small extinction and fluctuations in the signal. Because of the problem with the laser this evening it is impossible to calculate an extinction coefficient, but it is possible to determine that the extinction was very small indicating that the particle concentration was very low that evening. If there were only molecular extinction (α_{532}=0.013 km^{-1}), the signal would decrease from 3500 counts at 1.5 km to 3410 counts at 2.5 km, a very small change in signal. Data from the bistatic lidar will show that the extinction was due primarily to scatterers in the Rayleigh size region.

5.2 Horizontal Bistatic Lidar Data Analysis

The last section described the conditions of four separate nights, 09/10, 09/14, 09/15, and 09/19 1995. Raman lidar profiles along with the local weather station data were used to verify the classification of either a 'clear' or hazy night. In this section examples of the bistatic lidar data will be analyzed from each of these evenings to validate the usefulness of the instrument and measurement technique.

The processing of the bistatic lidar data is fairly simple, but fitting a model to it is not. Each individual sample or image array is saved independently along with a dark count noise sample. One image is collected for each polarization measurement. The program that processes the data is called 'wallops.m' and is listed in Appendix D. Two data sets are read together, one for the parallel component and one for the perpendicular component. The background is subtracted from each data set and then the signals are filtered with a 21-point Hanning filter. These two filtered signals are then divided to obtain the ratio of curves modeled in Chapter 4. The next step is to assign the scattering angle associated with each pixel. From Figure 3.2 the target board is shown at a 179.73° scattering angle, this is where the data are normalized. The angle assignment is then incremented toward 155° by the tangent of the pixel length over the focal length of the lens. This is to account for the fact that the film plane is not curved but flat. Each ratio is normalized to unity at the target board. This is because the intensity of the scattering at 180° from the target board is independent of polarization. The error in the normalization of the data because the target board is at 179.73° instead of 180° is assumed to be negligible. This processed data is then used as the input to the inversion algorithm.

Figure 5.6 shows a plot of the raw data and background measurement from the night of September 15, 1995. Figure 5.6a shows the signals for both polarizations before filtering or subtracting the background. Here the target board is identified by a spike in the signal at pixel number 46, while the rest of the signal amplitude remains fairly flat across the entire field of view of the array. This is because the decrease in signal due to the greater distance from the receiver is balanced by the fact that the observed volume

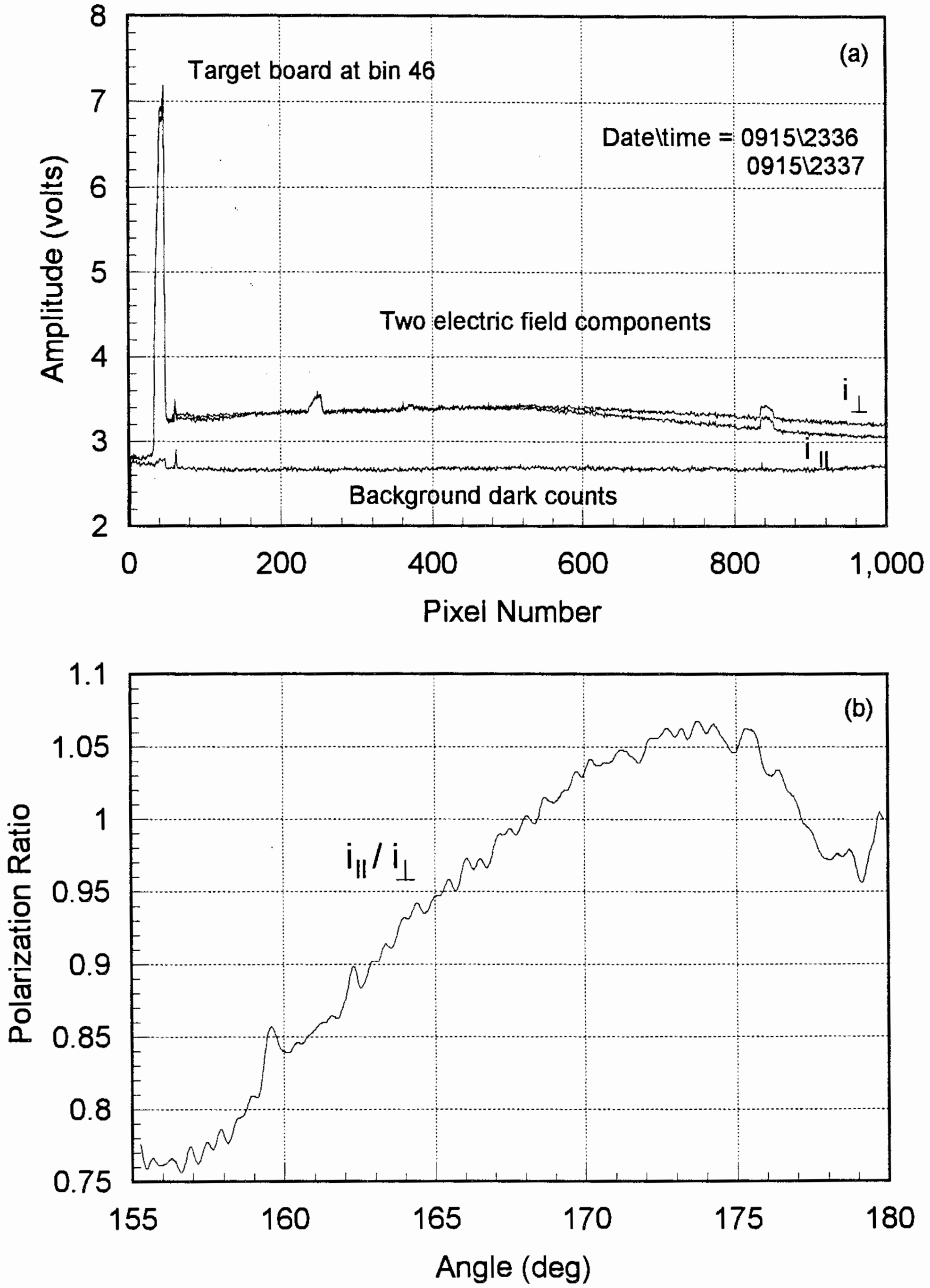

Figure 5.6. (a) A Plot of raw bistatic lidar data, for both polarizations from September 15, 1995 including the dark count background measurement. (b) Plots of the profiles in (a) after subtracting the background and applying a 21-point Hanning filter.

increases with distance. Less than one order of magnitude in dynamic range is all that is needed to conduct this type of measurement. Figure 5.6b shows the data after subtracting the background and applying a 21-point Hanning filter. The magnitude of the return from the target board is a consistent measure of the relative changes in extinction through the night. In fact, if the laser power is stable, the intensity of the return from the target board can be used to determine the number density of the distributions. This is accomplished as follows. On a clear night when only one mode of particles exists, the scattering is strongly influenced by the molecules in the atmosphere, therefore the number density of the single particle mode is fixed by the number of molecules at the surface (2.54×10^{25} m^{-3}). The extinction coefficient is directly calculated from the model since all three parameters are defined. This extinction coefficient is then used to calculate I_0 in the Beer-Lambert law (4.31), setting I equal to the signal from the target board, in this case, 7 volts. If the laser power remains constant from evening to evening and the reflectivity of the target board does not vary, then this I_0 can be used every night to calculate the total extinction coefficient and determine the number density of each lognormal distribution. Preliminary calculations show this method to be within the errors of the fit between the data and the model.

5.2.1 Clear Night Results

This section presents the results of the bistatic lidar from the three clear nights described in Section 5.1. As was just explained, clear evenings offer the added bonus that all three parameters of the lognormal single-mode aerosol distribution can be uniquely specified due to the significance of the scattering from molecules. The data from these evenings are also the easiest to invert because only three parameters need to be specified. Therefore the inversion algorithm discussed in Chapter 6 can be used to obtain the least squares fit to the data.

Figure 5.7a shows the raw data, for both the parallel and perpendicular components, with the background subtracted on the night of September 19, 1995. The

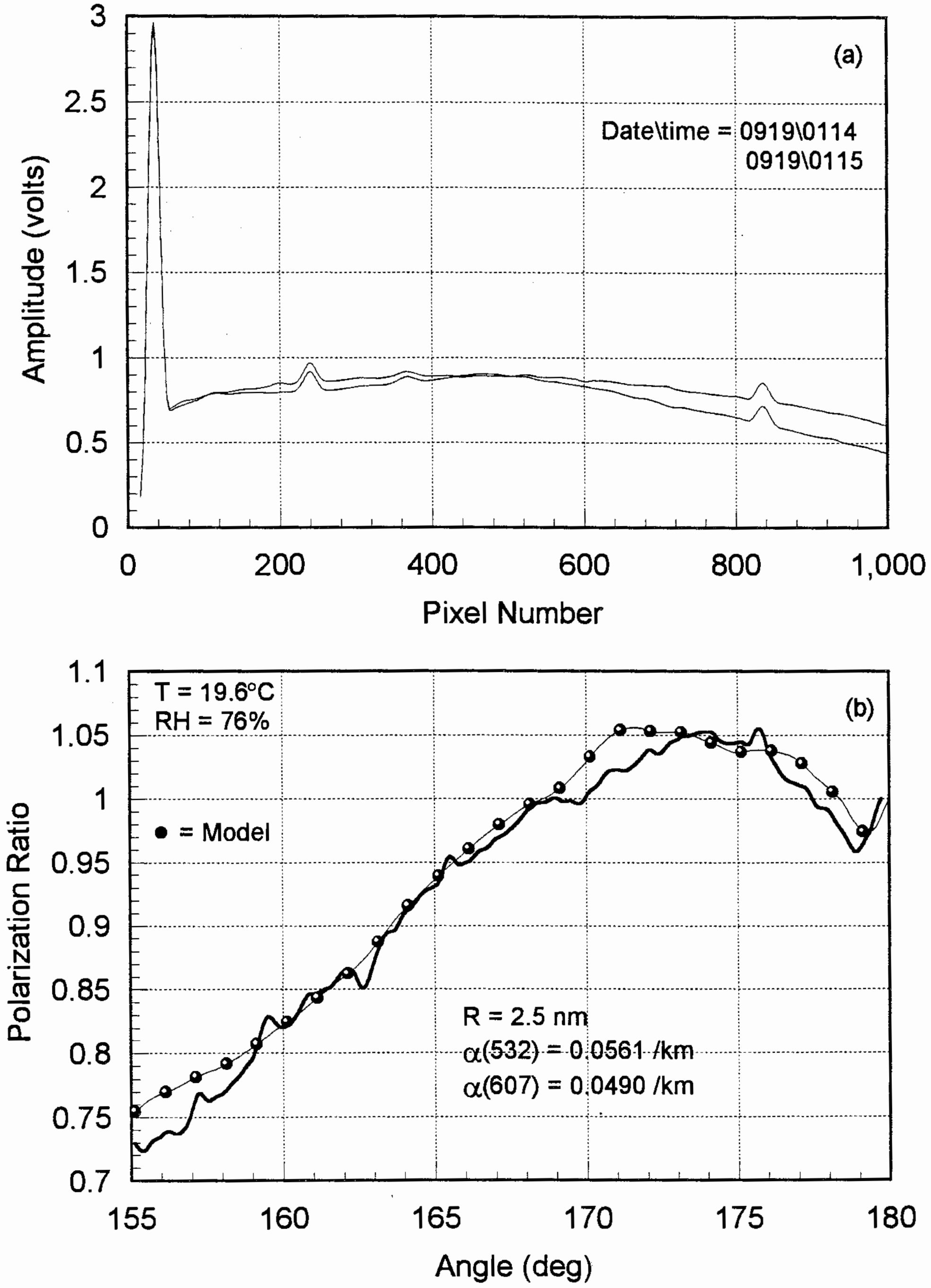

Figure 5.7. (a) Plots of both electric field components from the night of September 19, 1995. (b) The ratio of the curves in (a) plotted with the best fit single mode model. The particle size distribution from the model is consistent with a clear, high transmission optical path.

target board signal is seen to reach three volts while the rest of the signal is near 0.8 volts. This information alone indicates that the night is clear or free of large particle scattering. The processed bistatic lidar data is shown in Figure 5.7b as a ratio of the two polarization components versus scattering angle by the thick solid line, while the best fit model is shown with a dotted thin line. The parameters of this distribution are, R=2.5 nm, σ_g=4.86, and N=186 cm^{-3}. This distribution is very similar to the first mode of either a maritime or background aerosol distribution (see Table 4.3 and Hobbs, 1993). The sensitivity of the fit on each of the three parameters is shown in Chapter 6. All the profiles from this night match with the same single-mode distribution and have a calculated extinction coefficient consistent with the value of $\alpha_{607}=0.049$ km^{-1}. This extinction is consistent with the 30 minute average extinction coefficient of $\alpha_{607}=0.058$ km^{-1} calculated from the Raman 607 nm channel in Figure 5.3. The difference of 15% is most likely due to error in the determination of both extinction coefficients and due to the fact that one measurement is an average over 30 minutes while the other is an instantaneous measurement. At this point the data and model are shown to prove that there is a correlation between the two that is consistent with the observed atmospheric conditions. Figure 5.8 is a plot of the single mode distribution for the aerosols of September 19, 1995. The molecules are still included in the model, but will not be shown to simplify the plot. Calculations for extinction coefficients will be shown for wavelengths other than 607 nm, however these numbers have limited meaning because it is not possible to verify them with the actual extinction. The extinction at 607 nm was calculated from the model and shown for each case because this wavelength was not used to by the bistatic lidar to obtain the measurements, and because it can be referenced to an independent measurement of the extinction at the same wavelength. Extinction at 530 nm is also calculated but this cannot be considered a prediction because this wavelength is too close to the wavelength used to derive the size distribution. It would be expected that the extinction at this wavelength is correct. Using Eq. 4.31 the transmission to the target board is then 85.2%, whereas, the transmission for an aerosol free atmosphere would be 95.8%. Multiple scattering would

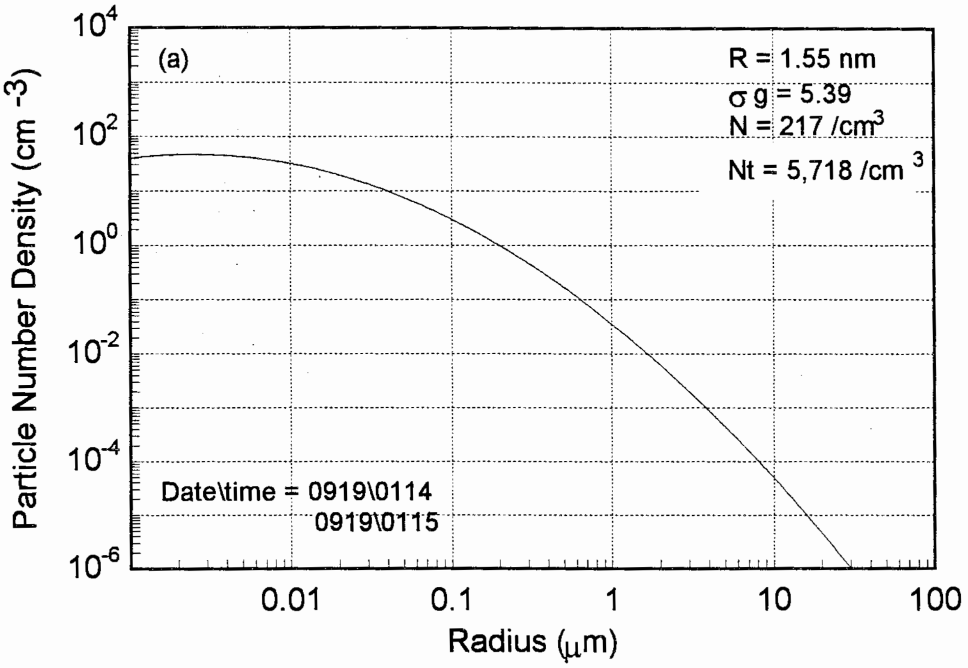

Figure 5.8. A plot of the single mode distribution function that describes the aerosols on the night of September 19, in Figure 5.7b.

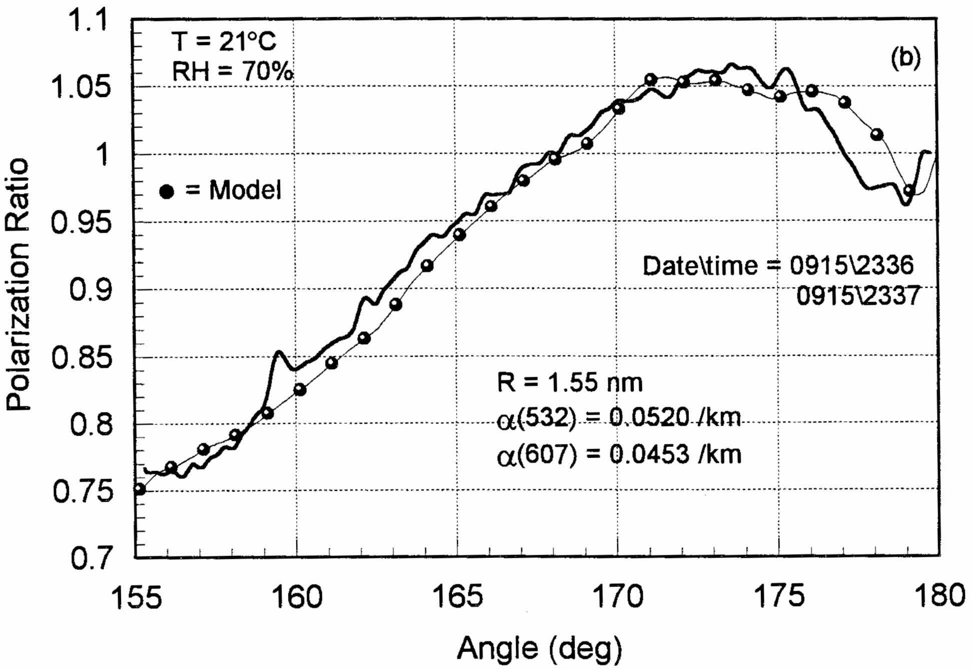

Figure 5.9. An example of bistatic lidar data from another clear night on September 15, 1995, with conditions similar to those in Figure 5.7.

definitely not contribute to the observed radiance at the receiver on this evening. Figure 5.9 shows one more example of data collected during a clear night from September 15, 1995. The best fit for a distribution is slightly different than the previous case, but the particle size distribution is essentially the same with mean radius of R=1.6 nm, σ_g=5.37, and N=217 cm^{-3}. It is important to remember that N is not the number density of the particles, but instead a parameter in the lognormal function related to the number density. Summing over the lognormal distribution function reveals the total particle number density, N_T, for each mode, in this case the N_T =5,718 cm^{-3}. This is close to the total particle number density from September 19, of N_T=5,807 cm^{-3}. Chapter 6 will show that there can be quite a bit of variation between the mean radius and distribution width for the single mode, which would explain the difference in radius of the particles from September 19th to September 15th. This is due to the fact that the model cuts off the distribution at 1 nm. The same actual number density of particles could be obtained with a broader distribution shifted to a smaller radius because of the cutoff at 1 nm. This is not just a function of the model. If the real atmosphere particle sizes do not exist below 1 nm, the same ambiguity would result in the first mode of the aerosols. In both cases the end result of the distribution and extinction would be the same, the parameters would just be different. This does not happen in the other modes that are allowed to continue to both smaller and larger sizes.

The last case of a single mode distribution is from the night of September 10, 1995, shown in Figure 5.10. This evening was considerably clearer than other evenings on which we made measurements. The first indication of this is the magnitude of the scattering received from the target board. This was the coldest night with a temperature of 17.6°C and relative humidity of only 54%. The ratio of the two polarizations in Figure 5.10b looks similar to the ratio in Figure 4.6d for molecular scatterers. Because all the scattering occurs from particles small compared to the wavelength (Rayleigh theory) it is impossible to find a unique distribution and extinction. A distribution with parameters of R=10 nm, σ_g=1.59, and N=1842 was found to fit the data. However, any radius less

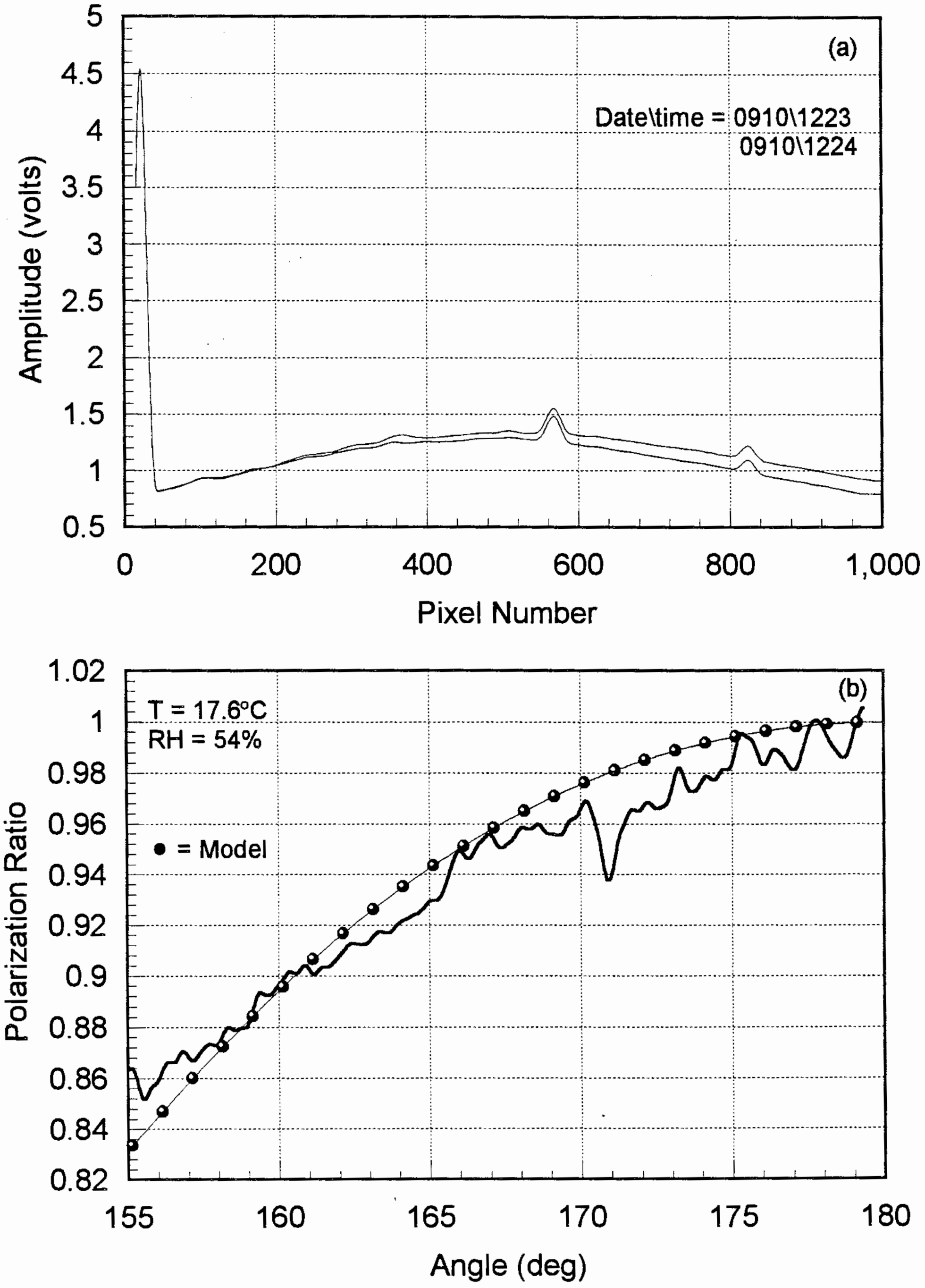

Figure 5.10. (a) An example of unprocessed bistatic lidar data from an extremely clear night on September 10, 1995. (b) The ratio of the two components in (a) that look similar to the Rayleigh ratio in Figure 4.6d.

then 30 nm, with a small distribution width, less than $\sigma_g=1.8$, and any number density will fit the data. This is because no significant scattering occurs out of the molecular scattering region. The fact that this evening is clearer than any other is also shown from the Raman 607 profile in Figure 5.5 by the lack of a significant slope in the curve between 1.5 and 2.5 km. Even though a unique size distribution cannot be calculated for this night, valuable information about what scatterers are not present is available. This is useful for determining a small range of possible extinction coefficients from those just above molecular scattering of 0.013 km^{-1} to those just below the typical clear night of about 0.03 km^{-1}. This example does bring out the question of the lower limit of detectable size distributions with a wavelength of 532 nm. If wavelengths of 266 or 355 nm were used, the Rayleigh limit would not be reached until particle radii of about 15 or 20 nm, respectively, were encountered. This would provide the added advantage of distinguishing particles smaller than 30 nm, while the upper limit for detectable particle sizes will move down from radii of 10 μm (See Figure 4.11). In this case the particle extinction could be extrapolated to longer wavelengths, like 607 or 1064 nm, but to extrapolate the data to shorter wavelengths would be ill-advised because of the strong effects of the scattering by particles in the Rayleigh region for the wavelength of 532 nm. Because of this ambiguity extinction coefficients were not calculated for this case.

5.2.2 Hazy Night Results

The last examples to show the usefulness of this bistatic lidar and measurement technique are from the night of September 14, 1995. This was a visibly hazy night where the extinction increased while the temperature dropped between 11:00 pm and 1:30 am as shown in Figure 5.1. Photographs of the scattering from the laser beam on this night are shown in Chapter 3 in Figures 3.6 and 3.7. The aerosols from this evening will be shown to clearly consist of three independent lognormal distributions of particles that grow as the temperature decreases. Data from evenings with multiple aerosol modes can be difficult to invert because of the sensitivity of the model to small changes in both the median radius and particle distribution width. Each data set can take hours and sometimes days to invert because of all the possible combinations of nine parameters with nearly unlimited range and resolution. And there is always the possibility that the model just will not describe the data. One case will be shown where the model can not be made to fit the data, due probably to either the presence of non-spherical particles, or to an incorrect choice of refractive index. Because of the long hours required to invert a given data set, not all of the profiles have been inverted. A total of seven data sets were inverted and presented in this thesis, while a much larger sampling of the raw data is presented in Appendix E. These data samples should be studied to obtain a feel for the variability from one measurement to the next. However, almost all the ripple and structure in the signals is due to scattering and not to noise.

Figure 5.11a shows a plot of raw data for both scattered polarization components early in the evening at 11:20 pm, corresponding to the first data point in Figure 5.1. From this figure it can be seen that the night on which the measurements were made is not clear, by the small return of only 0.8 volts from the target board. It will be shown that this signal from the target board decreases through the night as the extinction increases until the target board is not distinguishable from the rest of the signal. Spikes in the signal that occur on only one component, like the one at pixel number 400, are caused by insects flying through the laser beam. Figure 5.11b shows the ratio of the two components in Figure 5.11b with a solid line normalized to one at the target board. The first step of the inversion process is to find a first order fit to the data. This is done by choosing standard aerosol distribution parameters, like those listed in Table 4.3, as starting points. For data collected in hazy conditions, at least two modes are needed to find a first order fit. The six parameters required for two modes are then adjusted interactively until the sum of the differences between the model and the data is minimized. An example of a good first-order fit for the ratio of the two components in Figure 5.11a is shown in Figure 5.11b with a dotted thin line. This process is difficult to automate because of the many local minima encountered before the best fit is found. The parameters for this distribution are listed in

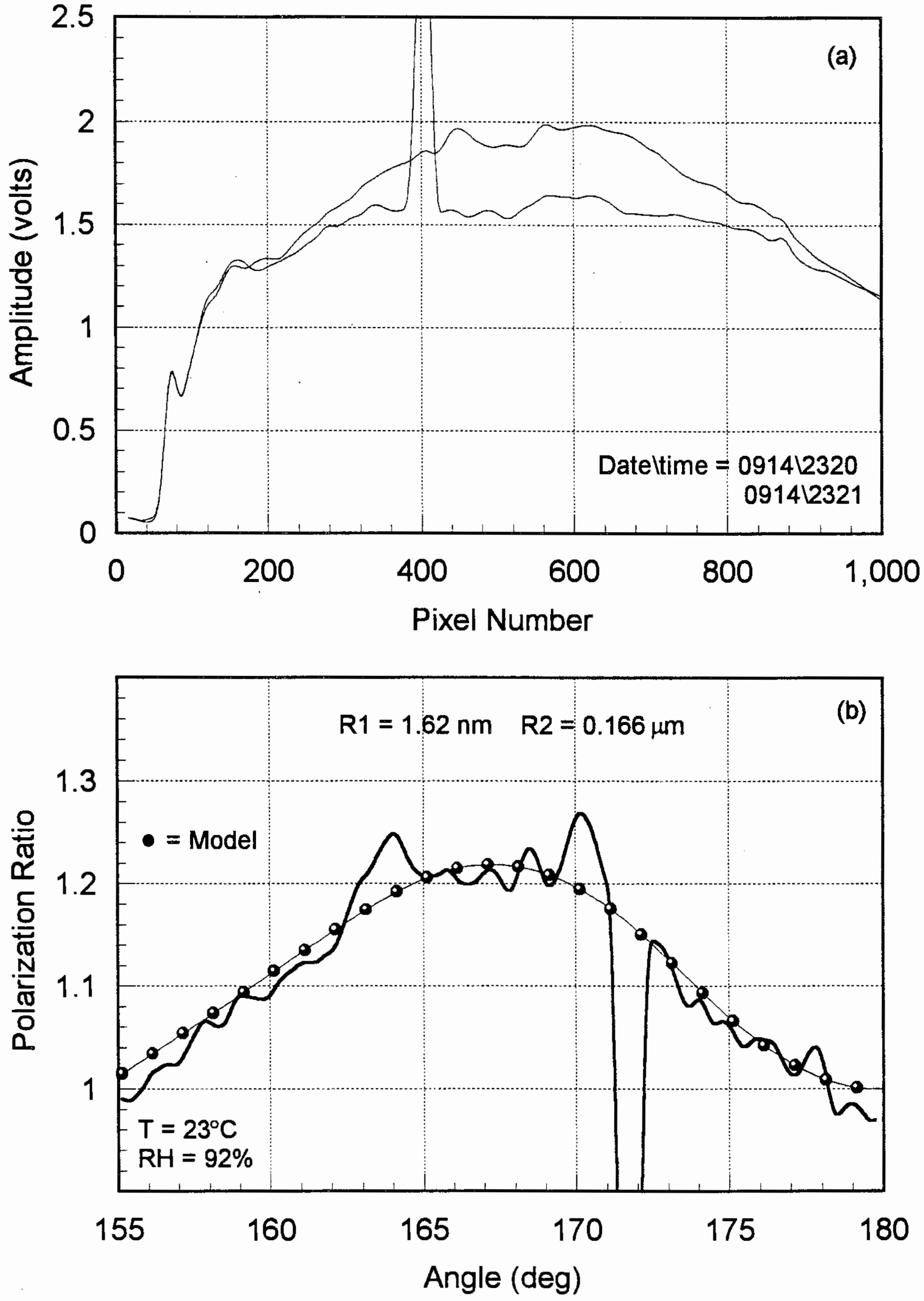

Figure 5.11. (a) A Plot of the raw bistatic lidar data on a hazy night from September 14, 1995. The small value of only 0.8 volts from the target board indicates that there is a significant amount of extinction of the laser beam. (b) The ratio of the two electric field components from (a) is shown with the best first order fit of the model.

Figure 5.11b. These parameters are not unique without an absolute reference to determine the particle number density. On a clear night with a single mode distribution the number density of molecules was used as the absolute reference to determine the number density of the aerosol distribution. On this night however, the second mode of the aerosol distribution, not the molecules, is dominating the scattering. The extinction calculated from the Raman lidar, shown as the first point in Figure 5.1a, is used to normalize the first two modes of the distribution. This is done by varying the number densities and sometimes the median radius and distribution width of the first mode until the extinction equals that calculated from the Raman lidar. The first modes may need to be adjusted again if the addition of a third mode significantly alters the extinction. In most cases the extinction can not be continuously varied without losing the fit to the data. This means that given a good fit to the data, only a few extinction coefficients are possible. The Raman lidar is used to determine which extinction coefficient is the correct one. The next step of the inversion process is to determine what third mode, if any, will fit the model to the ripples and sharp features in the data. For this night, the last mode was extremely difficult to find because the third modes described in the literature did not improved the fit. In fact, the ripples in the data started to look more and more like noise after a few days of trying to find an aerosol distribution that would match the data. Finally, very narrow distributions were tried, and an excellent match was found with a particle radius of 6.46 μm, a distribution width of $\sigma_g=1.01$, and a total number density of 1.5×10^4 m^{-3}, as shown in Figure 5.12. Nearly monodispersed particle distributions like these are often called radiation fog, and generally form from condensation of water vapor molecules onto the surface of the particles as the temperature drops on calm, humid nights. The disagreement between the model and the data from 175° to 180° is probably due to a different particle size distribution near the target board. Figure 5.12b lists the total number density for each mode, and the extinction calculated by the model for a range of common laser wavelengths. Future experiments will include transmissometers operating at a couple of these wavelengths to check the accuracy of the retrieved particle size

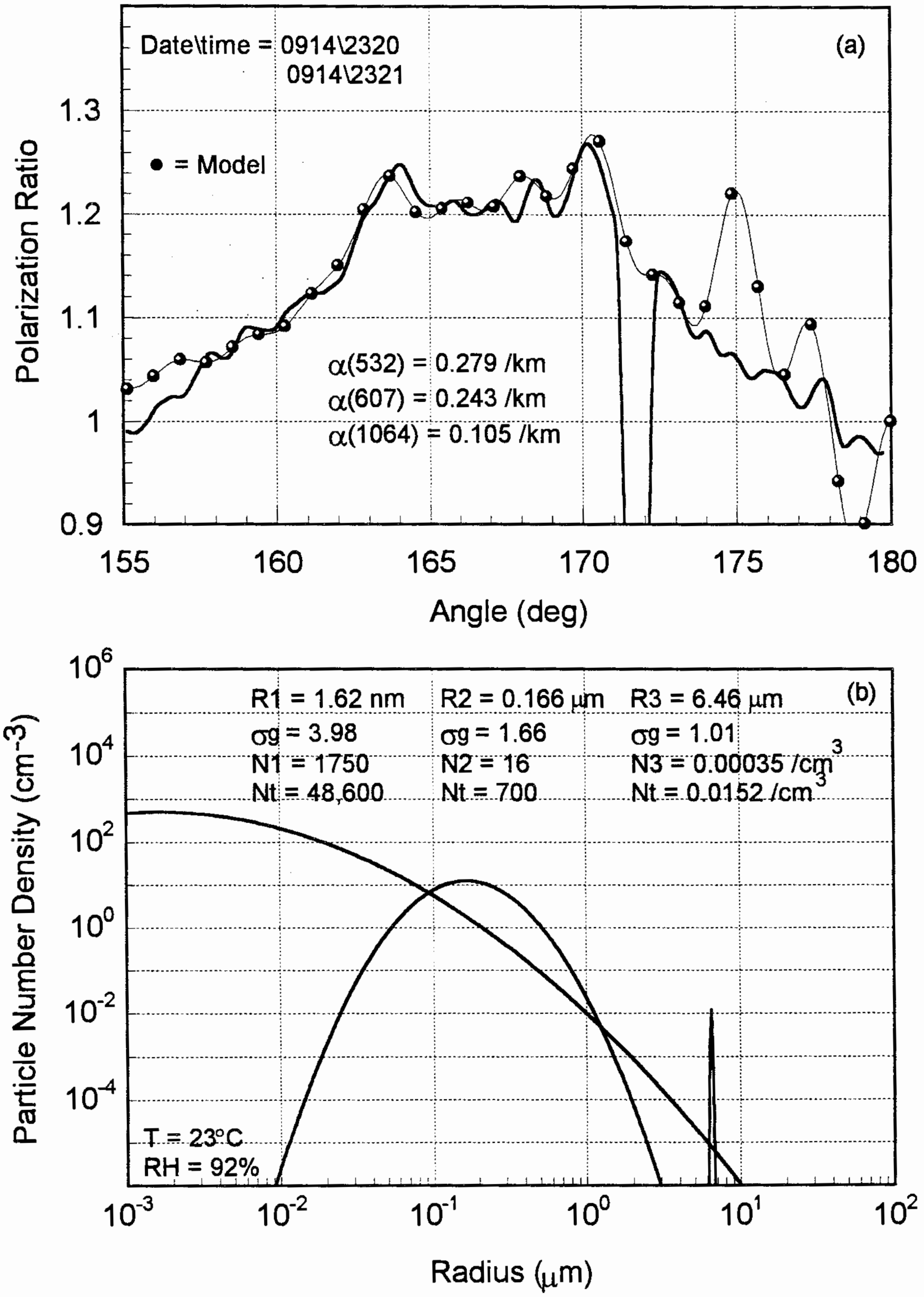

Figure 5.12. (a) A good trimodal fit of the model (dotted line) to the data (solid line) showing a nearly monodispersed radiation fog forming. Each sharp wiggle and feature is accurately modeled. (b) The lognormal distributions used to fit the model to the data in (a).

distributions. The number density of the third mode is equivalent to 9.1 particles per beam path scattering volume, and is a reasonable amount to uniformly affect the scattering at each volume element. The sensitivity of the model to small changes of the nine parameters will be demonstrated from the following examples as the particle distribution slowly increases in size.

Because the evening of September 14 was calm with low wind speed, it can be assumed that the particle number density will not significantly change throughout the course of the night. If the particle number density does not change, then only six of the nine parameters should be altered to fit the model to each consecutive data set. And since the distribution width of the lognormal function (σ_g) represents either the production mechanism or origin of the particle, it will be adjusted only if necessary.

Figure 5.13a shows the raw unprocessed data collected eight minutes later than the data in Figure 5.12. Since the amplitude of the signal from the target board is the same as that in Figure 5.13, the extinction calculated by the model should also remain the same at about $\alpha_{607}=0.2433$ km^{-1}. The ratio of the two components shown in Figure 5.13b bears almost no resemblance to the ratio from Figure 5.12b only eight minutes earlier. However, only modest changes to the aerosol distribution parameters are required to produce a good fit between the model and the data. A first-order fit to the data was attempted by only increasing the median radii of the first two modes, but this failed to match the peak of the profile which shifted 2° to the left. Increasing the mode radii moved the peak of the curve up from 1.22 to 1.24. The only way to move the peak to the left was to decrease the distribution width of the second mode from $\sigma_g=1.66$ to 1.55. This best first order fit is shown in Figure 5.13b with a dotted line. In eight minutes, the second mode of the distribution has clearly grown from 0.166 μm to 0.182 μm, while the width of the distribution has decreased from $\sigma_g=1.66$ to 1.55. The distribution width of this mode will continue to decrease with particle growth, until the limit of $\sigma_g=1.38$ is reached. The distribution width will then remain constant as the particles continue to grow. Next, a third mode is added by looking for the best fit with a particle distribution

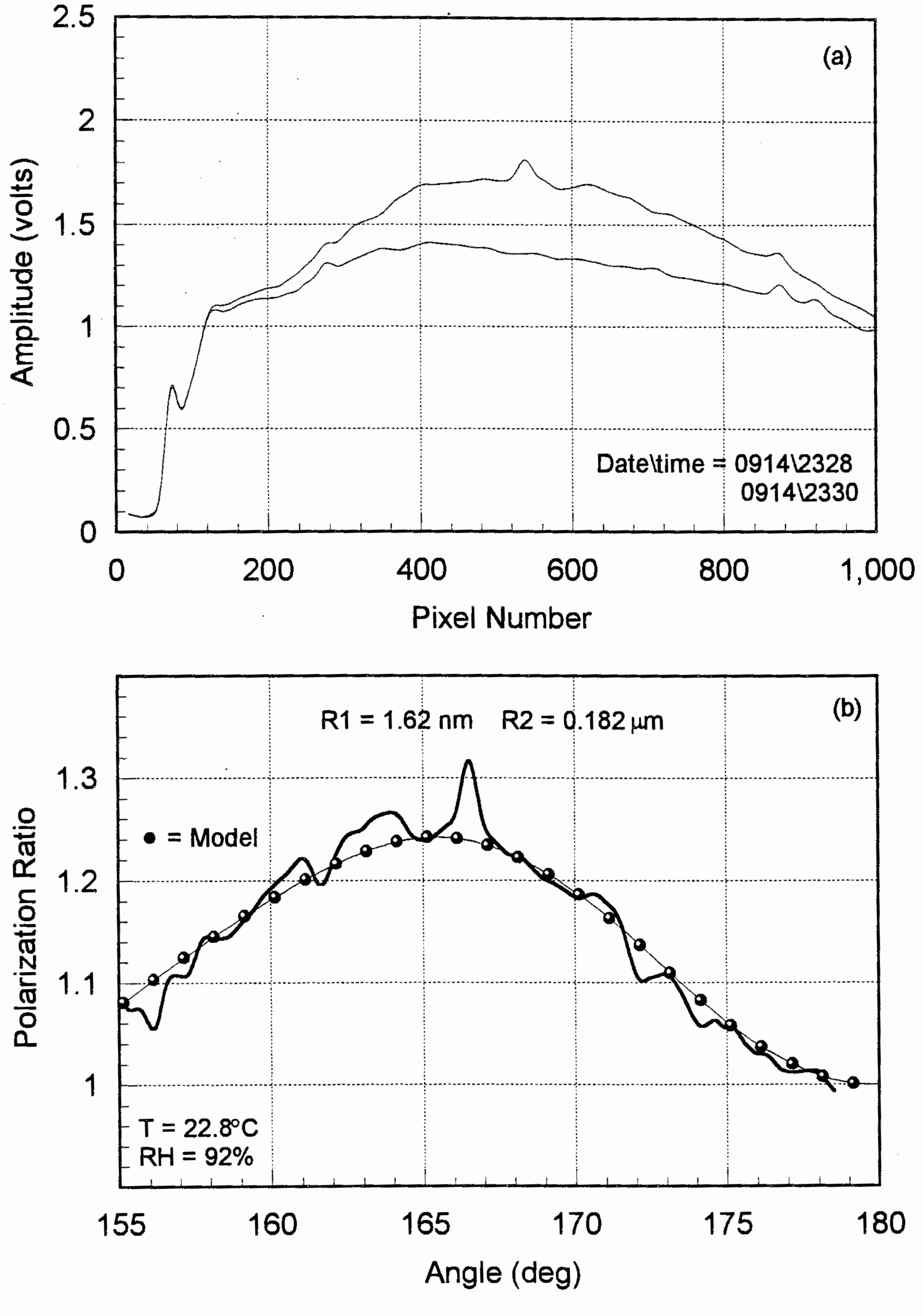

Figure 5.13. (a) The two electric field components from the bistatic lidar collected eight minutes after the data in Figure 5.12. (b) Ratio of the two components from (a) shown with a solid line, and a first order fit with the model shown with a dotted line.

similar to, but with a larger radius than the last mode in Figure 5.12a. A particle radius of 7.59 μm, a 17% growth in radius in eight minutes, was found to have the best match with the data. Although the bimodal distribution from Figure 5.13b would appear to have a better mathematical fit, evidence of the third mode at a radius of 7.59 μm can be clearly seen. Each scattering angle is measured at a different location, and this distribution has on average only six particles per scattering path volume. Therefore, the uniformity of this third mode in time and space could definitely be questioned. Figure 5.14a shows the results from the model plotted with a dashed line on top of the data, while Figure 5.14b shows the trimodal lognormal distribution and parameters that best describe this data set. The extinction coefficients in Figure 5.14 are unique because the number density of each mode is fixed due to the atmospheric conditions.

The next example corresponds with point two in Figure 5.1 and is shown in Figure 5.15. Since the extinction was observed by the Raman lidar to increase, a proper fit of the model to the curve in Figure 5.15b should also reveal an increased extinction. Again this ratio of the two polarization components has changed considerably from the profile collected one hour earlier. But a slight increase in the mode radii and a decrease of the distribution width to $\sigma_g=1.38$ for the second mode, represents a first-order approximation of the data very well. The first mode has now grown to a radius of 2 nm, and mode two has grown to 0.224 μm. Figure 5.16a shows that an increased third mode radius of 7.94 μm best matches the ripples in the data. Using these new lognormal parameters, the model calculates the extinction at each wavelength and determines $\alpha_{660}=0.3361\ \text{km}^{-1}$. Because the number densities of the three modes were not changed, the increase in the mode radii accounts for the increased extinction measured with the Raman lidar. These small changes in the median radii are causing large and significant effects in the ratio of the two polarization components. This evening with slowly growing particles is the best way to demonstrate the sensitivity of the model and data to each parameter, and therefore establish confidence in the inverted particle size distribution and calculated extinction. Figure 5.16b shows the three lognormal distribution functions that best model the data,

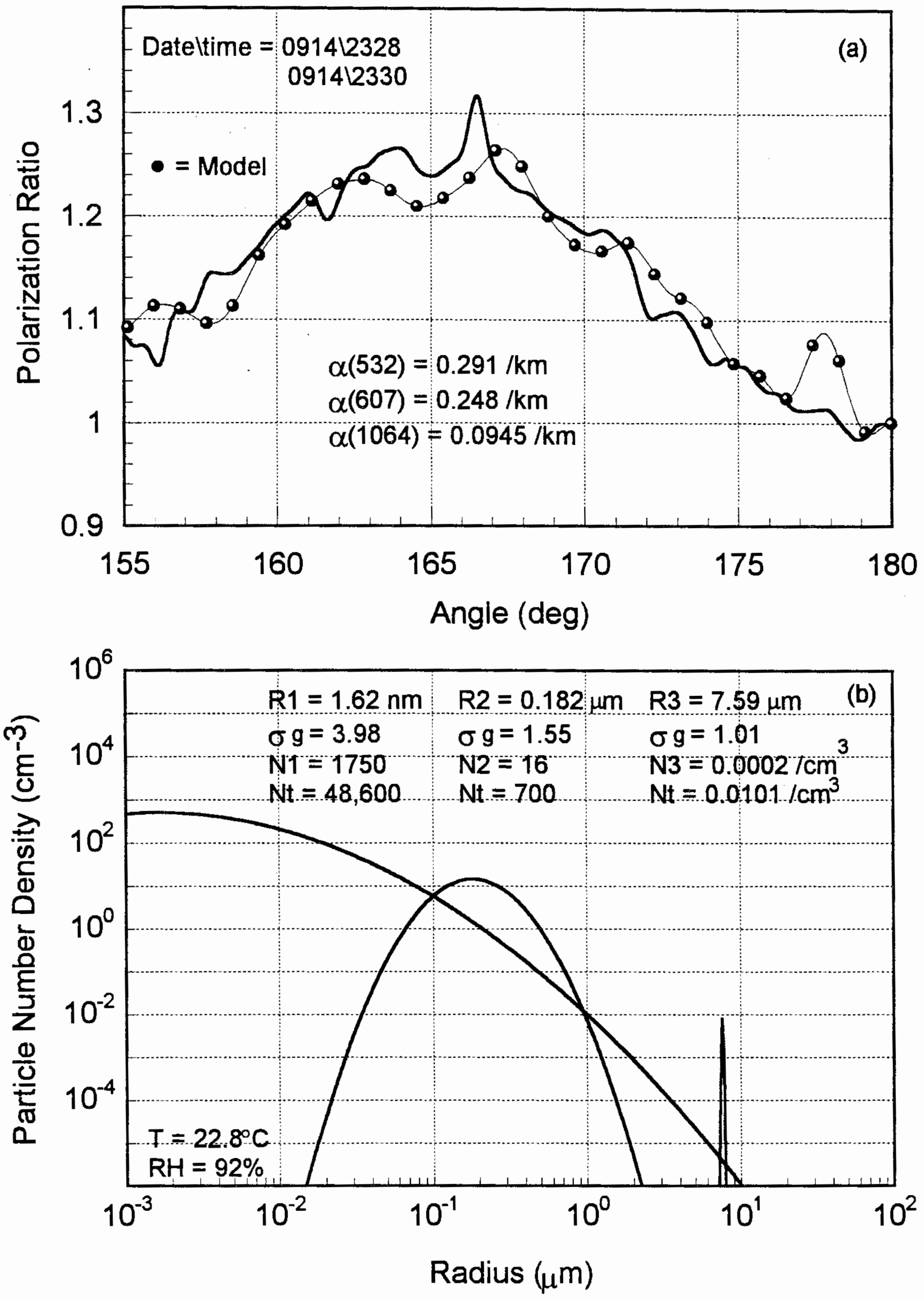

Figure 5.14. (a) A plot of the data and the model for another data set from September 14 showing the growth of all three modes of the distribution. (b) The trimodal lognormal distribution for the best fit of the model to the data in (a).

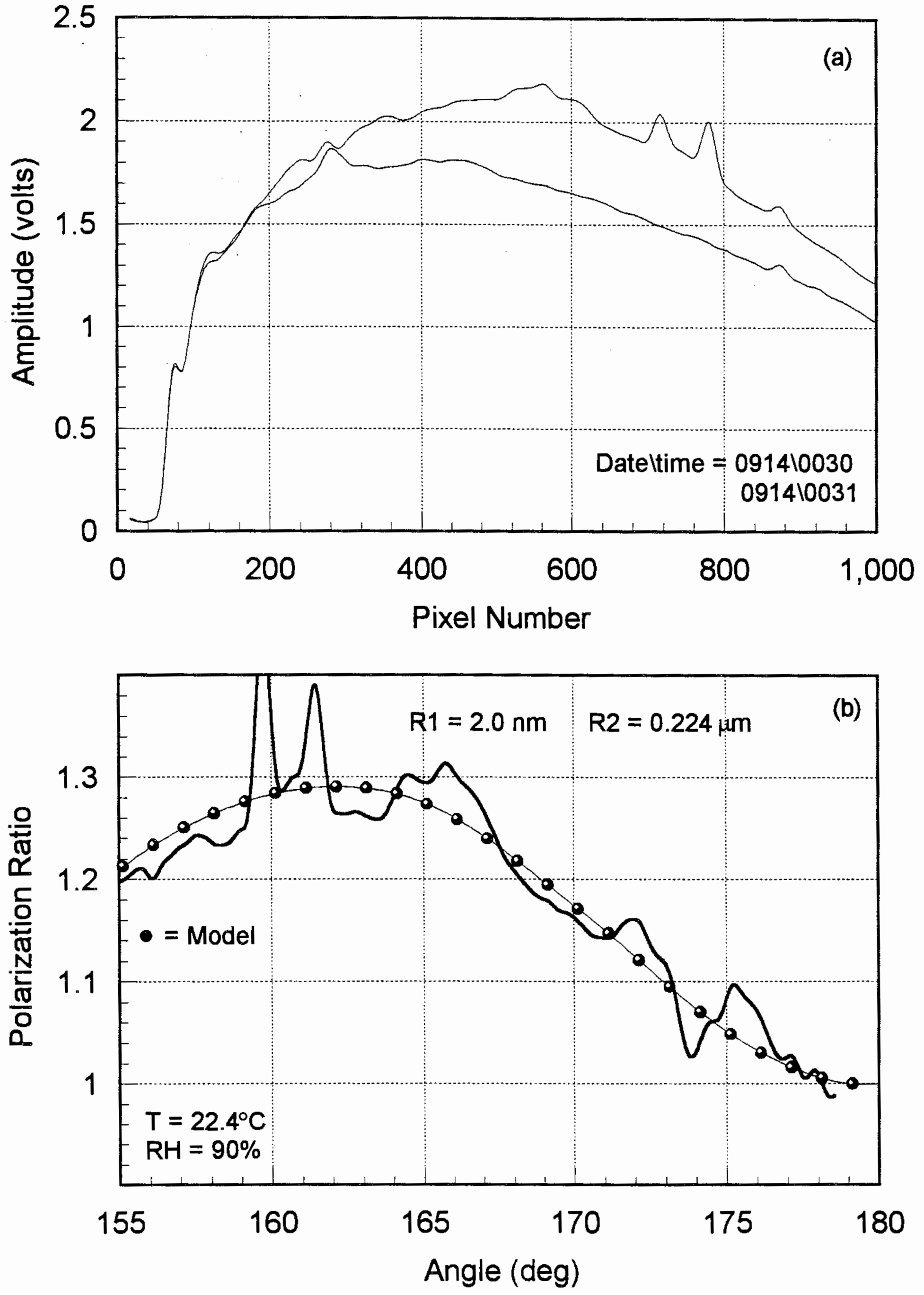

Figure 5.15. (a) Another example of bistatic lidar data as the aerosols grow on the humid night of September 14. (b) Ratio of the two components from (a) plotted with the best first order fit of the model.

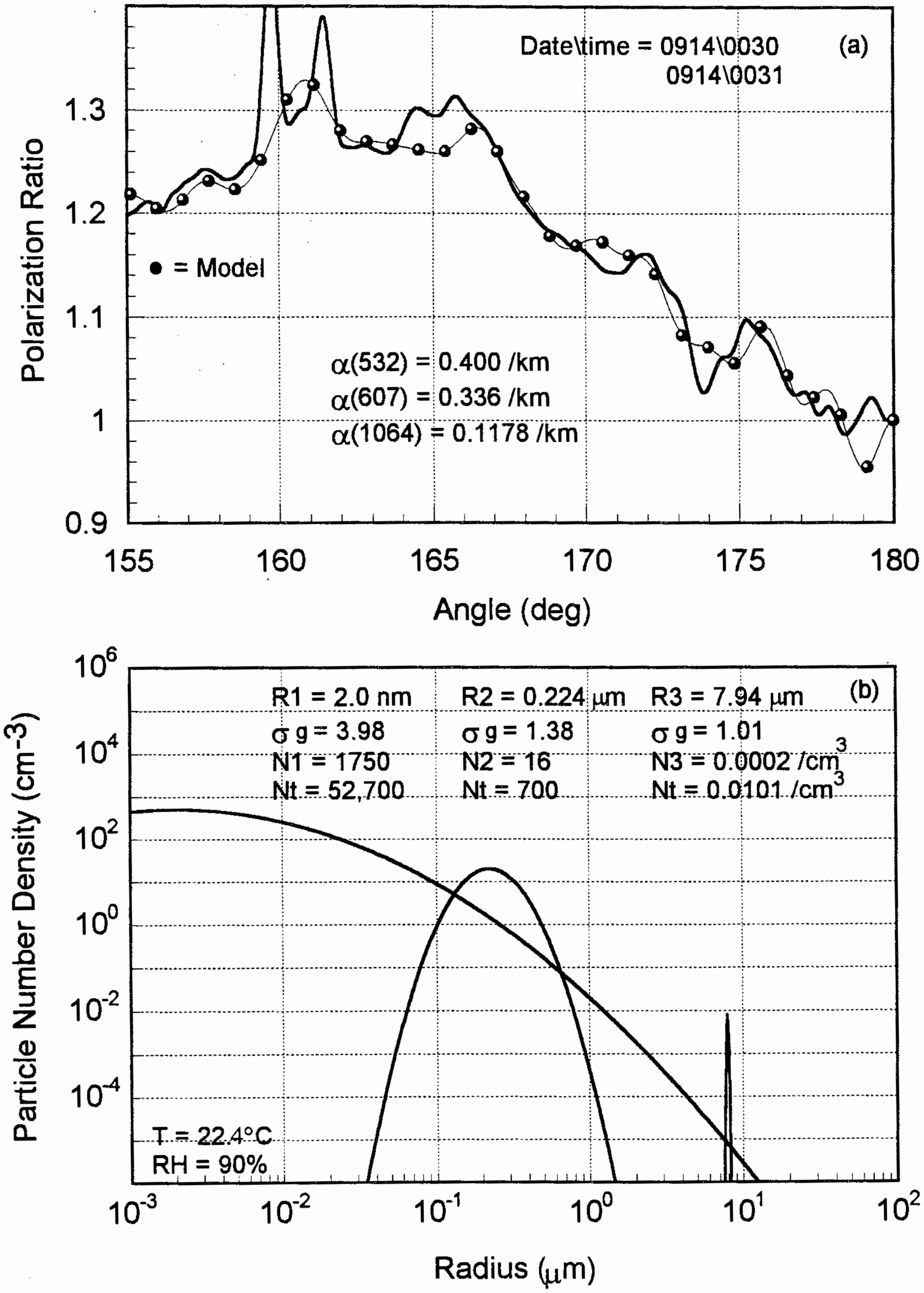

Figure 5.16. (a) A Plot of the best trimodal fit of the model with the bistatic lidar data. Here the radiation fog has grown to a radius of 7.94 μm. (b) Lognormal distribution for the model in (a).

with the total number density listed at the bottom.

The final and probably most convincing example of this measurement technique is shown in Figure 5.17, and corresponds with point three in Figure 5.1. The temperature decreased while the extinction increased one last time before the wind brought a new air mass and different scatterers into the area. From Figure 5.17a it can be seen that the extinction has increased to the point that the target board can no longer be distinguished from the rest of the received signal. The best first order fit was found by slightly increasing the first two median radii is shown in Figure 5.17b. The fact that the first order fit is not as good as in previous examples, is an indication that the third mode is starting to dominate the scattering. This time only an increase in the median radii from 2 to 2.5 nm and 0.224 to 0.237 μm, was necessary to achieve a first order fit to the data. However, the addition of a third mode with a radius that grew from 7.94 to 8.91 μm, produces a remarkable representation of the data. This data set is most striking because the model follows almost every bump and wiggle in the data between 155° and 175° as seen in Figure 5.18a. Not only does the model fit the data almost perfectly after increasing only the median radii, but the calculated extinction coefficients are also the same as those measured by the Raman lidar. This case works as well as it does because the third mode is now uniformly distributed throughout the horizontal path. But, from the previous examples it was shown that the third mode did not necessarily have to be uniformly distributed in order to determine the most likely distribution of particles. Figure 5.18b shows the lognormal particle distribution that best describes the bistatic lidar data from Figure 5.17 along with the extinction coefficients. The extinction coefficient of α_{532}=0.4984 km^{-1}, represents a horizontal transmission to the target board of only 19.5%. This corresponds to a visual range of only 7.8 km at 532 nm, whereas the visual range on September 19 from Figure 5.7b was 79.6 km at 532 nm.

Before the wind came, the third mode grew to 10 μm while the other two modes remained the same size. Figure 5.19 summarizes the growth of the three modes throughout the evening. Between 1:30 and 2:00 am a new air mass entered the

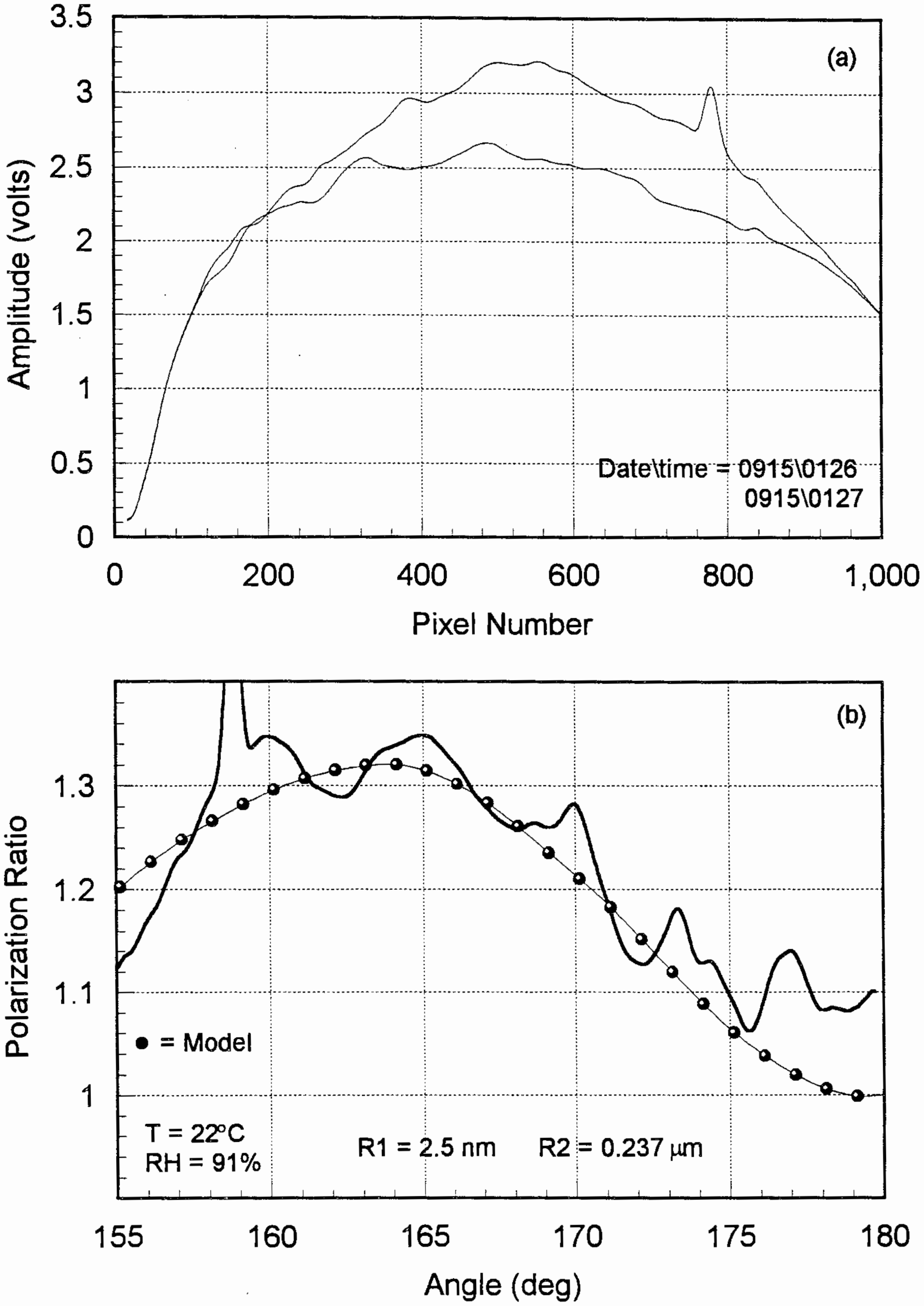

Figure 5.17. A final example of the growth of the modes before a different air mass is brought in by the wind. (b) The ratio of the two components in (a) with the best first order fit to the model.

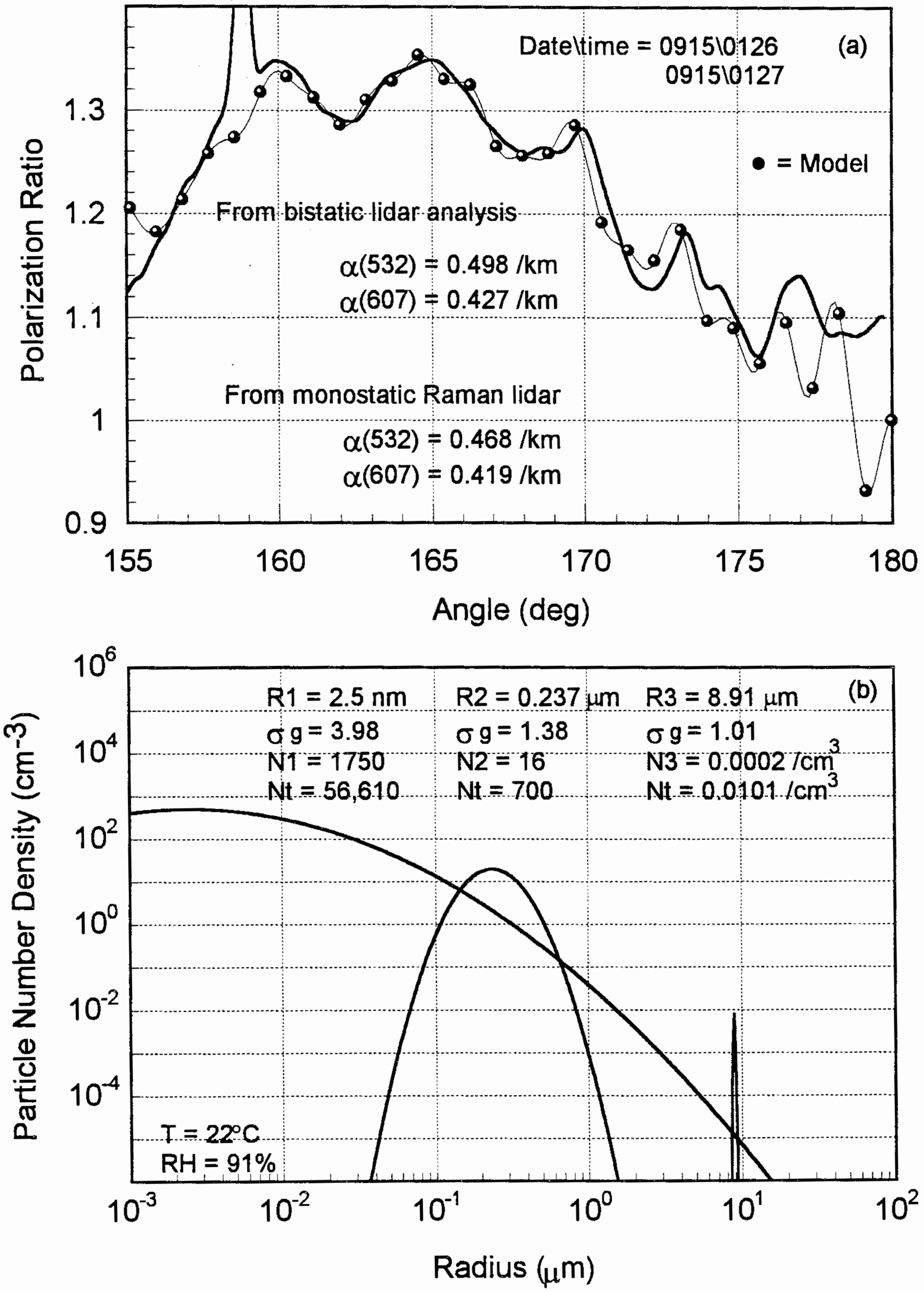

Figure 5.18. (a) A final and most convincing example of this measurement technique, showing the addition of a third mode to accurately model the data. (b) The distribution parameters for the model in (a).

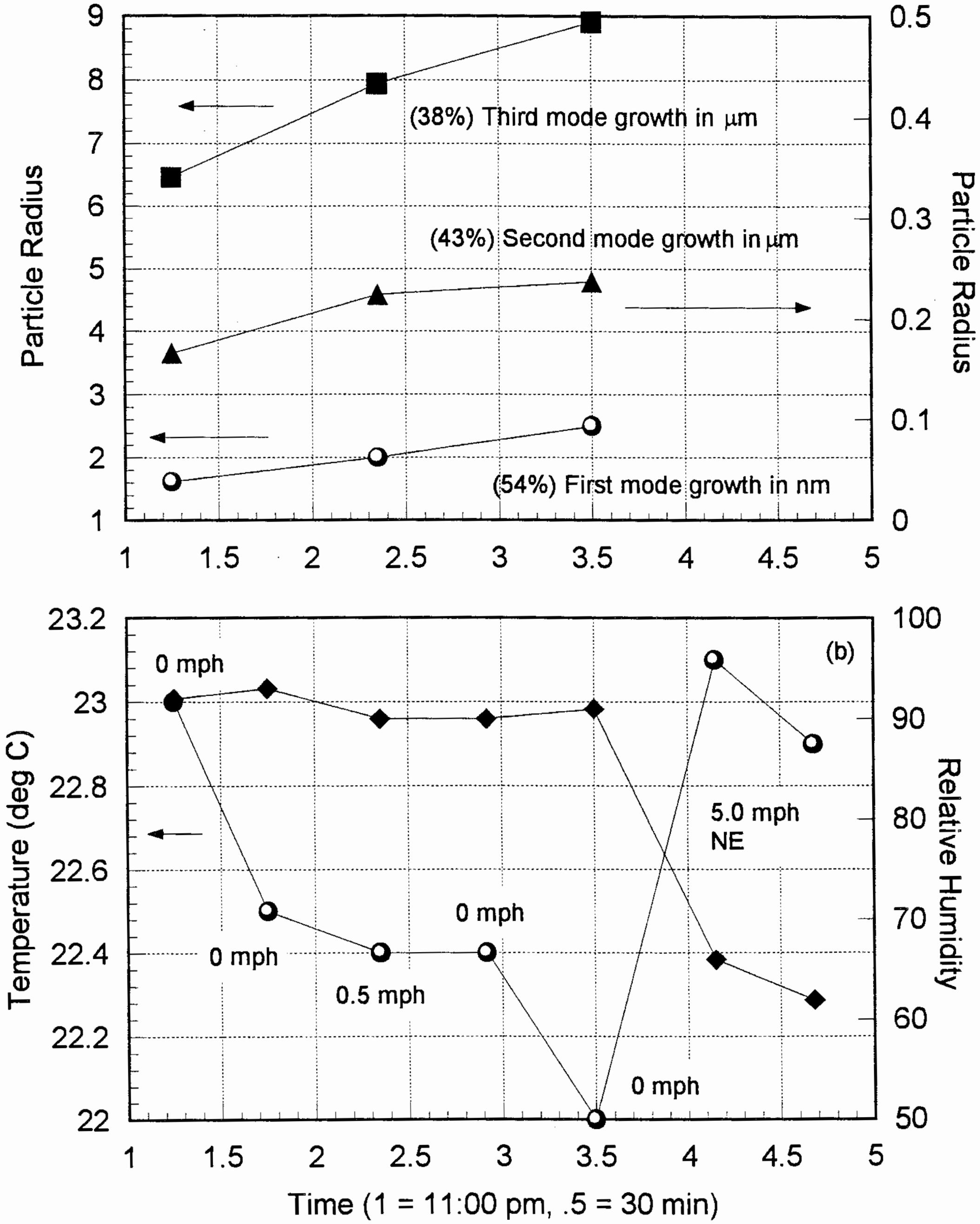

Figure 5.19. A summary of the growth of the particles through the night, with the temperature and humidity plotted for reference.

measurement area and the conditions changed from cold and humid to warm and dry. Figure 5.20 is an example of the data after the atmosphere cleared up. From the amplitude of the signal at the target board in Figure 5.20a it can be seen that the extinction decreased to levels typical of a clear night. It is believed that the aerosols that contributed the scattering for these data were not spheres. After days of trial and error, no combination of modes could be found to fit this data. The wind came from the north-east, so it is plausible that this new group of dry aerosols (RH=62%), that came from inland, could consist of non-spherical particles. In fact, it is more likely that they are non-spherical than spherical in shape. Most of the difficulty in trying to fit the model to the data in Figure 5.20 was in the angle range of 170° and 180°. According to Bohren and Singham (1991), the scattering of electromagnetic radiation is most sensitive to the particle shape near the backward direction. However, It is easy to concede and assume that the data will not fit the model because the scatterers were non-spherical, indeed particles in general are not spheres. But given the success of the model in describing the data on every other night, both clear and hazy, maybe other possible explanations should be considered. The model was run with one other refractive index of 1.52, but attempts to model any of the data collected at Wallops Island with this index of refraction were not successful. Maybe the refractive index of these particles was smaller that 1.38, or maybe there were two or three modes each with significantly different indices of refraction. These ideas will be address further in Chapter 7.

5.2.3 Discussion

One of the benefits of describing aerosols with lognormal distribution functions is the relationship between the geometric standard deviation of the aerosol mode and the specific aerosol type and/or origin. Often a geometric standard deviation in combination with a particle median radius can help one to identify a specific particle (ie. fine Al particles, Buhrman and Granqvist, 1978). The same association could be applied to tropospheric aerosols given enough collected data from a single measurement technique.

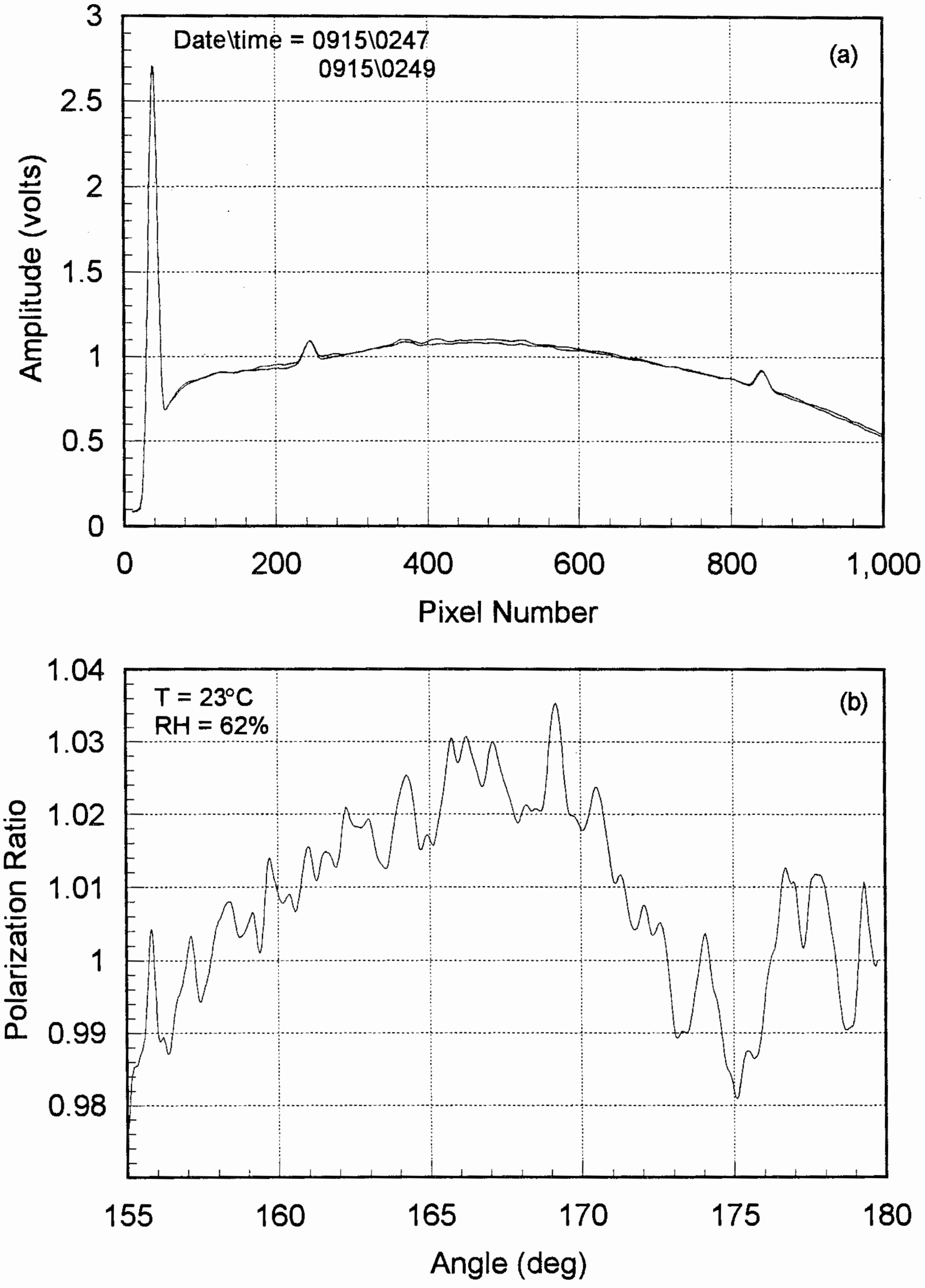

Figure 5.20. (a) Bistatic lidar data right after the dry air mass blew in on September 14. (b) The ratio of the components in (a) that could not be fit to the bistatic lidar model, possibly due to non-spherical particles.

Size distributions of atmospheric aerosols have been measured and compared to lognormal distribution functions over sites in continental and marine regions by many groups. The three different aerosol distributions presented in sections 5.2.1 and 5.2.2 are compared with in-situ particle measurements from Tanaka et al. (1983), Fitch and Cress (1983), Patterson and Gillette (1977), Whitby (1977), Buhrman and Granqvist (1976), Hobbs (1993), Kim et al. (1988), and Jaenicke (1988).

Table 5.1. Summary of the retrieved lognormal parameters for September 14, 1995.

Lognormal function parameters	Mode #1	Mode #2	Mode #3
Median radius (R_i)	1.62 - 2.5 nm	0.166 - 0.237 μm	6.46 - 8.91 μm
Geometric standard deviation (σ_g)	3.98	1.66 - 1.38	1.01
Number density weighting (n_i)	1750 cm^{-3}	16.2 cm^{-3}	0.00035 cm^{-3}

Table 5.1 lists the lognormal parameters retrieved from the bistatic lidar data for the night of September 14, 1995. The median radius of the first aerosol mode in Table 5.1 is consistent with the Aitken or nucleation particle mode ($0.001 < R_i < 0.1$ μm) shown in Table 1.1 for maritime aerosols (see also Table 4.3). The first maritime aerosol mode originates from the background aerosol and has an average median radius of 3.9 nm and an average geometric standard deviation of 4.54 (Jaenicke, 1988; Hobbs, 1993). The values of $\sigma_g = 3.98$ and $R_1 = 1.62$-2.5 nm obtained from the bistatic lidar are certainly in the range of the nucleation particle mode aerosol reported by Jaenicke and Hobbs. Buhrman and Granqvist (1976) measured ultra fine metal particles and found them to fit a lognormal particle distribution with a median radius of 4.1 nm and a geometric standard deviation of $\sigma_g = 1.55$. This particle distribution is similar to the first mode median radius with the second mode geometric standard deviation. Many types of distributions of particles including, fine metal particles (Buhrman and Granqvist, 1976), soil-derived particles (Epstein, 1947), and atmospheric particles (Fitch and Cress, 1983; Whitby, 1978), can be described by one, two or three lognormal distribution functions.

The second mode listed in Table 5.1 is also consistent with the definition of the maritime aerosol derived from sea salt (Hobbs, 1993; Jaenicke, 1988), although this mode can be explained with a soil derived aerosol (Patterson and Gillette, 1977). The median radius of 0.133 μm listed in Table 4.3 is smaller than the radius of 0.166 μm measured with the bistatic lidar, possibly due to the growth of the particles during the humid night of September 14, 1995. The geometric standard deviation (σ_g=1.66) measured by the bistatic lidar at the beginning of the night is very close to the value of σ_g=1.62 given by Hobbs (1993) in Table 4.3. Patterson and Gillette (1977) measured aerosol size distributions in Colorado at the National Center for Atmospheric Research (NCAR) using a variety of in-situ measurement techniques. Under light aerosol loading they report a geometric standard deviation of σ_g=1.56 for a median radius of 0.14 μm, similar to the second mode measured with the bistatic lidar at Wallops Island. Fitch and Cress (1983) measured particle size distributions within the lower troposphere in western Europe from an airplane. They were able to fit their data to a trimodal lognormal distribution function and called the three modes: the accumulation mode, the middle mode, and the coarse particle mode. Their values for the accumulation mode of σ_g=1.28, and R=0.25-0.47 μm are similar to the second aerosol mode in Table 5.1. The coarse particle mode they report is of the same median radius as the third mode in Table 5.1 but the geometric standard deviation of σ_g=1.59 is much too large to describe the third aerosol mode measured at Wallops Island on September 14, 1995. Kim et al. (1988) measured tropospheric aerosols above 1450 m from an airplane using a Particle Measuring Systems, Inc., probe during four seasonal periods over the central United States. They divide their results into two modes, course and fine. Their results from the fine particle mode for spring at an altitude of 1450 m (σ_g=1.70, R=0.24 μm) agree with the second mode measured with the bistatic lidar shown in Table 5.1. One last comparison will be presented from a group that used a polar nephelometer to measure the same two polarization components that were measured with the bistatic lidar in this thesis. Tanaka et al. (1983) measured the angular distributions of the intensity of light scattered by airborne particles for both parallel and perpendicular scattered components, and then fit a single lognormal distribution function to the data using an inversion library method to determine the complex index of refraction. They report a median radius of 0.138 μm and a geometric standard deviation of σ_g=2.56. The median radius would correspond to an accumulation mode aerosol or to the second aerosol mode in Table 5.1. However, their geometric standard deviation is too large for the accumulation mode aerosol. They could be in error with this value because of fitting a possible two or three mode aerosol distribution to only one mode. The work from Tanaka et al. (1983) is of particular interest for this thesis because he measured the same two electric field components and used a model to fit an aerosol distribution and particle index of refraction to his data. It was mentioned earlier in this thesis that the complex index of refraction could be used as two more parameters when fitting the data to the model. Tanaka et al. simplified the problem from 11 variables to 5 variables by assuming a unimodal particle distribution.

5.3 Cross Polarization and Multiple Scattering

By applying Mie theory to the data sets in the previous section, it was implied that multiple scattering was negligible. Two tests were mentioned in Chapter 4, a cross polarization test, and an optical depth limit for multiple scattering. The largest optical depth of 0.174 was encountered at 1:30 am at the peak of the extinction. From Chapter 4 it can be seen that this value is in the middle of the grey area (0.1 to 0.3) for the beginning of significant multiple scattering. The next test is to look at the results of the cross polarization measurements. When the laser's polarization was oriented vertically, the receiver's polarizer would be rotated to transmit horizontal polarization only, and visa versa. Figure 5.21a shows the results for the cross polarized test with the laser's electric field polarized parallel to the scattering plane (1), and with the laser's electric field polarized perpendicular to the scattering plane (2). The voltages of both curves in Figure 5.21a are nearly two orders of magnitude smaller than the voltages of the curves earlier

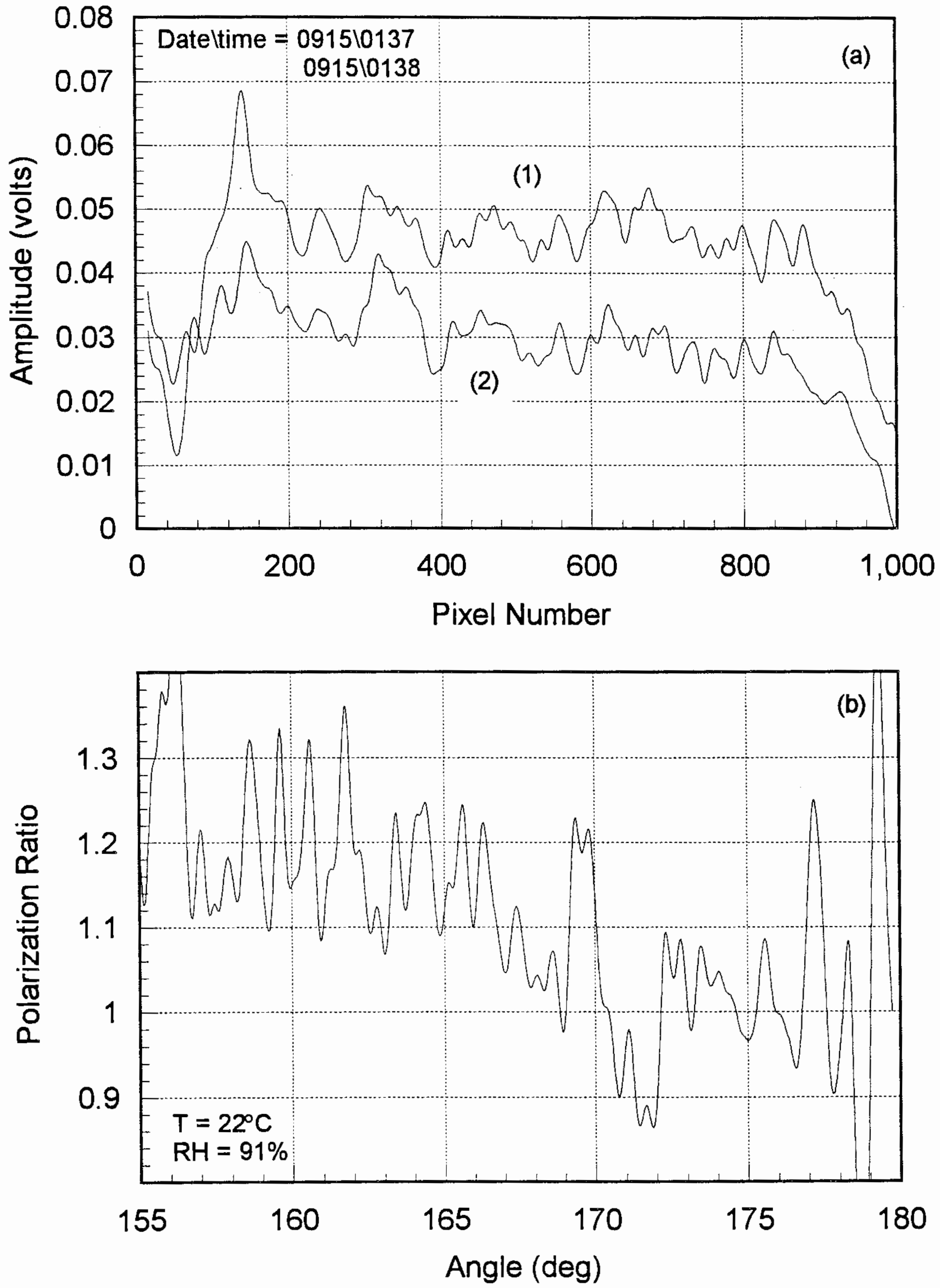

Figure 5.21. (a) Results from the cross polarizer tests for the last point in Figure 5.1 on the night of September 14. (b) A very noisy ratio similar to others during the evening can be seen from a small amount of signal not being blocked by the polarizer.

in the evening (e.g. Figure 5.17). Because of the small voltages in Figure 5.21a neither case shows any signs of scattered radiation due to multiple scattering or non-spherical particles. This however, does not mean that there are no non-spherical particles or that there is no multiple scattering. It just says that any contribution to the scattered intensity from multiple scattering or non-spherical particles is undetectable after being attenuated by the linear polarizer. This is an important distinction, because there are indeed cross polarized components scattered to the receiver, if only due to the anisotropy of the molecules or from vibrational and rotational Raman scattered radiation. It is probably safe to assume that if the cross polarized terms are too weak to be detected by the receiver, they are probably too weak to cause considerable difficulties for the spherical model.

One last point should be mentioned about testing for multiple scattering, and predicting extinction coefficients at wavelengths other than the one used for the data collection. The effects of multiple scattering may not be significant at 532 nm, but at shorter wavelengths, multiple scattering could become a factor causing the extinction coefficients calculated by the model to be useless. For example, the extinction calculated for 266 nm was 0.7842 km^{-1} while the extinction for 532 nm was 0.4984 km^{-1}, for the last data set on September 14, 1995. Here multiple scattering is probably not a problem for the 532 nm wavelength, but for 266 nm multiple scattering is most surely a significant factor causing a smaller extinction than would be calculated using the Beer-Lambert law. This is an example where given a perfectly retrieved particle size distribution, the extinction still cannot be predicted for the shorter wavelengths, unless a known correction can be applied.

Chapter 6

BISTATIC LIDAR ERROR ANALYSIS AND INVERSION TECHNIQUE

The preceding chapter presented bistatic lidar examples from several nights with varying atmospheric conditions. In all but one case, a spherical scattering model could be made to fit the data by carefully adjusting nine parameters of a trimodal lognormal distribution of scatterers. This should not be interpreted to suggest that all the data collected could be modeled as spheres or with a trimodal lognormal distribution, indeed one case was shown where the model could not be made to fit the data. The data collected from the bistatic lidar has been approached with the attitude, "guilty until proven innocent" as far as particle non-sphericity is concerned. However, once a few data sets have been shown to fit the model, questions arose as to why the model and data matched so well in certain cases. Were all the particles actually spheres?

This chapter will focus on the different errors involved in the collection and modeling of the bistatic lidar data. The errors will be divide into three categories, modeling errors, measurement errors, and instrument errors. First, the errors that can occur from an improper model will be presented. Non-spherical particles probably cause the greatest error between the model and the data. Second, measurement errors associated with this type of experiment, like a non-uniform path or sampling interval will also be presented. Error bars will be plotted on two of the plots from Chapter 5, and a discussion will follow describing how these error bars were calculated. The error in determining each of the nine parameters will be presented, along with the propagation of that error into the prediction of extinction at different wavelengths. And finally automated data inversion and the Newton-Raphson method will be discussed.

6.1 Modeling Errors

One of the largest reason for discrepancies between the bistatic lidar data and the model is probably due to incorrect modeling of the scatterers. Even when the model seems to almost perfectly describe the data, the differences between the model and data are barely within two standard deviations of the measured data, as will be shown in Section 6.3. These errors are difficult if not impossible to quantify. Much work has been done on the modeling of particles with shapes other than spherical (Koepke and Hess, 1988). The differences between the scattering phase function of spheres and prolate spheroids has been calculated and shown to be small in the forward scattering region and large in the backscattering region (Bohren and Singham, 1991). However, tropospheric aerosols can be described no better by a prolate spheroid model than by a spherical model. If the prolate spheroids are broken and not perfect prolate spheroids, which model would best describe them, a spherical or a prolate spheroid model? An excellent paper on this subject is titled, "Scattering functions of tropospheric aerosols: the effects of non-spherical particles", by Peter Koepke and Michael Hess. In this paper they quote their goal as, "to determine the influence of non-spherical particles on the scattering phase function (i.e., the scattered intensity as a function of angle) of tropospheric aerosols, which are always a mixture of particles of different sizes". They measured and calculated scattering phase functions for a wide range of particles from, NaCl crystals for maritime aerosols, to desert dust storm aerosols, to continental and urban aerosols. Their conclusions are as follows. The non-spherical influence of the NaCl crystals rapidly decreases as the particles grow with increasing relative humidity. Therefore the particle shape becomes similar to spheres with the result that the scattering phase function is correctly modeled with Mie theory, as was also found from direct measurement (Shettle et al., 1984) and (this thesis, 1996). For aerosols with a great amount of large particles the effect of non-sphericity on the scattering phase function becomes significant. However, "For aerosol types with a low number of large particles, the uncertainty due to the particle shape is of the same order of magnitude as that caused by the other uncertain microphysical parameters." (Koepke and Hess, 1988).

Therefore they conclude that the scattering phase functions of continental and urban aerosols can be satisfactorily modeled with Mie theory. This does not suggest that the particles are spheres, just that a spherical model is probably the best overall method to describe the scatterers. They go on to conclude that the different sizes and not the random orientation of the particles is why in many cases it is sufficient to model the scattering with Mie theory. The aerosol whose non-sphericity was found to clearly have an effect on the scattering phase function was desert dust storm aerosol near its source and up to 2000 km away (Koepke and Hess, 1988). This could help to explain the success of the bistatic lidar model when describing the data collected during the CASE I program at Wallops Island. The real question is, how good is the modeled trimodal lognormal distribution of spheres at predicting the extinction at other wavelengths? This question cannot be answered with the data in this thesis, additional experiments will need to be conducted. However, the best possible error for the predicted extinction from each parameter independently can be calculated from the known error of the measurement, and is presented in Section 6.3.

The other significant modeling error is that due to an incorrect estimation of the particles complex index of refraction. Figure 5.20b shows an example of data that cannot be modeled with spherical scatterers and an index of refraction of 1.38. It is impossible to determine whether the model will not fit due to non-spherical particles or to an incorrect index of refraction until the data is described by changing one or the other, or maybe both. This could be checked by running the model at various refractive indices and again looking for the best fit. One other index of refraction, 1.53 + i 0.005, was used in the model to determine if a better fit could be found. The polarization ratio curves generated from this index of refraction could not be found to match any of the data. In fact, they were drastically different, adding confidence to the choice of 1.38 for the refractive index.

It is known that the refractive index of the aerosol is dependent on the relative humidity (Richter and Huges, 1991). In other words, the refractive index will change as the particle grows from condensation on a humid night. The results in Chapter 5 showed particles growing from condensation of water vapor onto their surfaces as the temperature decreased. When the measurement period started the radiation fog layer had already formed, therefore the index of refraction probably did not change too much during the small amount of growth for the particles. An even larger error should result from the choice of the same index of refraction for all three modes, separated by more than three orders of magnitude. Time and computer power limited this research to only two different refractive indices and to the use of one refractive index for all three aerosol modes. The errors from an improper choice of refractive index could be calculated by simulating data at one refractive index, and finding the best fit with a model calculated using a slightly different refractive index. This should be done for the data in Figure 5.18, because in this case the spherical model appears to describe the data exceptionally well. Finally, the question can arise, if the index of refraction is changed, can the model still be made to fit just by changing the distribution of the aerosols? If this is the case, then varying the index of refraction along with the nine distribution parameters when inverting the data would not be advisable, because many multiple solutions would exist. It is more likely that the sharp features in the modeled profile would move with respect to angle as the index of refraction changes, therefore changing the goodness of the fit. The modeling errors in the Section 6.3 will be more quantitative, and in doing so will have to assume that the errors discussed in this section are negligible.

6.2 Measurement Errors

The second type of error that contaminates the bistatic lidar data is error involved in the actual experiment or measurement. There are two errors in this category; error due to the non-uniformity of the horizontal path, and error due to the time difference between the measurement of the two polarization components. Figure 6.1 shows the plot from Figure 5.14 with error bars on the data to illustrate this point. The error bars represent plus and minus one standard deviation in the data, and will be explained in Section 6.3. The model matches the data very well but not always within the error bars of the instrument, therefore the difference between the two must be due either to modeling errors or measurement errors. At several angles, 170°, 167°, and 163°, the model shows the proper structure but not quite at the correct angle. I would argue that this is due to a small index of refraction error described in Section 6.1. However, these errors do not diminish the confidence of the modeled size of the scatters, the fact that the features are present, if only slightly shifted, is reason to believe that the model is useful. The discrepancies that are cause for concern are at angles of, 156°,158°, and 177°. Here the most probable explanation for the error is that the horizontal path was not uniform during the measurement. For small path lengths the horizontal path would most definitely be uniform, but for larger path lengths it would be expected that variations would be present. The measurement area for the angles between 155° and 175° was over a salt marsh between the mainland and Wallops Island. However, the measurement area for the angles between 175° and 180° covered a distance from 175 m to 3.28 km from the receiver. Errors would be expected in that angle range on calm, hazy nights, but on a clear, breezy night a constant distribution of particles should be moving through the entire path length. This was shown with the clear night results in Chapter 5, with a good fit to the data all the way to 180° or 3.280 km.

The disagreements between the data and model between 155° and 160° in Figure 6.1 cannot be explained as easily. This is the beginning of the horizontal path between 30 and 40 meters in front of the laser source. An explanation for these errors is possibly due

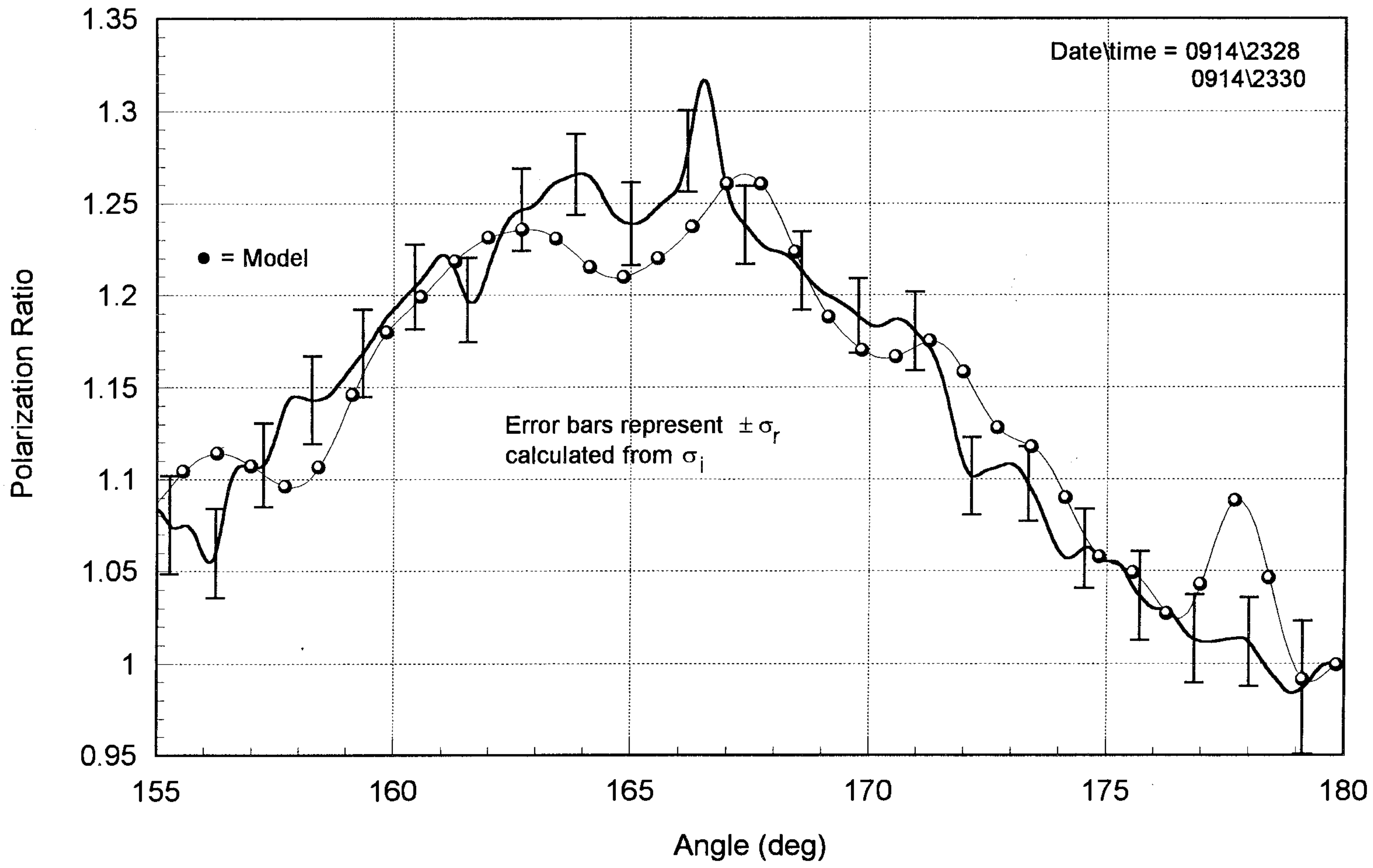

Figure 6.1. A plot of data from Chapter 5 now with error bars showing plus and minus one standard deviation in the instrument error. This data set is used as an example to demonstrate errors due to modeling and errors due to a non-uniform horizontal path.

to a time difference between the collection of the two polarization components. Each ratio consists of two independent measurements taken one minute apart, explaining why sometimes a spike will appear in one component and not the other. The particle distribution from this evening was shown to include a very small number of scatterers in a third mode, only between 6 and 9 particles per scattering volume. Isolated differences between the data and model could be explained by fluctuations over time in the observed number density and size of small distributions of particles. The best way to prove whether this is a correct assumption is to fit different sections of the curve at a time. This is exactly what was done for most of the inversions, the region between 175° and 180° was ignored, and the model was fit between 155° and 175°. In these isolated regions where the model and data do not match, the model's parameters could be changed slightly to determine if a few less particles or a different particle radius were present.

6.3 Bistatic Receiver Error Analysis

The errors discussed in the previous sections were all non-instrument related errors making them difficult to quantify. This section will determine the propagation of errors through the calculations of the desired lognormal parameters and to the predicted extinction derived from instrumentational uncertainties. Even though errors are not always linear and easily added, it is still useful to determine the errors from each part of the experiment separately. In this section the model will be assumed perfect and only the errors contributed by the instrument will be considered. This analysis will lead to valuable information about the reliability of any method that attempts to determine extinction at any wavelength based on an inverted particle size distribution. First, the error of each measurement is calculated by a computer model using hours of background measurements and actual data from the bistatic receiver. Then this error is compared to the error between the data and the model, fixing a maximum allowable error for each parameter defined by the instrument. This error is then calculated as it propagates through to each of three chosen extinction coefficients. Conclusions can then be drawn about the influence of each of the nine trimodal lognormal parameters on the extinction at a range of wavelengths. Using a faster computer, the same error analysis could also be conducted for the propagation of errors due to different indices of refraction. Essentially, the following section will quantify how well each parameter can be determined given a particular instrument error, and in turn, determine how much the extinction effected by the uncertainty of a particular parameter.

6.3.1 Instrumentation Errors

The error of the instrument will be defined as the standard deviation of the output from one measurement to the next, when the input remains constant, on a pixel per pixel basis. One hundred background measurements over a period of two hours, taken with the shutter closed, were used as the constant input for the calculation of the standard deviation. Because it is important that the DC level of the signal remains constant over this period, the background signals were collected while the temperature did not change. This method of calculating the instrument error reveals the standard deviation for each individual pixel, called σ_i. Figure 6.2 shows a plot of the standard deviation versus pixel number calculated from background data collected on September 18, 1995. It can be seen below pixel number 200, that the standard deviation is not constant with pixel number. Fortunately, these pixels, with the higher associated standard deviation, collect scattered radiation at angles above 179° near the target board, a region already full of errors due to the long horizontal path length. The average value of these standard deviations was calculated to be 0.0184 volts across the array, and are used in all the following calculations. Since the standard deviation is a voltage, this means that there is an error of $\pm\sigma_i = 0.0184$ volts when interpreting the results of each independent polarization measurement. This error is not the error associated with the ratio of the polarization measurement shown in most of the figures. This error σ_r, is dependent on the magnitude of the signals being divided and is much more difficult to calculate.

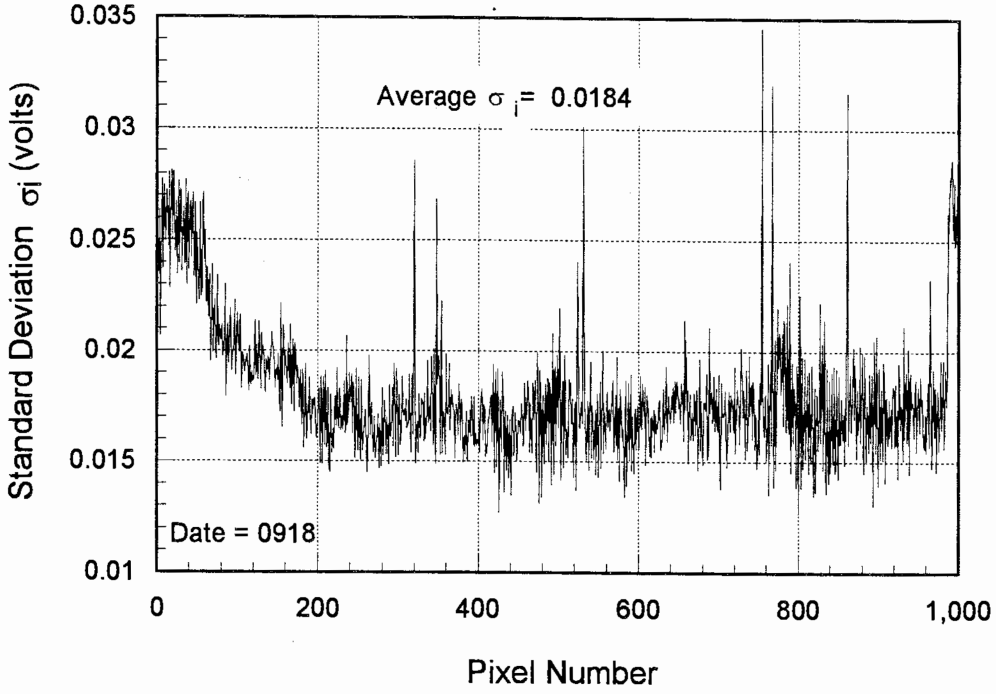

Figure 6.2. A plot showing the standard deviation of the bistatic lidar versus pixel number. These values were calculated from 100 background samples with the shutter closed.

Because the two electrical field components being divided are not completely independent of each other (i.e., they are related by a complex scattering function), there is no simple formula to calculate the error of the ratio given the error of each measurement. The easiest way to determine the error of the ratio was to model it using a gaussian random number generator as follows. A typical error for each component was simulated using a gaussian random number with a standard deviation of the error in the instrument of $\sigma_i = 0.0184$. Different errors, each generated as above, were added to each pixel of each measured polarization component, and then the two resulting components with errors added were divided. This process was repeated 500 times to achieve an accurate sampling of real noise. The standard deviation σ_r, was then calculated for each pixel over the 500 arrays with the added simulated noise. Figure 6.3a shows the standard deviation versus pixel number for the ratio of the two components in Figure 5.13a. The error bars in Figure 6.1 were plotted using $\pm\sigma_r$ from Figure 6.3a. From Figure 6.3 it can

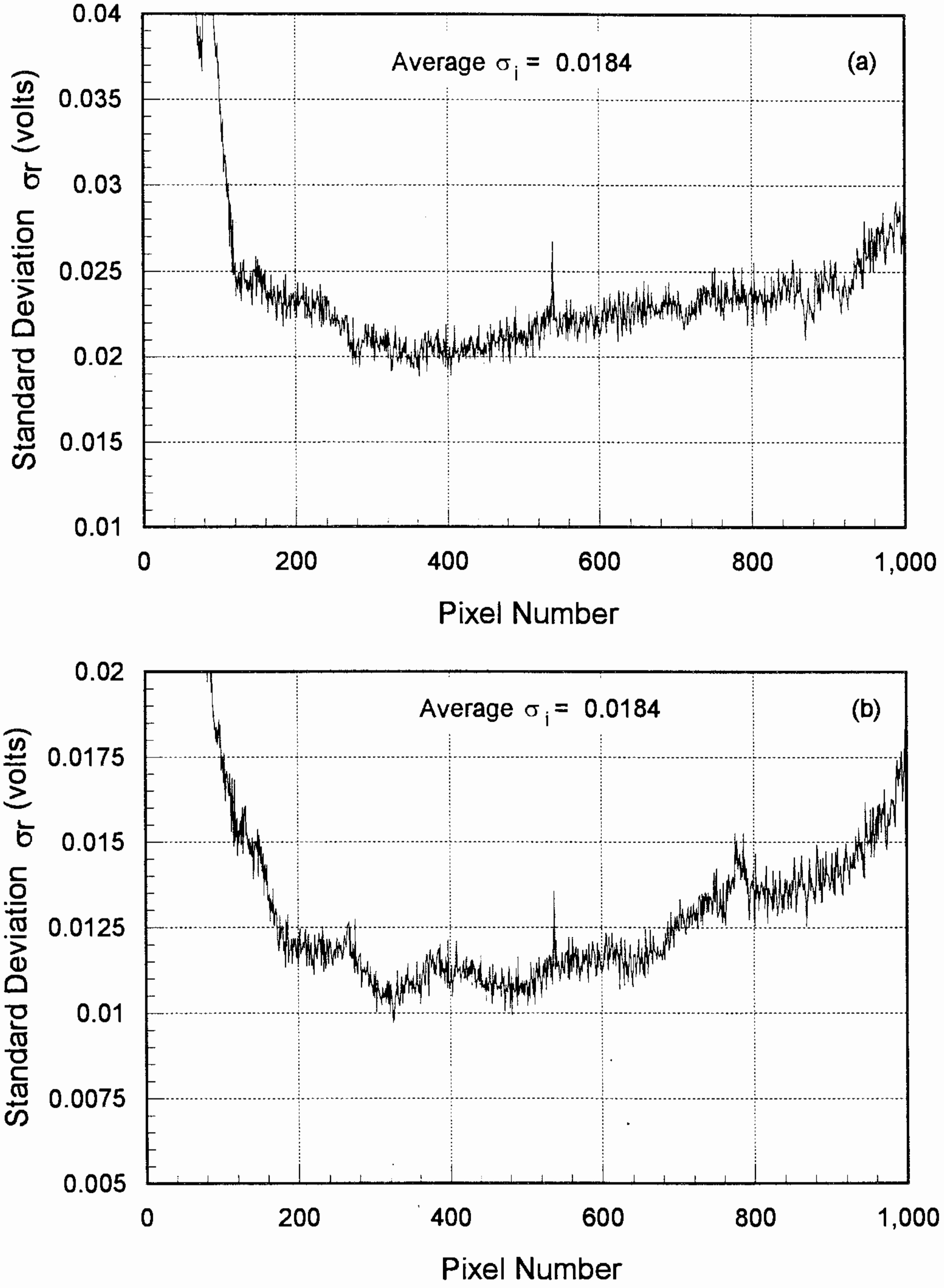

Figure 6.3. (a) A Plot of the standard deviation for the two measured components in Figure 5.13a. These values were used to plot ±σ error bars in Figure 6.1. (b) Same plot as in (a) but with the ratio of the components from Figure 5.17a. The resultant error for this data set is significantly less then in (a) because of the larger signals used for the ratio.

be seen that the standard deviation of the ratio σ_r, varies with pixel number. This is because the resultant error is dependent on both the amplitude of each measured component and the difference between the components. Figure 6.3b demonstrates this fact with the standard deviation calculated for the ratio of the two components in Figure 5.17a. Here the standard deviations are much smaller than those in Figure 6.3a because the signals were nearly two volts larger. In fact, in Figure 6.3b, the standard deviation of the ratio σ_r, is actually smaller than the standard deviation $\sigma_{i,}$ of the individual components.

The error of the instrument has now been quantified for two separate data sets, allowing further calculations of how this error can effect the inverted parameters. The following section demonstrates how this instrument error affects the error of the retrieved particle distribution parameters.

6.3.2 Error Propagation (Extinction Errors)

The propagation of errors through calculations in an inversion process is important because small instrument errors can lead to very large errors in the retrieved parameters, or visa versa. Cases will be shown where large errors in the determination of a size parameter have little effect on the calculated extinction, and where the smallest error in a size parameter can have a large effect on the extinction. The data set from Figure 5.17 is used for this analysis because it contained three modes and could be described almost perfectly by the model. Figure 6.7a shows the error σ_r for this data ratio calculated using $2\sigma_i$ from Figure 6.2 as the instrument error. The value of twice the instrument standard deviation was used to better illustrate the effects of error propagation through the inversion. The standard deviations σ_r, shown in Figure 6.4a are used to plot individual error bars of $\pm\sigma_r$ for each pixel in Figure 6.4b. The model describes the data so well in this case, that over most of the profile the model is within $\pm\sigma_r$ error bars of the data. For the following analysis, the differences between the data and the model along the profile will need to be compared to the errors associated with the data in order to quantify the error in determining each distribution parameter. The following equations describe

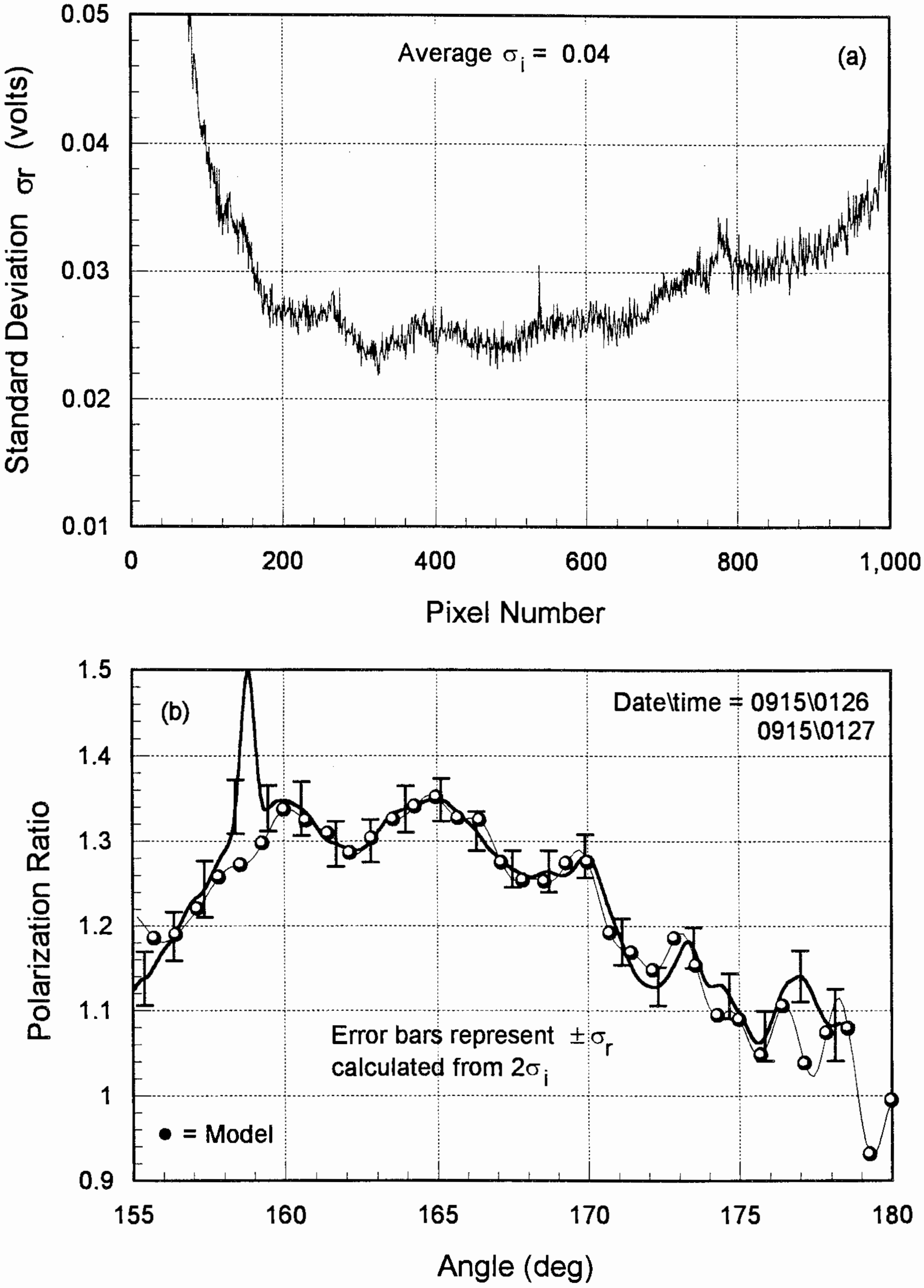

Figure 6.4. (a) The standard deviation σ_r calculated for the data from Figure 5.17 using the instrument standard deviation of $2\sigma_i$. (b) The ratio of the two electric field components from Figure 5.17 shown with $\pm\sigma_r$ error bars from (a).

how the total error along the profile for both the data error and the modeling error were calculated;

$$RMS(data\ error) = \sqrt{\frac{\sum_{i=1}^{N} \sigma_r^2}{N}}, \tag{6.1}$$

$$RMS(model\ error) = \sqrt{\frac{\sum_{i=1}^{N} (D-M)^2}{N}}, \tag{6.2}$$

where (D-M) is the difference between the data and the model for each angle element in the array, and N is the number of angle elements being fit to the data.

These two root mean square errors are calculated for the best fit of the model to the data in Figure 6.4b and are, RMS(data error) = 0.027, and RMS(model error) = 0.0165. The exercise is to now vary each of the nine parameters in the distribution above and below the best fit point, and record the new RMS(data error). Figures 6.5 through 6.7 a, b, and c show the results of the RMS error as each parameter was increased and decreased until the modeling error went well above the data error of 0.027. Figures 6.5a, b, and c show the radius, distribution width, and number density parameters respectively for the first mode. Figures 6.6, and 6.7a, b, and c present the same information for the second and third modes respectively. The dashed line represents the error in the data, and where it intersects with the model error curve defines the best possible error in determining the distribution parameters. Figure 6.5a shows vertical dotted lines drawn from the intersection of the model error and the data error down to the radius axis. Where these dotted lines intersect the radius axis defines the upper and lower limits of how well the particle radius for this mode can be determined. In this case the radius can be determined with an error of +8% or -12% to remain within the $\pm 2\sigma_i$ of instrument error. A smaller instrument error would decrease this 8-12% error considerably. The uncertainty for each

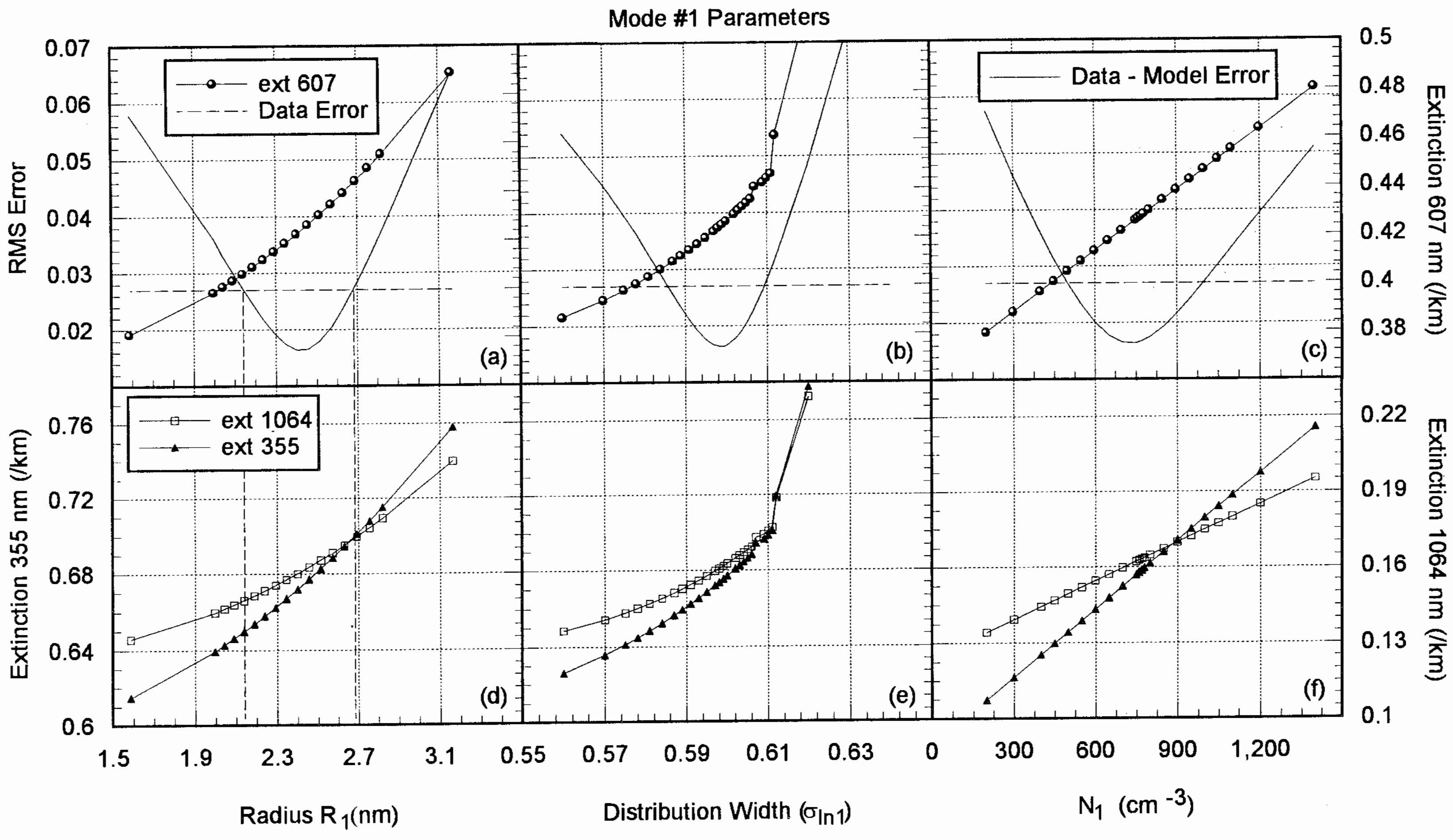

Figure 6.5. Figures a, b, and c show the goodness of the fit of the model to the data for each parameter in the first mode as the parameter is varied above and below the best fit value. The dashed line is the instrument error and where it intersects the model error curve is where the confidence of the retrieved parameter is defined. The extinction at 355, 607, and 1064 nm is also plotted to determine how the error propagates from the parameters to the extinction.

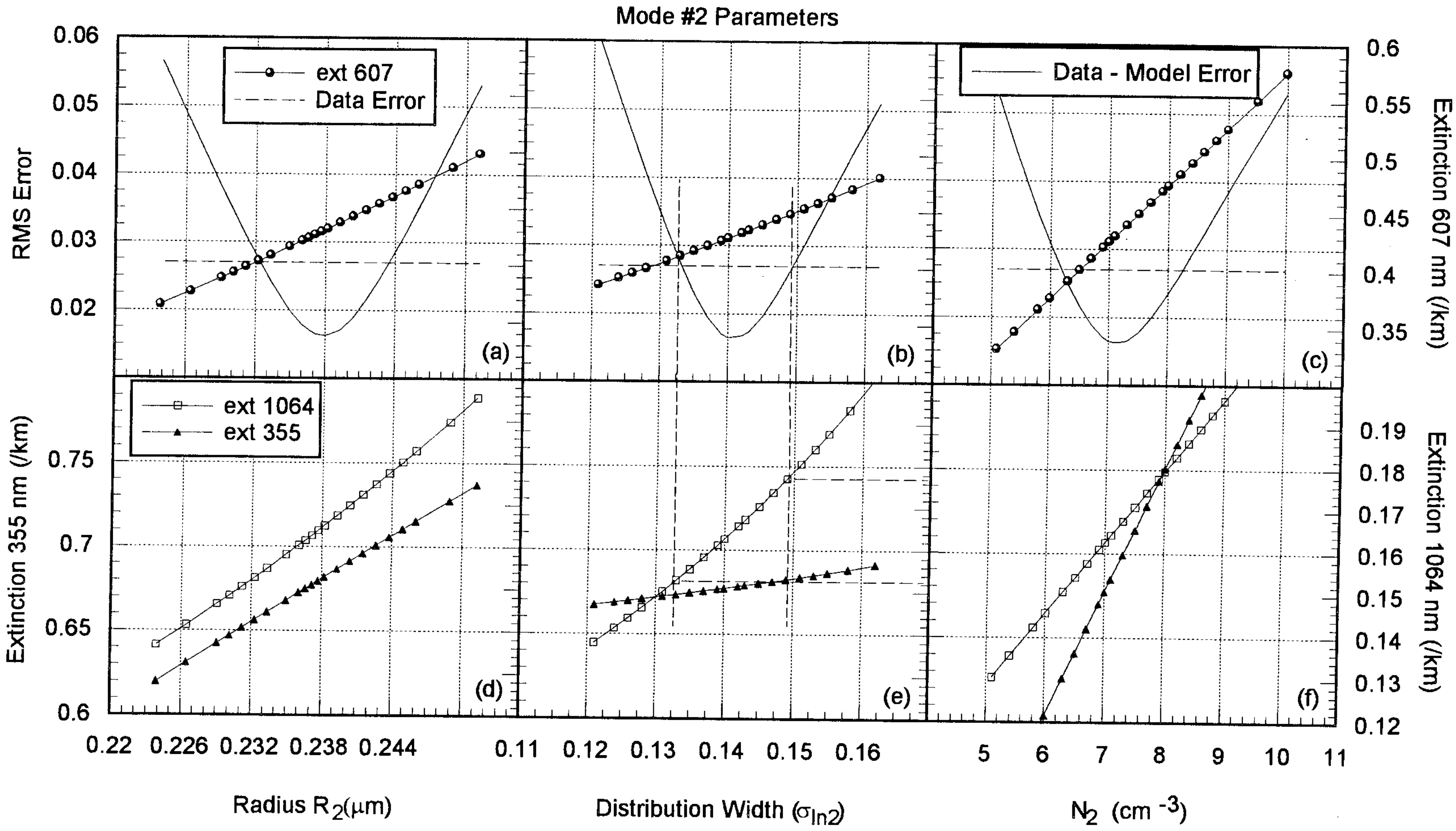

Figure 6.6. Figures a, b, and, c show the error between the model and the data as a function of each parameter for the second aerosol mode. The extinction is also plotted for 355, 607, and 1064 nm, to determine how the errors in the parameter retrieval affects the error in the calculated extinction.

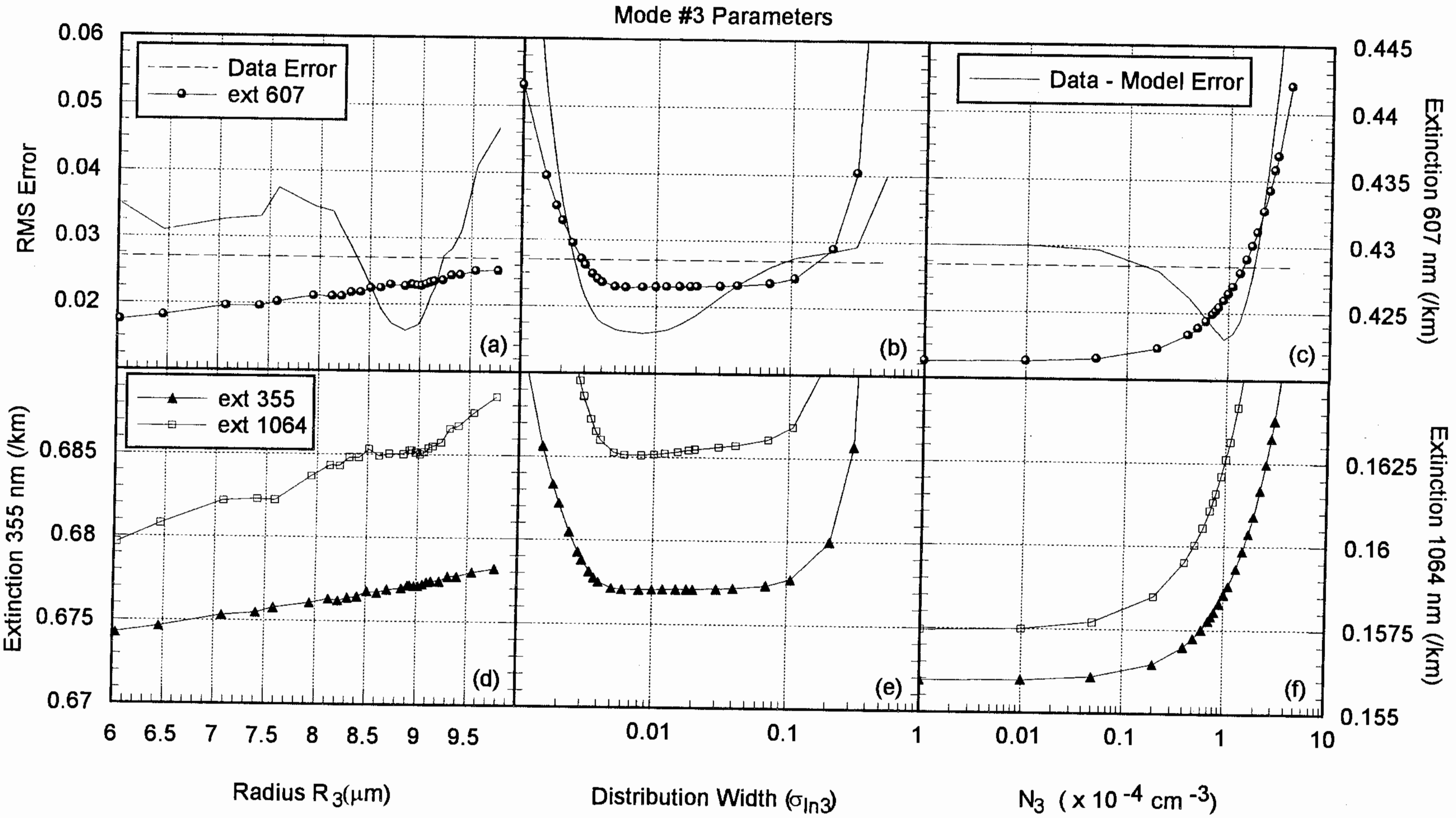

Figure 6.7. The same set of plots as in Figures 6.5 and 6.6 calculated for the third mode of the distribution. (a) shows that the model is very sensitive to changes in the radius, while large changes in the distribution width cause small changes in the model error. But this large error in determining the distribution width is shown to have little effect on the calculated extinction.

of the nine parameters was calculated with this method and is summarized in Table 6.1. From this table it can be seen that the errors are not symmetric about the best fit value. For the three parameters in the first two modes (Figures 6.5 to 6.6a, b, c) the model error resembles a hyperbolic function, tilted either to the left or the right. If this data error curve points directly upward, then the errors are symmetric about the best fit, however for most of the parameters the error is not symmetric. The width of this hyperbolic error function determines the sensitivity of the retrieved parameter to instrument error. If the model error plots a very tight and narrow hyperbolic curve, then changing the instrument error (i.e., moving the dashed line, at 0.270 RMS error, either up or down) will change the uncertainty of the desired parameter very little. However, if the model error resembles a very wide hyperbolic curve, like that in Figure 6.7b, then the instrument error can greatly affect the confidence of the retrieved parameter.

For the distribution width of mode 3, the error is highly unsymmetric going as high as 1700% until the model error goes above the instrument error. Figure 6.7b shows how this can happen, but a complete explanation requires a look at how the modeled profile changes with the distribution width. Figure 6.8a shows the data and the model with a distribution width of $\sigma_g=1.01$, and Figure 6.8b shows the data and the model with a distribution width of $\sigma_g=1.07$. As the distribution width becomes monodispersed more of the high frequency structure is visible as would be expected due to a lack of averaging over particle size. Because there are very few particles in this distribution, increasing the distribution width only washes out the higher frequency effects and smooths the curve.

Table 6.1. Percent errors shown for each parameter of each particle mode.

	Mode #1			**Mode #2**			**Mode #3**		
	Low	Best Fit	High	Low	Best Fit	High	Low	Best Fit	High
Radius	***12%***	2.45 nm	***8%***	***2.1%***	0.237μm	***2.5%***	***6.3%***	8.91μm	***3%***
σ_g	***2.3%***	3.98	***1.7%***	***6.4%***	1.38	***6.4%***	***56%***	1.01	***1700%***
N	***36%***	1750 cm^{-3}	***28%***	***11.4%***	16 cm^{-3}	***17%***	***87%***	2.3e-4	***40%***

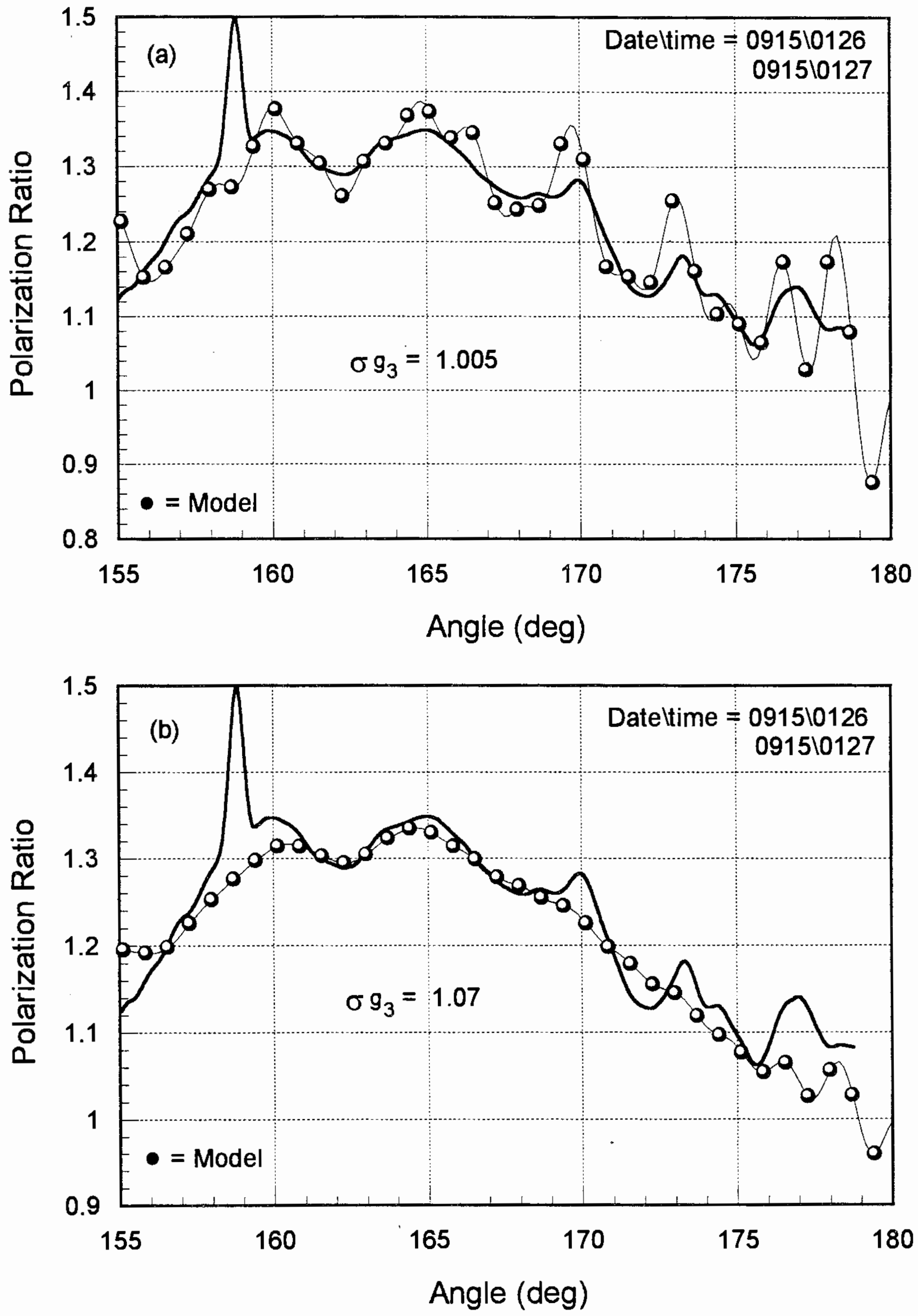

Figure 6.8. These two plots show how the model is affected by changes in the distribution width of the third mode. (a) shows a decrease in the distribution width from σ_g=1.01 to 1.005, while (b) shows an increase to σ_g=1.07.

This can be seen in Figure 6.7b as the model error levels off just above the data error. If the distribution width were to continue to increase, eventually the addition of larger scatterers from the larger distribution would alter the ratio and increase the error. Figure 6.7a shows an example where the error function is very narrow, and the particle radius can be determined with a very high level of confidence. Clearly the fit of the model to the data is very dependent on a particular radius of particles for the third mode. These small errors of only +3% and -6.3% for the radius of the third mode, help to verify the claim that radiation fog was present during these measurements.

The large errors for the distribution width and number density of the third mode are only of concern as far as they effect the calculated extinction. If a large error in a retrieved parameter has little effect on the calculated extinction, at any wavelength, then the large error for the parameter is of little concern for the desired result of extinction. However, the reverse is also true, small errors in some of the parameters will be shown to cause large errors in the calculated extinction. This leads us to the extinction coefficients plotted in Figures 6.5, 6.6, and 6.7. Extinction coefficients for 607 nm are plotted in a, b, and c of these three figures and scaled on the right y-axis. Extinction coefficients for 355 and 1064 nm are plotted in d, e, and f of the same figures and scaled on the left and right y-axis' respectively. The extinction coefficients are plotted versus each lognormal parameter as this parameter was varied to generate the model error curves in a, b, and c. It is important to note here that the overall error in the retrieval of extinction cannot be inferred from Figures 6.5, 6.6, and 6.7, due to the fact that the nine lognormal parameters are correlated. Therefore, these plots are meant to provide information on how dependent the extinction is on each of the nine parameters. We now have all the information needed to determine the effects on each extinction coefficient due to uncertainties in each of the retrieved parameters.

The slope of the extinction is what determines the dependence of the extinction on the error of the parameter. This is similar to how a transistor amplifier works, a very steep slope will amplify small changes on one axis and cause large changes on the orthogonal axis. Figure 6.6b and e demonstrate this effect for the extinction coefficient at 1064 and 355 nm. Two vertical dashed lines are drawn from the intersection of the model error and the data error in Figure 6.6b down to the extinction curves in Figure 6.6e. Horizontal dashed lines are then drawn from the intersection of the vertical dashed lines with the extinction coefficient curve over to the right y-axis. These two horizontal dashed lines define the range of extinction coefficients allowed within the instrument error. In this case the error is +8.2% and -6.5%. If the extinction changed more rapidly with the varying parameter, indicated by a steeper slope, the error would be even larger. However, the opposite is also true. The 355 nm extinction is also shown in Figure 6.6c, and has a much more shallow slope. The extinction error for this wavelength is only +1.7% and -0.3% due to instrument error.

The question still remains as to how the large uncertainties in the retrieval of the distribution width and number density of the third mode affect the extinction error. When the error in the extinction coefficients due to parameter errors is calculated as just explained, it is discovered that the extinction has very little dependence on this third mode. Although this would be expected because of the very small number of particles in that mode. Also, the fact that this mode has such a large error in its retrieval indicates that the scattering from this mode is negligible, therefore the total extinction due to this mode would also be less significant. This does not imply that this third mode is not important, it just means that it only accounts for 3% at 1064 nm, 1.2% at 607 nm, and 0.75% at 355 nm, of the total extinction from all three modes. With this small of an influence on the total extinction it would be expected that this mode would have large errors associated with the retrieval of its parameters.

Table 6.2 displays all the errors calculated from Figures 6.5, 6.6, and 6.7, for each parameter in each mode for three wavelengths, 355, 607, and 1064 nm. These wavelengths were chosen because 607 nm was used to tie off the number densities at the beginning of the night, and 355 and 1064 nm are wavelengths that could easily be used in the future to test these results. The errors shown in Table 6.2 represent the plus and minus percent error in the extinction coefficient due to the uncertainties in the retrieval of the

Table 6.2. Errors in extinction due to uncertainties in the lognormal parameter retrievals.

	355 nm		607 nm		1064 nm	
Mode #1	Low	High	Low	High	Low	High
R_1	*4.70%*	*0.43%*	*4.81%*	*4.10%*	*7.70%*	*7.60%*
σg_1	*3.30%*	*2.94%*	*4.34%*	*4.10%*	*7.70%*	*7.60%*
N_1	*4.70%*	*4.12%*	*5.30%*	*5.30%*	*7.70%*	*7.60%*
Mode #2						
R_2	*3.26%*	*4.12%*	*6.20%*	*7.90%*	*6.52%*	*8.20%*
σg_2	*0.31%*	*1.17%*	*3.87%*	*5.50%*	*6.52%*	*8.20%*
N_2	*8.43%*	*11.5%*	*9.70%*	*14.9%*	*7.70%*	*12.6%*
Mode #3						
R_3	*0.10%*	*0.13%*	*0.12%*	*0.12%*	*0.10%*	*0.20%*
σg_3	*0.02%*	*0.43%*	*0%*	*0.82%*	*0.06%*	*0.50%*
N_3	*0.60%*	*0.43%*	*1.10%*	*1.10%*	*2.65%*	*1.50%*

lognormal parameters listed on the right of the table. A large percent error indicates a strong dependence of extinction on that parameter, whereas, a small percentage indicates a weak dependence on that parameter. Each of the parameter errors was ultimately derived from a calculated instrument error of $\pm 2\sigma_i$. However, decreasing the instrument error will not always decrease the derived extinction error the same amount. As was shown earlier, the effect of the instrument error on parameter retrieval errors is dependent on the width of the hyperbolic model error function shown in Figures 6.5, 6.6, and 6.7a, b, and c. Table 6.1 tells us how well the extinction coefficients at each wavelength can be determined based on errors in the retrieved lognormal parameters. Just from this table it can be seen that the third mode contributes very little error to the calculation of the extinction, it also contributes very little to the extinction, which is one reason its errors are so small. The errors for the extinction at 355 nm are the smallest and the errors at 1064 nm are the largest, due partly to the fact that the extinction at 355 nm is over four times greater than that at 1064 nm. Therefore, the same fluctuation in both signals will cause a larger percent error in the smaller of the two.

From Table 6.1 the average errors in the retrieval of the lognormal size parameters for the data set from Figure 5.17 on September 14, 1995 at Wallops island are as follows;

- The entire first mode can be determined with an average error of ±14% for each parameter, with its distribution width having the least error at only ±2%.
- The entire second mode can be determined with an average error of ±7% for each parameter, with its radius being determined within only ±2% error.
- The radius of mode three has an uncertainty of only ±3%, while the distribution width and number density have over 100% errors in their determination.

These errors were calculated for a maximum instrument error of $\pm 2\sigma_i$, and as the instrument error decreases, the accuracy of the retrieved parameters could become more dependent on the other errors discussed earlier in this chapter. The reason this data set was used for this analysis was because the other errors associated with this type of measurement appeared to be negligible, due to how well the model fit the data. The question as to how well the model could describe the data, and how dependent the extinction is on variations in each lognormal parameter has been answered. However, the total error in the calculated extinction from the retrieved parameters is left for further research.

6.4 Inversion Method for the Retrieval of the Nine Distribution Parameters

As was discussed earlier, most of the data inversion was done manually, although the inversion routine that was written for Matlab worked rather well under certain circumstances. The code that was used to invert the bistatic lidar data is listed in Appendix C. The following discussion will focus more on the designing of a better inversion method for the bistatic lidar than on the details of the Newton-Raphson method.

The concept of the Newton-Raphson method is simple, perturb each parameter in the system, reevaluate the model, and determine if the resulting changes caused a greater or lesser error between the model and the data. Implementing it is more difficult than it sounds. The small perturbations are equivalent to evaluating the numerical derivative of Mie theory for each of the nine lognormal distribution parameters at each point tested for convergence. The Newton-Raphson method is known for its powerful quadratic conversion near a root, but far from the true root this method is also known for its poor global convergence properties (Press, et al., 1988). This is why this inversion technique was more useful at 'polishing up' a root once it was found, than finding the root. Solutions like the monodispersed radiation fog layer would never be found with the Newton-Raphson method because the convergence window is too small, and there are far too many local extremum on the way to the true root.

The Matlab program was designed check for convergence with all of the nine parameters, or with as few as two of the parameters at a time. A single mode distribution with three parameters could be found rather quickly, iterating two parameters at a time. However, the initial guess had to be near the root or the inversion routine would not converge. The radius and distribution width would first be iterated three times, then the distribution width and the number density would be iterated three times, then back to the radius and distribution width. This total process would usually converge after about five iterations of three iterations for each pair. All three parameters could not be iterated at the same time because when the Jacobian (essentially the numerical derivative of each variable) was evaluated to solve for the correction parameter, the resulting matrix would be indeterminate. When inverting all three modes the same technique was used, each of the parameters were iterated in pairs, and then cycled through for five iterations. The problem with inverting all three modes at once was the same as for one mode, one must already have a good idea what distribution parameters are near the solution. This was easy for the single mode distributions, but for the multi-mode data sets, most of the work was in finding the locations of the three modes. However, the inversion method was very useful in finding the exact parameters that minimized the error between the data and the model.

In developing a better inversion algorithm for the bistatic lidar data, two problems would need to be solved with the Newton-Raphson method. The size of the difference used to calculate the numerical derivative would need to be a variable adjusted as each parameter changes. When very small perturbations are used in the Rayleigh scattering region, the resulting derivative shows no change and the inverted matrix is indeterminate. Whereas, if the perturbations are increased, high frequency variations in the larger particle sizes are overlooked. The same problem results when a large distribution width is narrowed causing higher frequency oscillations to exist. So clearly the inversion algorithm would have to be programed with intelligent numerical derivative steps. The second problem is the poor convergence far from the true root. This could be partially solved by programing better initial guesses based on the actual atmospheric conditions, similar to how the solution is found manually. Large particle sizes would not be searched for on clear nights. Many sets of common conditions could also be stored and tried. If the first initial guess did not converge to a solution, a second one for different conditions could be tried. If a solution could not be found by the inversion algorithm, that data set would be later analyzed by humans. Once a solution was found for this unique data set, the parameters would be programed into the inversion program to be used as an initial guess. As this inversion algorithm was used it would learn new particle distribution that could be tried as initial guesses. Each particle distribution would be rated to describe its probability of occurrence and tried accordingly.

Chapter 7

CONCLUSIONS

7.1 Summary

The purpose of this thesis was to investigate the application of a unique bistatic lidar measurement technique to the retrieval of particle size distributions in a humid coastal marine environment. The motivation for developing this new lidar technique was to be able to remotely determine extinction along a horizontal path at any wavelength and with a single-ended instrument operating at only one wavelength. This is a complex problem because the scatterers must be well defined, including their composition, shape, size, distribution width, and number density, in order to extend the extinction calculation to shorter or longer wavelengths. To solve this problem a linear photodiode array bistatic lidar was built to collect information on the particle scattering phase function, and a model was developed to relate the information from the bistatic receiver to a lognormal distribution of spherical scatterers. The bistatic lidar and model were then tested during September 1995 at Wallops Island, Virginia during the CASE I (Coastal Aerosol Scattering Experiment) measurement program.

Previous attempts by other groups to remotely determine particle size distributions with lidar experiments have all relied upon multiple point measurements separated in both time and space (Reagan and Herman, 1970; Devara and Raj, 1987). These measurements would use one polarization component and several isolated scattering angles to construct a phase function for the particles. Because of large spatial and temporal differences between each of the angle measurements, errors on the order of 40% are typical. The technique described in this thesis uses a linear photodiode array to image a horizontally propagating laser beam, and collect the scattering from a continuous range of angles from 155° to 180°. Instead of constructing a phase function form one measurement, a ratio is obtained from the scattering of two orthogonal polarization components, one in the scattering plane and one perpendicular to the scattering plane. The use of a ratio cancels the effects of many problems including nonlinearities across the field-of-view of the receiver and extinction differences due to different path lengths for each scattering angle. Although this polarization ratio contains the information needed to characterize the scatterers, it is useless without a model to relate this ratio to desired parameters, such as extinction, and particle size distributions.

Because the goal was to measure particle size distributions in a humid coastal marine environment, one of the focuses of this thesis was to determine how well Mie theory with a lognormal distribution of scatterers would describe actual data. A program was written using several Matlab and Fortran subroutines including BHMIE from Bohren and Huffman (1983), that modeled the ratio of the two polarization components from the bistatic lidar with a trimodal lognormal distribution of spherical scatterers. It was discovered that in order to accurately model the return from a clear night, the molecular scattering component had to be added to the aerosol distribution. The equivalent radius of a spherical particle that would scatter the same as the assortment of molecules at the Earth's surface was found to be 0.198 nm. The average number density of molecules, (2.54×10^{19} cm^{-3}), at a radius of 0.198 nm was added to the model to account for molecular scattering. It was shown that on clear nights the number density of the first aerosol mode could be determined relative to the number of molecular scatterers.

The second focus of this work was to determine how well a spherical model would describe the particles in a humid marine environment. The results in Chapter 5 from the Wallops Island CASE I program show cases from both clear and hazy nights when the model describes the data almost perfectly. Variations over angles as small as one degree are followed by the model on the night of September 14, 1995. A radiation fog layer of nearly monodispersed particles is shown growing from 6.46 μm to 8.91 μm, as the temperature drops from 23 to 22 °C in a period of 2.5 hours. During this same period the second aerosol mode grew from 0.166 μm to 0.237 μm while its distribution width decreased from $\sigma_g=1.66$ to 1.38. This corresponds to a 54% growth for the first mode, a 43% growth for the second mode and a 38% growth for the third mode in 2.5 hours. These results are then confirmed by the increasing extinction measured with the Raman lidar during the same period. The bistatic lidar is shown to accurately determine the extinction through the night as the temperature drops, after the number densities of the three modes were tied off with the Raman lidar extinction early in the evening.

The third focus of this work was to determine how accurately each parameter in the trimodal lognormal function, used to describe the particle distribution, could be retrieved within the system noise. Chapter 6 presented an error analysis for three types of errors; model error, measurement error, and instrument error. An error analysis was conducted on the data from September 14, 1995, when the error between the model and the data was a minimum, indicating that instrument errors would play a bigger role in the total error. From this analysis it was determined that the radius of the radiation fog mode at 8.91 μm, could be calculated to an accuracy of ± 0.41 μm, while the radius of the second mode at 0.237 μm, could be calculated to an accuracy of ± 5.5 nm. An analysis was also conducted to determine how much influence each parameter has on the extinction.

It has been determined that the bistatic linear photodiode array lidar, along with a spherical scattering model and a trimodal lognormal distribution can accurately determine particle size distributions in a humid environment like that encountered at Wallops Island.

7.2 Future Work

The results obtained from this thesis have answered many questions, although many more questions have been created in the process. The spherical model with a trimodal lognormal distribution was shown to fit the data very well during the Wallops CASE I program, but how well will the model describe the data in other locations with different environments? Why did the model fit the data as well as it did? Were all the particles actually spheres with an index of refraction of 1.38, or is there an averaging effect that can cause a mixture of particles of varying shapes, sizes, and composition to fit to a trimodal lognormal distribution of spherical scatterers? For a desert storm aerosol, an averaging effect is known **not** to happen, but what about other environments with different aerosols? It was shown in Chapters 6 and 7 that all three modes of aerosols contributed significantly to the goodness of the fit between the model and the data, so it can not be argued that the largest mode, at 8.91 μm and most likely spherical, dominated the scattering. In fact this mode was shown to contribute the least, only 3% to the overall extinction. One possible answer would be that a collection of lognormaly distributed spherical scatterers could be made to fit anything. However, it would be unlikely that the trimodal distribution of spheres found to best match the data and extinction, would be realistic. Therefore, examples like those shown in Chapter 5, are probably very close to the actual distribution of aerosols encountered on the Island. It was shown in this thesis that a large portion of the first aerosol mode consists of particles with radii considerably smaller than the probing wavelength, therefore the scattering is approximated with molecular scattering or Rayleigh scattering for which the shape of the particle does not factor into the scattering phase function. However, It should be pointed out that size distributions determined from aerosols that are successfully modeled with Rayleigh theory, cannot reliably predict extinction at smaller wavelengths. If these small particles are not spherical, then their shape becomes increasingly more important as the wavelength decreases. Measuring the particles with an in-situ particle sizing device could help to verify the bistatic lidar measurements, but many of these instruments rely on similar assumptions of spherical scatterers and common refractive indices. And those that don't, have a limited range of sizing. The only way to completely verify the results of this thesis would be to measure the transmission along the same path at a wide range of wavelengths, and compare those measurements with the calculated transmission from the inferred size distributions.

Other areas for future work could be focused toward improving both the model and the experiment. The suggestion of including the index of refraction as one of the parameters to be inverted, was mentioned earlier in the thesis. A refractive index of 1.38 was used for all the data inversions, however it is not known whether a value of 1.30 or 1.40 would provide a better fit to the data. It was not too long ago when generating the modeled numbers for Figures 4.9 to 4.11 would have taken an enormous amount of computer time, now it can be done on a personal computer in a matter of hours. Essentially, the amount of modeled data in all three of these plots have to be generated for each different index of refraction. Eventually, each aerosol mode would need to be represented with its own separate index of refraction. This would be equivalent to computing three sets of Figures 4.9 to 4.11 for each iteration of an inversion algorithm, definitely too much for a personal computer. However, the lognormal function was chosen for its ability to characterize each aerosol individually due to the many different production mechanisms and therefore, refractive indices. To fully take advantage of the lognormal functions ability to represent the aerosols, different refractive indices would have to be used for each mode.

In order to fully test the results and conclusion in this thesis, all of the data should be inverted, and a second identical experiment should be conducted. But until a stable inversion algorithm is developed for the bistatic lidar, 90% of the data will remain unprocessed due to the time required to analyze each set of two 15 second measurements. Some of the improvements that could be made to the Newton-Raphson inversion method, written for this thesis, were discussed in Chapter 6. However, a different inversion method should be considered due to the Newton-Raphson's poor global convergence when inverting parameters that go through many local minima and maxima, like those encountered in the model of the bistatic lidar.

Finally, improvements could be made to the experiment that would allow operation in different environments, possibly more populated where a different group of anthropogenic aerosol would exist. This would allow the bistatic lidar measurement technique to be tested with aerosols that are more likely not spheres. Urban aerosols are known to contain even more particles in the nanometer range, a range easily modeled as molecular or Rayleigh scattering. To accomplish this, the lidar would have to operate with a low power, eye safe laser, and use a much more sensitive and cooled linear array detector.

7.3 Recent Work

Although a one dimensional array was used for the work in this thesis, a natural progression of this type of lidar experiment would lead to the use of a two dimensional array. Between January 22 and February 9, 1996 at the University of California in San Diego, an experiment was conducted using two-dimensional CCD arrays to characterize the surf aerosol plume structure off of La Jolla shores.

Organizations from all over the world including, Austriala, England, The Netherlands, and The United States, worked together to study and characterize surf-generated coastal aerosols and background continental aerosols to improve the transmission and extinction calculations of existing Navy aerosol models. This measurement campaign was titled EOPACE (Electro-Optical Propagation Assessment in the Coastal Environment) and was organized by Dr. Douglas R. Jensen of NRaD (Naval Research and Development).

Penn State's role in this campaign was to characterize the plumes by providing information on their position, height, width, and scattering intensity. This was accomplished with a vertically fanned laser beam transmitted over the ocean's surface, and with two thermoelectrically cooled high resolution imagers. The imagers were operated in two of four positions; three backscatter locations, and one forward scatter location. Although an experiment such as this could have been conducted with a searchlight and a camera with high speed film years ago, this experiment was the first of its kind, and yielded fascinating images of plumes caused from the breaking of ocean waves. The height of the plumes was discovered to exceed 40 meters on nights without wind, but with good wave activity. Three distinct categories of plumes were observed during the measurement period, a pyramid and a fiery type structure on calm evenings, and tall cylindrical plumes in the area of breaking waves on slightly breezy evenings. Figures 7.1 and 7.2 show two examples of images obtained from the pyramid and fiery type plumes. All the images were collected from the scattering of light transmitted from a 514 nm laser. The false coloring in the figures is used to represent the intensity of the scattered radiation.

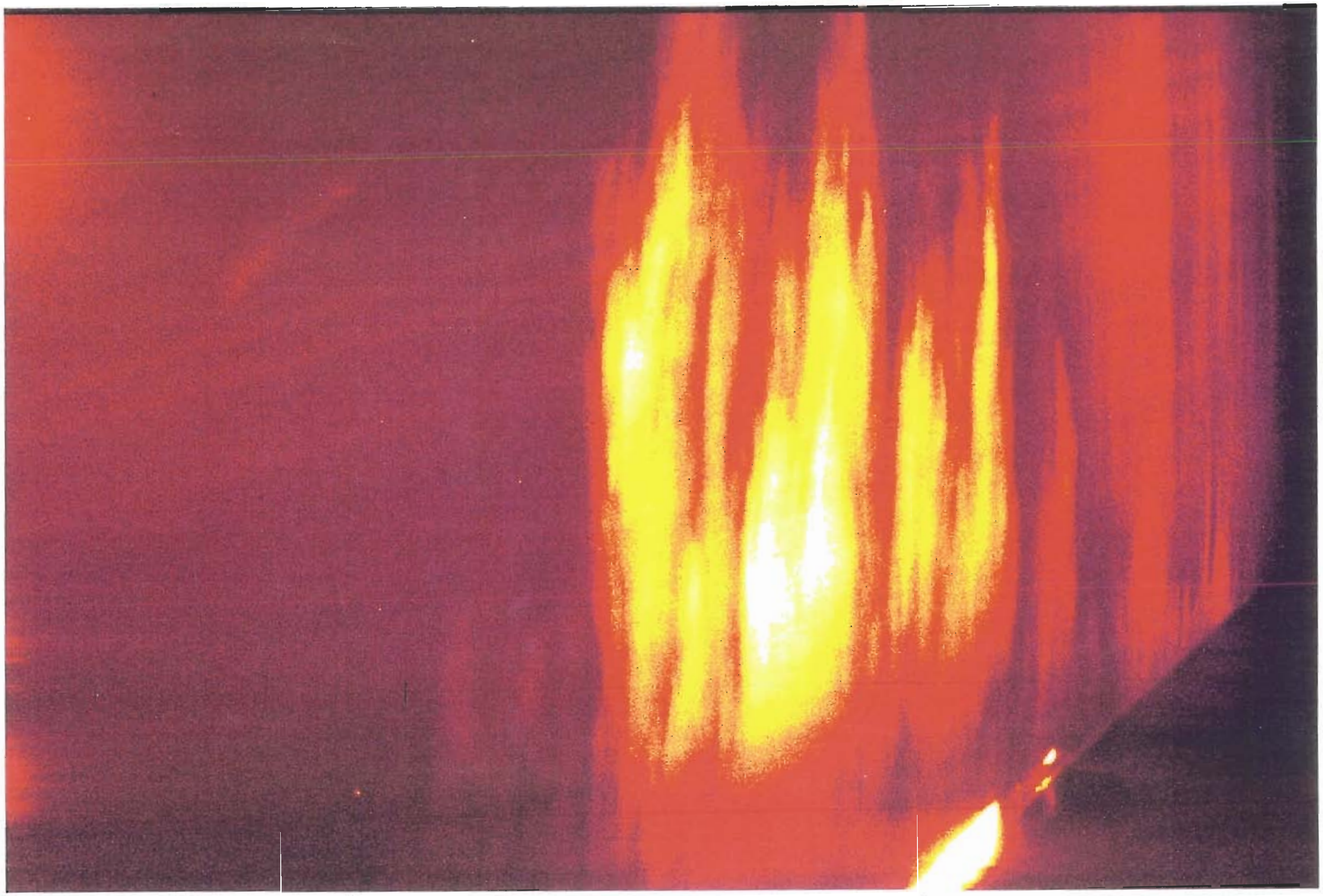

Figure 7.1. This image was collected on January 26, and is a good example of the fiery structure found on several calm evenings. There was alot of surf this evening. Filename: bspo1.tif of 1/26/96.

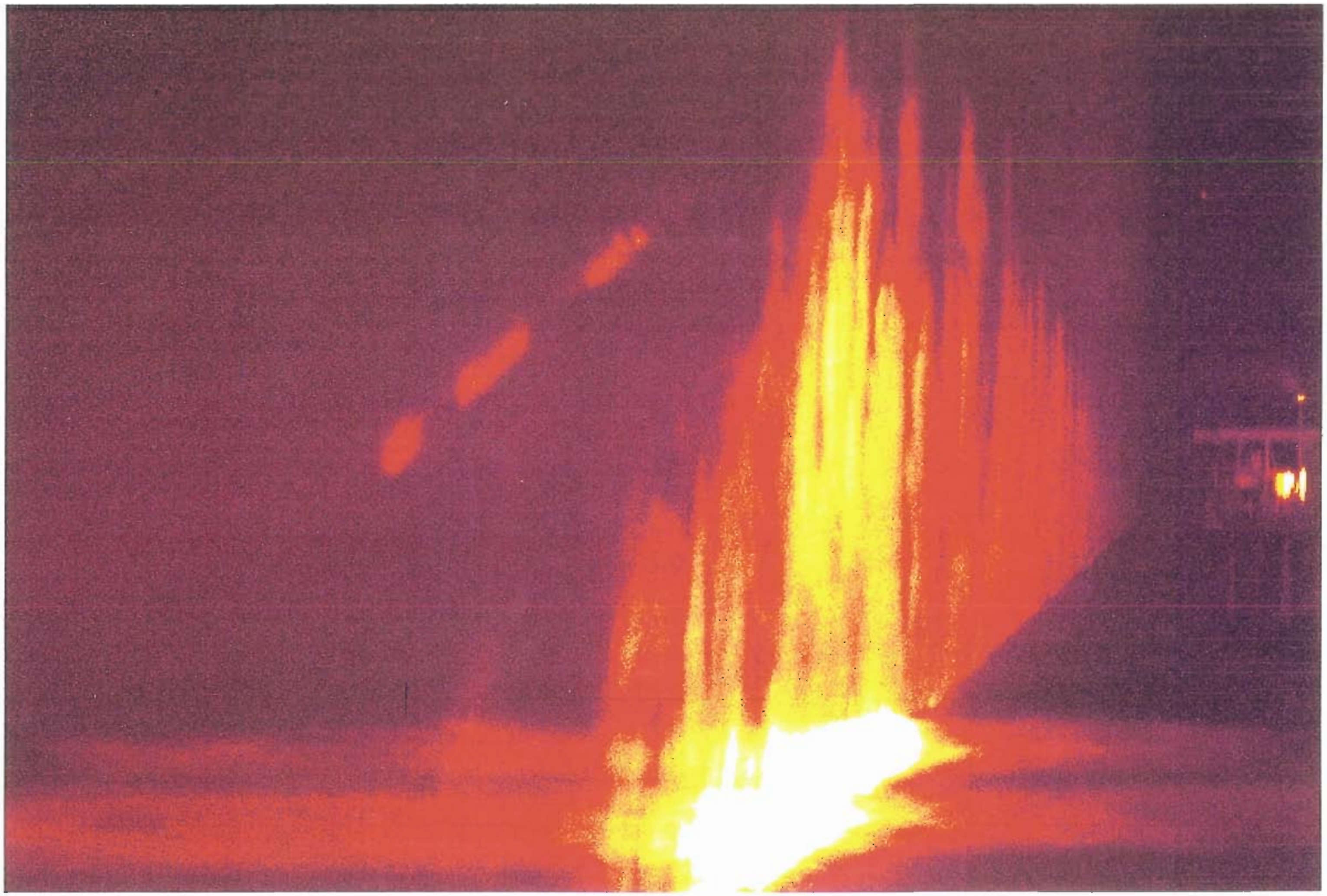

Figure 7.2. This image collected on February 2 is an excellent example of the pyramid structure. This evening was clear with no winds. Filename: sbs11.tif on 2/2/96.

Figure 7.1 is a good example of the fiery structure, with the plumes reaching 35 meters tall. Figure 7.2 shows the pyramid type structure with a wave breaking and generating more aerosols. The data are just starting to be analyzed to determine the exact location and dimensions of each plume. These data will then be related to the atmospheric conditions and correlated with transmissometer and particle sizing data from other instruments. Because of the non-uniformity of the aerosols with distance from the shore (as seen in Figures 7.1 and 7.2) particle sizing with the technique described in this thesis is not possible. Due to the large size of the particles, probably greater than 10 μm, 514 nm would not be a good choice of wavelength to characterize the scattering phase function. Figure 4.11 shows the high frequency oscillations that occur versus angle for particle radii above 10 μm. Wavelengths in the near infrared would be a more practical choice.

This last section gave a brief look into the possibilities of bistatic lidar with the new capabilities of two dimensional imaging systems. As imaging systems become more sensitive allowing the use of lower power lasers, lidar instrumentation and its applications will probably be redefined within the next five to ten years.

REFERENCES

Air Force Geophysics Laboratory, 1985. *Handbook of Geophysics and the Space Environment,* United States Air Force.

Aitchison, J., and J. A. C. Brown, 1957. *The Lognormal Distribution, With Special Reference to its Uses in Economics*, Cambridge University Press.

Amato, U., V. Cuomo, F. Fontana, M. Macchiato, and C. Serio, 1988. "Inference of atmospheric aerosol size distribution from ground measurements of solar radiation," *In Aerosols and Climate*, Deepak Publishing.

Bohren, C. F., and S. B. Singham, 1991. "Backscattering by nonspherical particles: A review of methods and suggested new approaches," *J. Geophys. Res.* Vol. 96, No. D3, p. 5269.

Bohren, C. F., and D. R. Huffman, 1983. *Absorption and Scattering of Light by Small Particles,* Wiley-Interscience, New York.

Buhrman, R. A., and C. G. Granqvist, 1976. "Log-normal size distributions from magnetization measurements on small superconducting Al particles," *J. Appl. Phys.*, Vol. 47, No. 5, p. 2220.

Buhrman, R. A., and C. G. Granqvist, 1976. "Ultrafine metal particles," *J. Appl. Phys.*, Vol. 47, No. 5, p. 2200.

Carnuth, W., and R. Reiter, 1986. "Cloud extinction profile measurements by lidar using Klett's inversion method," *Appl. Opt.* Vol. 25, p. 2899.

Clark, W. E., and K. T. Whitby, 1967. "Concentration and size distribution measurements of atmospheric aerosols and a test of the theory of self-preserving size distributions," *J. Atmos. Sci.*, Vol. 24, p. 677.

Crow, E. L., and K. Shimizu, 1988. *Lognormal Distributions, Theory and Applications,* Marcel Dekker, Inc, New York and Basel.

Coulson, K. L., 1988. *Polarization and Intensity of Light in the Atmosphere.* A. Deepak Publishing.

d'Almeida, G. A., P. Koepke, and E. P. Shettle, 1991. *Atmospheric Aerosols, Global Climatology and Radiative Characteristics*, A. Deepak Publishing.

Davies, C. N., 1974. "Size distribution of atmospheric particles," *Aerosol Sci.*, Vol. 5, p. 293.

Deepak, A. and G. P. Box, 1979. "Analytic modeling of aerosol size distributions," *Nasa Contractor Report 159170.*

Deepak, A.,Editor, 1982. *Atmospheric Aerosols, Their Formation, Optical Properties, and Effects,* Spectrum Press.

Devara, P. C. S., and P. Ernest Raj, 1987. "A bistatic lidar for aerosol studies," *IETE Tech. Rev.* Vol. 4, p. 412.

Devara, P. C. S., and P. Ernest Raj, 1991. "Study of atmospheric aerosols in a terrain-induced nocturnal boundary layer using bistatic lidar," *Atm. Enviro.*, Vol. 25A, No. 3/4, p. 655.

Elterman, L., 1951. "The measurement of stratospheric density distribution with the searchlight technique," *Geophy. Reasearch Papers*, No. 10.

Epstein, B., 1947. "The mathematical description of certain breakage mechanisms leading to the logarithmic-normal distribution," *J. Franklin Inst.*, Vol. 244, p. 471.

Fitch, B. W., and T. S. Cress, 1983. "Spatial and temporal variations of tropospheric aerosol volume distributions," *J. Climate & Appl. Meteor.*, 22, p.1262.

Gathman, S. G., 1983. "Optical properties of the marine aerosol as predicted by a basic version of the navy aerosol model," *NRL Memorandum Report 5157.*

Grams, G. W., 1981. "In-situ measurements of scattering phase functions of stratospheric aerosol particles in Alaska during July 1979," *Geophys. Res. Lett.*, Vol. 8, p. 13.

Gordon, J. I., R. W. Johnson, 1985. "Integrating nephelometer: theroy and implications," *Appl. Opt.*, Vol. 24, No. 16, p. 2721.

Hansen, J. E., and L. D. Travis, 1974. "Light scattering in planetary atmospheres," *Space Sci. Rev.*, Vol. 16, p. 527.

Haris, P. A. T., 1995. "*Pure rotational Raman lidar for temperature measurements in the lower troposphere*," Ph.D. Dissertation, The Pennsylvania State University.

Haris, P. A. T., T. D. Stevens, Y.-C. Rau and C. R. Philbrick, 1994. "Latitudinal variations of middle atmospheric temperatures," *Advances in Space Research*, 13, p. (9)83.

Harrison, R. M., and C. A. Pio, 1983. "Size-differentiated composition of inorganic atmospheric aerosols of both marine and polluted continental origin," *Atmospheric Environment,* Vol. 17, No. 9, p. 1733.

Herman, B. M., S. R. Browning, and J. A. Reagan, 1971. "Determination of aerosol size distributions from lidar measurements," *J. Atmos. Sci.*, Vol. 28, p. 763.

Hobbs, P. V., 1993. *Aerosol-Cloud-Climate Interactions*, Academic Press, Inc., 3-16.

Hobbs, P. V., and M. P. McCormick, 1988. *Aerosols and Climate*, A. Deepak Publishing.

Holland, A. C., G. Gagne, 1970. "The scattering of polarized light by polydisperse systems of irregular particles," *Appl. Opt.*, Vol. 9, No. 5, p. 1113.

Hunt, A. J., and D. R. Huffman, 1973. "A new polarization-modulated light scattering instrument," *Rev. Sci. Instrum.*, Vol. 44, No. 12, p. 1753.

Hunt, A. J., and D. R. Huffman, 1974. "A polarization-modulated light scattering instrument for determining liquid aerosol properties," *Japan. J. Appl. Phys.* Vol. 14, Suppl. 14-1, p. 435.

Hayasaka, T., T. Nakajima, S. Ohta, and M. Tanaka, 1992. "Optical and chemical properties of urban aerosols in Sendai and Sapporo, Japan," *Atmospheric Environment*, Vol. 26A, No. 11, p. 2055.

Junge, C. E., 1955. "The size distribution and aging of natural aerosol as determined from electrical and optical data on the atmosphere," *J. Meteorol.*, Vol. 12, p. 13.

Kent, G. S., G. K. Yue, U. O. Farrukh, and A. Deepak, 1983. "Modeling atmospheric aerosol backscatter at CO2 laser wavelength. 1: Aerosol properties, modeling techniques, and associated problems," *Appl. Opt.* Vol. 22, No. 11, p. 1655.

Kim, Y. J, H. Sievering, and J. F. Boatman, 1988. "Airborne measurement of atmospheric aerosol particles in the lower troposphere over the central United States," *J. Geophys. Res.* Vol. 93, No. D10, p. 12,631.

Klett, J. D., 1981. "Stable analytical inversion solution for processing lidar returns," *Appl. Opt.,* Vol. 20, p. 211.

Koepke, P., and M. Hess, 1988. "Scattering functions of tropospheric aerosols: the effects of nonspherical particles," *Appl. Opt.* Vol. 27, p. 2422.

Kunz, G. J., 1987. "Bipath method as a way to measure the spatial backscatter and extinction coefficients with lidar," *Appl. Opt.* Vol. 26, p. 794.

Kyle, T. G., 1991. *Atmospheric Transmission Emission and Scattering*, Pergamon Press, Oxford.

Measures, R. M., 1984. *Laser Remote Sensing: Fundamentals and Applications*, Krieger Publishing Company, Malabar, Florida.

Parameswaran, K., K. D. Rose, and B. V. Krishna Murthy, 1984. "Aerosol characteristics from bistatic lidar observations," *J. Geophys. Res.* Vol. 89, No. D2, p. 2541.

Parameswaran, K., and G. Vijayakumar, 1993. "A comparison of aerosol size distributions obtained from bistatic lidar and low-pressure impactor experiments at a coastal station," *Ind. J. of Rad. and Space Phys.*, Vol. 22, p. 42.

Patterson, E. M. and D. A. Gillette, 1977. "Commonalities in measured size distributions for aerosols having a soil-derived component," *J. Geophys. Res.* Vol. 82, No. 15, p. 2074.

Paulson, M. R., 1987. "Evaluation of a dual-lidar method for measuring aerosol extinction," *Naval Ocean Systems Center*, TD-1075.

Pendorf, R., 1957. "Tables of the refractive index for standard air and the Rayleigh scattering coefficient for the spectral region between 0.2 and 20.0 u and their application to atmospheric optics," *J. Opt. Soc. Am.*, Vol. 47, No. 2, p. 176.

Philbrick, C. R., D.B. Lysak, and Y.-C. Rau, 1993. "Lidar measurements of aerosol scattering in the troposphere and stratosphere," *Proceedings of the IEEE Topical Symposium on Combined Optical-Microwave Earth and Atmosphere Sensing*, p. 107.

Philbrick, C. R., D. B. Lysak, T.D. Stevens, P.A.T. Haris, and Y.-C. Rau, 1994. "Atmospheric measurements using the LAMP lidar during the LADIMAS campaign," *Proceedings of the 11th ESA Symposium*, ESA-SP-355, p. 223.

Philbrick, C. R., 1994. "Raman lidar measurements of atmospheric properties, "*Proceedings of Atmospheric Propagation and Remote Sensing III*, SPIEE 2222, p. 922.

Pinnick, R. G., and D. J. Hofmann, 1973. "Efficiency of light-scattering aerosol particle counters," *Appl. Opt.*, Vol. 12, No. 11, p. 2593.

Post, M. P., 1975. "Limitations of cloud droplet size distribution by Backus-Gilbert inversion of optical scattering data," *J. Opt. Soc. Am.*, Vol. 66, No. 5, p. 483.

Post, M. P., 1996. "A non-mathematical method to retrieve size parameters from multiple observations," *Jtech in press.*

Press, W. H., B. P. Flannery, S. A. Teukolsky, and W. T. Vetterling, 1988. *Numerical Recipes in C*, Cambridge University Press.

Pritchard, B. S., and W. G. Elliot, 1960. "Two instruments for atmospheric optics measurements, *J. Opt. Soc. Am.*, Vol. 50, p. 191.

Raj, P. Ernest, and P. C. S. Devara, 1989. "Some results of lidar aerosol measurements and their relationship with meteorological parameters," *Atm. Env.* Vol. 23, No. 24, p. 831.

Rau, Y.-C., 1994. "*Multi-wavelength Raman-Rayleigh lidar for atmospheric remote sensing*," Ph.D. Dissertation, The Pennsylvania State University.

Reagan, J. A., and B. M. Herman, 1970. "Bistatic lidar investigations of atmospheric aerosols," *Proc. Conf. Radar Meteorol.*, 14th, p. 275.

Reagan, J. A., D. M. Byrne, M. D. King, J. D. Spinhirne, and B. M. Herman, 1980. "Determination of the complex refractive index and size distribution of atmospheric particulates from bistatic-monostatic lidar and solar radiometer measurements," *J. Geophys. Res.* Vol. 85, No. C3, p. 1591.

Richter, J. H., and H. G. Hughes, 1991. "Marine atmospheric effects on electro-optical systems performance," *Opt. Engr*, Vol. 30, No. 30, p. 1804.

Shettle, E. P., R. W. Fenn, 1979. "Models for the aerosols of the lower atmosphere and the effects of humidity variations on their optical properties," *AFGL-TR-79-0214, Environmental Research Paper No. 675, NTIS ADA 085951.*

Shettle, E. P., V. Turner, and L. W. Abreu, 1994. "Aerosol Phase Functions: Models and Measurements," in IRS'84: Current problems in atmospheric radiation, G. Fiocco, Ed. Deepak, Hampton, VA.

Spinhirne, J. D., J. A. Reagan, and B. M. Herman, 1980. "Vertical distribution of aerosol extinction cross section and inference of aerosol imaginary index in the troposphere by lidar technique," *J. Appl. Meteor.*, Vol. 19, p. 426.

Stephens, G. L., 1994. *Remote Sensing of the Lower Atmosphere, an Introduction*, Oxford University Press, Inc, New York.

Stevens, T. D., S. Maruvada, T. J. Kane, and C. R. Philbrick, 1993. "Lidar Observations of Mt. Pinatubo Aerosols: Effects on the Global Radiation Budget," *in Optical Remote Sensing of the Atmosphere Technical Digest*, 1993 (Optical Society of America, Washington, D.C.), Vol. 5, p. 313.

Stevens, T. D., P. A. Haris, Y.-C. Rau and C. R. Philbrick, 1994. "Latitudinal Lidar Mapping of Stratospheric Particle Layers," *Advances in Space Research*, 13, p. (9)83.

Stevens, T. D., and C. R. Philbrick, 1995. "Atmospheric extinction from Raman lidar and a bistatic remote receiver," *Proceedings of the IEEE Topical Symposium on Combined Optical-Microwave Earth and Atmosphere Sensing*, p. 170.

Stevens, T. D., 1992. *"An optical detection system for a Rayleigh/Raman lidar,"* MS Thesis, The Pennsylvania State University.

Tanaka, M., T. Takamura, and T. Nakajima, 1983. "Refractive index and size distribution of aerosols as estimated from light scattering measurements," *J. Climate & Appl. Meteor.*, 22, p.1253.

van de Hulst, H. C., 1957. *Light Scattering by Small Particles*, Dover Press, New York.

Ward, G., K. M. Cushing, R. D. McPeters, and A. E. S. Green, 1973. "Atmospheric aerosol index of refraction and size-altitude distribution from bistatic laser scattering and solar aureole measurements," *Appl. Opt.*, Vol. 12, No. 11, p. 2585.

Whitby, K. T., 1973. *In "VIII International Conference on Nucleation Leningrad."*.

Whitby, K. T., 1977. "The physical characteristics of sulfur aerosols," *Atmospheric Environment*, Vol. 12, p. 135.

Zuev V. E., 1982. *Laser Beams in the Atmosphere, Plenum Publishing*, New York.

Appendix A

COMPUTER PROGRAM FOR THE DATA ACQUISITION AND CONTROL OF THE BISTATIC RECEIVER

```
'DM5400, CMF8680 and CM102 Interface Program

'Tim D. Stevens
'Pennsylvania State University
'311 Electrical Engineering East
'University Park, PA     16802
'(814) 867-7032

'               MABLES1.BAS     (Ver 2.0)       8/31/94

'This program was written to control the PHASOR bistatic independent
'remote lidar receiver.

'This device was built to collect angle and polarization dependant
'scattering from any existing laser remote sensing system.
'PHASOR is a totally independent and stand-alone receiver,
'no connections are necessary between it and the laser or lidar system.

'The program performs the following functions:
'       - Initiates Real Time Devices interface board
'       - Controls SLR camera
'       - Controls Photo-diode array
'       - Digitizes Photo-diode output
'       - Saves digitized data directly to RAM
'       - Subtracts background from data and saves to PCMCIA
'       - Subroutine to dump PCMCIA data to 3.5" floppy disk
'       - Human interface (switches and led's)

STARTUP:

        CLS
        BA = 768                'SET BASE ADDRESS OF THE DM5400 TO 768

'SET UP COMPUTER SCREEN FOR EVALUATION

        CLS
        KEY(1) ON
        KEY(2) ON
        LOCATE 2, 20
        PRINT "MABLES1 CONTROL SOFTWARE FOR THE PHASOR DEVICE";
        LOCATE 24, 2
        PRINT "F1 = QUIT ";
        ON KEY(1) GOSUB ISTOP
        ON KEY(2) GOSUB QUIT

'THIS SECTION SETS UP THE ADDRESSES FOR THE DM5400 REGISTERS.

        STRTCONV = BA + 0       'ADDRESS TO START CONVERSIONS
        UPDATE = BA + 1         'ADDRESS TO UPDATE DACS
        CLR = BA + 2            'ADDRESS TO CLEAR BOARD POINTERS
        STAT = BA + 0           'ADDRESS TO READ STATUS
        DAT = BA + 1            'ADDRESS TO READ A/D DATA
```

```
        SCAN = BA + 3                     'ADDRESS TO PROGRAM CHANNEL SCAN
        PA = BA + 4                       'ADDRESS FOR 8255 PORT A
        PB = BA + 5                       'ADDRESS FOR 8255 PORT B
        PC = BA + 6                       'ADDRESS FOR 8255 PORT C
        CW = BA + 7                       'ADDRESS FOR 8255 CONTROL WORD
        TA = BA + 8                       'ADDRESS FOR 8254 TIMER A
        TB = BA + 9                       'ADDRESS FOR 8254 TIMER B
        TC = BA + 10                      'ADDRESS FOR 8254 TIMER C
        TCW = BA + 11                     'ADDRESS FOR 8254 CONTROL WORD
       OUT CW,137

GOSUB BEGIN

'THIS SECTION SETS ALL USED 'A' OUTPUTS TO THEIR DEFAULT VALUES

        'PA0 = SHUTTER RELEASE - DEFAULT = 0    TTL LOW
        'PA1 = MSTART          - DEFAULT = 0    TTL LOW
        'PA2 = RESET           - DEFAULT = 0    TTL LOW
        'PA3 = GO LED          - DEFAULT = 1    OFF
        'PA4 = STOP LED        - DEFAULT = 0    ON

            OUT PA, 8

'THIS SECTION INITIALIZES THE PACER CLOCK FOR A 100 kHZ CLOCK RATE

'THE COUNT REGISTERS ARE 16 BIT REGISTERS AND MUST BE LOADED   WITH
'TWO 8 BIT VALUES, LSB FIRST THEN MSB. THE MINIMUM DIVIDER VALUE IS 2 AND THE
'MAXIMUM VALUE IS 65535. THE PACER CLOCK INTERVAL IS CALCULATED WITH THE
'FOLLOWING FORMULA: CLOCK RATE = 8000000 / (DIVIDER A * DIVIDER B).
'IN THE FOLLOWING PROGRAM THE VALUES ARE:
'CLOCK RATE = 8000000 / (2 * 40) = 8000000 / 80 = 100000.
'THE PACER CLOCK IS RUNNING AT A 100 kHZ RATE.

        OUT TCW, &H34             'SET PACER CLOCK TIMER A FOR MODE 2 OPERATION
        OUT TCW, &H74             'SET PACER CLOCK TIMER B FOR MODE 2 OPERATION
        OUT TA, 2                'DIVIDER A LSB = 2
        OUT TA, 0                'DIVIDER A MSB = 0
        OUT TB, 40               'DIVIDER B LSB = 40
        OUT TB, 0                'DIVIDER B MSB = 0

'THIS SECTION SCANS THE ARRAY FOR ONE SWEEP TO BE CERTAIN THE DYNAMIC
'SHIFT REGISTER IS AT THE FIRST PIXEL.

        V = INP(PA)
        V2 = V OR 2
        OUT PA, V2                'MSTART GOES HIGH
        V = INP(PA)
        V2 = V AND 253
        OUT PA, V2                'MSTART GOES LOW

        DELAY 0.054         'WAIT 54 msec UNTIL THE PHOTO-DIODE ARRAY IS CLOCKED OUT
```

```
MAIN:

     KEY(1) ON
     ON KEY(1) GOSUB ISTOP
     V = INP(PA)                 'READ VALUE AT PORT A
     V2 = V OR 16
     OUT PA, V2                   'TURN RED LED OFF

     V = INP(PA)                 'READ VALUE AT PORT A
     V2 = V AND 247
     OUT PA, V2                   'TURN GREEN LED ON

'THIS SECTION LOOKS FOR THE START OR DATA SAVE SWITCH TO BE PRESSED

     V = INP(PC)                             'READ VALUE AT PORT C
     IF V = 253 THEN GOSUB SIGNAL            'TAKE A PICTURE
     IF V = 254 THEN GOSUB SAVE              'SAVE DATA TO 3.5" DISK
     GOTO MAIN

'THIS SECTION OF THE PROGRAM DIGITIZES AND SAVES TO RAM THE PHOTO-DIODE
OUTPUT

SIGNAL:
     V = INP(PA)                 'READ VALUE AT PORT A
     V2 = V AND 239
     OUT PA, V2                   'TURN RED LED ON

     V = INP(PA)                 'READ VALUE AT PORT A
     V2 = V OR 8
     OUT PA, V2                   'TURN GREEN LED OFF

'THE SIGNAL DATA IS SAVED TO PAGE 8 OF DMA CHANNEL 1

'THE NEXT SECTION SETS UP THE DMA CONTROLLER IN THE COMPUTER.
'FOR MORE INFORMATION ON THESE SETTINGS,
'REFER TO THE DMA CONTROLLER DATA SHEET IN THE MANUAL. THE SEQUENCE
'OF PROGRAMMING IS AS FOLLOWS:
'              (A) DISABLE DMA CHANNEL
'              (B) SET DMA MODE (CHANNEL 1; WRITE OPERATION; NO AUTOINITIALIZE)
'              (C) CLEAR THE BYTE POINTER FLIP - FLOP
'              (D) SET DMA BASE ADDRESS (STARTING POINT WITHIN THE 64K PAGE)
'              (E) SPECIFY NUMBER OF BYTES TO TRANSFER ((NUMBER OF SAMPLES * 2) - 1)
'              (F) SET DMA MEMORY PAGE (0 TO 248 FOR A 16 MBYTE SYSTEM)
'              (G) ENABLE DMA CHANNEL

     OUT 10, 5                    'DISABLE DMA CHANNEL MASK
     OUT 11, &H5                    'SET DMA MODE (DEMAND MODE)
     OUT 12, 0                    'CLEAR DMA BYTE FLIP - FLOP
     OUT 2, 0                    'SET DMA BASE ADDRESS LSB = 0
     OUT 2, 0                    'SET DMA BASE ADDRESS MSB = 0
     OUT 3, 255                  'SET NUMBER OF BYTES TO TRANSFER LSB = 255
     OUT 3, 7                    'SET NUMBER OF BYTES TO TRANSFER MSB = 7
```

```
     OUT &H83, 8                     'SET DMA MEMORY PAGE TO 8
     OUT 10, 1                      'ENABLE DMA CHANNEL MASK

'THIS IS THE BEGINNING OF DATA COLLECTION

   OUT PB, 64                     'SELECT CHANNEL = 1, GAIN = 1,
                                  'ENABLE EXTERNAL TRIGGER

'THE PACER CLOCK WILL CONTINUE TO TRIGGER CONVERSIONS UNTIL THE DMA DONE
'BIT = 1.

START:
                          'ENABLE PHOTO-DIODE ARRAY TO INTEGRATE
     V = INP(PA)
     V2 = V OR 4
     OUT PA, V2                   'LR GOES HIGH

                          'OPEN AND CLOSE SHUTTER
     V = INP(PA)
     V2 = V OR 1
     OUT PA, V2                   'SHUTTER RELEASE GOES HIGH
     DELAY 0.2
     V = INP(PA)
     V2 = V AND 254
     OUT PA, V2                   'SHUTTER RELEASE GOES LOW

     DELAY 30                      'WAIT 30 SECONDS FOR SHUTTER TO CLOSE

        V = INP(PA)                    'CLOSE SHUTTER
        V2 = V OR 1
        OUT PA, V2
        DELAY 0.2
        V = INP(PA)
        V2 = V AND 254
        OUT PA, V2



                           'DIGITIZE PHOTO-DIODE ARRAY INTO RAM
     V = INP(PA)
     V2 = V OR 2
     OUT PA, V2               'MSTART GOES HIGH
     V = INP(PA)
     V2 = V AND 253
     OUT PA, V2               'MSTART GOES LOW

'DATA IS TRANSFERED TO MEMORY AT 50 kHZ (20 usec X 1024 = 20.48 msec)

DONE:
     DN = INP(STAT) AND 2              'CHECK TO SEE IF DMA IS DONE
     IF DN < > 2 GOTO DONE               'WAIT TILL DN = 1
     OUT PB, 0                        'DISABLE DMA OPERATION
```

```
                        'DISABLE PHOTO-DIODE ARRAY INTEGRATION
   V = INP(PA)
   V2 = V AND 251
   OUT PA, V2              'LR GOES LOW
   DELAY 0.054
   GOSUB AGAIN
   GOSUB BACKGROUND
   GOSUB DATA1
   GOSUB AGAIN
   BEEP 2
     RETURN


BACKGROUND:

   DELAY 0.054           'WAIT 54 msec TILL TIMING CIRCUIT IS RESET
'THIS SECTION COLLECTS DATA WITH THE SHUTTER CLOSED TO ESTIMATE DARK NOISE

'THE DARK NOISE IS SAVED TO PAGE 9 OF DMA CHANNEL 1

'THE NEXT SECTION SETS UP THE DMA CONTROLLER IN THE COMPUTER. FOR MORE
‘INFORMATION
'ON THESE SETTING, REFER TO THE DMA CONTROLLER DATA SHEET IN THE MANUAL.
‘THE SEQUENCE
'OF PROGRAMMING IS AS FOLLOWS:
'              (A) DISABLE DMA CHANNEL
'              (B) SET DMA MODE (CHANNEL 1; WRITE OPERATION; NO AUTOINITIALIZE)
'              (C) CLEAR THE BYTE POINTER FLIP - FLOP
'              (D) SET DMA BASE ADDRESS (STARTING POINT WITHIN THE 64K PAGE)
'              (E) SPECIFY NUMBER OF BYTES TO TRANSFER ((NUMBER OF SAMPLES * 2) - 1)
'              (F) SET DMA MEMORY PAGE (0 TO 248 FOR A 16 MBYTE SYSTEM)
'              (G) ENABLE DMA CHANNEL

   OUT 10, 5                'DISABLE DMA CHANNEL MASK
   OUT 11, &H5                'SET DMA MODE (DEMAND MODE)
   OUT 12, 0                'CLEAR DMA BYTE FLIP - FLOP
   OUT 2, 0                 'SET DMA BASE ADDRESS LSB = 0
   OUT 2, 0                 'SET DMA BASE ADDRESS MSB = 0
   OUT 3, 255               'SET NUMBER OF BYTES TO TRANSFER LSB = 255
   OUT 3, 7                 'SET NUMBER OF BYTES TO TRANSFER MSB = 7
   OUT &H83, 9                'SET DMA MEMORY PAGE TO 9
   OUT 10, 1                'ENABLE DMA CHANNEL MASK

'THIS IS THE BEGINNING OF DATA COLLECTION

 OUT PB, 64                'SELECT CHANNEL = 1, GAIN = 1,
                          'ENABLE EXTERNAL TRIGGER

'THE PACER CLOCK WILL CONTINUE TO TRIGGER CONVERSIONS UNTIL THE DMA DONE
'BIT = 1.
```

```
START2:
                         'ENABLE PHOTO-DIODE ARRAY TO INTEGRATE
    V = INP(PA)
    V2 = V OR 4
    OUT PA, V2                   'LR GOES HIGH

    DELAY 30                     'WAIT 50 SECONDS TO BE CONSISTANT WITH SIGNAL

                          'DIGITIZE PHOTO-DIODE ARRAY INTO RAM
    V = INP(PA)
    V2 = V OR 2
    OUT PA, V2             'MSTART GOES HIGH
    V = INP(PA)
    V2 = V AND 253
    OUT PA, V2             'MSTART GOES LOW

'DATA IS TRANSFERED TO MEMORY AT 50 kHZ (20 usec X 1024 = 20.48 msec)

DONE2:

    DN = INP(STAT) AND 2              'CHECK TO SEE IF DMA IS DONE
    IF DN < > 2 GOTO DONE2              'WAIT TILL DN = 1
    OUT PB, 0                       'DISABLE DMA OPERATION

                       'DISABLE PHOTO-DIODE ARRAY INTEGRATION
    V = INP(PA)
    V2 = V AND 251
    OUT PA, V2                   'LR GOES LOW
    RETURN

DATA1:

'THE FOLLOWING SECTION READS THE DATA BACK FROM THE COMPUTER'S MEMORY
'SUBTRACTS THE BACKGROUND AND SAVES IT TO THE PCMCIA CARD

'GOTO TIM

       LD$=LEFT$(DATE$,2)
       MD$=MID$(DATE$,4,2)
       LT$=LEFT$(TIME$,2)
       MT$=MID$(TIME$,4,2)
       NAM$=LD$+MD$+LT$+MT$
'     CHDIR "A:\DATA"
       OPEN "O",1,"A:\DATA\" + NAM$ + ".TXT"
     SAMPLE = 0
     FOR I = 1 TO 1024
     DEF SEG = &H8000
     SAMPLE = SAMPLE + 1
     ADDR = (I - 1) * 2
     MSB1 = (PEEK(ADDR) AND 15) * 256
     LSB1 = PEEK(ADDR + 1)
     RESULT = LSB1 + MSB1
```

```
     DEF SEG = &H9000
     MSB2 = (PEEK(ADDR) AND 15) * 256
     LSB2 = PEEK(ADDR + 1)
     NOISE = LSB2 + MSB2
     TOTAL = RESULT - NOISE
     VOLT = TOTAL * (10 / 4096)
        VNOISE = NOISE * (10 / 4096)
        VRESULT = RESULT * (10 / 4096)
     PRINT #1, USING "#### ##.### ##.###"; SAMPLE ; VRESULT ; VNOISE
     NEXT I
     CLOSE
        RESET
     BEEP 1
     RETURN
TIM:

     SAMPLE = 0
     FOR I = 1 TO 1024
     DEF SEG = &H8000
     SAMPLE = SAMPLE + 1
     ADDR = (I - 1) * 2
     MSB1 = (PEEK(ADDR) AND 15) * 256
     LSB1 = PEEK(ADDR + 1)
     RESULT = LSB1 + MSB1
     DEF SEG = &H9000
     MSB2 = (PEEK(ADDR) AND 15) * 256
     LSB2 = PEEK(ADDR + 1)
     NOISE = LSB2 + MSB2
     TOTAL = RESULT - NOISE
     VOLT = TOTAL * (10 / 4096)
     GOSUB PRINTDAT
     NEXT I
     RETURN

PRINTDAT:
'THIS SECTION PRINTS THE A/D DATA ON THE COMPUTER SCREEN.
'TO CONVERT THE DATA FROM THE A/D INTO A VOLTAGE VALUE THE RESULT MUST
'BE MULTIPLIED BY A SCALING FACTOR. THE FACTOR FOR 10 VOLT UNIPOLAR AND
'5 VOLT BIPOLAR OPERATION IS (10 / 4096). THE FACTOR FOR 10 VOLT BIPOLAR
'IS (20 / 4096).

     PRINT "SAMPLE # ";
     PRINT USING "####"; SAMPLE;
     PRINT " = ";
     PRINT USING "#####"; RESULT;
     PRINT USING "#####"; NOISE;
     PRINT USING "######.###"; VOLT;
     PRINT "  VOLTS"
     RETURN
```

```
EOC:
     DONE = INP(STAT) AND 1          'CHECK TO SEE IF CONVERSION IS DONE
     IF DONE < > 1 GOTO EOC           'WAIT TILL EOC = 1
     RETURN

SAVE:
     V = INP(PA)               'READ VALUE AT PORT A
     V2 = V AND 239
     OUT PA, V2                 'TURN RED LED ON

     V = INP(PA)               'READ VALUE AT PORT A
     V2 = V OR 8
     OUT PA, V2                 'TURN GREEN LED OFF

        SHELL "COP.BAT"

        BEEP 2
     RETURN

BEGIN:
             'THIS SECTION INITIALIZES THE BOARD FOR OPERATION

     'OUT CW, 137                  'PROGRAM 8255 FOR PORT A OUT: PORT B OUT: PORT C IN
     OUT PB, 0                      'RESET PORT B
     OUT SCAN, 0                     'DISABLE AUTOMATIC CHANNEL  SCAN
     OUT CLR, 0                      'CLEAR BOARD POINTERS
     OUT STRTCONV, 0                   'START CONVERSION
     GOSUB EOC                        'WAIT TILL CONVERSION IS DONE
     OUT CLR, 0                      'CLEAR BOARD POINTERS

     X = INP(BA + 13)                   'THIS LINE MUST BE ADDED
                                    'FOR DMA TO OPERATE PROPERLY
                                    'ON REAL TIME DEVICES CMF8680 CPUMODULE.
     RETURN

AGAIN:

     OUT 10, 5                 'DISABLE DMA CHANNEL 1 MASK

     X = INP(BA + 12)                'THIS LINE MUST BE ADDED
                           'FOR DMA TO OPERATE PROPERLY
                           'ON REAL TIME DEVICES CMF8680
                           'CPUMODULE. (PLEASE CALL THE FACTORY
                           'FOR DETAILS)
     GOSUB BEGIN
     RETURN

ISTOP:
     OUT 10, 5                 'DISABLE DMA CHANNEL 1 MASK

     X = INP(BA + 12)                'THIS LINE MUST BE ADDED
                           'FOR DMA TO OPERATE PROPERLY
```

```
                        'ON REAL TIME DEVICES CMF8680
                        'CPUMODULE. (PLEASE CALL THE FACTORY
                        'FOR DETAILS)
    GOSUB BEGIN
    GOTO MAIN

QUIT:
    OUT 10, 5              'DISABLE DMA CHANNEL 1 MASK

    X = INP(BA + 12)          'THIS LINE MUST BE ADDED
                        'FOR DMA TO OPERATE PROPERLY
                        'ON REAL TIME DEVICES CMF8680
                        'CPUMODULE. (PLEASE CALL THE FACTORY
                        'FOR DETAILS)
    END
```

Appendix B

FORTRAN COMPUTER SUBROUTINES FOR THE CALCULATION OF MIE SCATTERING PARAMETERS

This Fortran program, BHMIE.for was used by the following two Fortran programs, 2d.for, and qs.for, to calculate the amplitude scattering matrix parameters S_1 and S_2. This program is shown almost identical to its original publication in (Bohren and Huffman, 1983) except for some dimensioning changes to a few variables.

The second Fortran program, 2d.for, creates the 87,500 element scattering matrix discussed in Chapter 4 and demonstrated in Table 4.1. All the parameters including, angle range, radius range, complex index of refraction, wavelength, and file names are defined in this program, which then repeatedly calls BHMIE to calculate S_1 and S_2 for each element. This program generates the modeled data that is used by the Matlab subroutine to find a lognormal distribution, that matches the bistatic lidar data.

The third Fortran program, Qs.for, calculates the scattering cross section at six different wavelengths, 265, 355, 532, 607, 1064, and 3500 nm for each individual particle radius used in 2d.for. These scattering cross sections are saved in a vector format and used by the Matlab subroutines to calculate extinction coefficients for the inverted particle size distributions, as described in Section 4.2.3.

```
C     ****************************************
C     BHMIE.for form (Bohren and Huffman, 1983)
C     ****************************************

      SUBROUTINE BHMIE (X,REFREL,NANG,S1,S2,QEXT,QSCA,QBACK)

      DIMENSION AMU(700),THETA(700),PI(700)
      DIMENSION TAU(700),PI0(700),PI1(700)
      COMPLEX D(50000),Y,REFREL,XI,XI0,XI1,AN,BN
      COMPLEX S2(1300),S1(1300)
      DOUBLE PRECISION PSI0,PSI1,PSI,DN,DX

      DX=X
      Y=X*REFREL

C        *******************************************
C        SERIES TERMINATED AFTER NSTOP TERMS
C        *******************************************

      XSTOP=X+4.*X**.3333+2.0
      NSTOP=XSTOP
      YMOD=CABS(Y)
      NMX=AMAX1(XSTOP,YMOD)+15
      DANG=1.570796327/FLOAT(NANG-1)

      DO 555 J=1,NANG
        THETA(J)=(FLOAT(J)-1.)*DANG
 555  AMU(J)=COS(THETA(J))

C        ************************************************************
C        LOGARITHMIC DERIVATIVE D(J) CALCULATED DOWNWARD
C        RECURRENCE BEGINNING WITH INITIAL VALUE 0.0 + I*0.0
C        AT J=NMX
C        ************************************************************

      D(NMX)=CMPLX(0.0,0.0)
      NN=NMX-1

      DO 120 N=1,NN
        RN=NMX-N+1
 120    D(NMX-N)=(RN/Y)-(1./(D(NMX-N+1)+RN/Y))

      DO 666 J=1,NANG
        PI0(J)=0.0
 666    PI1(J)=1.0

      NN=2*NANG-1

      DO 777 J=1,NN
        S1(J)=CMPLX(0.0,0.0)
 777    S2(J)=CMPLX(0.0,0.0)
```

```
C       ****************************************************
C       RICCATI-BESSEL FUNCTIONS WITH REAL ARGUMENT X
C       CALCULATED BY UPWARD RECURRENCE
C       ****************************************************

      PSI0=DCOS(DX)
      PSI1=DSIN(DX)
      CHI0=-SIN(X)
      CHI1=COS(X)
      APSI0=PSI0
      APSI1=PSI1
      XI0=CMPLX(APSI0,-CHI0)
      XI1=CMPLX(APSI1,-CHI1)
      QSCA=0.0
      N=1
  200 DN=N
      RN=N
      FN=(2.*RN+1.)/(RN*(RN+1.))
      PSI=(2.*DN-1.)*PSI1/DX-PSI0
      APSI=PSI
      CHI=(2.*RN-1.)*CHI1/X - CHI0
      XI=CMPLX(APSI,-CHI)
      AN=(D(N)/REFREL+RN/X)*APSI - APSI1
      AN=AN/((D(N)/REFREL+RN/X)*XI - XI1)
      BN=(REFREL*D(N)+RN/X)*APSI - APSI1
      BN=BN/((REFREL*D(N)+RN/X)*XI - XI1)
      QSCA=QSCA+(2.*RN+1.)*(CABS(AN)*CABS(AN)+CABS(BN)*CABS(BN))

      DO 789 J=1,NANG
        JJ=2*NANG-J
        PI(J)=PI1(J)
        TAU(J)=RN*AMU(J)*PI(J) - (RN+1.)*PI0(J)
        P=(-1.)**(N-1)
        S1(J)=S1(J)+FN*(AN*PI(J)+BN*TAU(J))
        T=(-1.)**N
        S2(J)=S2(J)+FN*(AN*TAU(J)+BN*PI(J))
        IF (J.EQ.JJ) GO TO 789

        S1(JJ)=S1(JJ) + FN*(AN*PI(J)*P+BN*TAU(J)*T)
        S2(JJ)=S2(JJ)+FN*(AN*TAU(J)*T+BN*PI(J)*P)
  789   CONTINUE

      PSI0=PSI1
      PSI1=PSI
      APSI1=PSI1
      CHI0=CHI1
      CHI1=CHI
      XI1=CMPLX(APSI1,-CHI1)
      N=N+1
      RN=N
```

```
    DO 999 J=1,NANG
        PI1(J)=((2.*RN-1.)/(RN-1.))*AMU(J)*PI(J)
        PI1(J)=PI1(J)-RN*PI0(J)/(RN-1.)
999       PI0(J)=PI(J)

      IF (N-1-NSTOP) 200,300,300

300     QSCA=(2./(X*X))*QSCA
      QEXT=(4./(X*X))*REAL(S1(1))
      QBACK=(4./(X*X))*CABS(S1(2*NANG-1))*CABS(S1(2*NANG-1))
      RETURN
      END
```

```
C  Fortran program 2D.for, adapted from (Bohren and Huffman, 1983).

*****************************************************************
*        This program defines the parameters for the subroutine   *
*         BHMIE, and calculates the elements for the               *
*.        scattering matrix devined in Section 4.1.              *
*                                                                  *
*****************************************************************

      COMPLEX REFREL, S1(1300),S2(1300)
      REAL*8 XX
      DIMENSION S11NOR(700)
      INTEGER AJ

      CHARACTER*25 FNAM, FNAM2

      PRINT*, ' '
      PRINT*, ' '

      PRINT*, 'ENTER DRIVE, PATH, AND FILE NAME,IN APOSTROPHES.'
      PRINT*, 'FOR PARALLEL COMPONENT.'
      PRINT*, '(D:\SCATDAT2\COMP1.TXT)'
      READ*, FNAM
      IF (FNAM .EQ. '0') FNAM='D:\TEST\DATATIM.TXT'

      PRINT*, FNAM

      OPEN(UNIT=10,FILE= FNAM,STATUS='UNKNOWN')

      PRINT*, ' '
      PRINT*, 'ENTER DRIVE, PATH, AND FILE NAME,IN APOSTROPHES.'
      PRINT*, 'FOR PERPENDICULAR COMPONENT.'
      PRINT*, '(D:\SCATDAT2\COMP2.TXT)'
      READ*, FNAM2
      IF (FNAM .EQ. '0') FNAM='D:\TEST\DATATIM.TXT'

      PRINT*, FNAM2

      OPEN(UNIT=11,FILE= FNAM2,STATUS='UNKNOWN')

      WRITE (10,11)
      WRITE (11,11)

C      *******************************************************
C      REFMED = (REAL) REFRACTIVE INDEX OF SURROUNDING MEDIUM
C      *******************************************************

        REFMED=1.0

C      *******************************************************
C      REFRACTIVE INDEX OF SPHERE = REFRE + I*REFIM
C      *******************************************************
```

```
      PRINT*, ' '
      PRINT*, ' '
      PRINT*, 'ENTER THE REAL PART OF THE REFRACTIVE INDEX'
      PRINT*, '(0 FOR DEFULT)'
      READ*, REFRE
      IF (REFRE .EQ. 0)  REFRE=1.53

      PRINT*, ' '
      PRINT*, ' '
      PRINT*, 'ENTER THE FAKE PART OF THE REFRACTIVE INDEX'
      PRINT*, '(0 FOR DEFULT)'
      READ*, REFIM

      PRINT*, ' '
      PRINT*, ' '

      IF (REFIM .EQ. 0) REFIM=5.0E-3

      REFREL=CMPLX(REFRE,REFIM)/REFMED
      WRITE (10,12) REFMED,REFRE,REFIM
      WRITE (11,12) REFMED,REFRE,REFIM

C      ****************************************************
C      NOW CALL MENU SUBROUTINE TO DISPLAY CHOICES
C      ****************************************************

       CALL MENUMIE(MRADIUS,STDEV,WAVEL,NUMDEN)

C      ****************************************************
C      RADIUS (RAD) AND WAVELENGTH (WAVEL) SAME UNITS
C      ****************************************************

      WAVEL = 532
      WAVEL = WAVEL * 1.0E-3

C      ****************************************************
C      NANG = NUMBER OF ANGLES BETWEEN 0 AND 90 DEGREES
C      MATRIX ELEMENTS CALCULATED AT 2*NANG - 1 ANGLES
C      INCLUDING 0, 90, AND 180 DEGREES
C      ****************************************************

      NANG=7*90+1
      DANG=1.570796327/FLOAT(NANG-1)
      NAN = 2*NANG-1

      DO 100 N = 1,NAN
      AJ = N
      ANG=DANG*(AJ-1.)*57.2958
      WRITE (10,72) ANG
      WRITE (11,72) ANG

  100 CONTINUE
```

```
      NYZ = 0

      DO 131 XX = -3.7, 3.0, .01

      RAD = 10**XX
      X=2.*3.14159265*RAD*REFMED/WAVEL
      PRINT*, XX, 3
      CALL BHMIE(X,REFREL,NANG,S1,S2,QEXT,QSCA,QBACK)

      NYZ = NYZ+1
      S11NOR(NYZ)=0.5*(CABS(S2(1))**2+CABS(S1(1))**2)


      WRITE (10,71)
      WRITE (11,71)
          DO 141 N = 1, NAN
          BJ=N

        S11=0.5*CABS(S2(BJ))*CABS(S2(BJ))
        S11=S11+0.5*CABS(S1(BJ))*CABS(S1(BJ))
        S12=0.5*CABS(S2(BJ))*CABS(S2(BJ))
        S12=S12-0.5*CABS(S1(BJ))*CABS(S1(BJ))

C         S11=S11/(X*X)
C         S12=S12/(X*X)
C         FIN(BJ)=(S11+S12)/(S11-S12)

        WRITE (10,72) (S11+S12)
        WRITE (11,72) (S11-S12)

  141 CONTINUE
  131 CONTINUE

   65 FORMAT (//,1X,'QSCA= ',E13.6,3X,'QEXT = ',E13.6,3X,
     + 'QBACK = ',E13.6)
   71 FORMAT (1X,F13.6\)
   72 FORMAT (1X,E13.6\)
   75 FORMAT (1X,F6.2,2X,E13.6,2X,E13.6,2X,E13.6,2X,E13.6,2X,E13.6)
   76 FORMAT (1X,E13.6,2X,E13.6,2X,E13.6,2X,E13.6)
   11 FORMAT(/'SPHERE SCATTERING PROGRAM'//)
   12 FORMAT(5X,'REFMED = ',F8.4,3X,'REFRE =',E14.6,3X,
     + 'REFREIM = ',E14.6)
   13 FORMAT(5X,'SPHERE RADIUS = ',F7.3,3X,'WAVELENGTH = ',F7.4,3X,
     + 'SIGMA = ',F7.4)
   14 FORMAT(5X,'SIZE PARAMETER = ',F8.3/)
   17 FORMAT(//,2X,'ANGLE',7X,'S11+S12',13X,'S11-S12'//)
   18 FORMAT(1X,F8.3,2X,E13.6,2X,E13.6,2X,E13.6)
   19 FORMAT(//,2X,'SIZE PARAMETER',7X,'QSCA',7X,'QEXT',13X,'QBACK')
      STOP
      END
```

```
C   Fortran program Qs.for, adapted from (Bohren and Huffman, 1983).

*****************************************************************
*     This program Qs.for calculates the scattering cross section        *
*      for each wavelength to be used by the Matlab subroutines          *
*      to calculate extinction as described in Section 4.2.3.            *
*****************************************************************

      COMPLEX REFREL, S1(1300),S2(1300)
      REAL*8 XX
      DIMENSION S11NOR(700)
C      DIMENSION FIN(1300)
C       INTEGER AJ

      CHARACTER*25 FNAM

      PRINT*, ' '
      PRINT*, ' '

      PRINT*, 'ENTER DRIVE, PATH, AND FILE NAME,IN APOSTROPHES.'
      PRINT*, 'FOR PARALLEL COMPONENT.'
      PRINT*, '(D:\SCATDAT2\COMP1.TXT)'
      READ*, FNAM
      IF (FNAM .EQ. '0') FNAM='D:\TEST\DATATIM.TXT'

      PRINT*, FNAM

      OPEN(UNIT=10,FILE= FNAM,STATUS='UNKNOWN')


C       *******************************************************
C       REFMED = (REAL) REFRACTIVE INDEX OF SURROUNDING MEDIUM
C       *******************************************************
       REFMED=1.0

C       *******************************************************
C       REFRACTIVE INDEX OF SPHERE = REFRE + I*REFIM
C       *******************************************************

      PRINT*, ' '
      PRINT*, ' '
      PRINT*, 'ENTER THE REAL PART OF THE REFRACTIVE INDEX'
      PRINT*, '(0 FOR DEFULT)'
      READ*, REFRE
      IF (REFRE .EQ. 0)  REFRE=1.379

      PRINT*, ' '
      PRINT*, ' '
      PRINT*, 'ENTER THE FAKE PART OF THE REFRACTIVE INDEX'
      PRINT*, '(0 FOR DEFULT)'
      READ*, REFIM
```

```
      PRINT*, ' '
      PRINT*, ' '

      IF (REFIM .EQ. 0) REFIM=0

      REFREL=CMPLX(REFRE,REFIM)/REFMED
      WRITE (10,12) REFMED,REFRE,REFIM

C       *****************************************************
C       NOW CALL MENU SUBROUTINE TO DISPLAY CHOICES
C       *****************************************************

      CALL MENUMIE(MRADIUS,STDEV,WAVEL,NUMDEN)

C       ******************************************************
C       RADIUS (RAD) AND WAVELENGTH (WAVEL) SAME UNITS
C       ******************************************************

      WAVEL = 532
      WAVEL = WAVEL * 1.0E-3

C       *********************************************************
C       NANG = NUMBER OF ANGLES BETWEEN 0 AND 90 DEGREES
C       MATRIX ELEMENTS CALCULATED AT 2*NANG - 1 ANGLES
C       INCLUDING 0, 90, AND 180 DEGREES
C       *********************************************************

      NANG=1*90+1
      DANG=1.570796327/FLOAT(NANG-1)
      NAN = 2*NANG-1

      NYZ = 0

      DO 131 XX = -4.0, 2.0, .01

      RAD = 10**XX
      X=2.*3.14159265*RAD*REFMED/WAVEL
      PRINT*, XX, 3
      CALL BHMIE(X,REFREL,NANG,S1,S2,QEXT,QSCA,QBACK)

      NYZ = NYZ+1
      S11NOR(NYZ)=0.5*(CABS(S2(1))**2+CABS(S1(1))**2)

        RAD = RAD/(10.**6.0)

        WRITE (10,76)  QSCA*3.14159265*RAD*RAD, RAD

  131 CONTINUE
```

```
65 FORMAT (//,1X,'QSCA= ',E13.6,3X,'QEXT = ',E13.6,3X,
 + 'QBACK = ',E13.6)
71 FORMAT (1X,F13.6\)
72 FORMAT (1X,E13.6\)
75 FORMAT (1X,F6.2,2X,E13.6,2X,E13.6,2X,E13.6,2X,E13.6,2X,E13.6)
76 FORMAT (1X,E13.6,2X,E13.6)
11 FORMAT(/'SPHERE SCATTERING PROGRAM'//)
12 FORMAT(5X,'REFMED = ',F8.4,3X,'REFRE =',E14.6,3X,
 + 'REFREIM = ',E14.6)
13 FORMAT(5X,'SPHERE RADIUS = ',F7.3,3X,'WAVELENGTH = ',F7.4,3X,
 + 'SIGMA = ',F7.4)
14 FORMAT(5X,'SIZE PARAMETER = ',F8.3/)
17 FORMAT(//,2X,'ANGLE',7X,'S11+S12',13X,'S11-S12'//)
18 FORMAT(1X,F8.3,2X,E13.6,2X,E13.6,2X,E13.6)
19 FORMAT(//,2X,'SIZE PARAMETER',7X,'QSCA',7X,'QEXT',13X,'QBACK')
   STOP
   END
```

Appendix C

MATLAB COMPUTER PROGRAMS FOR THE INVERSION OF THE BISTATIC RECEIVER DATA

This next group of programs were written to complete the modeling of the aerosols by applying a trimodal lognormal distribution to the matrices calculated using the Fortran programs in Appendix B, and to invert the bistatic lidar data and retrieve up to nine parameters for the lognormal distributions.

The first program Fpdist.m reads the two 176 x 600 element matrices for each polarization component ('comp1' and 'comp2'), and accepts up to nine parameters for a trimodal lognormal distribution. Fpdist.m models the lognormal distributions, add the molecules and does a matrix multiplication of the distribution vector with each scattering matrix, yielding two vectors of scattering intensities versus angle with a lognormal distribution applied to them. These two vectors, one for the parallel component and one for the perpendicular component are then divided to obtain the polarization ratio versus angle that the bistatic lidar observes. The vectors generated by the Qs.for program, for each wavelength are also read by Fpdist.m in order to calculate the extinction at each wavelength due to the given particle distribution. The data vector and model, versus angle, are plotted as the output for each particle distribution.

The second program apinv.m is the Matlab inversion subroutine written to take as input, the data and the two polarization component matrices ('comp1' and 'comp2') generated by the Fortran program 2d.for. This program uses the Newton-Raphson method to determine the nine parameters that provide the best fit to the data. The Matlab program distrib.m returns the polarization ratio vector after each perturbation of the parameters. Distrib.m is similar to Fpdist, without all the output plots, so it will not be listed.

```
%%%%%%%%%%%%%%%%%%%%%%%%%%%%%%%%%%%%%
% Fpdist.m, this program takes up to a nine parameter input and outputs %
%                   the ratio of intensities for the two polarizations, as              %
%                    would be observed by the bistatic lidar.                                %
%%%%%%%%%%%%%%%%%%%%%%%%%%%%%%%%%%%%%

function  Fpdist(R1,S1,N1,R2,S2,N2,R3,S3,N3,R4,S4,N4)

%pdist(R1,S1,N1,R2,S2,N2,R3,S3,N3,R4,S4,N4)
%Particle distribution for ratios
%input mean radius and then standard deviation

global data       % define global variables
tglobal
ch3 = 1;
ch2 = 1;
ch = 1;
ni = 1;

% look for number of inputs and assign variables
if nargin < 12
    ch3 = 0;
    N4 = 1;
    R4 = 1;
    S4 = .2;
end
if nargin < 9
    ch = 0;
    N3 = 1;
    R3 = 1;
    S3 = .2;
end
if nargin < 6
     ch2 = 0;
     N2 = 1;
     R2 = 1;
     S2 = .2;
end
maxr = 3;
global fpdist
R1 = 10 .^ R1
R2 = 10 .^ R2
R3 = 10 .^ R3
R4 = 10 .^ R4

% Define trimodal lognormal distribution
x = (-3.7:.01:maxr)';
rm = 10.0 .^x;
Pdist1a = (N1 / ((2 * pi) ^ 0.5 * S1));
Pdist1b = exp(-(log10((rm) ./ R1) .^2) ./ (2 .* S1 .^2));
Pdist2a = (N2 / ((2 * pi) ^ 0.5 * S2));
Pdist2b = exp(-(log10((rm) ./ R2) .^2) ./ (2 .* S2 .^2));
```

```
Pdist3a = (N3 / ((2 * pi) ^ 0.5 * S3));
Pdist3b = exp(-(log10((rm) ./ R3) .^2) ./ (2 .* S3 .^2));
Pdist4a = (N4 / ((2 * pi) ^ 0.5 * S4));
Pdist4b = exp(-(log10((rm) ./ R4) .^2) ./ (2 .* S4 .^2));
PdistM = zeros(671,1);
PdistM(1,1) = 2.547e19; % Enter number of molecules at the Earth's surface

pdist1 = Pdist1a .* Pdist1b;
pdist2 = Pdist2a .* Pdist2b .*ch2;
pdist3 = Pdist3a .* Pdist3b .*ch;
pdist4 = Pdist4a .* Pdist4b .*ch3;

% Set number density of particles below 1 nm and above 250 μm to zero
a = (1:70);
pdist1(1:70) = zeros(size(a));
pdist1(602:671) = zeros(size(a));
pdist2(1:70) = zeros(size(a));
pdist2(602:671) = zeros(size(a));
pdist3(1:70) = zeros(size(a));
pdist3(602:671) = zeros(size(a));

a = (1:70);
pdist123 = pdist1 + pdist2 + pdist3 + pdist4;
pdist123(1:70) = zeros(size(a));
pdist123(602:671) = zeros(size(a));
pdist123 = pdist123 + PdistM;
%pdist123(1:70) = 1./zeros(size(a));
%pdist(602:671) = 1./zeros(size(a));

%z = max(pdist1)
pdistf = pdist123;
pdistf = pdistf';
end

startup
close all
%subplot(2,1,1);

% Plot distribution function
loglog(rm,pdist2,'r',rm,pdist1,'g',rm,pdist3,'y',rm,pdist4,'c')
%loglog(rm,pdist2,'r',rm,pdist1,'g',rm,pdist3,'y',rm,pdist4,'c',rm,PdistM,'y')
%loglog(rm,pdist123)
%subplot(2,1,2);
%semilogx(rm,pdistf-PdistM','c');
%loglog(rm,pdistf,'c');
axis([10e-6 10e3 10e-7 10e4])
grid

pdistr(:,1) = rm;
pdistr(:,2) = pdist123;
pdistr(:,3) = pdist1;
pdistr(:,4) = pdist2;
```

```
pdistr(:,5) = pdist3;
pdistr(:,6) = PdistM;
save dist2.txt pdistr -ascii -tabs

global comp1
global comp2
global ratcompb qs532
global ang data ang2

% Calculate extinction at each wavelength
ext532 = pdistf * qs532 .*1e9;
ext355 = pdistf * qs355 .*1e9;
ext266 = pdistf * qs266 .*1e9;
ext1064 = pdistf * qs1064 .*1e9;
ext3500 = pdistf * qs3500 .*1e9;
ext607 = pdistf * qs607 .*1e9;

% Calculate total particle number density for each mode
nd1 = pdist1' * qs532
nd2 = pdist2' * qs532
nd3 = pdist3' * qs532
ndm = PdistM' * qs532
nd123 = nd1 +nd2 +nd3

% Calculate visibility
vis532 = 3.9 ./ext532

% Apply distribution to each polarization component matrix and then divide the two
dcomp1b = pdistf * comp1;
dcomp2b = pdistf * comp2;
ratcompb = dcomp1b ./ dcomp2b;

% Plot model output and data
figure
plot(ang,ratcompb,'r');
%,ang,data,'g')
%hold
plot(dataf(50:1024,5),dataf(50:1024,4),'g')
%axis([155 180 .9 1.6])
grid
pdcomp(:,1) = ang';
pdcomp(:,2) = ratcompb';
%pdcomp(:,3) = dcomp2b';
%save pdrat2.txt pdcomp -ascii -tabs

figure
plot(ang,dcomp1b,ang,dcomp2b),
```

```
%%%%%%%%%%%%%%%%%%%%%%%%%%%%%%%%%%%%%%
%     Matlab subroutine apinv.m                                %
%      This program accepts as input the bistatic lidar data and the      %
%       two polarization component matrices modeled with 2d.for.      %
%       The Newton-Raphson method is then applied to retrieve the      %
%        nine parameters of the trimodal lognormal distribution that      %
%        minimizes the difference between the model and the data.      %
%%%%%%%%%%%%%%%%%%%%%%%%%%%%%%%%%%%%%%

function  mdata = apinv(data,comp1,comp2);
close all
global comp1 comp2;

% Declare initial guess for all parameters
R1 = -2.225;
S1 = .507;
N1 = 976;
R2 = -.68;
S2 = .186;
N2 = 4.5;
R3 = .925;
S3 = .01;
N3 = .00009;
figure
hold

% Define parameter vector for distribution
s = [R1,S1,N1,R2,S2,N2,R3,S3,N3]
%s = [R1,S1,N1]

plot(data,'g')
plot(distrib(s),'y')
end
%Start total for all five iterations.
NN = 5;
P = 5
clear JF;
for j = 1: 1: 3;

%Start first iteration (#1).
for I = 1 : 1 : NN-P;

% define numerical derivative (difference) for each parameter
ds1 = [.0001,0,0,0,0,0,0,0,0];
ds2 = [0,.001,0,0,0,0,0,0,0];
ds3 = [0,0,100,0,0,0,0,0,0];
ds4 = [0,0,0,.001,0,0,0,0,0];
ds5 = [0,0,0,0,.001,0,0,0,0];
ds6 = [0,0,0,0,0,1,0,0,0];
ds7 = [0,0,0,0,0,0,.001,0,0];
ds8 = [0,0,0,0,0,0,0,.001,0];
ds9 = [0,0,0,0,0,0,0,0,.000001];
```

```
% Determine ratio vector for given distribution s
F = distrib(s);

% Perturb only two parameters at a time
JF(:,1) = (distrib(s + ds1) - F) ./ (.0001);
JF(:,2) = (distrib(s + ds2) - F) ./ (.001);
%JF(:,3) = (distrib(s + ds3) - F) ./ (100);
%JF(:,2) = (distrib(s + ds4) - F) ./ (.001);
%JF(:,3) = (distrib(s + ds5) - F) ./ (.001);
%JF(:,1) = (distrib(s + ds1) - F) ./ (.0001);

er = data - F;          % Difference between data and model
ds = JF \ er;           % Use Matlab's built in function (\) to solve for ds (more accurate than inverse fnt)

% Define new parameters for best fit.
ds(1:2)=ds;
ds(3)=0;
ds(4)=0;
ds(5)=0;
ds(6)=0;
ds(7)=0;
ds(8)=0;
ds(9)=0;
ds

s = s + ds'
end
plot(data,'g')
plot(distrib(s),'y')

% Repeat for different set of parameters
%Start of second Iteration. (#2)
clear JF;
for I = 1 : 1 : NN-P;
ds1 = [.001,0,0,0,0,0];
ds2 = [0,.001,0,0,0,0];
ds3 = [0,0,.000001,0,0,0,0,0,0];
ds4 = [0,0,0,.001,0,0];
ds5 = [0,0,0,0,.001,0];
ds6 = [0,0,0,0,0,100];

F = distrib(s);
%JF(:,1) = (distrib(s + ds1) - F) ./ (.1);
%JF(:,1) = (distrib(s + ds2) - F) ./ (.001);
JF(:,1) = (distrib(s + ds3) - F) ./ (.000001);
%JF(:,2) = (distrib(s + ds4) - F) ./ (.001);
%JF(:,3) = (distrib(s + ds5) - F) ./ (.001);
%JF(:,3) = (distrib(s + ds5) - F) ./ (.001);

er = data - F;
ds = JF \ er;
ds(3)=ds;
```

```
ds(1)=0;
ds(2)=0;
ds(4)=0;
ds(5)=0;
ds(6)=0;
ds(7)=0;
ds(8)=0;
ds(9)=0;

ds'
s = s + ds
end
plot(data,'g')
plot(distrib(s),'r')

%Start of third iteration. (#3)
clear JF
for I = 1 : 1 : NN-P;
ds1 = [.001,0,0,0,0,0];
ds2 = [0,.001,0,0,0,0,0,0,0];
ds3 = [0,0,.001,0,0,0,0,0,0];
ds4 = [0,0,0,.001,0,0,0,0,0];
ds5 = [0,0,0,0,.001,0,0,0,0];

F = distrib(s);
%JF(:,1) = (distrib(s + ds1) - F) ./ (.1);
%JF(:,2) = (distrib(s + ds2) - F) ./ (.01);
%JF(:,1) = (distrib(s + ds3) - F) ./ (.001);
JF(:,1) = (distrib(s + ds4) - F) ./ (.001);
JF(:,2) = (distrib(s + ds5) - F) ./ (.001);
%JF(:,2) = (distrib(s + ds5) - F) ./ (.001);

er = data - F;
ds = JF \ er;
ds(4:5)=ds;
ds(1)=0;
ds(2)=0;
ds(3)=0;
ds(6)=0;
ds(7)=0;
ds(8)=0;
ds(9)=0;
ds
s = s + ds'
end
plot(data,'g')
plot(distrib(s),'b')

%Start of fourth iteration.(#4)
clear JF
for I = 1 : 1 : NN-P;
ds1 = [.001,0,0,0,0,0];
```

```
ds2 = [0,.001,0,0,0,0];
ds3 = [0,0,.001,0,0,0];
ds4 = [0,0,0,.001,0,0];
ds5 = [0,0,0,0,.001,0];
ds6 = [0,0,0,0,0,.100,0,0,0];

F = distrib(s);
%JF(:,1) = (distrib(s + ds1) - F) ./ (.1);
%JF(:,2) = (distrib(s + ds2) - F) ./ (.01);
%JF(:,1) = (distrib(s + ds3) - F) ./ (.001);
%JF(:,1) = (distrib(s + ds4) - F) ./ (.001);
%JF(:,1) = (distrib(s + ds5) - F) ./ (.001);
JF(:,1) = (distrib(s + ds6) - F) ./ (.1);

er = data - F;
ds = JF \ er;
ds(6)=ds;
ds(1)=0;
ds(2)=0;
ds(3)=0;
ds(4)=0;
ds(5)=0;
ds(7)=0;
ds(8)=0;
ds(9)=0;
ds'
s = s + ds
end
plot(data,'g')
plot(distrib(s),'m')

%Start of fifth iteration.(#5)
clear JF
for I = 1 : 1 : NN;
ds1 = [.0001,0,0,0,0];
ds2 = [0,.001,0,0,0];
ds3 = [0,0,.001,0,0];
ds4 = [0,0,0,.001,0];
ds5 = [0,0,0,0,.001];
ds6 = [0,0,0,0,0,10];
ds7 = [0,0,0,0,0,0,.0001,0,0];
ds8 = [0,0,0,0,0,0,0,.0001,0];

F = distrib(s);
%JF(:,1) = (distrib(s + ds1) - F) ./ (.0001);
%JF(:,2) = (distrib(s + ds2) - F) ./ (.01);
%JF(:,1) = (distrib(s + ds3) - F) ./ (.001);
%JF(:,1) = (distrib(s + ds4) - F) ./ (.001);
%JF(:,2) = (distrib(s + ds5) - F) ./ (.001);
%JF(:,1) = (distrib(s + ds6) - F) ./ (10);
JF(:,1) = (distrib(s + ds7) - F) ./ (.0001);
JF(:,2) = (distrib(s + ds8) - F) ./ (.0001);
```

```
%JF(:,1) = (distrib(s + ds6) - F) ./ (10);

er = data - F;
ds = JF \ er;
ds(7:8)=ds;
ds(2)=0;
ds(3)=0;
ds(4)=0;
ds(1)=0;
ds(5)=0;
ds(6)=0;
ds(9)=0;
ds
s = s + ds'
end
plot(data,'g')
plot(distrib(s),'c')

%Start of sixth iteration.(#6)
clear JF
for I = 1 : 1 : NN;
ds1 = [.0001,0,0,0,0];
ds2 = [0,.001,0,0,0];
ds3 = [0,0,.001,0,0];
ds4 = [0,0,0,.001,0];
ds5 = [0,0,0,0,.001];
ds6 = [0,0,0,0,0,10];
ds7 = [0,0,0,0,0,0,.001,0,0];
ds8 = [0,0,0,0,0,0,0,.001,0];
ds9 = [0,0,0,0,0,0,0,0,.0001];

F = distrib(s);
%JF(:,1) = (distrib(s + ds1) - F) ./ (.0001);
%JF(:,2) = (distrib(s + ds2) - F) ./ (.01);
%JF(:,1) = (distrib(s + ds3) - F) ./ (.001);
%JF(:,1) = (distrib(s + ds4) - F) ./ (.001);
%JF(:,2) = (distrib(s + ds5) - F) ./ (.001);
%JF(:,1) = (distrib(s + ds6) - F) ./ (10);
%JF(:,1) = (distrib(s + ds7) - F) ./ (.001);
%JF(:,2) = (distrib(s + ds8) - F) ./ (.001);
JF(:,1) = (distrib(s + ds9) - F) ./ (.0001);

er = data - F;
ds = JF \ er;
ds(9)=ds;
ds(2)=0;
ds(3)=0;
ds(4)=0;
ds(1)=0;
ds(5)=0;
ds(6)=0;
ds(8)=0;
```

```
ds(7)=0;
ds'
s = s + ds
end
plot(data,'g')
plot(distrib(s),'c')

end
figure
plot(distrib(s),'c')
hold
plot(data,'g')
```

Appendix D

DATA PROCESSING PROGRAMS

The next three programs; wallops3.m, hfiltera.m, and pholamp.m, are Matlab subroutines used to perform initial processing on the bistatic lidar data, and the horizontal monostatic Raman lidar data, respectively.

The first program, wallops3.m, reads in two consecutive data sets, one perpendicular component and one parallel component. The data is then filtered with hfiltera.m (listed next), and then the background is subtracted. Wallops3.m includes a routine that simulates the noise for the ratio of the two components given a particular instrument noise. This program also assigns the scattering angle associated with each pixel. Finally, the data are plotted on two graphs, one with raw data, and one with the ratio of the two components.

The second program, hfiltera.m was written to filter any odd numbered vector, with a Hanning filter of any specified width. This subroutine was used with the bistatic lidar data and the Raman monostatic lidar data.

The third program, pholamp.m was originally written by Dr. Franz Balsiger and later modified to process the horizontal monostatic Raman lidar data. This program filters the data and subtracts the background and corrects for the $1/R^2$ dependence of the signal with range. The slope of the curve is then found, and the Beer-Lambert law is applied to find the extinction coefficient at that wavelength.

```
%%%%%%%%%%%%%%%%%%%%%%%%%%%%%%%%%%%%
%   Matlab subroutine wallops3.m                                   %
%       This program reads the two consecutive raw bistatic lidar data   %
%       at a time to be processed.  The data are filtered, angles are    %
%       assigned, and noise calculations can be conducted if desired.    %
%       The data are then plotted for a quick first look.                %
%%%%%%%%%%%%%%%%%%%%%%%%%%%%%%%%%%%%

function   dataf = wallops(file1, file2,b);
%
%   function   wallops(file1, file2,b);
%   calculates the ratio.
%
% Check for number of inputs
if nargin < 2
   file2 = file1;
end

% Read data files using subroutine written by Dr. Franz Balsiger
data1 = readfile(file1);
data2 = readfile(file2);

% Filter data using filter subroutine written for wallops data, then subtract background
data1(1:1024,4) = hfiltera(data1(:,2)-data1(:,3),21);
data2(1:1024,4) = hfiltera(data2(:,2)-data2(:,3),21);
dataf(:,1) = data1(:,1);
dataf(:,2) = data1(:,4);
dataf(:,3) = data2(:,4);
dataf(:,4) = data2(:,4)./data1(:,4);
%dataf(7:1018,4) = hfiltr13(dataf(:,4));
x=data2(:,4)';
y=data1(:,4)';

% Simulate random gaussian noise, to estimate total noise for ratio
for i = 1:500;
randn('seed',i);
ra1=randn(1,1024)*0.0414;
ra2=randn(1,1024)*0.0414;
bmatrx(i,:) = (x+ra1)./(y+ra2);
i
end
ye=std(bmatrx)';

dataf = dataf';

startup3
close all

dataf = dataf';
%subplot(2,1,1),plot(data1(1:1000,1),data1(1:1000,2),data1(1:1000,1),data1(1:1000,3),data2(1:1000,1),data
2(1:1000,2))
%grid
```

```
%title('Bistatic receiver lidar data')
%xlabel('Pixel #')
%ylabel('Relative Intensity (Volts)')

% Plot raw data profiles
%figure
subplot(2,1,1),plot(dataf(1:1000,1),dataf(1:1000,2),dataf(1:1000,1),dataf(1:1000,3),'-')
grid
title(['Bistatic receiver lidar data'])
xlabel('Pixel #')
ylabel('Relative Intensity (Volts)')
text(400,2,[file1 ' & ' file2])
%dataf(:,4) = dataf(:,4) + .3;

%startup2
%b = 48;

% Assign target board pixel number
c = 1024 - b;
%figure
n = 0:c;
n = n';

% Assign angle to pixel number
m=abs(n-512);
m2=abs(n-512)-1;
t=atan((25e-6*m)/50e-3)-atan((25e-6*m2)/50e-3);
t=t*180/pi;
ang = (89.73 - n.*t)+90;
dataf(b:1024,5) = ang;
adjust = 1.1/dataf(b,4);
dataf(b:1024,4) = dataf(b:1024,4).*adjust;

dataf(:,6)=ye;

% Plot second plot of polarization ratio
subplot(2,1,2),plot(dataf(b:1024,5),dataf(b:1024,4))
grid
title('Ratio of polarizations from bistatic receiver')
xlabel('Angle (Deg)')
ylabel('Polarization ratio')
text(170,.9,[file2 ' / ' file1])
orient tall

global file1, dataf;
%datasave(file1,dataf);
end
```

```
%%%%%%%%%%%%%%%%%%%%%%%%%%%%%%%%%%
%   Matlab subroutine hfiltera.m                                 %
%       This program will filter any odd numbered vector of data  %
%       using the Hanning filter                                  %
%                                                                 %
%%%%%%%%%%%%%%%%%%%%%%%%%%%%%%%%%%

function filtout = hfiltera(data,fb)
%hanning filter for column data
%dataout = hfiltera(datain,pt)
%where datain is one column or row of any length
%and pt is the filter window of any size
%pt must be odd!
data = data(:);
n = size(data,1);
h = hanning(fb);
s = sum(h);
w = (fb-1)./2;
v = w+1;
t = fb;
filtout = zeros(1,n) ./0;
data1 = conv(h,data');
filtout(v:n-w) = data1(t:t+(n-w)-v);
filtout = (filtout ./s)';
```

```
%%%%%%%%%%%%%%%%%%%%%%%%%%%%%%%%%%%%
%   Matlab subroutine pholamp.m                                %
%       This program processes the horizontal monostatic Raman  %
%       lidar data.  After filtering and subtracting background noise,  %
%       and correcting for the 1/R^2 dependance, the slope of the    %
%       curve is found to calculate the extinction using Beer's law.   %
%%%%%%%%%%%%%%%%%%%%%%%%%%%%%%%%%%%%

% Read data file from LAMP
%
% function data = readlamp(filetime, lambda);
%
% Returns a matrix
%  [M D Y
%   H MIN SEC                  % Starttime
%   integratredMinutes 0 0
%   E532 E355 E266
%   altitude(km) Counts SCounts]
%
% Note:  numofbins can be chosen.
%
% The Counts are equal Signal - Background.
%
% Franz Balsiger
%                          created   1. Jun. 1995
% Tim Stevens
%                          last mod  9-20-95
%
function data = readlamp(filetime, lambda);
startup
numofbins = 60;
if lambda == 277 name = [filetime '.a14']; end;
if lambda == 284 name = [filetime '.a16']; end;
if lambda == 295 name = [filetime '.a18']; end;
if lambda == 528 name = [filetime '.a08']; end;
if lambda == 530 name = [filetime '.a02']; end;
if lambda == 532 name = [filetime '.N06']; end;
if lambda == 607 name = [filetime '.a10']; end;
if lambda == 660 name = [filetime '.N12']; end;

datafile = fopen(name, 'r');

 %
 % Read the header of the file
line1 = fgetl(datafile);
line2 = fgetl(datafile);
line3 = fgetl(datafile);

 month = str2num(line1(53:54));
 day = str2num(line1(56:57));
 year = str2num(line1(59:60));
 hour = str2num(line1(62:63));
```

```
minutes = str2num(line1(65:66));
seconds = str2num(line1(68:69));
intMin = str2num(line2(16:18));
E532 = str2num(line2(45:51));
E355 = str2num(line2(60:67));
E266 = str2num(line2(77:83));
Bin1 = str2num(line3(21:23))
Bin1Start = str2num(line3(38:40));
AltInc = str2num(line3(53:55));
bg =  str2num(line3(88:96));      %
GroundAlt = 360;

% Reads the background and signal.
data = fread(datafile);
data = setstr(data');
data = sscanf(data,'%f', [11,inf])';
fclose(datafile);

% Calculation of the background standard deviation;
% note that the time base for the background is 14 times
% the base of measured data

[i,k] = size(data(2:20,2:11));
sbg = sqrt(1/14)*std(reshape(data(2:20,2:11), 1, i*k));

[i,k] = size(data(21:40,2:11));
signal = reshape(data(21:40,2:11)', i*k, 1);
%
signal = signal(Bin1: Bin1+numofbins);
ssignal = sqrt(signal);

counts = signal - bg;
scounts = sqrt(ssignal.^2 + sbg^2);

i = 1:numofbins+1;
ALT =[(i-1)* 75]'./1000;
eror=1./ (sqrt(abs(counts)))
counts = ALT.^2 .* counts;
counts = hfiltera(counts,3);

data = [[month  hour    intMin E532  ALT']'    ...
       [day   minutes  0     E355  counts']'  ...
        [year  seconds  0     E266  scounts']'    ];

datat(:,1) = ALT;
datat(:,2) = counts;
datat(:,3) = eror;
datat = datat';
%fname = ['f:\wallops\procesed\' filetime '.607'];
%fid = fopen(fname,'w');
%fprintf(fid,' Alt     607nm   error \n');
%fprintf(fid,' %1.3f\t %1.3e\t %1.3e\n',datat);
```

```
%fclose(fid);
% calculate the extinction using the slope of the curve and Beer's law.
a1 = 18;
a2 = 30;
p = polyfit(ALT(a1:a2),counts(a1:a2),1);
f = polyval(p,ALT(a1:a2));
i1 = polyval(p,ALT(a1))
i2 = polyval(p,ALT(a2))
deltaa = ALT(a2)-ALT(a1)
ext607 = log(i2./i1)./(-2.*deltaa)
plot(ALT,counts,'y',ALT(a1:a2),f,'r ')
%plot(ALT(13:30),f,'r ')

axis([0 3.5 0 6000])
grid
→
```

Appendix E

PROCESSED BISTATIC LIDAR DATA SAMPLES FROM THE WALLOPS CASE I 1995 PROGRAM

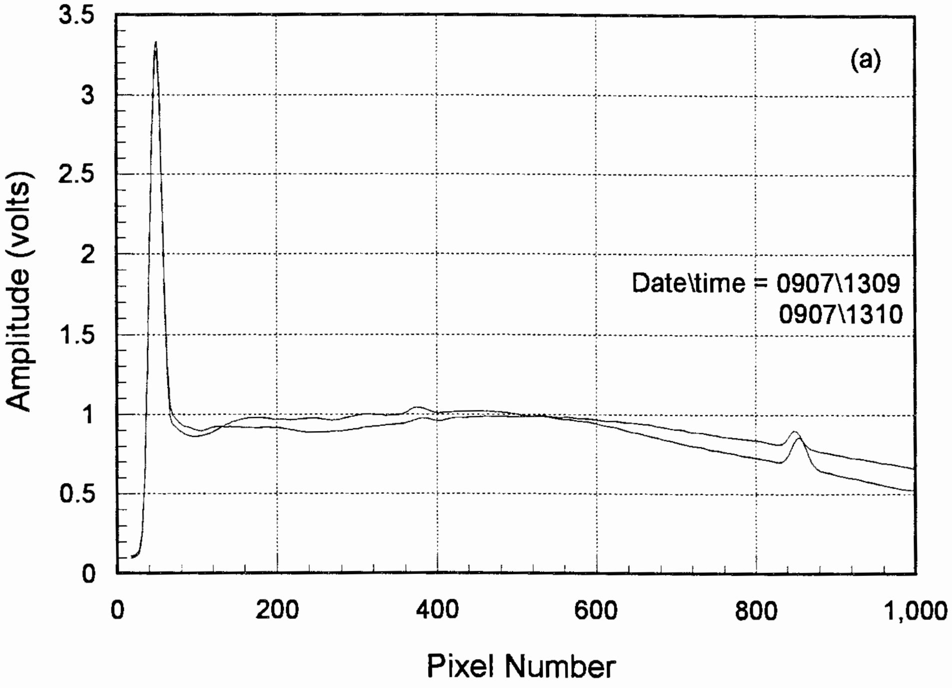
(a)
Amplitude (volts)
Pixel Number
Date\time = 0907\1309
0907\1310
0
0.5
1
1.5
2
2.5
3
3.5
0
200
400
600
800
1,000

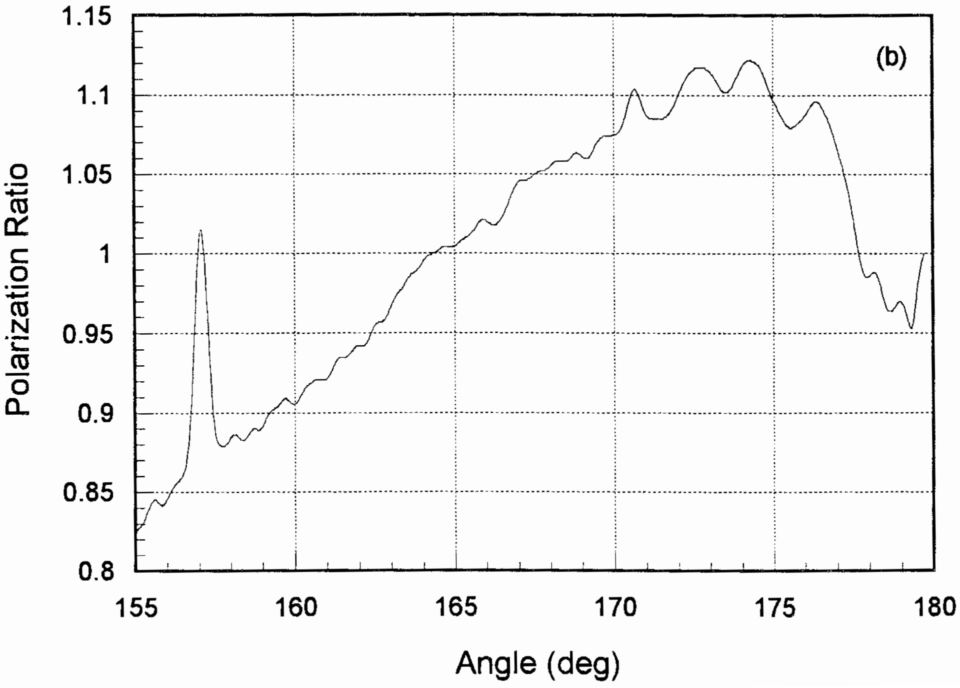
(b)
Polarization Ratio
Angle (deg)
0.8
0.85
0.9
0.95
1
1.05
1.1
1.15
155
160
165
170
175
180

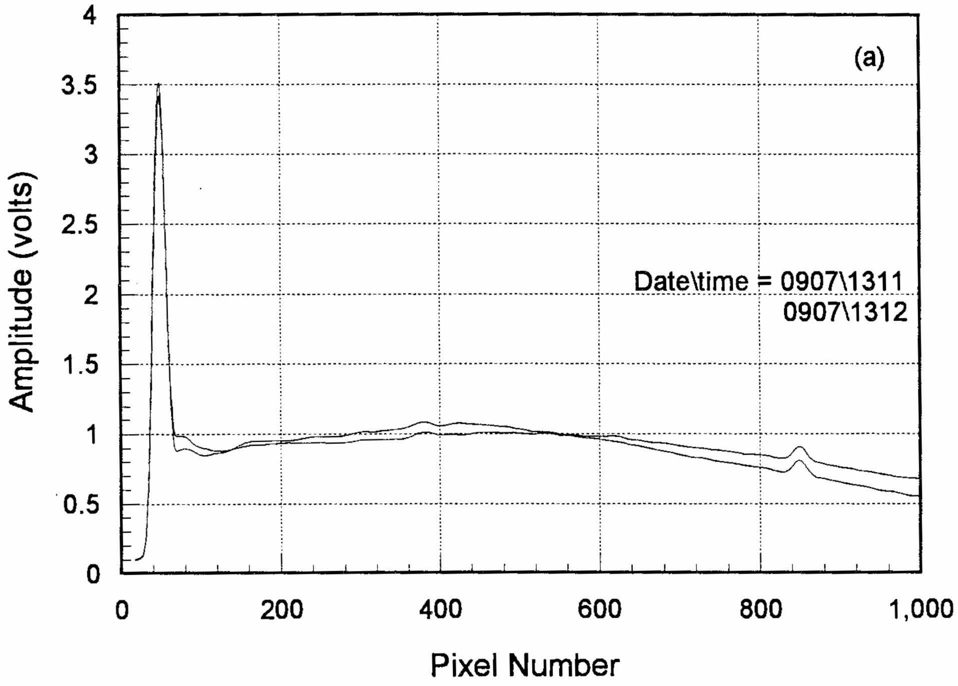
(a)
Amplitude (volts)
Pixel Number
0
0.5
1
1.5
2
2.5
3
3.5
4
0
200
400
600
800
1,000
Date\time = 0907\1311
0907\1312

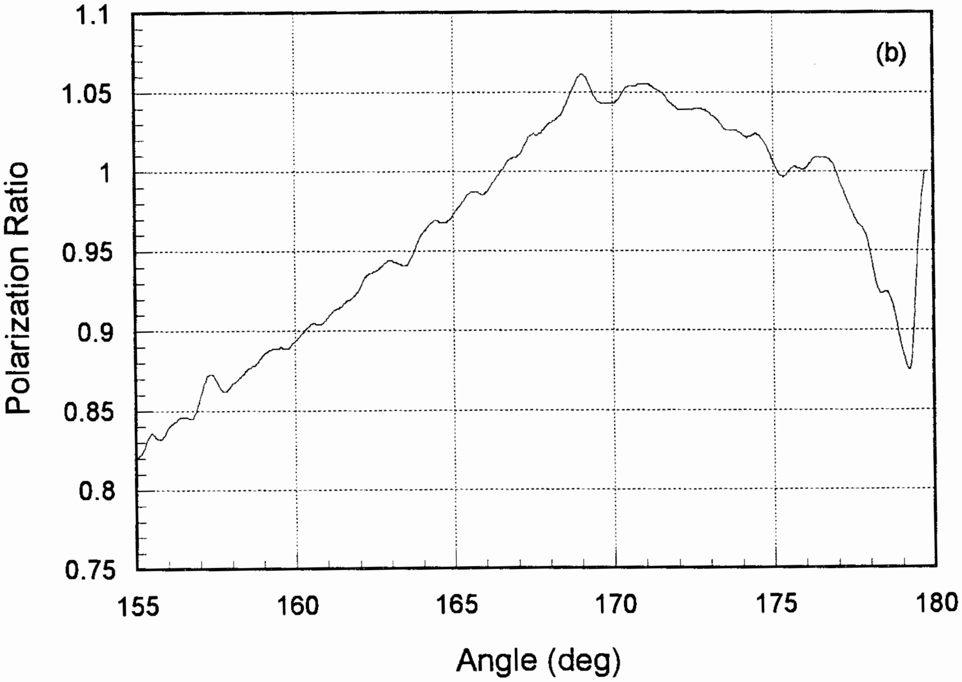
(b)
Polarization Ratio
Angle (deg)
0.75
0.8
0.85
0.9
0.95
1
1.05
1.1
155
160
165
170
175
180

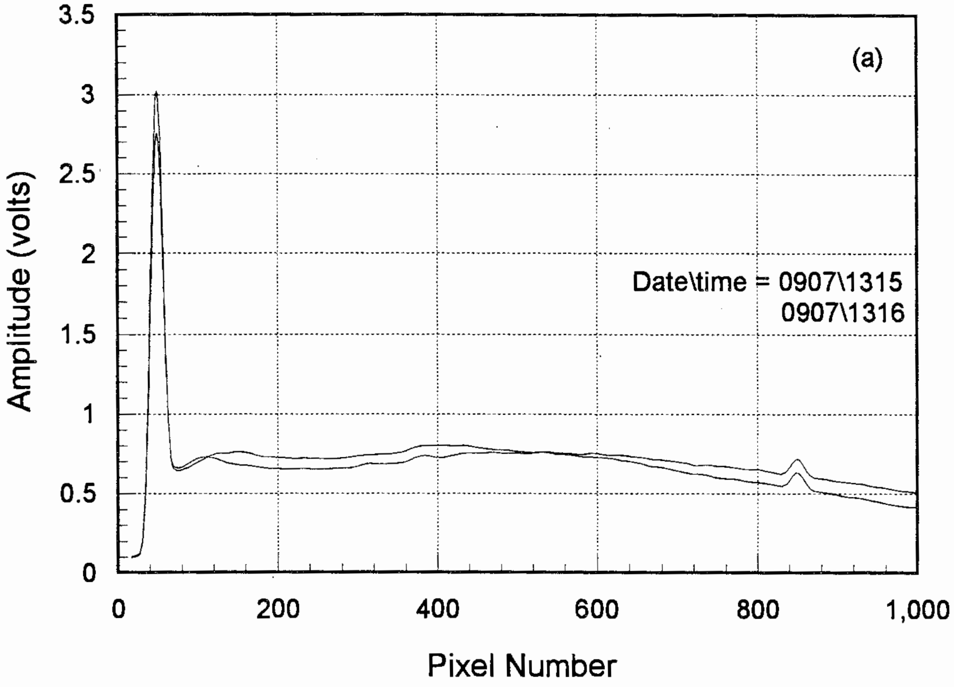
(a)
Amplitude (volts)
Pixel Number
Date\time = 0907\1315
0907\1316
0
0.5
1
1.5
2
2.5
3
3.5
0
200
400
600
800
1,000

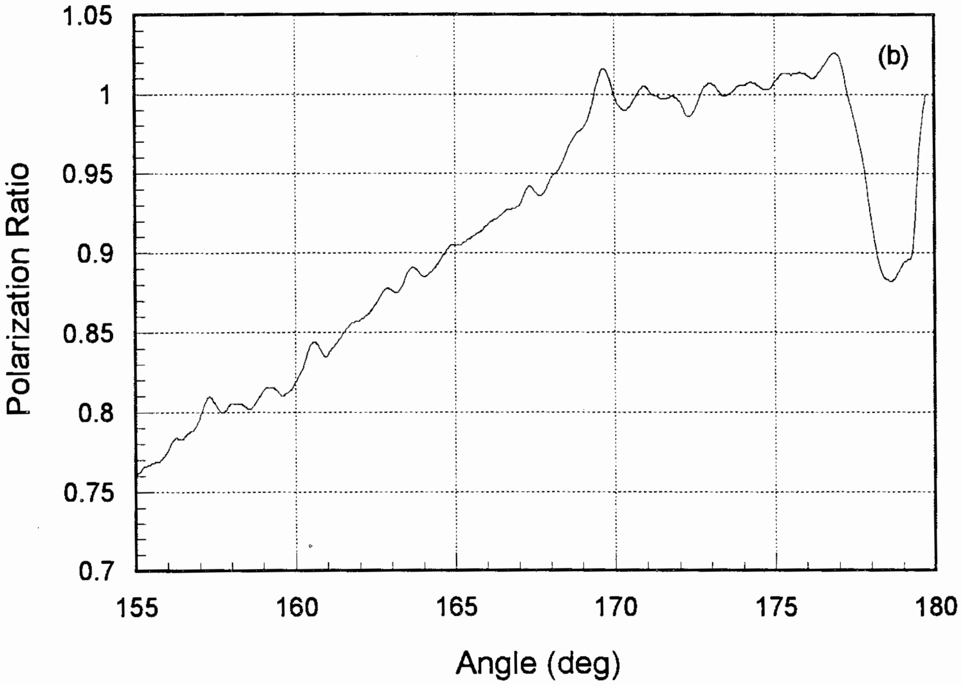
(b)
Polarization Ratio
Angle (deg)
0.7
0.75
0.8
0.85
0.9
0.95
1
1.05
155
160
165
170
175
180

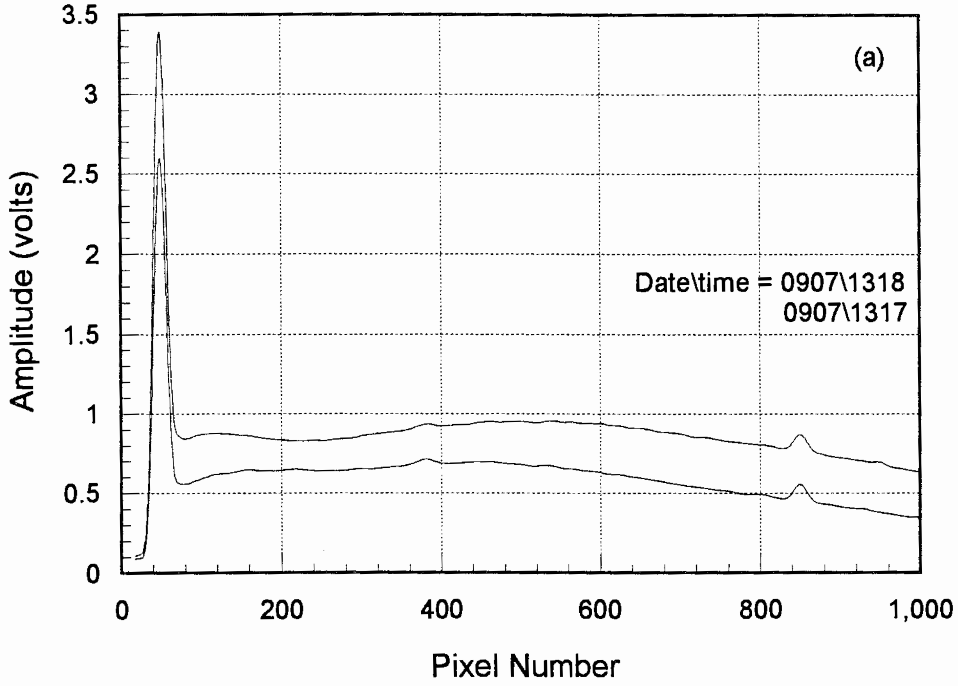
(a)
Amplitude (volts)
Pixel Number
Date\time = 0907\1318
0907\1317
0
0.5
1
1.5
2
2.5
3
3.5
0
200
400
600
800
1,000

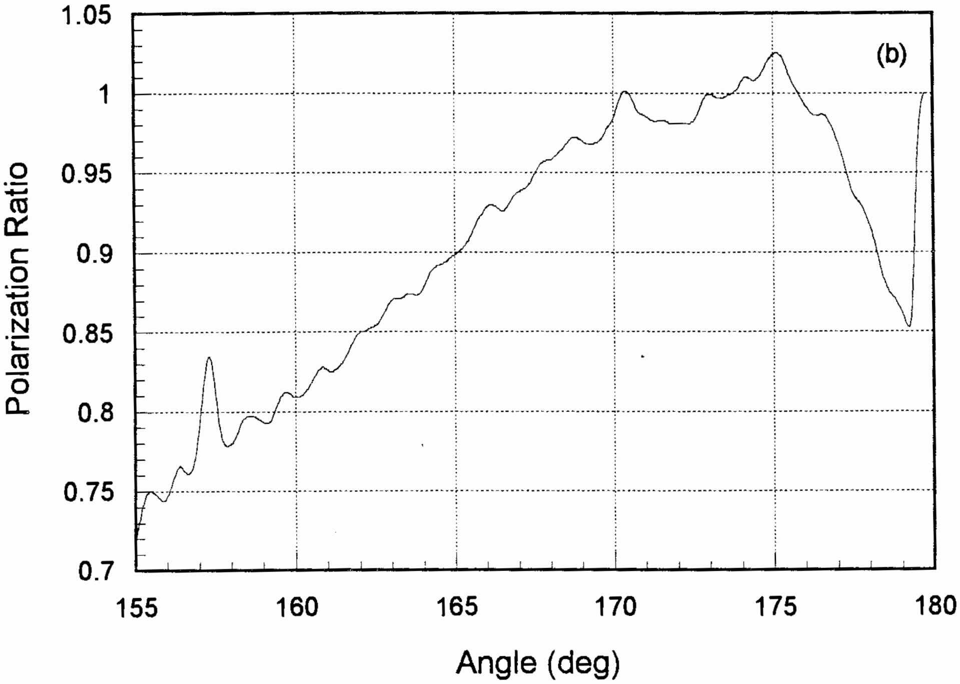
(b)
Polarization Ratio
Angle (deg)
0.7
0.75
0.8
0.85
0.9
0.95
1
1.05
155
160
165
170
175
180

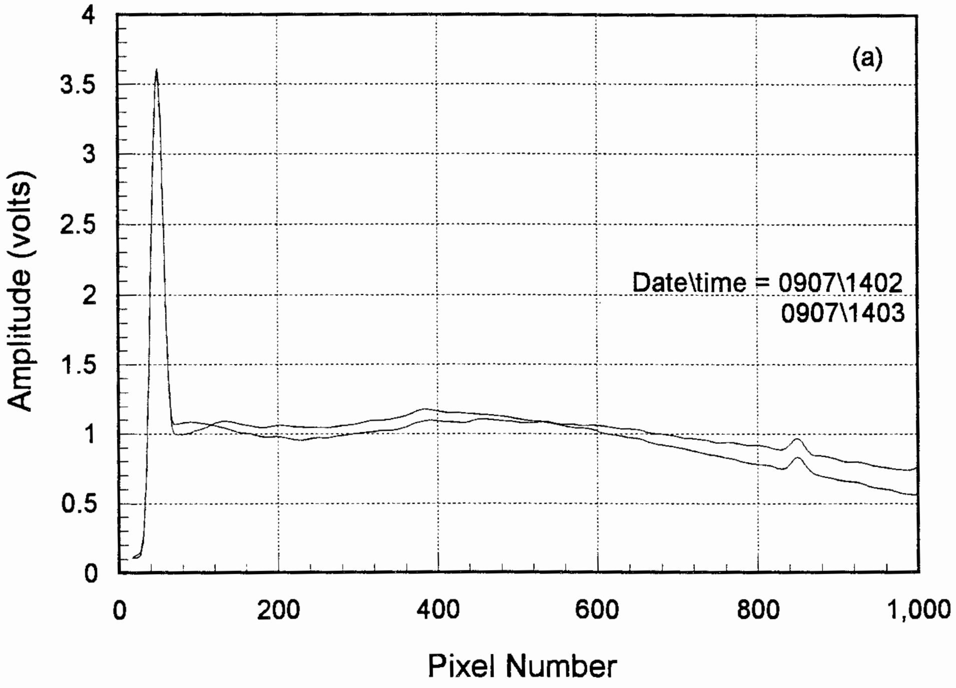
(a)
Amplitude (volts)
Pixel Number
0
0.5
1
1.5
2
2.5
3
3.5
4
0
200
400
600
800
1,000
Date\time = 0907\1402
0907\1403

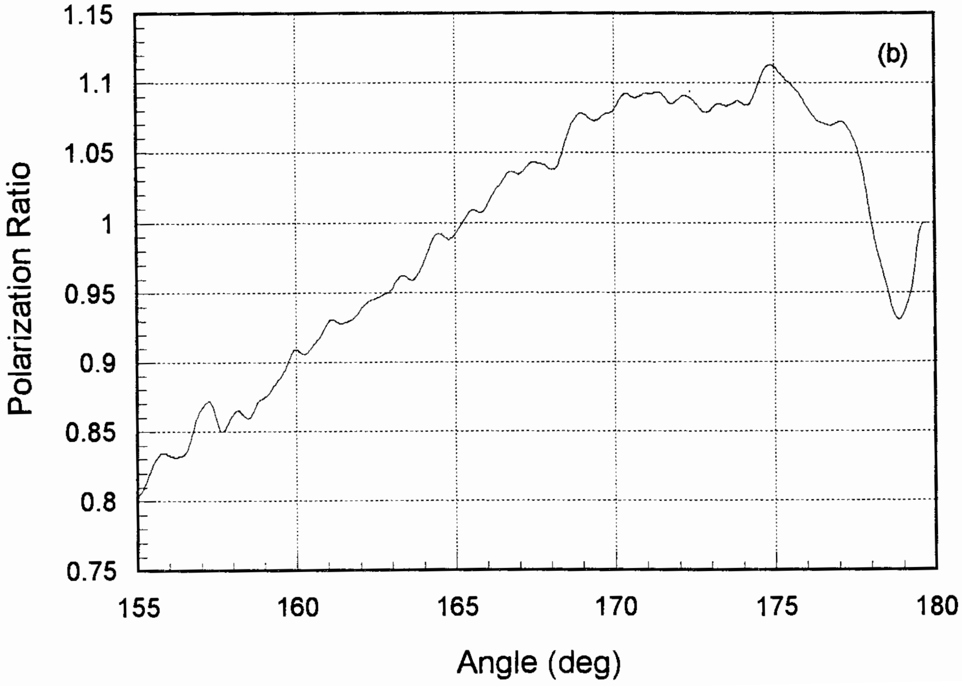
(b)
Polarization Ratio
Angle (deg)
0.75
0.8
0.85
0.9
0.95
1
1.05
1.1
1.15
155
160
165
170
175
180

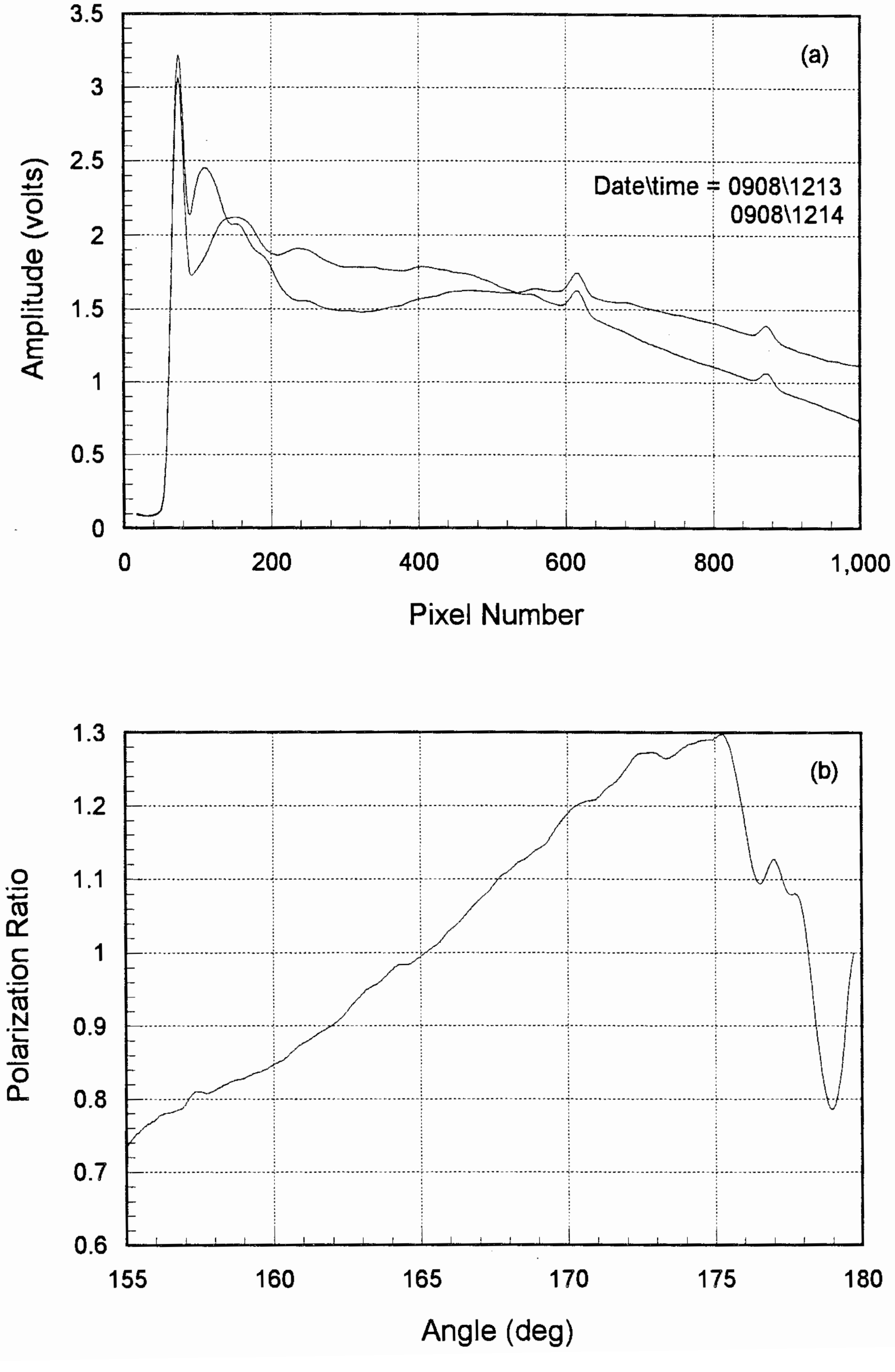
(a)
Amplitude (volts)
3.5
3
2.5
2
1.5
1
0.5
0
0
200
400
600
800
1,000
Pixel Number
Date\time = 0908\1213
0908\1214
(b)
Polarization Ratio
1.3
1.2
1.1
1
0.9
0.8
0.7
0.6
155
160
165
170
175
180
Angle (deg)

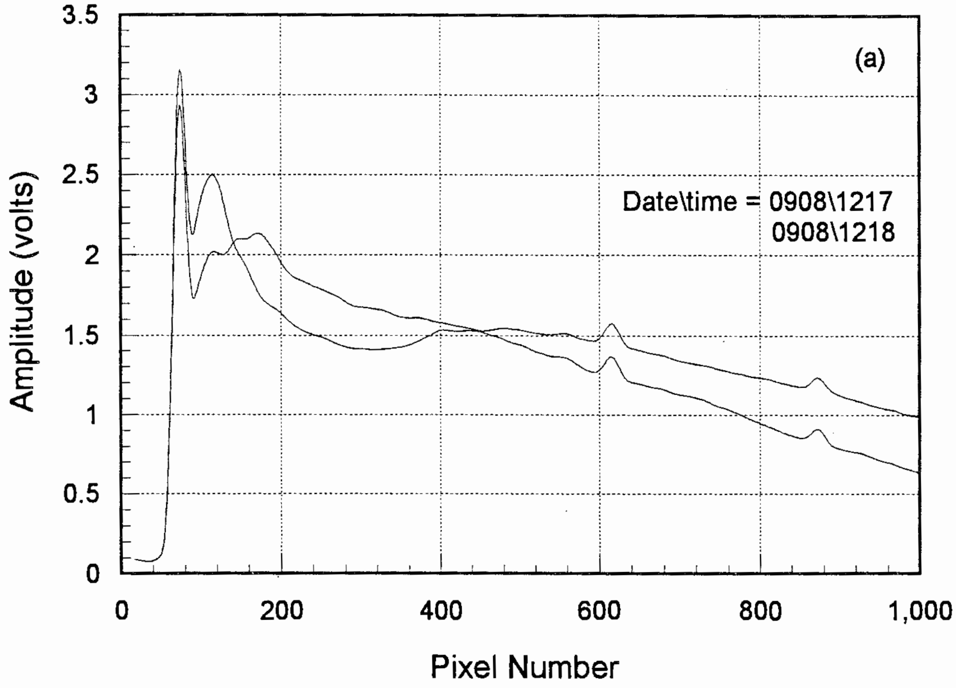
(a)
Date\time = 0908\1217
0908\1218
Amplitude (volts)
3.5
3
2.5
2
1.5
1
0.5
0
0
200
400
600
800
1,000
Pixel Number

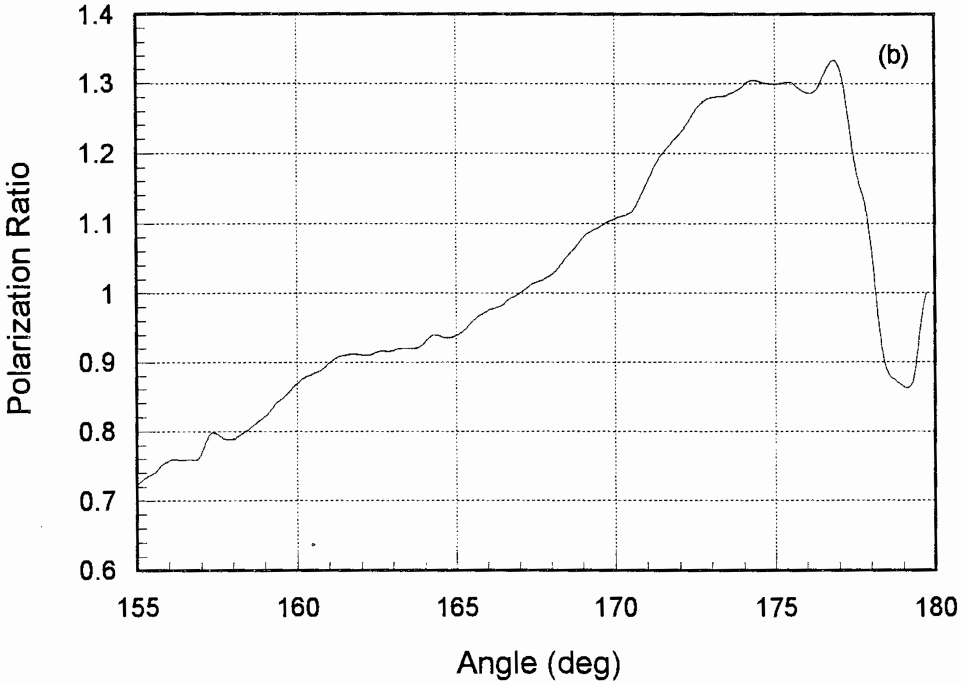
(b)
Polarization Ratio
1.4
1.3
1.2
1.1
1
0.9
0.8
0.7
0.6
155
160
165
170
175
180
Angle (deg)

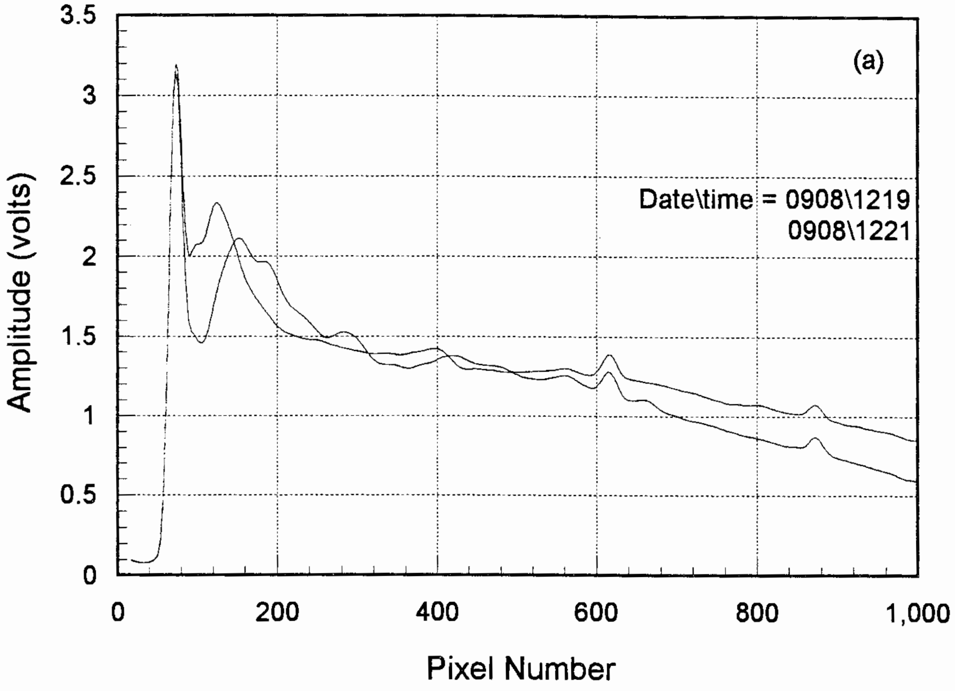
(a)
Amplitude (volts)
Pixel Number
Date\time = 0908\1219
0908\1221
0
0.5
1
1.5
2
2.5
3
3.5
0
200
400
600
800
1,000

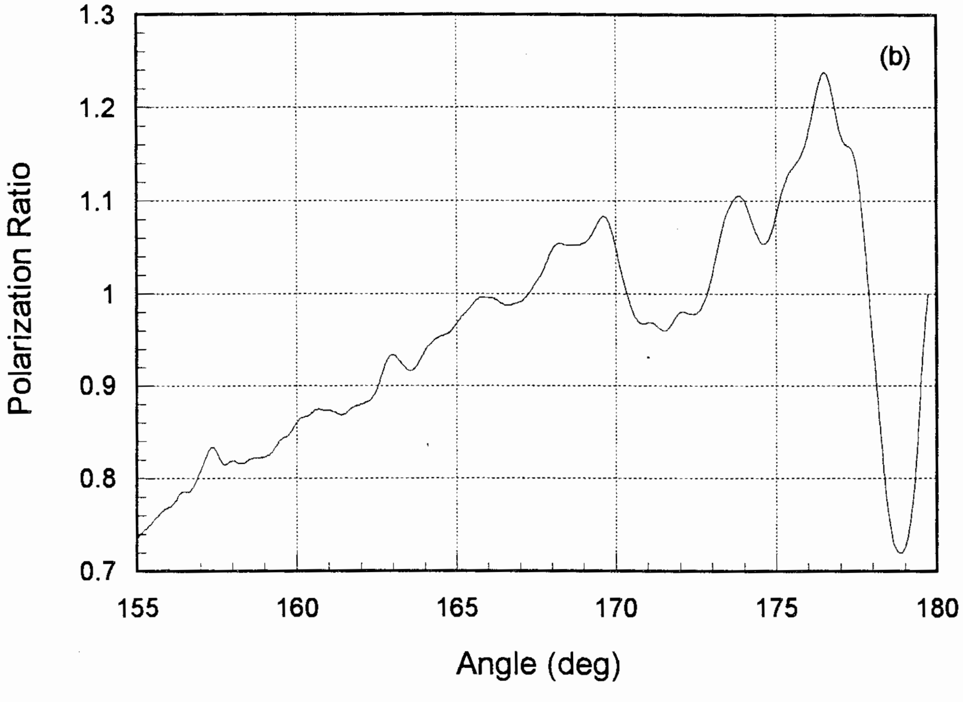
(b)
Polarization Ratio
Angle (deg)
0.7
0.8
0.9
1
1.1
1.2
1.3
155
160
165
170
175
180

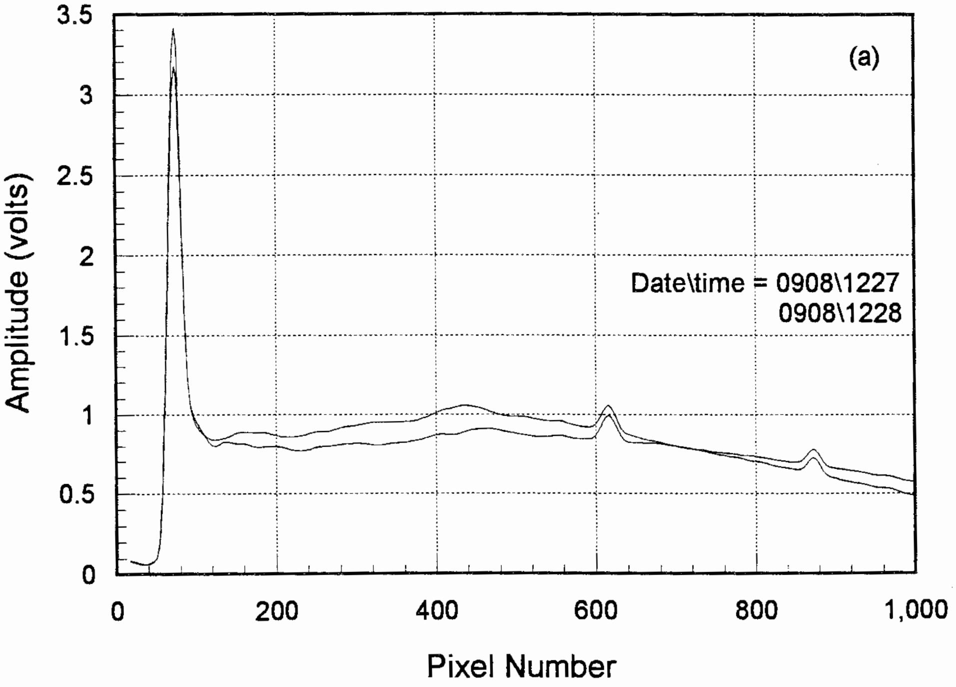
(a)
Date\time = 0908\1227
0908\1228
Amplitude (volts)
0
0.5
1
1.5
2
2.5
3
3.5
Pixel Number
0
200
400
600
800
1,000

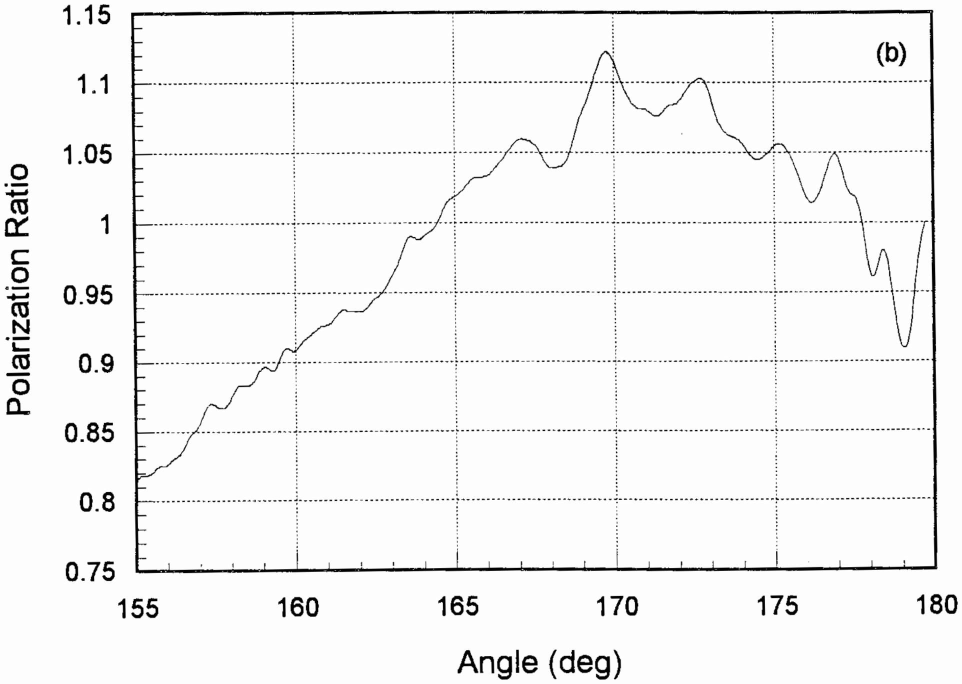
(b)
Polarization Ratio
0.75
0.8
0.85
0.9
0.95
1
1.05
1.1
1.15
Angle (deg)
155
160
165
170
175
180

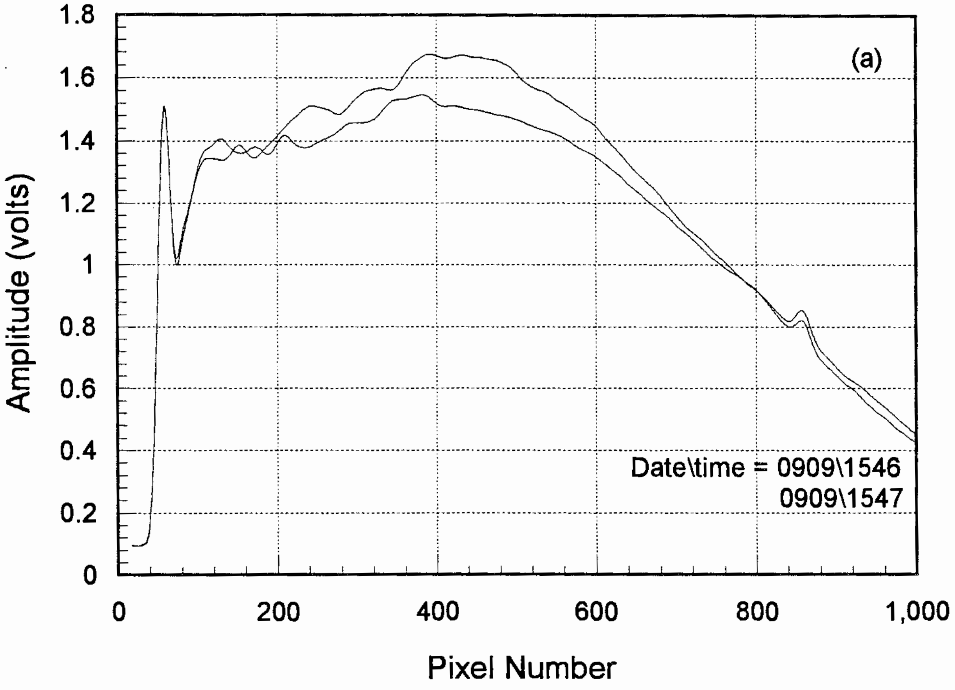
(a)
Amplitude (volts)
1.8
1.6
1.4
1.2
1
0.8
0.6
0.4
0.2
0
0
200
400
600
800
1,000
Pixel Number
Date\time = 0909\1546
0909\1547

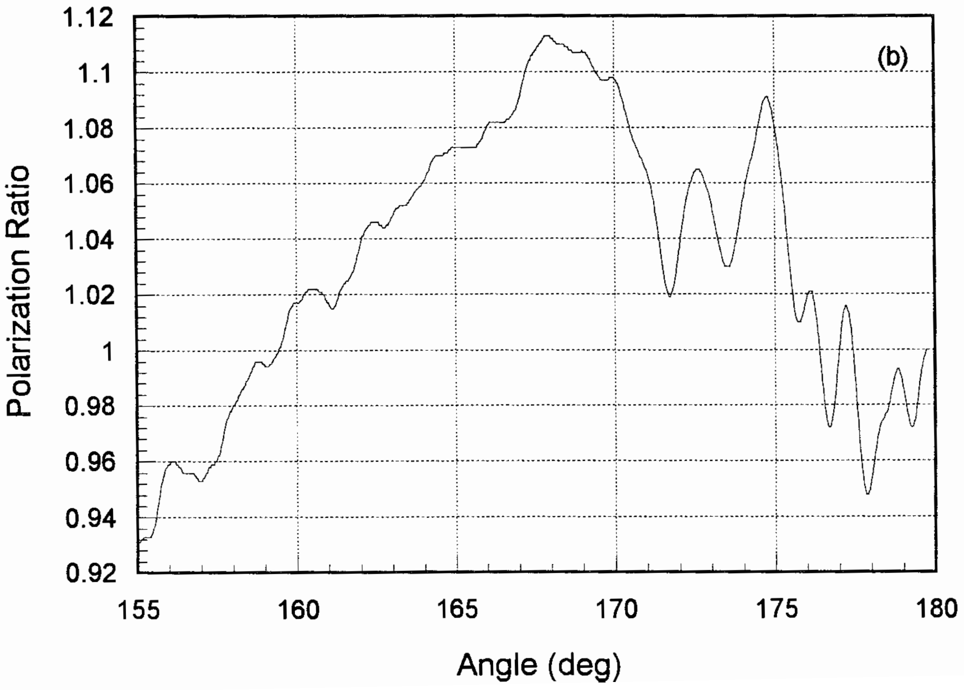
(b)
Polarization Ratio
1.12
1.1
1.08
1.06
1.04
1.02
1
0.98
0.96
0.94
0.92
155
160
165
170
175
180
Angle (deg)

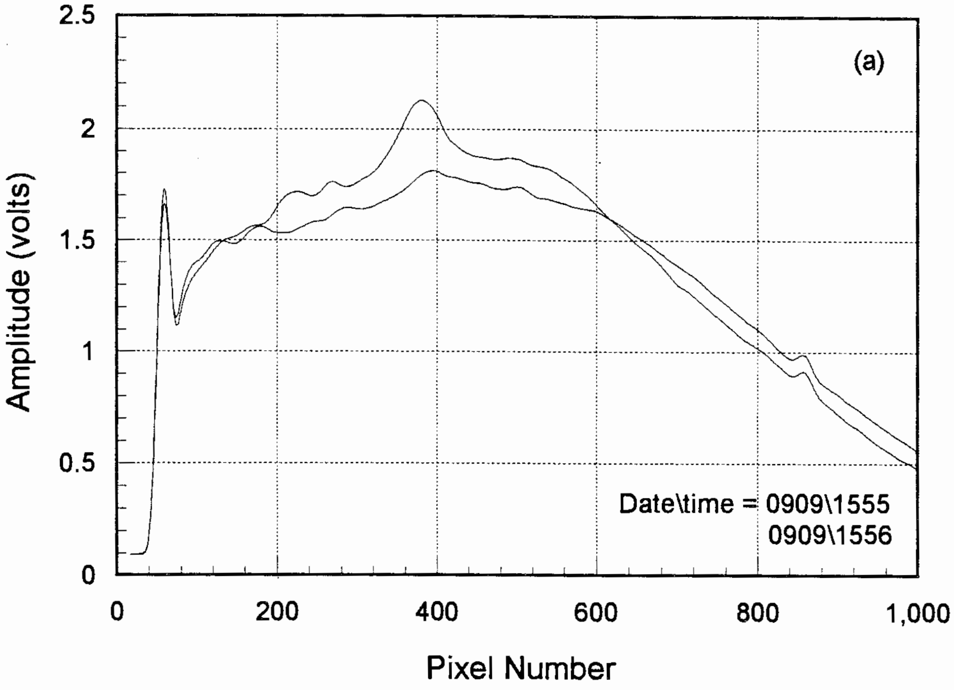
(a)
Amplitude (volts)
2.5
2
1.5
1
0.5
0
0
200
400
600
800
1,000
Pixel Number
Date\time = 0909\1555
0909\1556


(b)
Polarization Ratio
1.2
1.15
1.1
1.05
1
0.95
0.9
0.85
0.8
155
160
165
170
175
180
Angle (deg)

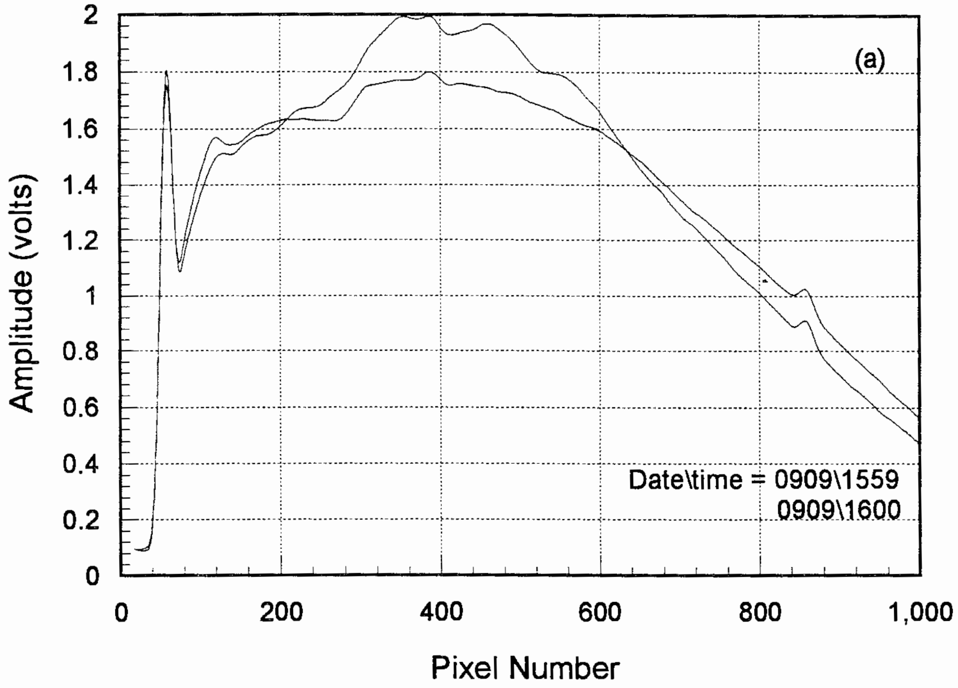
(a)
Amplitude (volts)
2
1.8
1.6
1.4
1.2
1
0.8
0.6
0.4
0.2
0
0
200
400
600
800
1,000
Pixel Number
Date\time = 0909\1559
0909\1600

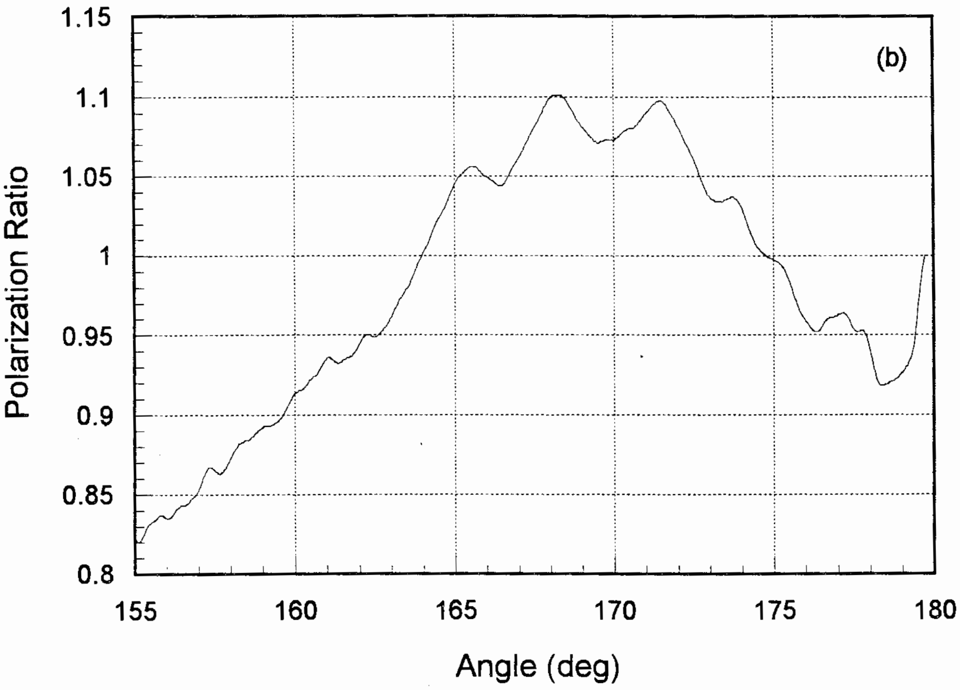
(b)
Polarization Ratio
1.15
1.1
1.05
1
0.95
0.9
0.85
0.8
155
160
165
170
175
180
Angle (deg)

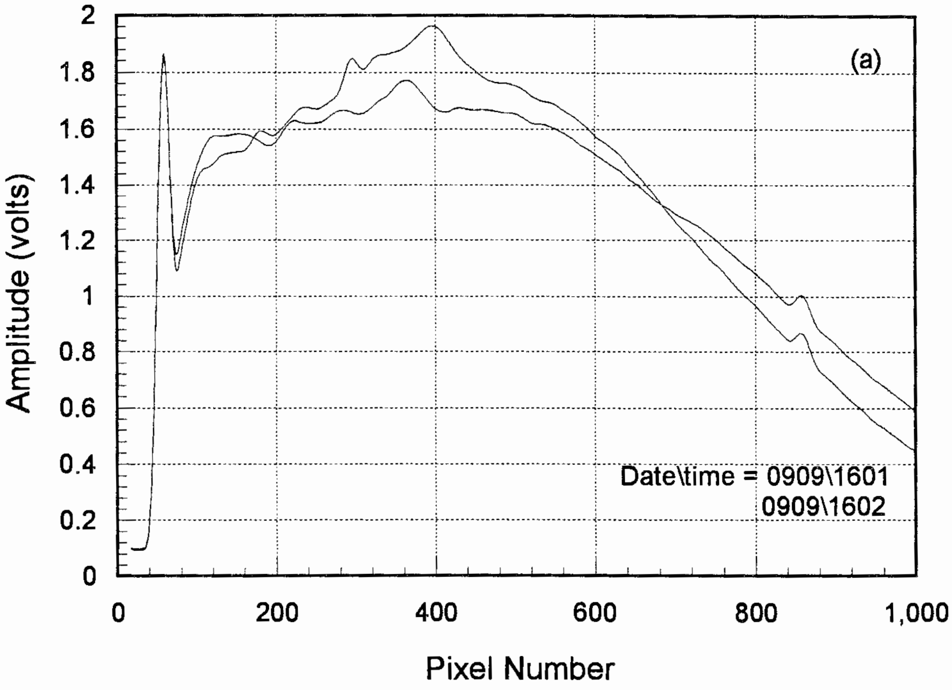
(a)
Amplitude (volts)
2
1.8
1.6
1.4
1.2
1
0.8
0.6
0.4
0.2
0
0
200
400
600
800
1,000
Pixel Number
Date\time = 0909\1601
0909\1602

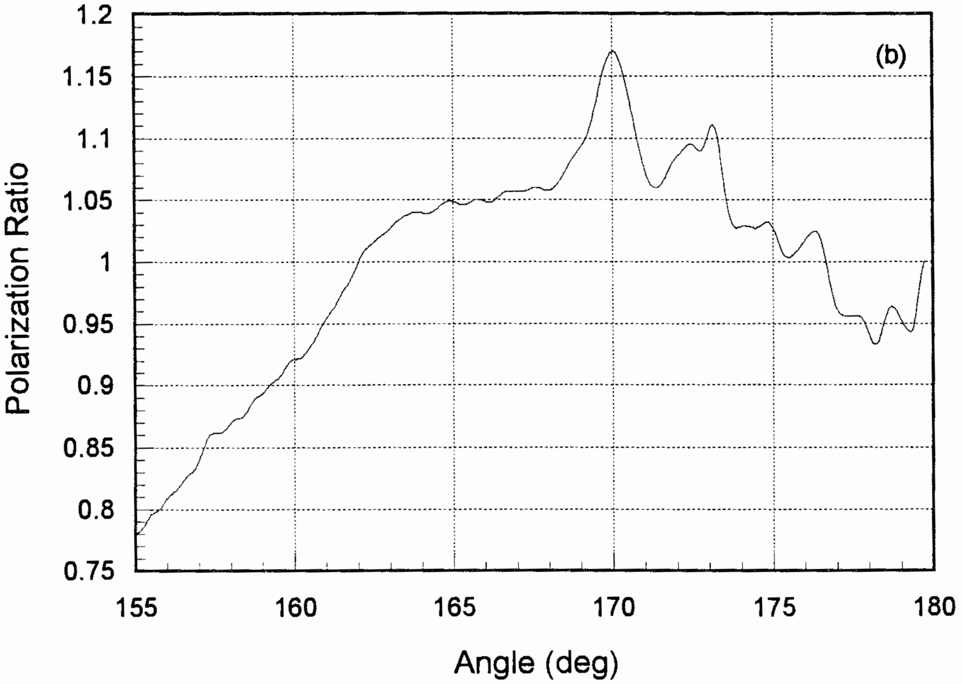
(b)
Polarization Ratio
1.2
1.15
1.1
1.05
1
0.95
0.9
0.85
0.8
0.75
155
160
165
170
175
180
Angle (deg)

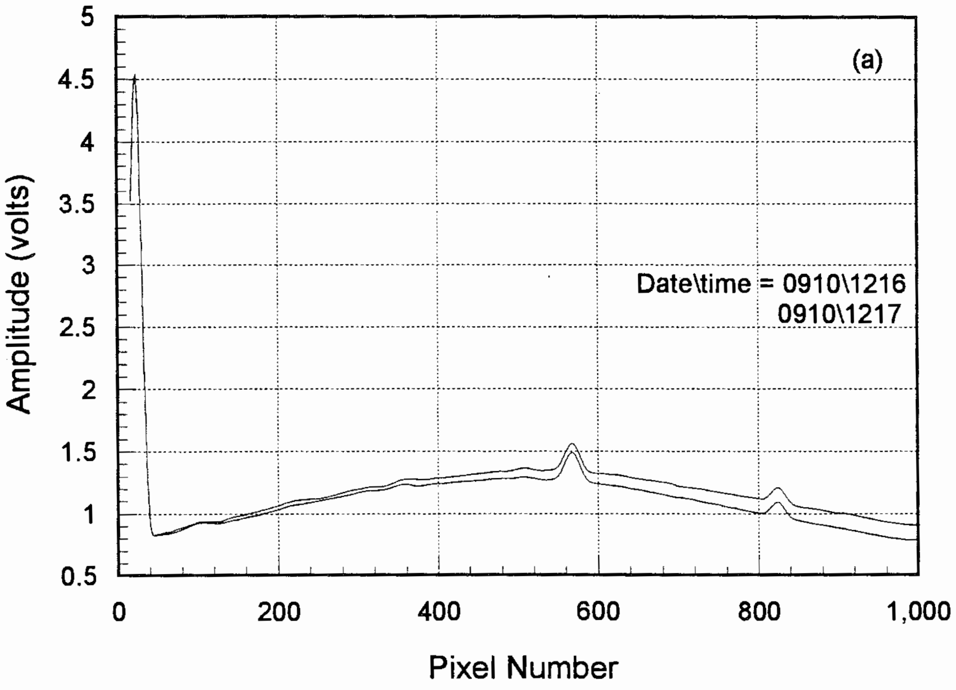
(a)
Date\time = 0910\1216
0910\1217
Amplitude (volts)
5
4.5
4
3.5
3
2.5
2
1.5
1
0.5
0
200
400
600
800
1,000
Pixel Number

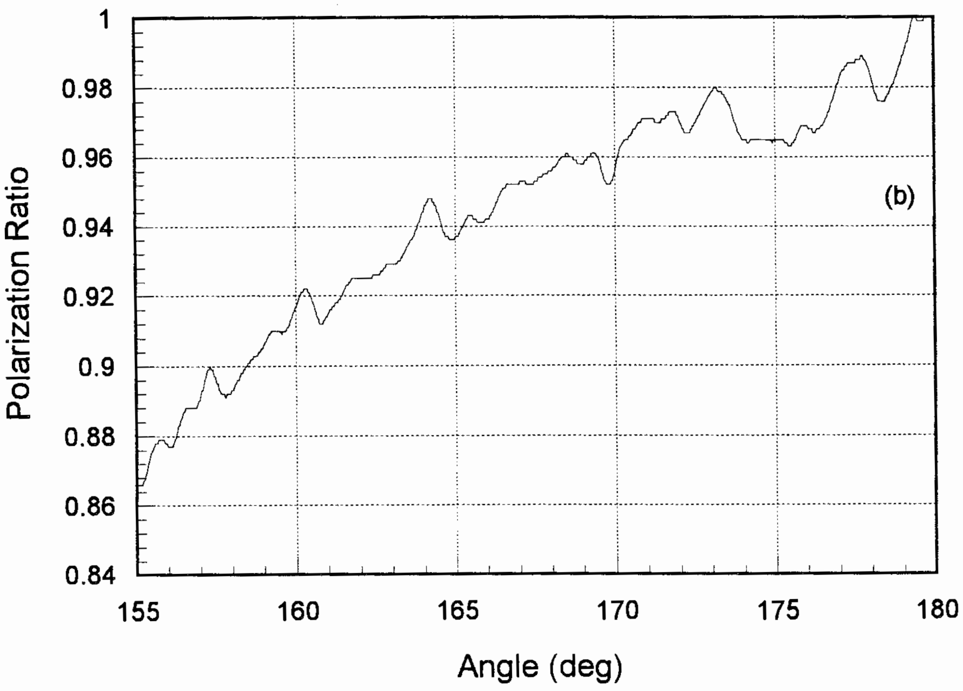
(b)
Polarization Ratio
1
0.98
0.96
0.94
0.92
0.9
0.88
0.86
0.84
155
160
165
170
175
180
Angle (deg)

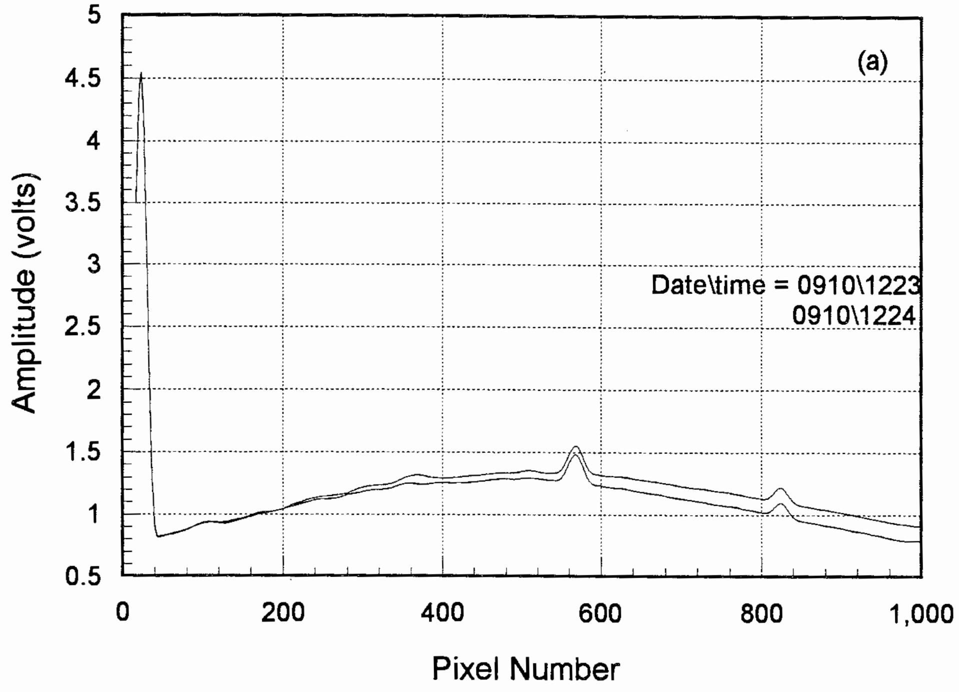
(a)
Amplitude (volts)
5
4.5
4
3.5
3
2.5
2
1.5
1
0.5
0
200
400
600
800
1,000
Pixel Number
Date\time = 0910\1223
0910\1224

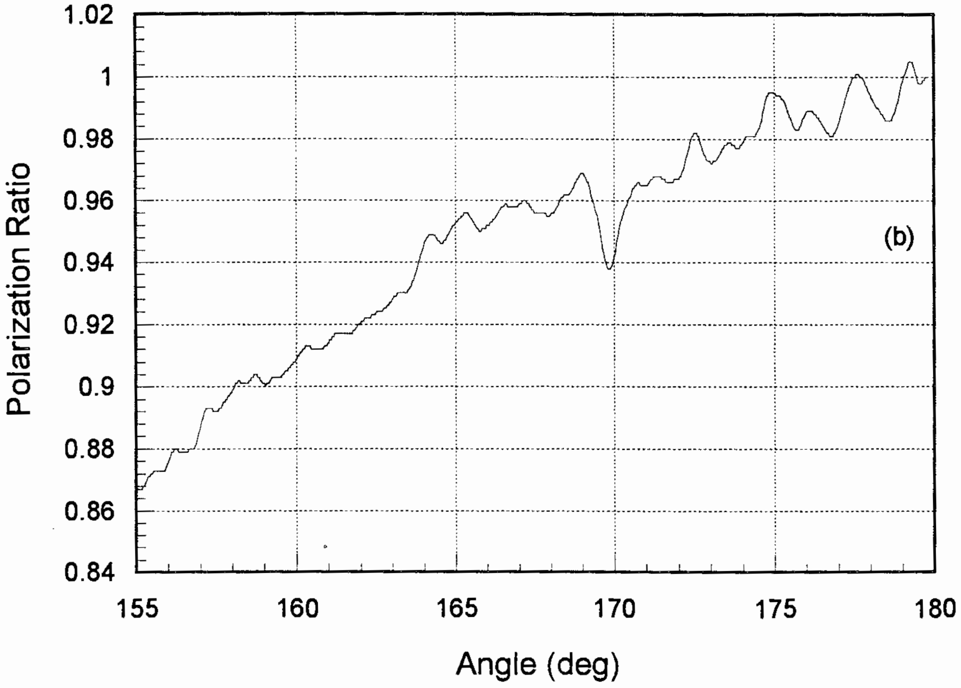
(b)
Polarization Ratio
1.02
1
0.98
0.96
0.94
0.92
0.9
0.88
0.86
0.84
155
160
165
170
175
180
Angle (deg)

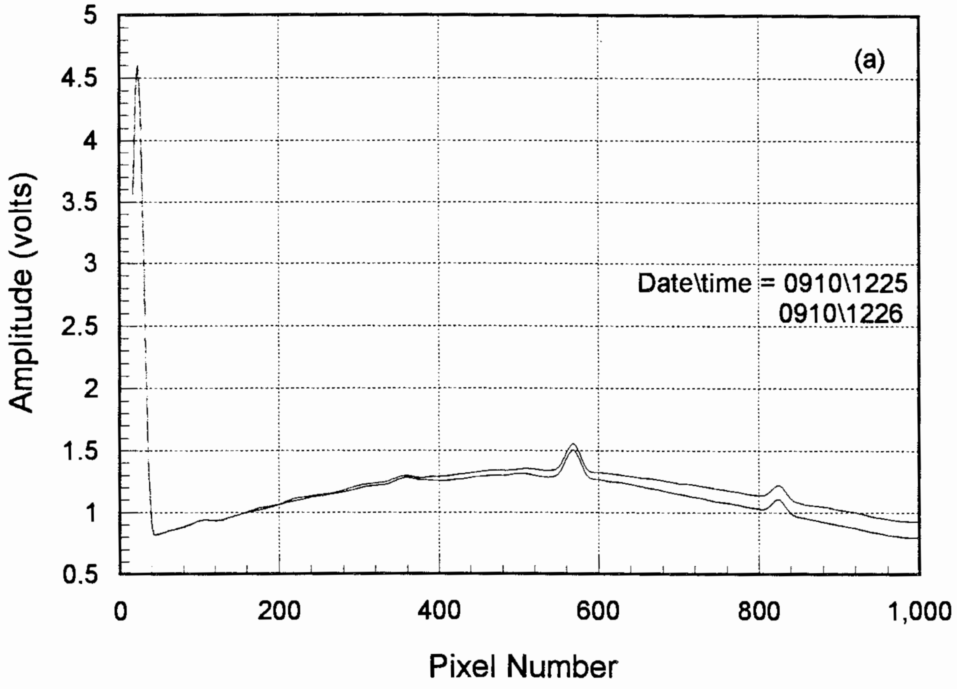
(a)
Date\time = 0910\1225
0910\1226
Amplitude (volts)
Pixel Number
0.5
1
1.5
2
2.5
3
3.5
4
4.5
5
0
200
400
600
800
1,000

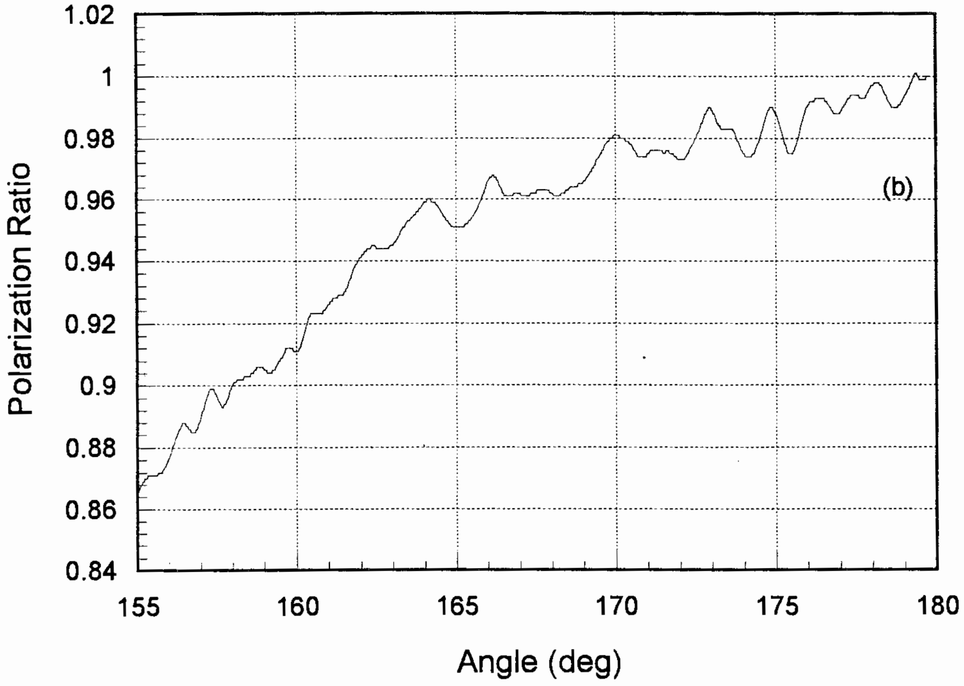
(b)
Polarization Ratio
Angle (deg)
0.84
0.86
0.88
0.9
0.92
0.94
0.96
0.98
1
1.02
155
160
165
170
175
180

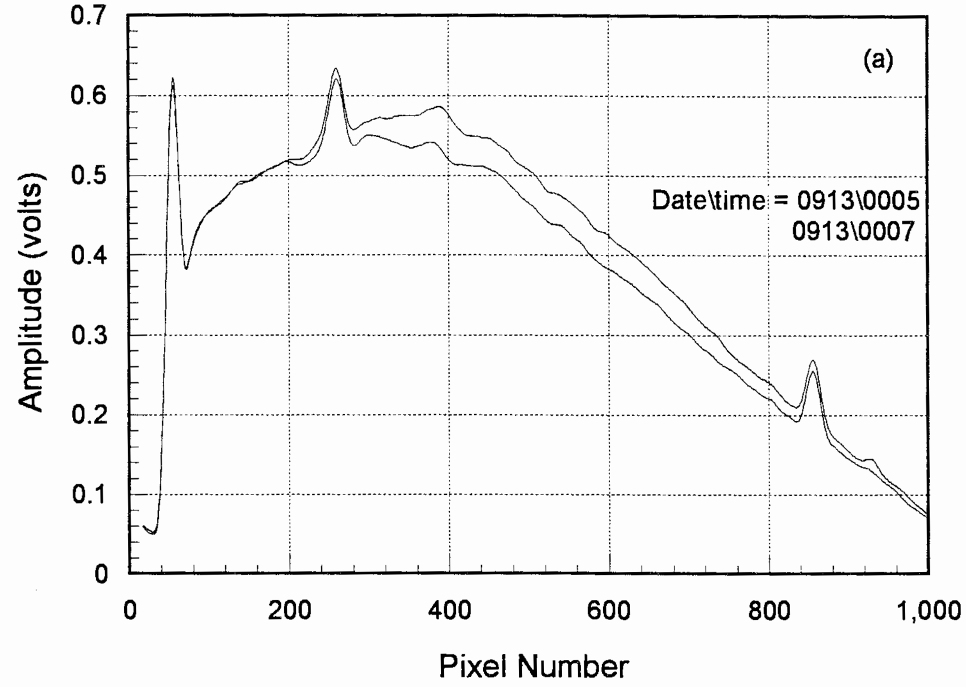
(a)
Amplitude (volts)
0.7
0.6
0.5
0.4
0.3
0.2
0.1
0
0
200
400
600
800
1,000
Pixel Number
Date\time = 0913\0005
0913\0007

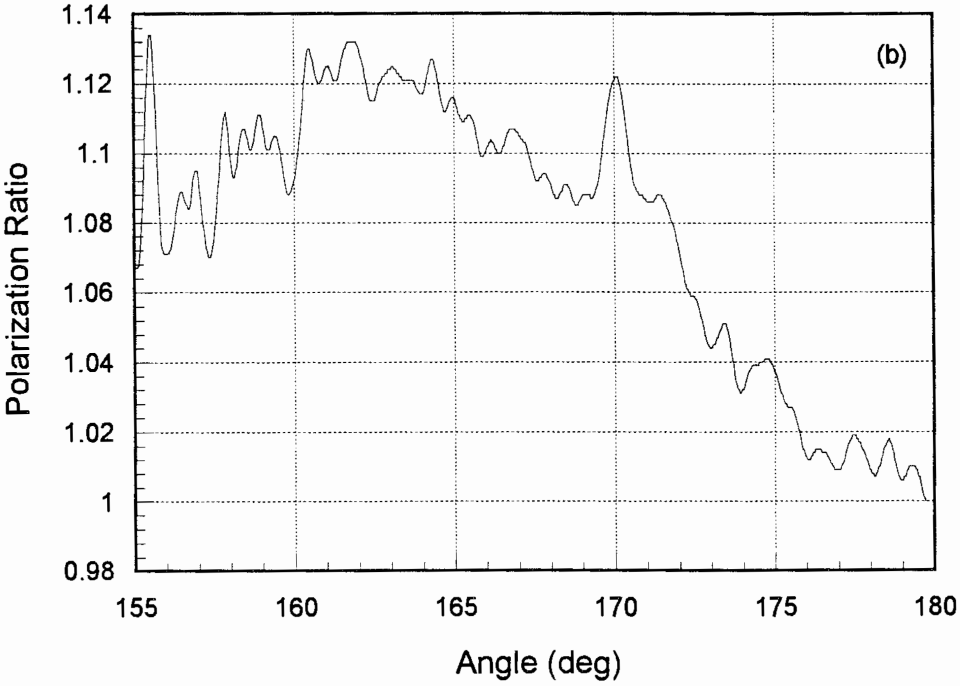
(b)
Polarization Ratio
1.14
1.12
1.1
1.08
1.06
1.04
1.02
1
0.98
155
160
165
170
175
180
Angle (deg)

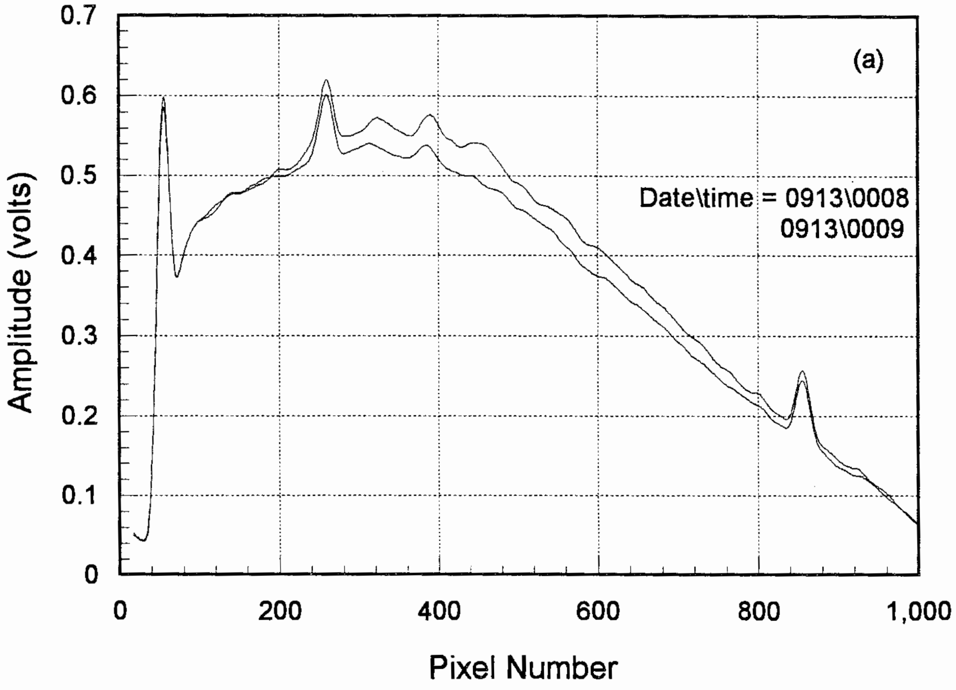

(a)
Amplitude (volts)
Pixel Number
Date\time = 0913\0008
0913\0009
0
0.1
0.2
0.3
0.4
0.5
0.6
0.7
0
200
400
600
800
1,000

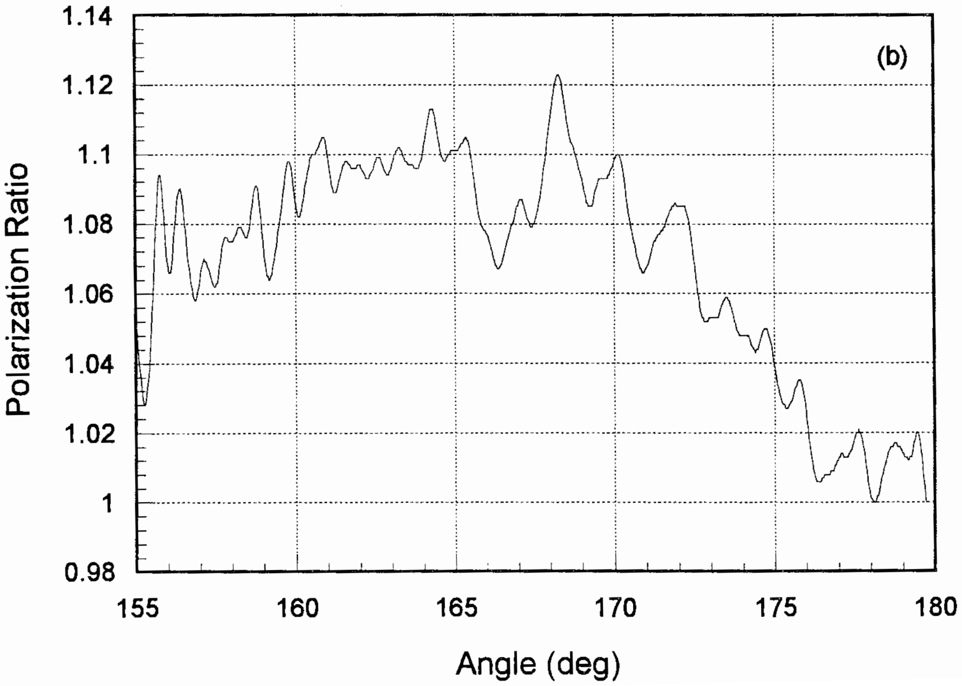

(b)
Polarization Ratio
Angle (deg)
0.98
1
1.02
1.04
1.06
1.08
1.1
1.12
1.14
155
160
165
170
175
180

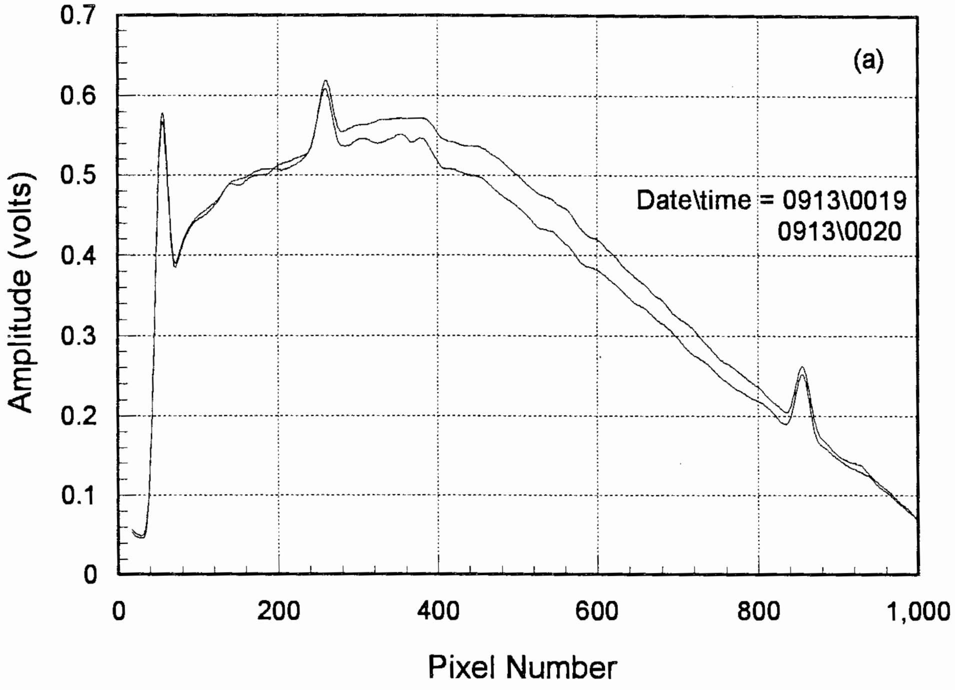
(a)
Amplitude (volts)
0
0.1
0.2
0.3
0.4
0.5
0.6
0.7
Pixel Number
0
200
400
600
800
1,000
Date\time = 0913\0019
0913\0020

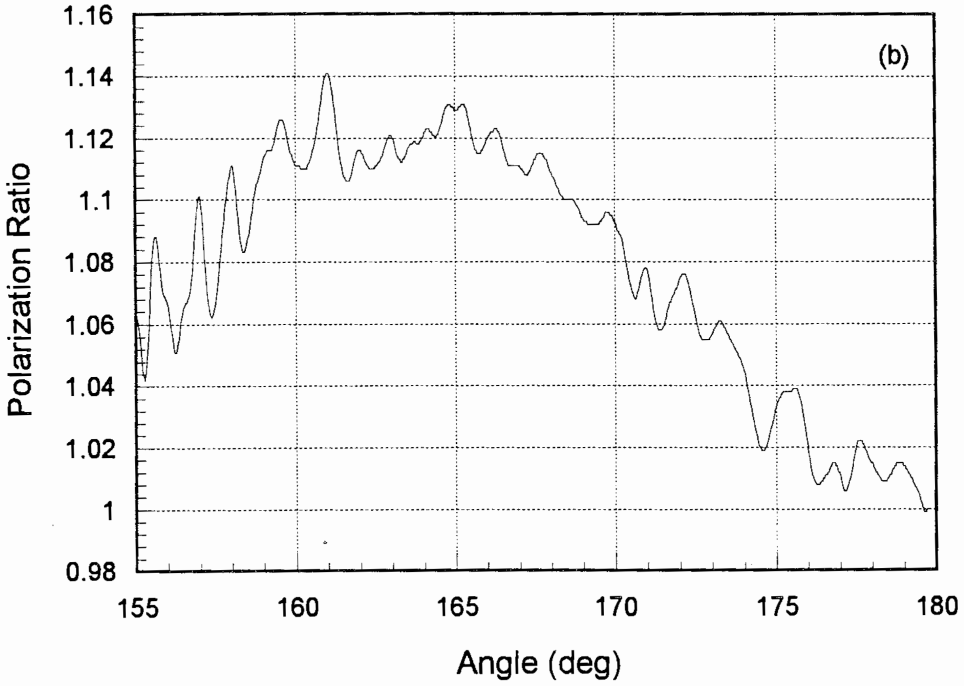
(b)
Polarization Ratio
0.98
1
1.02
1.04
1.06
1.08
1.1
1.12
1.14
1.16
Angle (deg)
155
160
165
170
175
180

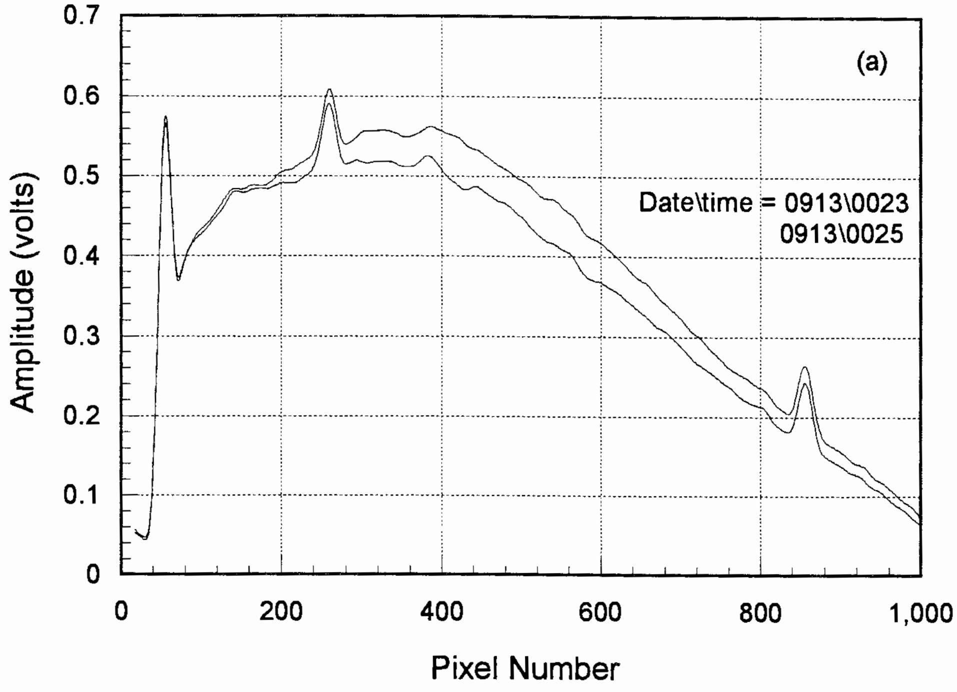
(a)
Amplitude (volts)
0.7
0.6
0.5
0.4
0.3
0.2
0.1
0
Pixel Number
0
200
400
600
800
1,000
Date\time = 0913\0023
0913\0025

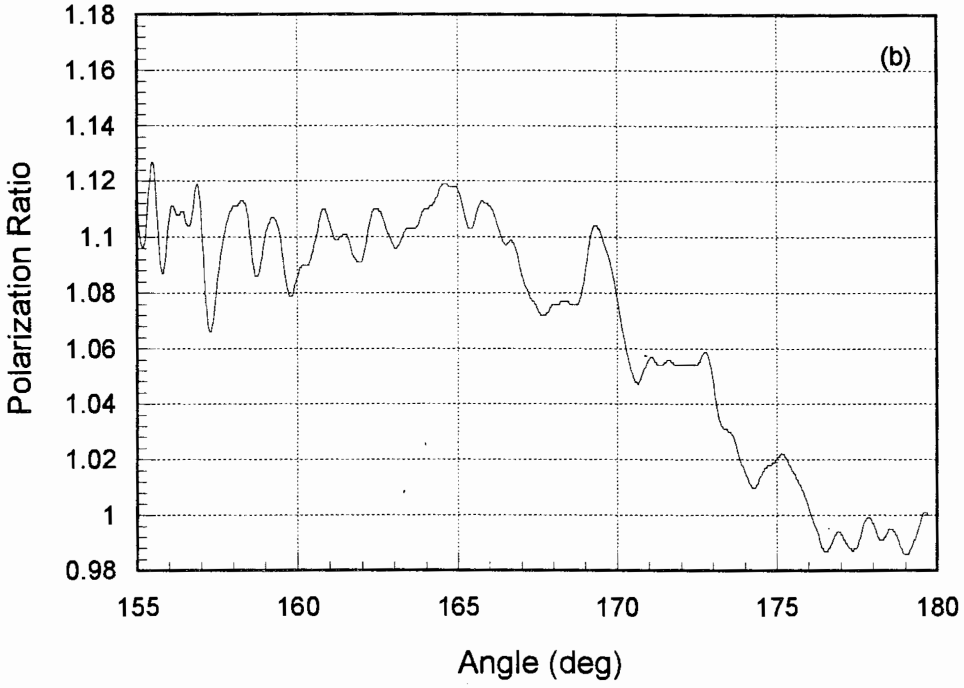
(b)
Polarization Ratio
1.18
1.16
1.14
1.12
1.1
1.08
1.06
1.04
1.02
1
0.98
Angle (deg)
155
160
165
170
175
180

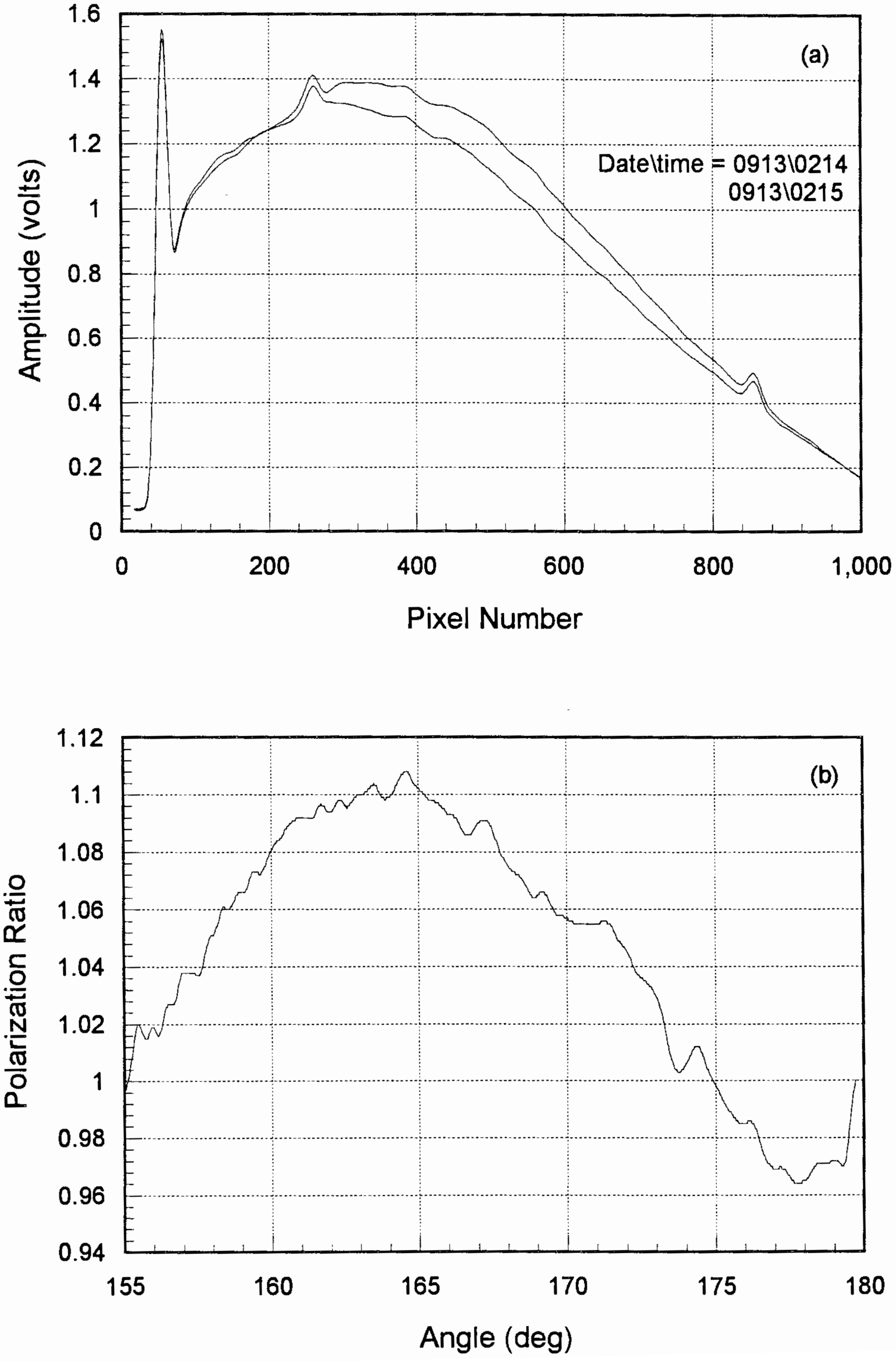
(a)
Amplitude (volts)
1.6
1.4
1.2
1
0.8
0.6
0.4
0.2
0
0
200
400
600
800
1,000
Pixel Number
Date\time = 0913\0214
0913\0215
(b)
Polarization Ratio
1.12
1.1
1.08
1.06
1.04
1.02
1
0.98
0.96
0.94
155
160
165
170
175
180
Angle (deg)

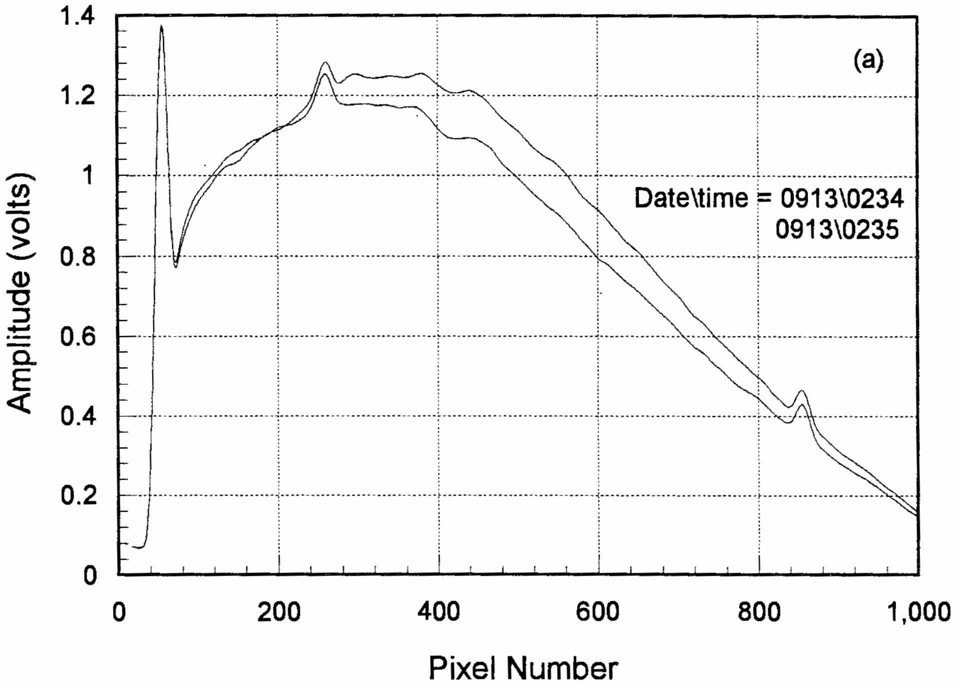
(a)
Date\time = 0913\0234
0913\0235
Amplitude (volts)
1.4
1.2
1
0.8
0.6
0.4
0.2
0
0
200
400
600
800
1,000
Pixel Number

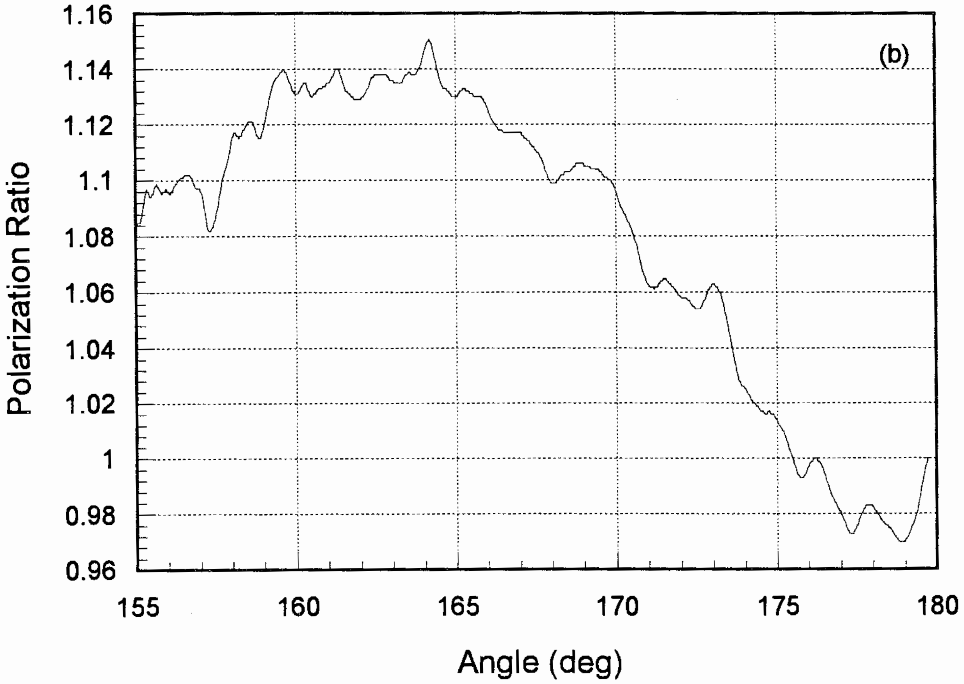
(b)
Polarization Ratio
1.16
1.14
1.12
1.1
1.08
1.06
1.04
1.02
1
0.98
0.96
155
160
165
170
175
180
Angle (deg)

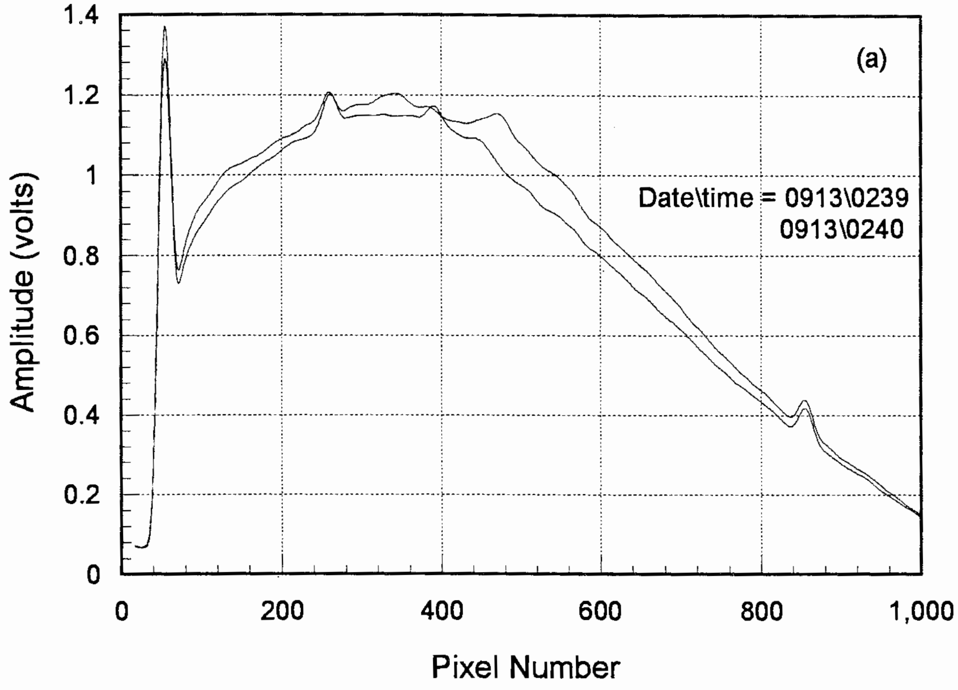
(a)
Date\time = 0913\0239
0913\0240
Amplitude (volts)
1.4
1.2
1
0.8
0.6
0.4
0.2
0
0
200
400
600
800
1,000
Pixel Number

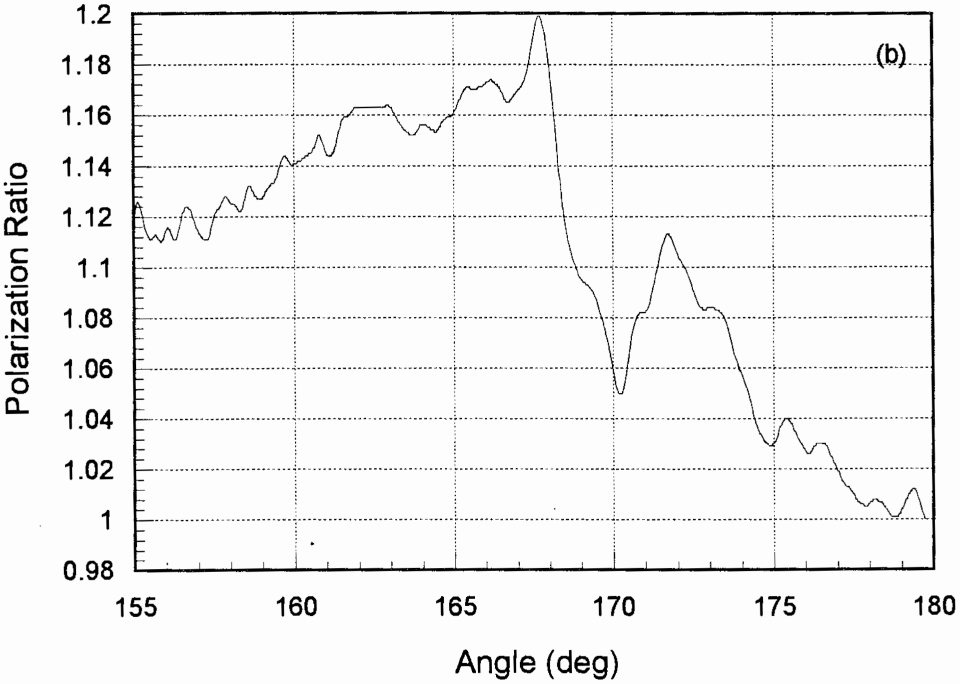
(b)
Polarization Ratio
1.2
1.18
1.16
1.14
1.12
1.1
1.08
1.06
1.04
1.02
1
0.98
155
160
165
170
175
180
Angle (deg)

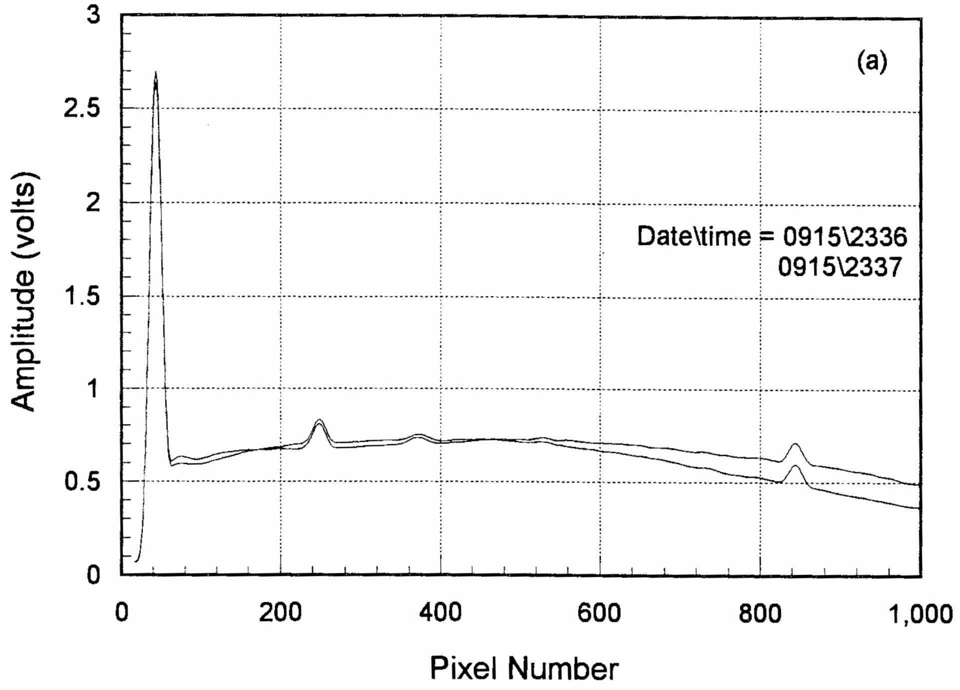
(a)
Amplitude (volts)
Pixel Number
Date\time = 0915\2336
0915\2337
0
0.5
1
1.5
2
2.5
3
0
200
400
600
800
1,000

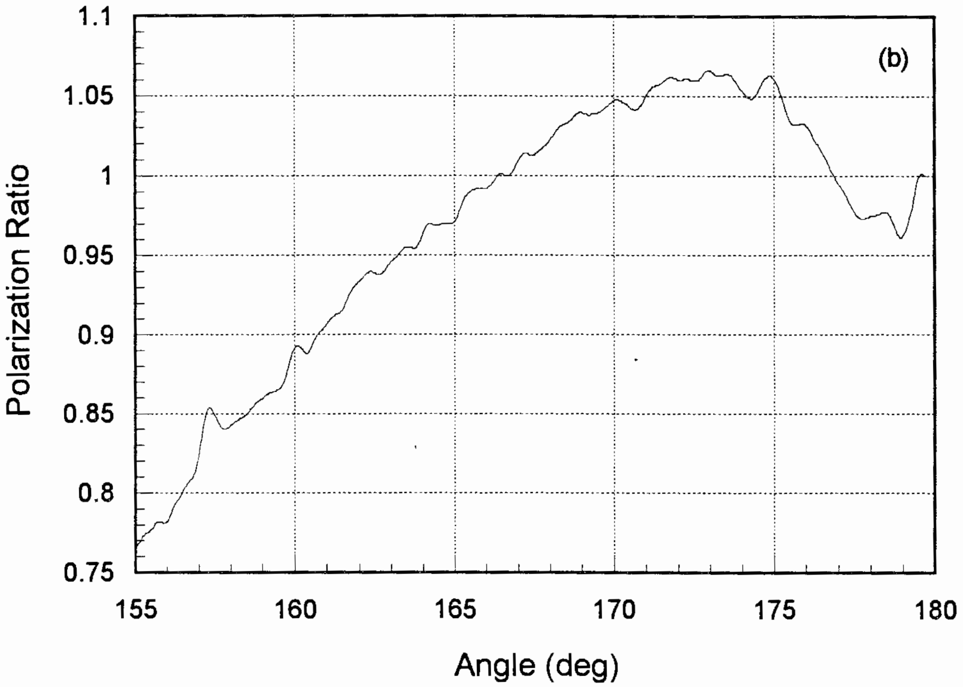
(b)
Polarization Ratio
Angle (deg)
0.75
0.8
0.85
0.9
0.95
1
1.05
1.1
155
160
165
170
175
180

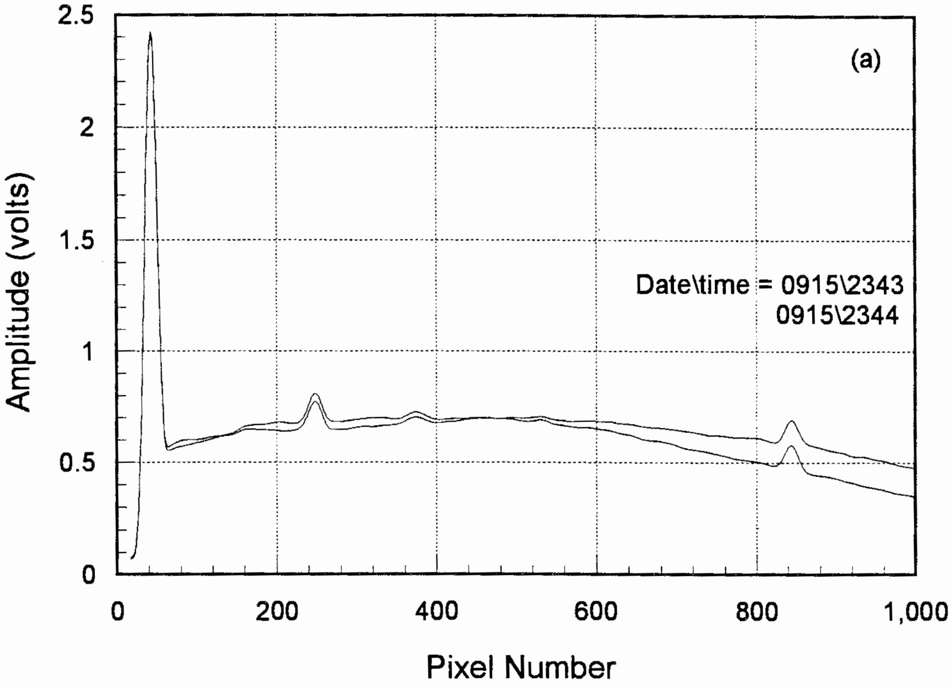
(a)
Date\time = 0915\2343
0915\2344
Amplitude (volts)
2.5
2
1.5
1
0.5
0
0
200
400
600
800
1,000
Pixel Number

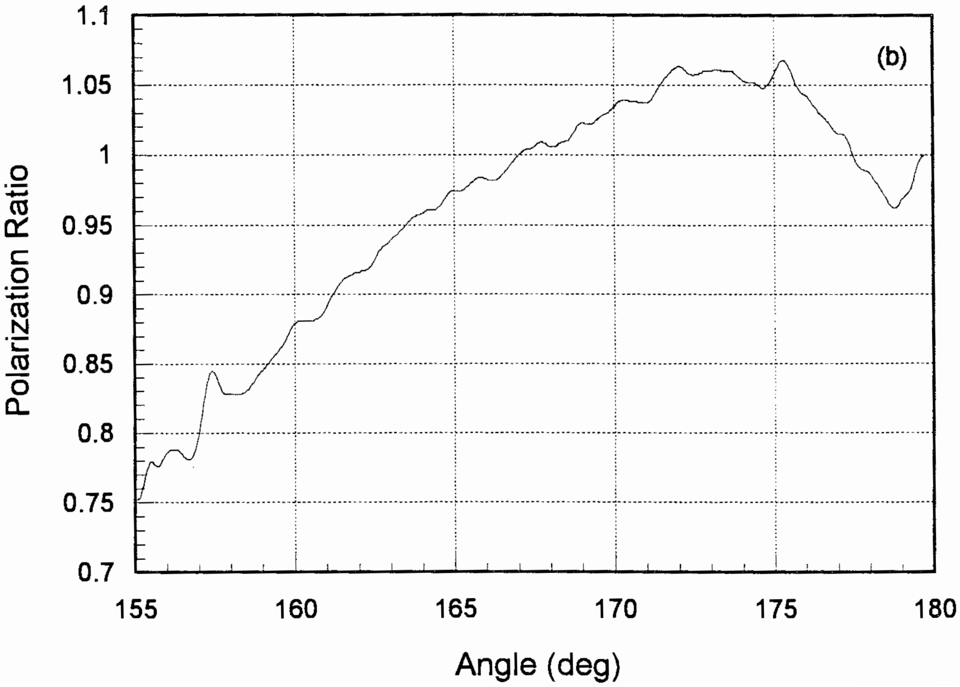
(b)
Polarization Ratio
1.1
1.05
1
0.95
0.9
0.85
0.8
0.75
0.7
155
160
165
170
175
180
Angle (deg)

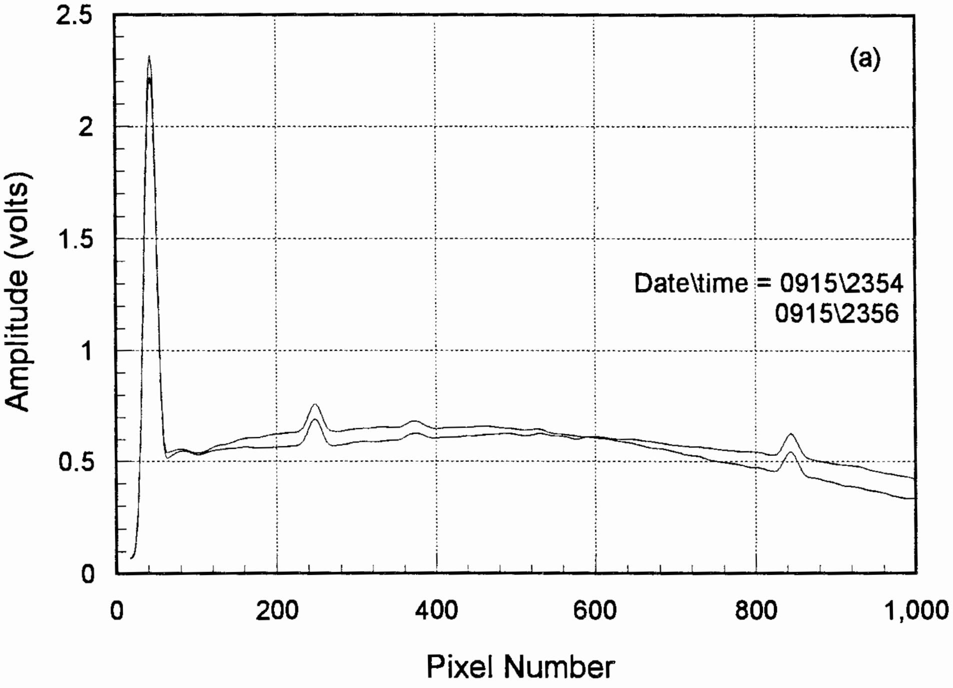
(a)
Amplitude (volts)
Pixel Number
Date\time = 0915\2354
0915\2356
0
0.5
1
1.5
2
2.5
0
200
400
600
800
1,000

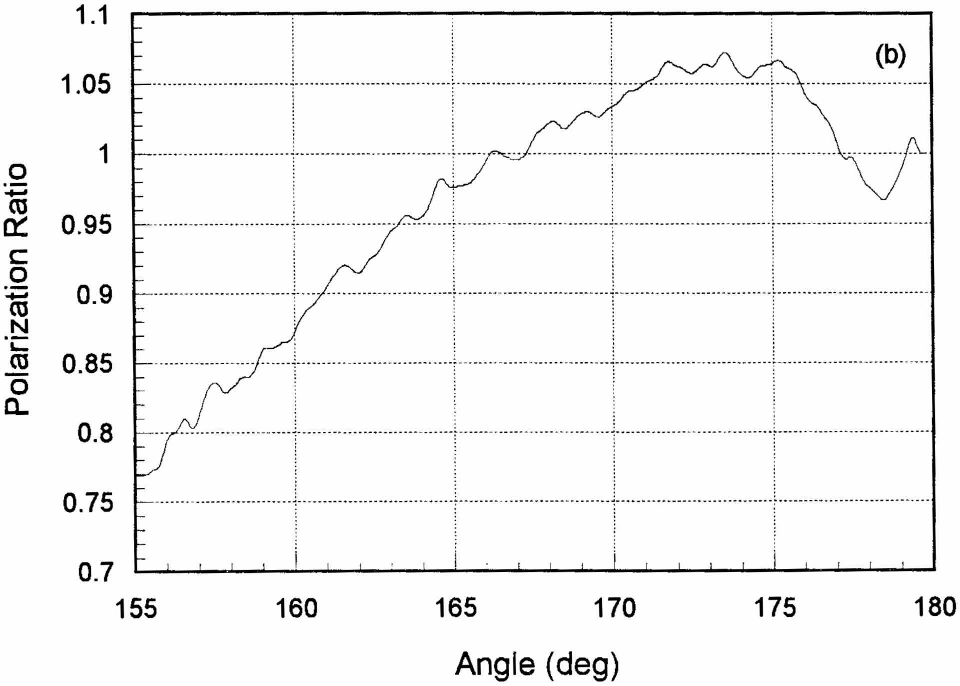
(b)
Polarization Ratio
Angle (deg)
0.7
0.75
0.8
0.85
0.9
0.95
1
1.05
1.1
155
160
165
170
175
180

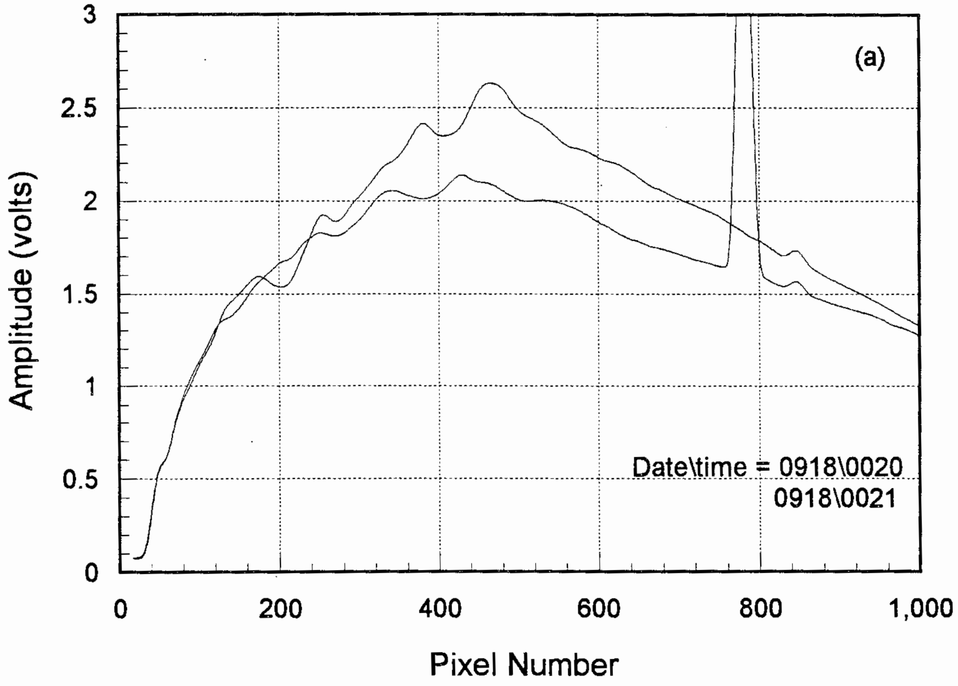
(a)
Amplitude (volts)
Pixel Number
0
0.5
1
1.5
2
2.5
3
0
200
400
600
800
1,000
Date\time = 0918\0020
0918\0021

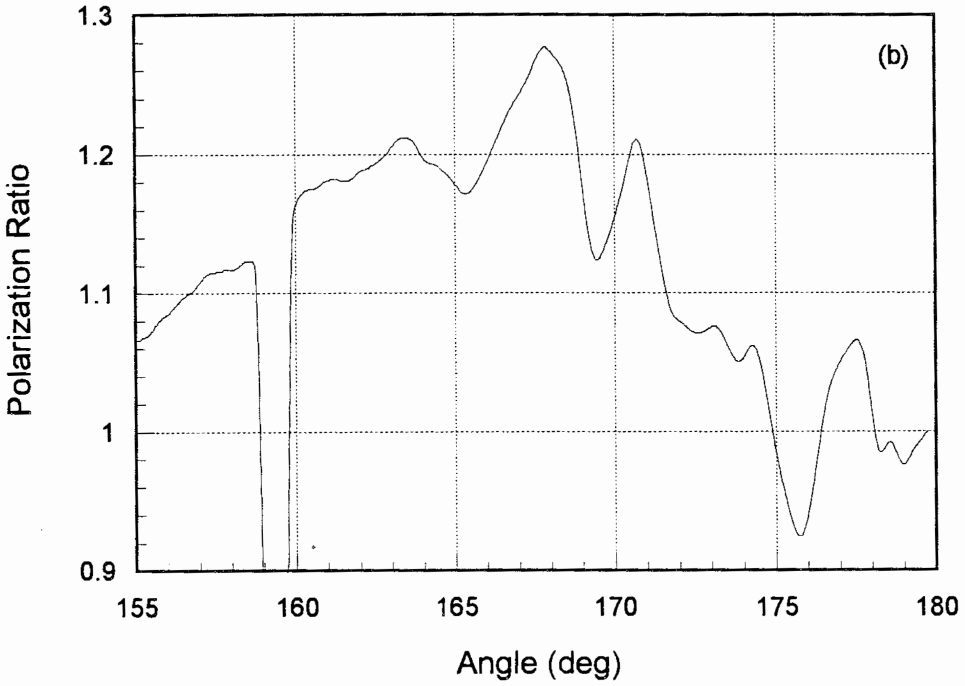
(b)
Polarization Ratio
Angle (deg)
0.9
1
1.1
1.2
1.3
155
160
165
170
175
180

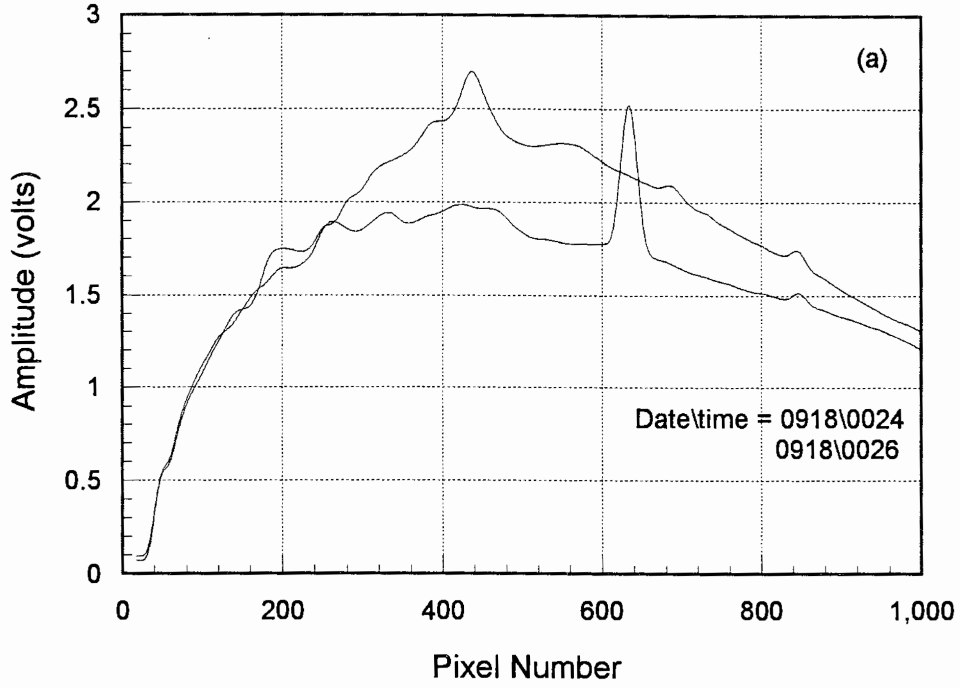
(a)
Amplitude (volts)
Pixel Number
0
0.5
1
1.5
2
2.5
3
0
200
400
600
800
1,000
Date\time = 0918\0024
0918\0026

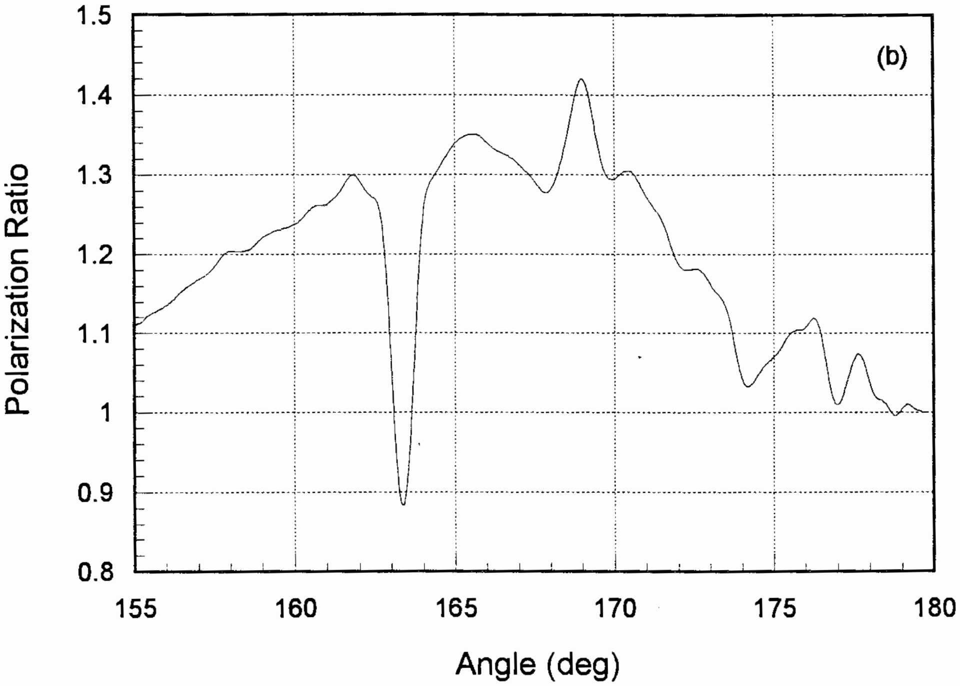
(b)
Polarization Ratio
Angle (deg)
0.8
0.9
1
1.1
1.2
1.3
1.4
1.5
155
160
165
170
175
180

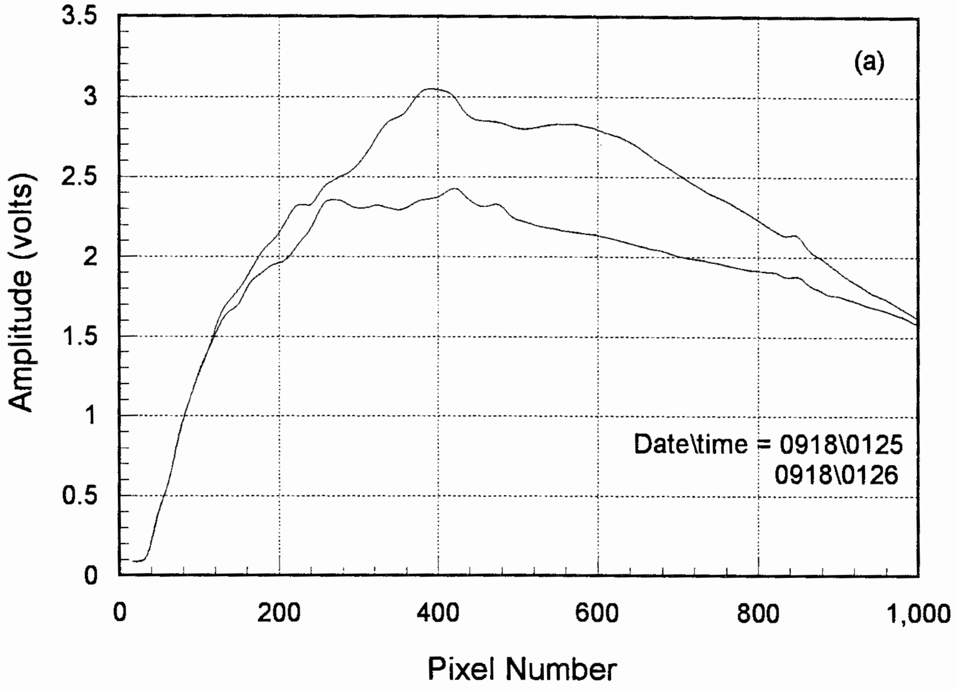
(a)
Amplitude (volts)
3.5
3
2.5
2
1.5
1
0.5
0
0
200
400
600
800
1,000
Pixel Number
Date\time = 0918\0125
0918\0126

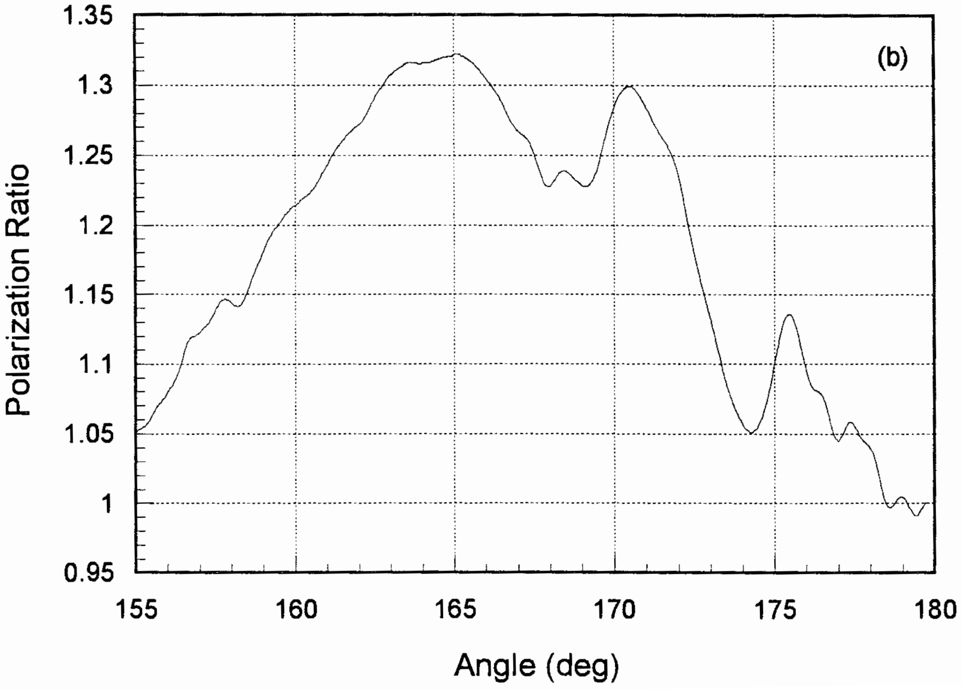
(b)
Polarization Ratio
1.35
1.3
1.25
1.2
1.15
1.1
1.05
1
0.95
155
160
165
170
175
180
Angle (deg)

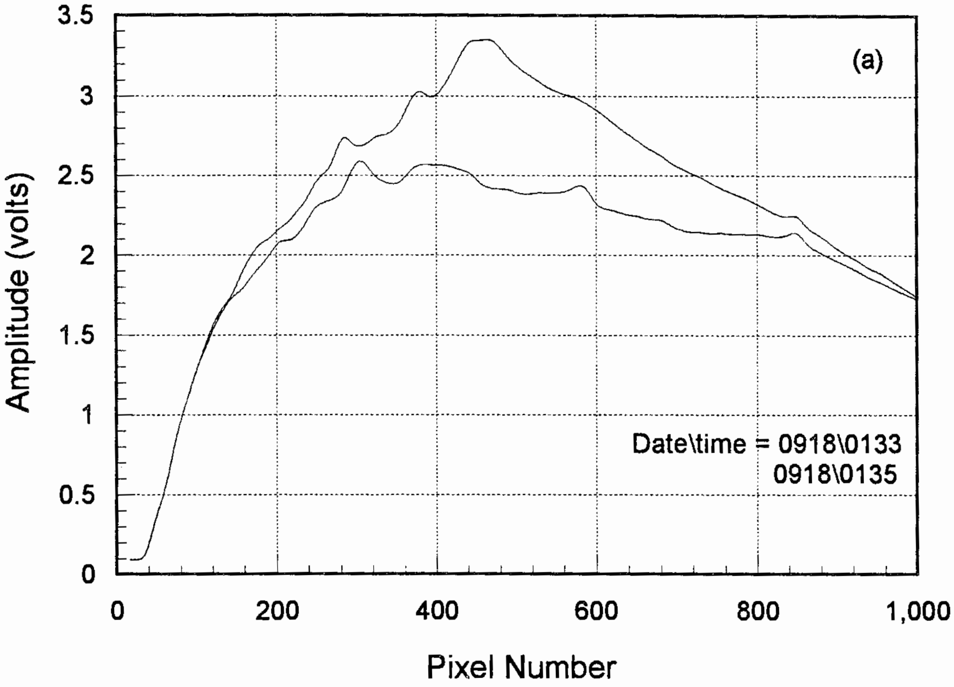
(a)
Amplitude (volts)
3.5
3
2.5
2
1.5
1
0.5
0
0
200
400
600
800
1,000
Pixel Number
Date\time = 0918\0133
0918\0135

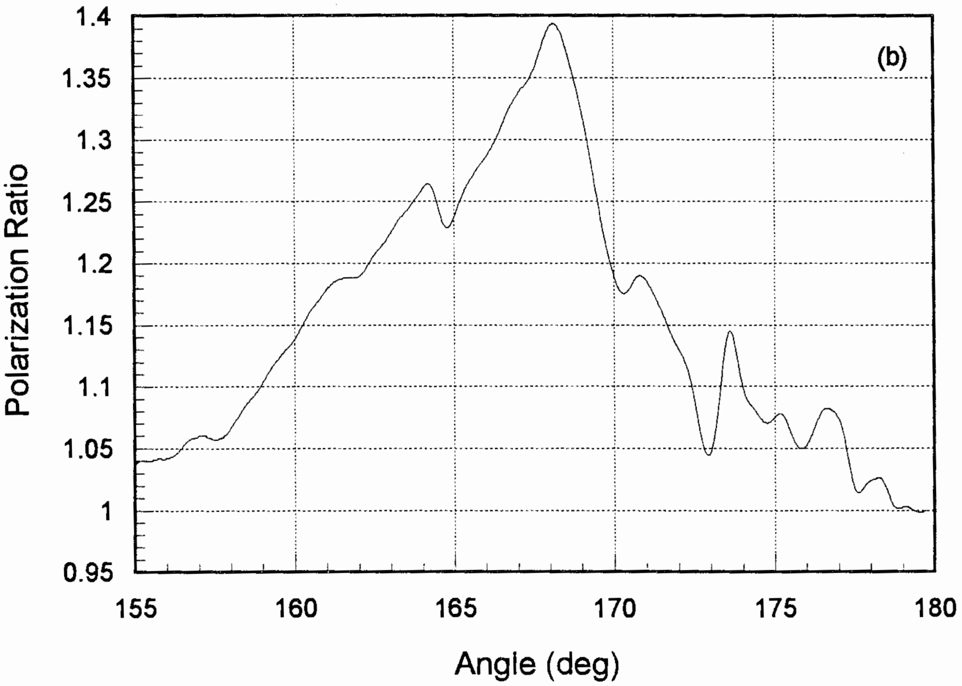
(b)
Polarization Ratio
1.4
1.35
1.3
1.25
1.2
1.15
1.1
1.05
1
0.95
155
160
165
170
175
180
Angle (deg)

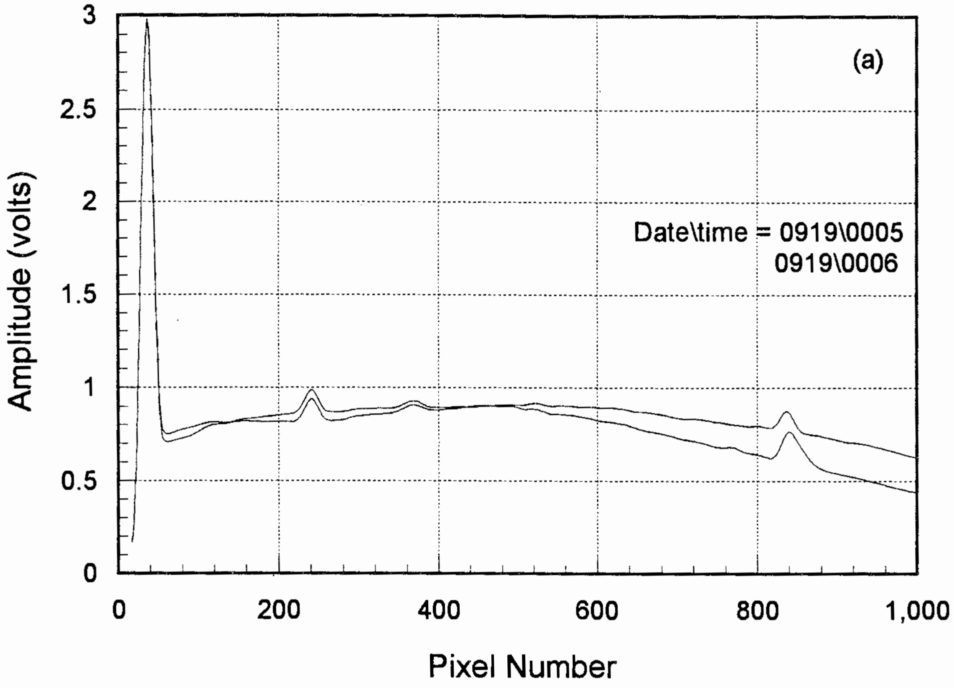
(a)
Amplitude (volts)
Pixel Number
Date\time = 0919\0005
0919\0006
3
2.5
2
1.5
1
0.5
0
0
200
400
600
800
1,000

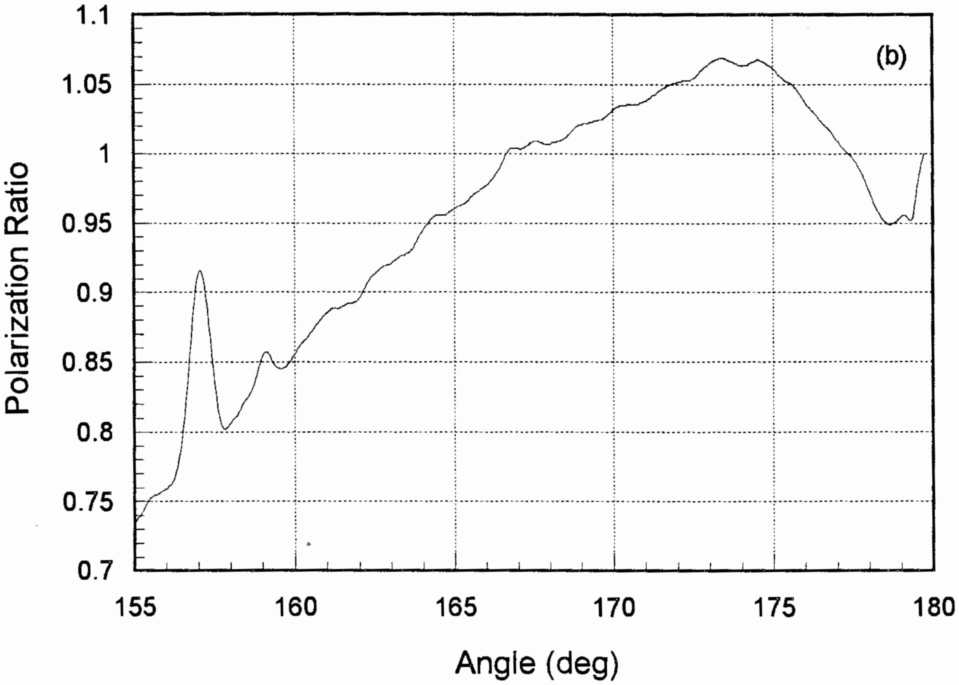
(b)
Polarization Ratio
Angle (deg)
1.1
1.05
1
0.95
0.9
0.85
0.8
0.75
0.7
155
160
165
170
175
180

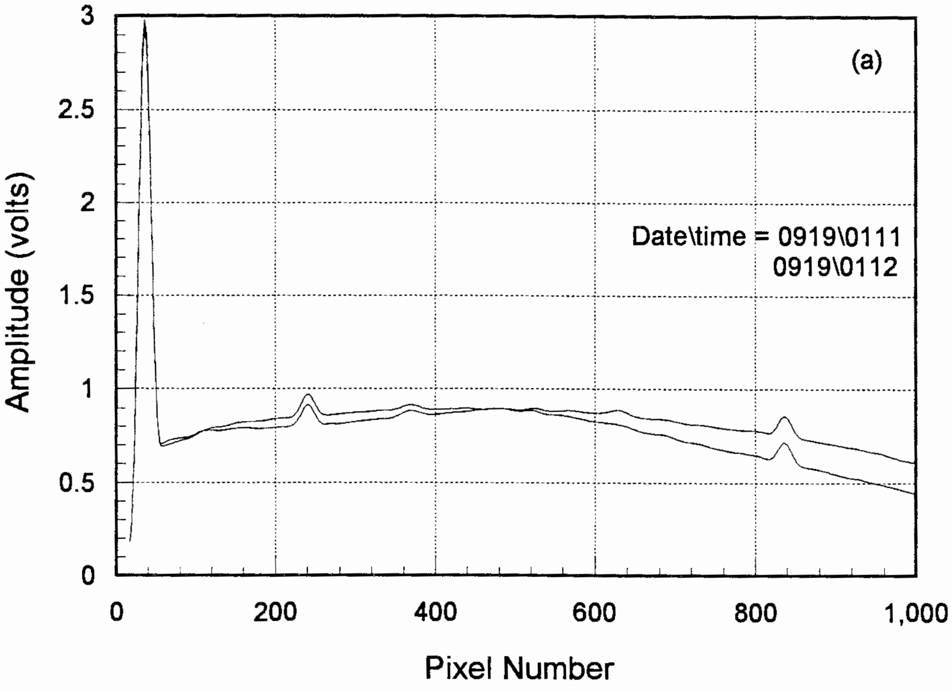
(a)
Date\time = 0919\0111
0919\0112
Amplitude (volts)
Pixel Number
3
2.5
2
1.5
1
0.5
0
0
200
400
600
800
1,000

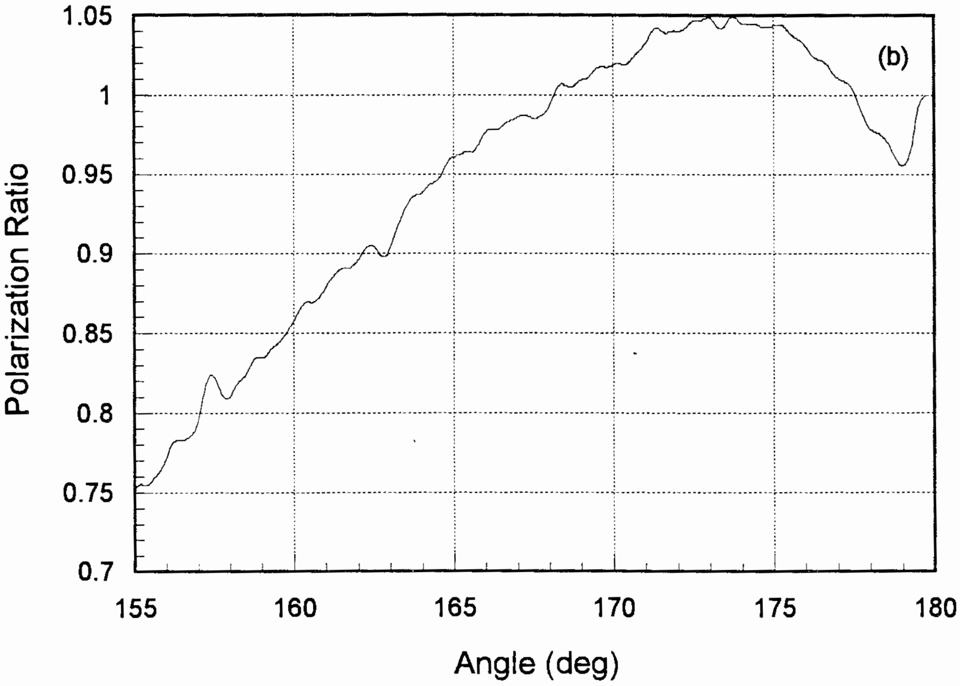
(b)
Polarization Ratio
Angle (deg)
1.05
1
0.95
0.9
0.85
0.8
0.75
0.7
155
160
165
170
175
180

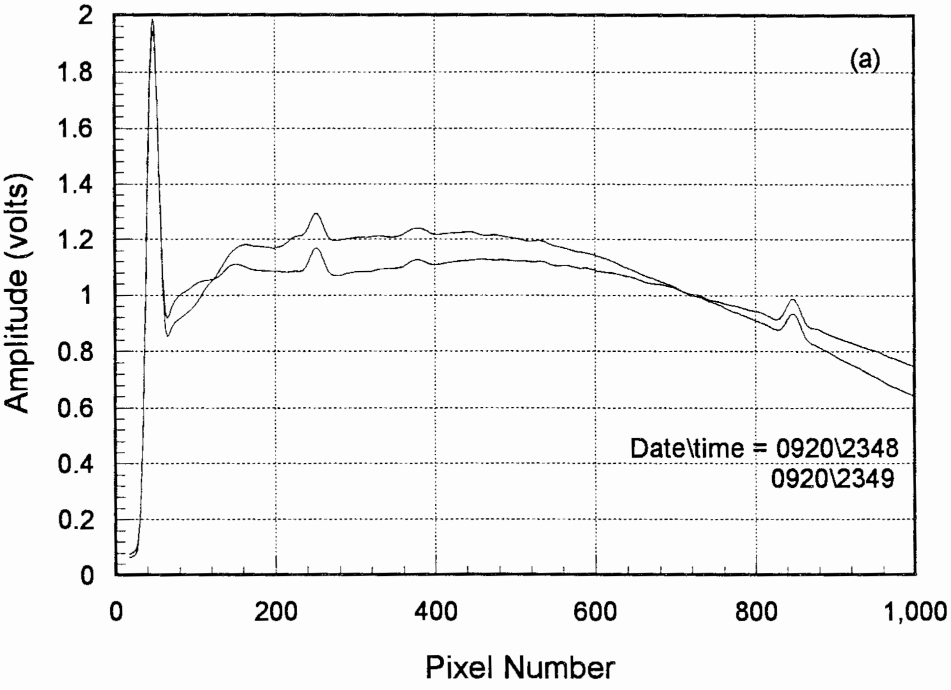
(a)
Amplitude (volts)
Pixel Number
Date\time = 0920\2348
0920\2349
0
0.2
0.4
0.6
0.8
1
1.2
1.4
1.6
1.8
2
0
200
400
600
800
1,000

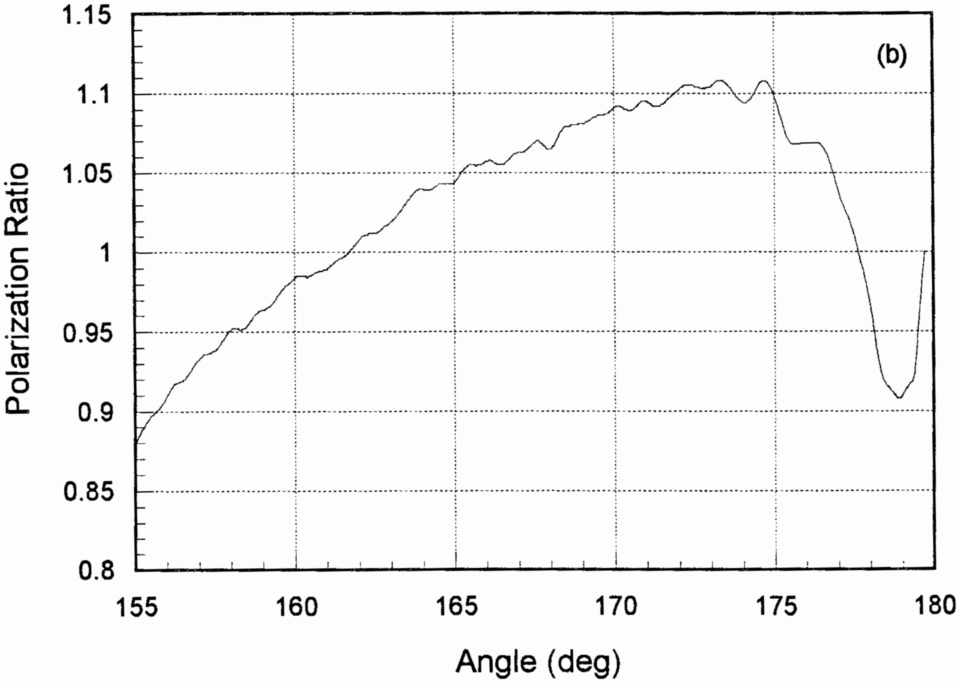
(b)
Polarization Ratio
Angle (deg)
0.8
0.85
0.9
0.95
1
1.05
1.1
1.15
155
160
165
170
175
180

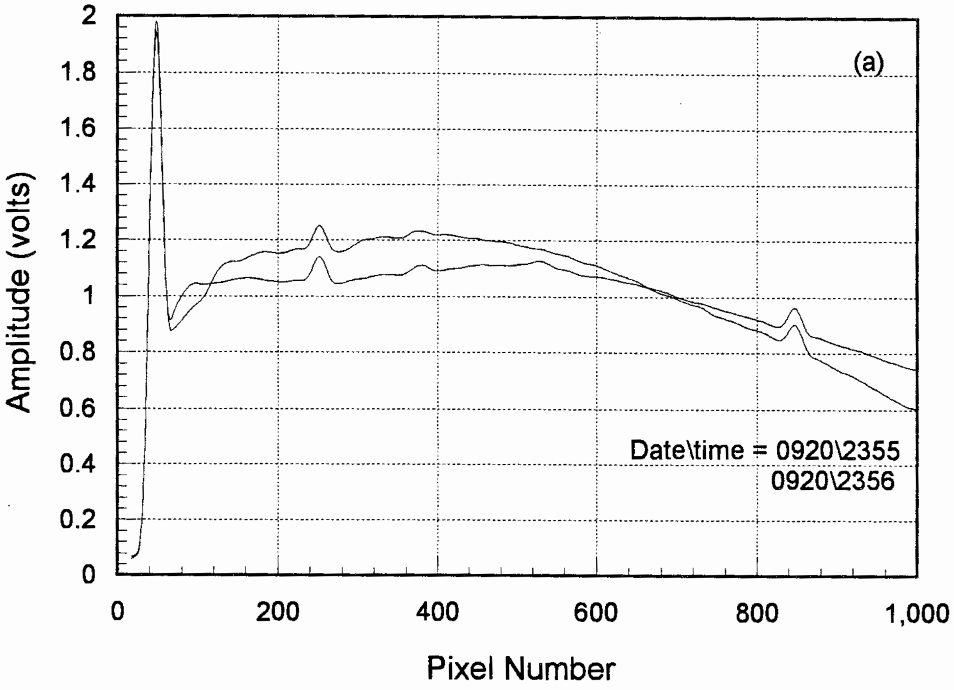
(a)
Amplitude (volts)
0
0.2
0.4
0.6
0.8
1
1.2
1.4
1.6
1.8
2
0
200
400
600
800
1,000
Pixel Number
Date\time = 0920\2355
0920\2356

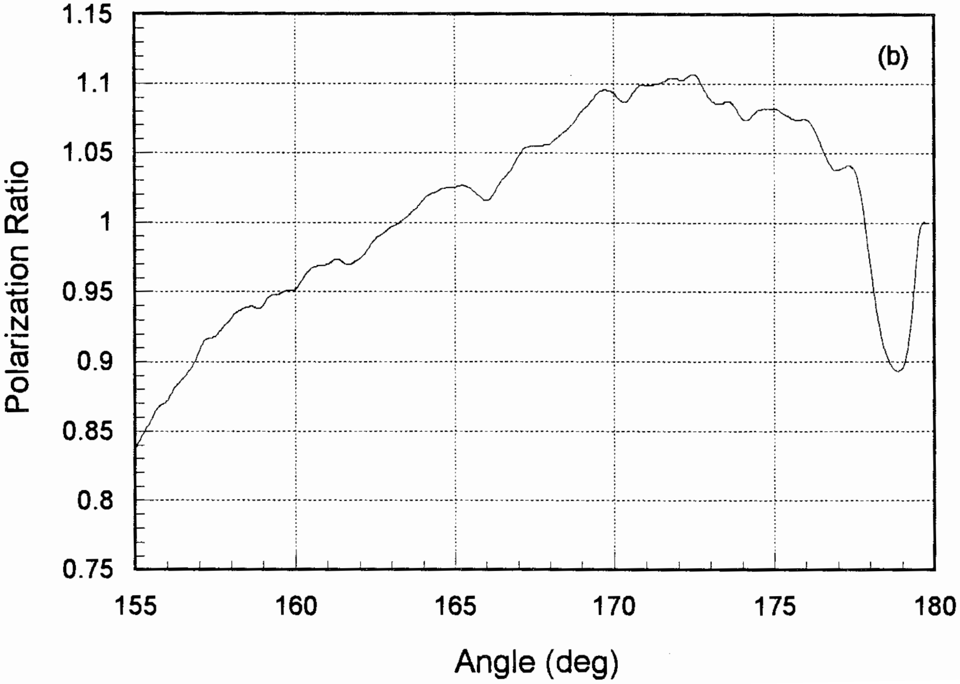
(b)
Polarization Ratio
0.75
0.8
0.85
0.9
0.95
1
1.05
1.1
1.15
155
160
165
170
175
180
Angle (deg)

VITA

Timothy D. Stevens was born in Clearfield, PA on April 25, 1967. He grew up in Lebanon, PA where he attended the Eastern Lebanon County High School and graduated in 1985. During the years between 1987 and 1990 he worked with two separate divisions of the E.I.DuPont De Nemours Company, and received an outstanding engineering achievement award for the design of an optical defect scanner for magneto-optic disks. In 1990 he obtained a Bachelor of Science degree in Electrical Engineering with Honors and Distinction from the Pennsylvania State University. He was partially funded by DuPont and Dow Chemical Company for his undergraduate work. In 1990 he received the DuPont graduate fellowship and in 1993 he received additional support from a DuPont teaching fellowship, which allowed him the opportunity to instruct a senior level electrical engineering class. He also received the outstanding student paper award from the American Geophysical Union in 1992, and a second place award at the CEDAR poster presentation in 1993. After returning from the LADIMAS campaign, which entailed operating the Penn State LAMP lidar in Norway and aboard the German research vessel RV Polarstern as it sailed from the Arctic circle down to Antarctic, he received his Masters of Science in Electrical Engineering from the Pennsylvania State University, in 1992. During his doctoral work, he has studied the atmospheric sciences with an emphasis on tropospheric aerosols, and designed and built several laser remote sensing instruments. His field research experience includes lidar measurements at the Pt. Mugu Naval Weapons Test Center, CA, both bistatic and monostatic lidar measurements at a NASA launch facility on Wallops Island, VA, and laser studies of coastal aerosols at Scripps Pier, San Diego CA, at part of the EOPACE campaign. He was funded throughout his graduate studies by a Research Assistantship under the Exploratory and Educational Grant from the Applied Research Laboratory and the Office of Naval Research. He is a member of Sigma Xi Scientific Research Society, Tau beta Pi Engineering Honor Society, The Optical Society of America, and The American Geophysical Union (AGU). He has authored and co-authored a number of scientific papers and received a Doctor of Philosophy in Electrical Engineering from The Pennsylvania State University in May 1996.